
SCUOLA DI DOTTORATO DI RICERCA
HIGH MECHANICS AND AUTOMOTIVE DESIGN AND TECHNOLOGY
(MECCANICA AVANZATA E TECNICA DEL VEICOLO)
INDIRIZZO TECNICHE E TECNOLOGIE DEL VEICOLO
XXI CICLO

TRANSITIONAL NATURAL CONVECTION REGIMES IN ENCLOSURES

Tutore scientifico

Chiar.mo Prof. Ing. Giovanni S. Barozzi

Candidato

Dott. Ing. Diego Angeli



UNIVERSITÀ DEGLI STUDI DI MODENA E REGGIO EMILIA
ANNO ACCADEMICO 2007-2008

*in memoria
di Marcello Faggioni*

Sommario in lingua italiana

Nel presente lavoro si affronta lo studio dei regimi di convezione naturale originati da sorgenti termiche confinate, e in particolare di alcune delle caratteristiche transizionali, proprie dell'evoluzione di simili sistemi al variare dei principali parametri che governano le equazioni dinamiche.

I casi in esame sono quelli di un cilindro scaldante, posto orizzontalmente e centrato in una cavità a sezione quadrata, e dell'anello tra due cilindri orizzontali concentrici. L'indagine è condotta per via numerica; si utilizza una tecnica bidimensionale di Direct Numerical Simulation, basata sulla discretizzazione ai Volumi Finiti delle equazioni di Navier-Stokes e dell'energia, secondo l'approssimazione di Boussinesq, su griglie Cartesiane, non uniformi e sfalsate. Per realizzare l'accoppiamento tra velocità e pressione, si utilizza un metodo detto *di proiezione*. Gli schemi di discretizzazione spaziale e temporale possiedono un'accuratezza globale del secondo ordine. Grazie al trattamento esplicito dei termini convettivi, le equazioni in forma discreta sono risolte tramite metodi diretti. La presenza di contorni irregolari e non allineati con la griglia è tenuta in conto mediante una tecnica originale di tipo *immersed boundary*.

Il testo è strutturato come segue. Nel primo capitolo vengono riportate le nozioni di base sui flussi di convezione naturale, assieme ad alcuni approfondimenti di argomenti non banali, a carattere fondamentale, riguardanti principalmente l'approssimazione di Boussinesq e l'analisi dimensionale.

Il secondo capitolo traccia il quadro generale entro il quale lo studio si inserisce. È inclusa un'approfondita analisi della letteratura sui maggiori risultati ottenuti finora, per quanto riguarda la convezione naturale in strati di Rayleigh-Bénard, cavità a riscaldamento laterale, anelli orizzontali e cavità contenenti sorgenti termiche.

Nel terzo capitolo viene presentata, nei suoi tratti salienti, la tecnica computazionale utilizzata per le analisi numeriche.

Nei capitoli successivi si presentano e si discutono i risultati delle analisi. Per il caso della cavità quadrata contenente un elemento scaldante cilindrico (Capitolo 4) viene riportato un quadro completo degli andamenti bidimensionali del flusso e delle transizioni, per un ampio raggio del numero di Rayleigh, Ra , e per valori selezionati del rapporto tra diametro del cilindro e dimensione laterale della cavità, e del numero di Prandtl, Pr . Si discute anche l'effetto sulla stabilità del flusso e sull'entità dello scambio termico, dell'imposizione di diverse condizioni termiche al contorno, per il caso $Pr = 0.7$. Si mostra come, per bassi valori del rapporto geometrico, le dinamiche transizionali siano dominate dal comportamento del getto termico originato dalla sorgente cilindrica; per valori più alti del parametro, invece, la configurazione del flusso e le prime biforcazioni sono determinate in primo luogo dalla formazione di uno strato di Rayleigh-Bénard soprastante la sorgente. Si puntualizza inoltre che, nel range di Pr considerato, l'influenza delle proprietà del fluido

sul comportamento asintotico del sistema è molto più evidente per i bassi valori di Pr . Lo stesso accade per quanto riguarda lo scambio termico globale. Si propone inoltre una correlazione generale che riassume tutti i dati raccolti riguardanti lo scambio termico, in termini del numero di Nusselt medio sulla superficie del cilindro, in funzione di tutti e tre i parametri del sistema.

In secondo luogo, si analizza la natura della transizione da regimi dominati dalla diffusione a regimi di trasporto convettivo, per il caso della cavità anulare tra due cilindri orizzontali concentrici, a riscaldamento differenziale (Capitolo 5). Per questo studio, si utilizzano, oltre alle simulazioni numeriche, anche strumenti di tipo analitico. I risultati sono sintetizzati in una relazione di scala, che correla tra loro gli ordini di grandezza dei valori critici dei parametri di governo, per i quali avviene la transizione.

Introduction

Natural convection stands out as an excellent thermal control technique, since it does not require any mechanical power supply. Moreover, pure thermogravitational systems are inherently self-regulating, in that the heat transfer rate increases for increasing the characteristic temperature difference of the problem. However, the heat transfer coefficients are, in general, relatively low, and this sets precise applicative limits to the exploitation of such phenomenon. Nevertheless, given the undoubtable advantages provided by these techniques, towards forced convection systems, in terms of safety, cheapness and energy saving, it is very clear that any advance in basic knowledge and technology, which can improve the efficiency of such mechanisms, is of great technological and economic interest.

The correct design of heat transfer devices based on natural convection, is crucially influenced by the possibility of predicting the convective flow patterns. Buoyancy-induced flow regimes may be very complex in nature, and highly unpredictable in terms of thermal effectiveness, in that there is a strong dependence on the geometric and thermal configuration of the system.

The design of thermogravitational systems is still based on a limited knowledge basis related to few very simple configurations. This is heuristically extrapolated to real-world systems with complex geometries, thus introducing large uncertainties. A possible technique for the enhancement of natural convective heat transfer is based on the exploitation of transitional regimes, whose prediction is however difficult, due to the inherently three-dimensional and time-varying nature of the instabilities characterizing such regimes.

Moreover, from a physical-mathematical standpoint, the coupling of the complex Navier-Stokes set of equations with buoyancy, and therefore with the energy conservation equation results in a peculiar and highly non-linear dissipative dynamical system, whose variety of solutions is still undiscovered to its major extent.

The present work deals with natural convection flow regimes arising from enclosed thermal sources, and in particular with some of the transitional features characterising the evolution of such systems, as the main parameters governing the dynamical equations are varied.

The cases of a heated horizontal cylinder centred in a square-sectioned cavity and of the annulus between horizontal concentric cylinders are investigated, by numerical means. A two-dimensional Direct Numerical Simulation technique is employed, based on a Finite Volume discretization on non-uniform, staggered Cartesian grids of the Navier-Stokes and energy equations, cast under the Boussinesq approximation. A Projection Method is used for pressure-velocity coupling. The overall accuracy of the time and space discretization schemes is second-order. Due to the explicit treatment of convective terms, the discrete equations are solved through direct methods. Irregular boundaries, not aligned with the grid, are given special treatment, and are modeled according to an original immersed

boundary technique.

The work is structured as follows. In Chapter 1, the fundamentals of natural convection flows are reviewed, together with some in-depth examination of basic but non-trivial arguments, mainly concerning the Boussinesq approximation, and dimensional analysis.

In the second chapter, the general framework of the study is traced. A thorough literature survey is presented, covering the most important results achieved so far on natural convection in Rayleigh-Bénard layers, side-heated enclosures, horizontal annuli and enclosures containing heat sources.

In the third chapter, the numerical technique is presented in full detail.

In the subsequent chapters, the results of the analyses are reported and discussed. For the case of the square cavity containing a cylindrical heating element, a complete picture of the two-dimensional flow patterns and transitions is given, for a wide range of the Rayleigh number, Ra , and for selected values of the ratio between the cylinder diameter and the enclosure side length, and of the Prandtl number, Pr . The effect of different thermal boundary conditions on flow stability and heat transfer is also discussed, for the case $Pr = 0.7$. A general correlation is also proposed, summarizing all the collected heat transfer data in terms of the average Nusselt number on the cylinder surface, as a function of all the three parameters of the system.

Moreover, the nature of the transition from diffusion-dominated regimes to convective regimes is analyzed, for the case of a horizontal annulus between concentric, differentially heated cylinders. For this study, analytical tools have been used together with numerical simulations. The results are abridged in a scale relation, which correlates the orders of magnitude of the critical values of governing parameters, for which the transition occurs.

Contents

Sommario in lingua italiana	i
Introduction	iii
1 Natural convection: basics	1
1.1 Introduction	1
1.1.1 The buoyancy force	1
1.1.2 Classification of natural convection flows	2
1.1.3 Natural convection as a heat engine	4
1.2 General formulation of the equations of convection	5
1.2.1 Continuity equation	6
1.2.2 Navier-Stokes equation	7
1.2.3 Energy equation	8
1.3 The Boussinesq approximation	11
1.3.1 Reformulation of the governing equations	11
1.3.2 Boundary conditions	13
1.3.3 Considerations on the buoyancy force	15
1.3.4 Conditions for the onset of buoyancy-induced flows	15
1.3.5 Validity of the Boussinesq approximation	16
1.4 Dimensional analysis and pure numbers	22
1.4.1 Non-dimensionalization of the governing equations.	22
1.4.2 Role of pure numbers	24
1.4.3 The Nusselt number	26
1.4.4 Scale velocities in natural convection	26
1.4.5 Ostrach's velocity scale	30
1.4.6 Dimensionless equations of natural convection	31
1.5 Some classical scaling arguments	32
1.5.1 Boundary layer along a vertical plate	33
1.5.2 Buoyant plume from a line heat source	41
1.6 Summary	43
2 Background and literature review	45
2.1 Introduction	45
2.1.1 The equations of convection as a dynamical system	45
2.1.2 Stability and bifurcations in transitional convection problems	47
2.1.3 Brief systematic of flow regimes	53
2.2 Rayleigh-Bénard convection	54

2.2.1	Onset of convection	55
2.2.2	Instability of convection rolls	55
2.2.3	Effect of lateral confinement	56
2.2.4	Oscillatory behaviours	58
2.2.5	Routes to chaos	59
2.3	Side-heated enclosure	62
2.3.1	Main flow characteristics	63
2.3.2	Stability of steady-state regimes	65
2.3.3	Transition to chaotic flow	67
2.4	The horizontal annulus	68
2.4.1	General characteristics of the flow	69
2.4.2	Fundamental studies	71
2.4.3	Flow regimes in the transition region	71
2.4.4	The low Prandtl number range	74
2.4.5	Routes to chaos	75
2.5	Enclosures containing heat sources	77
2.6	Summary	80
3	Numerical methods	81
3.1	Introduction	81
3.2	Pressure-Velocity coupling	83
3.3	Time discretization	85
3.4	Space discretization on Cartesian grids	87
3.4.1	The Finite Volume method	88
3.4.2	Computational grids	88
3.4.3	Discretization of the generic transport equation	89
3.5	Approximate Factorization	92
3.6	Treatment of irregular boundaries	94
3.6.1	Computational grids, local stencils, control volumes	94
3.6.2	Discretization of the equations on the boundary cell	96
3.6.3	Boundary conditions	98
3.6.4	Reconstruction of convective fluxes and source terms	101
3.6.5	Pressure-velocity coupling	107
3.7	Summary	108
4	Square enclosure containing a horizontal cylinder	109
4.1	Introduction	109
4.1.1	Statement of the problem	109
4.1.2	Non-dimensionalization	109
4.1.3	Governing parameters	111
4.2	Construction of the computational grids	113
4.3	Grid sensitivity analysis	115
4.4	Overview of the simulations	116
4.5	Results and discussion	117
4.5.1	Steady-state regimes and transitional behaviour for $Pr = 0.7$	118
4.5.2	Influence of the Prandtl number	129
4.5.3	Heat transfer results	132

4.6 Summary	142
5 Limits of the pseudo-diffusive regime in horizontal annular gaps	145
5.1 Introduction	145
5.2 Analytical solutions	146
5.2.1 Governing equations and boundary conditions	146
5.2.2 Solution in the case of creeping flow and pure conduction	148
5.2.3 Solution in the narrow gap limit	150
5.2.4 Validity of the narrow-gap solution	151
5.3 Scale analysis	153
5.3.1 Isothermal cylinder in an infinite medium	154
5.3.2 Horizontal annulus	159
5.4 Numerical results and discussion	160
5.5 Summary	168
Concluding Remarks	169
A Rules of scale analysis	171
B Elements of bifurcation theory	173
B.1 Introductory definitions	173
B.2 Attractors	174
B.2.1 Attractors of a flow	175
B.2.2 Attractors of a map	176
B.3 Bifurcations	176
B.3.1 Bifurcations of a fixed point	176
B.3.2 Bifurcations of a periodic orbit	178
B.4 Routes to chaos	181
B.5 Methods for the analysis of dynamical systems	183
B.5.1 Determination of attractors	183
B.5.2 Power spectra	183
B.5.3 Autocorrelation function	184
B.5.4 Lyapunov exponents	184
B.5.5 Lyapunov dimension	186
B.5.6 Phase space reconstruction	187
C Linear stability analysis	189
D Streamfunction and heatfunction	191
List of Symbols	201
Bibliography	219
Ringraziamenti	221

Chapter 1

Natural convection: basics

1.1 Introduction

Heat transfer within fluids mainly takes place through two transport phenomena, diffusion and advection. Thermal diffusion is due to the transfer of energy at atomic scales, as a consequence of random molecular activity. Advection, on the contrary, indicates the transport of energy due to macroscopic fluid motion. The combination of both phenomena, which are unlikely to be observed separately in fluids, is commonly referred to as *convection*.

Thermo-fluid dynamics problems are subdivided on the basis of the causes originating flow. In particular, if the flow is produced by the presence of an externally operated propelling device, and the thermal field inside the domain has little or no influence on it, convection is said to be *forced*. The general definition of *natural* or *free convection*, instead, is representative of all flows for which there is no forced velocity, but convection currents exist within the fluid. Such situations originate under the action of a *buoyancy force* on the fluid.

Between these two limits, there exists a range of intermediate problems, where the two processes, the forced one and the natural one, interact to produce a dynamical result, which is, in general, quite different from what would originate in the presence of only one of the two sources of flow. Such cases are filed under the definition of *mixed convection*.

1.1.1 The buoyancy force

The present work focuses on natural convection, where buoyancy forces originate the flow. A buoyancy force is determined by the simultaneous presence of:

- a) a *density gradient*;
- b) a *body force* proportional to density [1].

In the majority of cases, the body force is gravity; however, there are a number of cases involving different sources of motion, including inertial accelerations and centrifugal forces in moving systems, or Coriolis forces in atmospherical or oceanic flows. On the other hand, density gradients are mainly related to the presence of temperature gradients, given that the density of a fluid is always temperature-dependent. However, density variations can also be related to concentration gradients in mixtures and solutions.

Anyhow, under the effect of the buoyancy force, the fluid at a minor density always tends to move in opposition to the imposed external field. In the specific case of gravity,

the heavier fluid will tend to descend, being warmed in the process, while the lighter, less dense fluid will tend to rise, cooling as it moves.

This rather simple principle, which underlies natural convection processes, produces a huge variety of flow regimes and configurations, depending on fluid characteristics, system geometry and boundary conditions. Its consequences are among the most complex and, sometimes, unpredictable features of fluid dynamics.

In the following, attention will be restricted to those cases for which the density gradients are due to temperature variations, and the body force is due to a uniform gravitational field. Single-phase, Newtonian fluids will be considered only.

1.1.2 Classification of natural convection flows

In heat transfer literature [2, 3], free convection flows are traditionally classified according to the level of confinement of the system under consideration:

- *external flows*: a vast mass of fluid, not bounded by walls, is put into motion by the presence of one or more thermal sources;
- *internal flows*: the fluid flow caused by thermal sources is confined by impermeable walls;
- *partially bounded flows*: the system is confined only partially by solid walls, which, in turn, influence the flow field but limitate its extension only partially.

The classification of natural convection flows does not differ much from the classical systematic of forced flows, except that the flow is induced by thermal sources rather than being produced mechanically. Moreover, as for the case of forced heat transfer, each category is identified by some fundamental cases that, despite their elementary character, concurred to a major extent to the formation of the knowledge base on the subject.

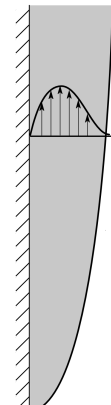
Boundary layer along a vertical plate

The simplest configuration for a buoyancy-induced flow is that of a vertical surface (a plate, a wall, etc.), kept at a certain temperature and immersed in a large reservoir of quiescent fluid at a different temperature. As clarified later (Section 1.3.4), such a situation unconditionally produces a convective flow along the surface itself.

Under certain conditions, extensively discussed in Section 1.4, a similar flow is told to have *boundary layer* character, in the sense that the flow and thermal gradients are confined in a thin layer of fluid close to the surface, outside of which the fluid remains isothermal and quiescent.

Boundary layers, either thermal or dynamic, are among the fundamental structures of convection flows; all the theoretical background underlying the study of boundary layers is easily found in specific monographs [4]. A brief derivation by scale analysis [3] of some fundamental results concerning this case is reported in Section 1.5.1, as well as the main hypotheses which lead to a radical simplification of the governing equations of convection for the boundary layer case.

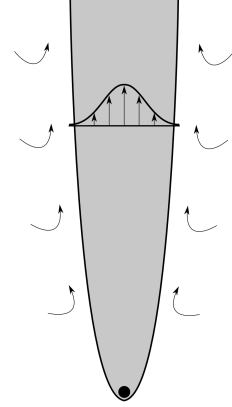
In analogy with the basic case of the forced convection flow over a flat horizontal plate [4], this example represents the prototype of external natural convection flows.



Buoyant plume from a line heat source

Another fundamental structure of external free convection flows is the so-called *buoyant jet* or *buoyant plume*, generated by a localized heat source, immersed in a quiescent fluid.

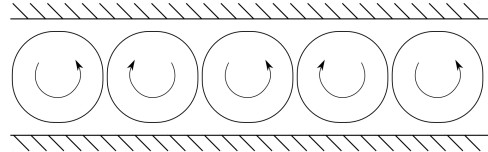
In its most basic configuration, the problem is referred to a horizontal line heat source, dissipating a constant heat power to the surrounding medium. The heated fluid rises above the source, forming a column of hot fluid. The pressure gradient created by the ascending stream constantly entrains fluid from the quiescent region. Although the width of the plume increases with distance from the source, the plume itself will eventually dissipate as a result of viscous effects and a reduction in the buoyancy force caused by the progressive cooling of the fluid in the plume.



The buoyant plume is the analogue of the heated jet in forced convection. A comprehensive summary of the main results for this case is found in [2]. Some fundamental textbooks [1] report, for this case, the definition of *free boundary flow*, because of the absence of an adjoining surface. Other texts [5] treat this case as another example of boundary layer flows, in the general sense of flows with much smaller transverse than longitudinal length scale. As a matter of fact, the same equations obtained under the boundary layer hypotheses are employed for the scale analysis reported in Section 1.5.2, following [5].

Rayleigh-Bénard convection

One of the most studied cases of natural convection is that of a layer of fluid enclosed between two parallel horizontal surfaces, the top one being cooler than the bottom one. The resulting convective flow is labeled as *Rayleigh-Bénard convection*, by the names of the two scientists who studied the phenomenon for the first time, in the early years of the XX century.



As discussed in Section 1.3.4, the presence of an inverse temperature gradient is a necessary but not sufficient condition for the onset of a buoyancy-induced flow. The temperature difference between the top and bottom walls must exceed a certain critical value [6], depending on the vertical extension of the system and on the properties of the enclosed fluid, before convective currents set on. After reaching that value, a variety of flow structures may be encountered, mainly determined by the geometry of the parallel surfaces and the conditions imposed at the horizontal boundaries. The classical representation of Rayleigh-Bénard flows consists in regularly spaced counter-rotating rolls, whose axis is aligned with the largest horizontal dimension of the domain.

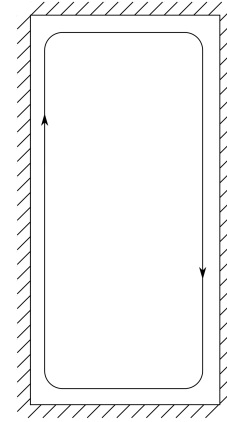
Besides being the simplest basic example of thermal instability, Rayleigh-Bénard convection is also the prototype of internal natural convection flows. In fact, although fundamental studies on such case [7] often consider a horizontally unbounded domain, on the practical side, Rayleigh-Bénard flows are frequently encountered when analyzing free convection in enclosures.

The main aspects concerning the stability of Rayleigh-Bénard convection will be covered in Chapter 2.

Rectangular enclosure heated from the side

The second fundamental example of internal natural convection is represented by an enclosure with rectangular cross-section, differentially heated at its side walls, and with the floor and the ceiling perfectly insulated. The case has a great practical importance, for it is representative of many applications, such as solar collectors, double-wall insulations, air circulations through the rooms in a building.

In a side-heated enclosure, in analogy with the boundary layer case, there is no possibility for the fluid to remain at rest when the temperature difference between the vertical walls of the enclosure is nonzero. Fluid motion is then characterized by a recirculating flow, for which fluid ascends along the hotter wall and descends along the cooler wall. Nevertheless, for sufficiently low values of the imposed temperature gradient, the buoyancy driven flow is very weak, and heat transfer is ruled by conduction across the fluid, as for the previous case.

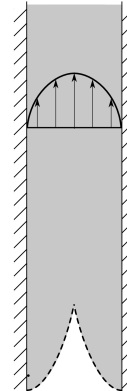


In comparison to Rayleigh-Bénard convection, side-heated enclosures represent a much younger subfield in convection heat transfer research. A good summary of the main literature results for this case is found in [3]. The main flow patterns and heat transfer characteristics for this case will be reviewed in Chapter 2.

Vertical channel between parallel walls

The classical example of partially bounded natural convection is the flow inside the vertical channel formed by two parallel and opposite heated walls.

In this case, the interaction between the boundary layers formed along the two walls is decisive for the determination of the flow characteristics. If the boundary layer thickness is much smaller than the spacing between the walls, the flow along each wall is substantially unaffected by the presence of the other wall. If, on the contrary, the boundary layer grows to the point that its thickness becomes comparable to the wall-to-wall gap width, the two flows merge into a single buoyant stream rising through the channel formed by the two walls. When this happens, in a region far from the inlet and outlet of the channel, the flow regime is called *fully developed*.



The interaction between wall layers is more complex in the case of a differentially heated channel. In fact, depending on the entity of the temperature gradient, regions of *flow reversal* may form inside the channel itself [2].

A comprehensive review of the most important results concerning free convection in channels is found in [2].

1.1.3 Natural convection as a heat engine

From the point of view of thermodynamics, natural convection can be seen as a heat engine in motion [3]. The model is shown in Figure 1.1: a vertical thermal source of temperature T_0 and height H is immersed in a fluid reservoir at temperature T_∞ , with $T_0 > T_\infty$. The air adjacent to the wall expands (becomes lighter, less dense) and rises. Heat is transported by the flow at a certain distance from the source inside the cold reservoir, until the fluid

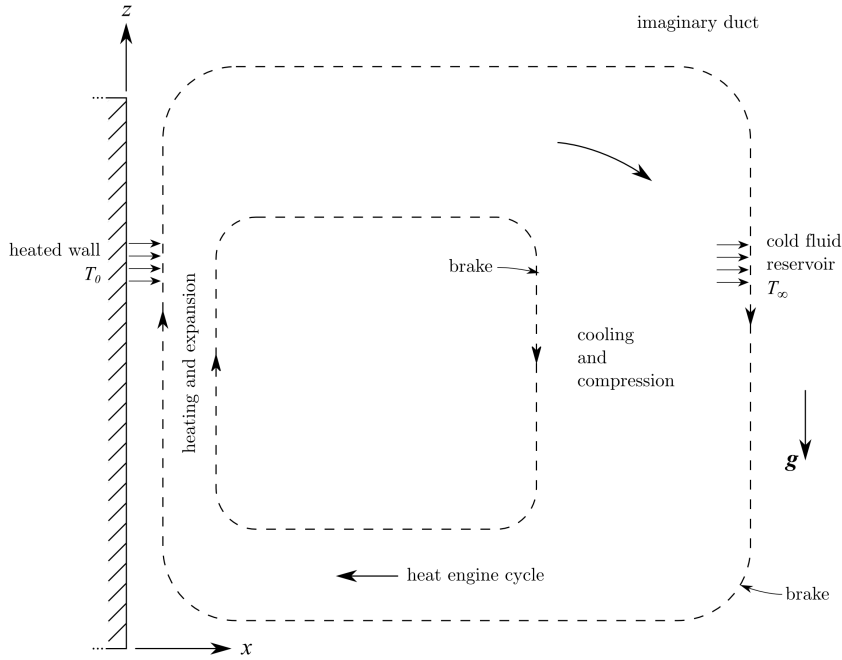


Figure 1.1: Scheme of a heat engine driven by natural convection.

redescends, cooling and increasing its density. The temperature difference between the wall and the environment determines a natural circulation cell.

The process is better understood by following a packet of fluid throughout its circulation path starting from the bottom of the vertical wall; this is heated by the wall and progressively expands, as it rises to lower pressures in the hydrostatic pressure field maintained by the reservoir. Later, along the downflowing branch of the cycle, the fluid packet is cooled by the reservoir and compressed. If the reservoir is big enough, the downflowing current will be very slow, and its temperature will again attain the value T_∞ .

The circulation loop of Figure 1.1 is equivalent to the cycle executed by the working fluid in a heat engine, operating between two reservoirs respectively at T_0 and T_∞ . This heat engine cycle should be capable of delivering work if a suitably designed propeller were inserted in the stream. The Carnot theorem would indicate the maximum net mechanical power available by the machine. However, since the characteristic velocity scales of free convection are very low, there is little chance for such a heat engine cycle to be effectively implemented. Without the presence of a device capable of extracting work, the available power is then entirely dissipated by viscous friction.

1.2 General formulation of the equations of convection

The problem of convection of heat in fluids belongs to the category of *continuum mechanics*, *i.e.* the branch of mechanics concerned with the stresses in solids, liquids and gases and the deformation or flow of these materials. In classical mechanics, a *continuous medium* is

a phenomenological model, suited to describe macroscopic physical systems, in cases where the dimensions of the observed phenomena are such that it does not resent of the molecular structure of matter, and for which it is assumed that matter is uniformly distributed. For fluids, under the *continuum hypothesis*, any volume of fluid, no matter how small, is supposed to contain a sufficient number of molecules, so that it is possible to associate with it the same macroscopic properties that are associated with the fluid in bulk.

The equations of continuum mechanics concern physical and mechanical quantities, such as temperature, stress, velocity, pressure, which, as the name itself suggests, are supposed to vary continuously from point to point throughout the medium considered. Such quantities are mathematically defined as continuous fields in \mathbb{R}^n .

For a liquid or a gas, the continuum hypothesis can be applied when the dimensions of the problem under consideration are much higher than the mean free path of the fluid molecules, ℓ_{mfp} , at a given temperature and pressure. In dimensionless terms, the continuum hypothesis is valid for very low values of the *Knudsen number*:

$$Kn = \frac{\ell_{mfp}}{L} \quad (1.2.1)$$

where L represents a characteristic length of the system under consideration.

Convection in a continuous fluid is described by three fundamental principles, namely mass conservation, Newton's second law of motion (or momentum balance) and the energy balance. The term *conservation* should be employed carefully: it applies, in fact, only to the former principle, since, in the other two laws, both dissipative effects and source terms come into play. The physical model is represented by a system of non-linear partial differential equations:

- Continuity equation
- Navier-Stokes equation
- Energy equation

Given a suitable set of initial and boundary conditions, these equations describe the spatial and temporal evolution of the fluid system from a kinetic and thermodynamic point of view. In particular, they express the relationship between the fluid velocity, and the thermodynamical properties pressure and temperature. The unknowns of the problem are thus the three components of the velocity field, $\mathbf{u} = \mathbf{u}(x, y, z, t)$, the temperature field $T = T(x, y, z, t)$, and the pressure field $p = p(x, y, z, t)$, where (x, y, z) and t designate general spatial coordinates and time.

In this section, the governing equations for convection in a continuous fluid are reported in their most complete form, and in vector notation, and then specialized for the case of a Newtonian fluid with constant viscosity and thermal conductivity.

1.2.1 Continuity equation

The continuity equation expresses mass conservation on the unit volume. Assuming that mass is neither generated, nor eliminated, the principle is formulated as follows:

$$\frac{\partial \rho}{\partial t} + \nabla \cdot (\rho \mathbf{u}) = 0 \quad (1.2.2)$$

The second term on the left hand side of equation (1.2.2) represents the net mass flux that crosses the boundary of the unit volume. Equation (1.2.2) can be recast in an alternative form by introducing the substantive (or lagrangian) derivative:

$$\frac{D\rho}{Dt} + \rho \nabla \cdot \mathbf{u} = 0 \quad (1.2.3)$$

However, the physical meaning of the latter form is less immediate than that of the former.

1.2.2 Navier-Stokes equation

In its most general form, the momentum balance on the unit volume is expressed by the following equation:

$$\frac{\partial(\rho\mathbf{u})}{\partial t} + \nabla \cdot (\rho\mathbf{u}\mathbf{u}) = \nabla \cdot \mathcal{T} + \mathbf{f} \quad (1.2.4)$$

Terms in equation (1.2.4) have the following physical meaning:

- $\frac{\partial(\rho\mathbf{u})}{\partial t}$ time variation of momentum in the unit volume
- $\nabla \cdot (\rho\mathbf{u}\mathbf{u})$ net momentum flux across the unit volume boundary
- $\nabla \cdot \mathcal{T}$ budget of surface forces acting on the unit volume boundary
- \mathbf{f} total body force acting on the unit volume

The *stress tensor*, \mathcal{T} , can be decomposed into its hydrostatic and deviatoric components, thus separating the contribution of pressure and shear stresses to the budget of surface actions:

$$\mathcal{T} = -p\mathbf{I} + \mathbf{T} \quad (1.2.5)$$

The *shear stress tensor* \mathbf{T} is symmetric, and its components τ_{ij} are related to velocity gradients. For the case of a Newtonian fluid, this relationship is linear, and it is expressed by the Stokes equation:

$$\mathbf{T} = \mu \left[2\mathbf{D} + \frac{2}{3}(\nabla \cdot \mathbf{u})\mathbf{I} \right] \quad (1.2.6)$$

where \mathbf{D} is the *strain rate tensor*, defined by the following relationship:

$$\mathbf{D} = \frac{1}{2} \left[(\nabla \mathbf{u}) + (\nabla \mathbf{u})^T \right] \quad (1.2.7)$$

As for the body force \mathbf{f} , only the gravitational field is concerned here:

$$\mathbf{f} = \rho\mathbf{g} \quad (1.2.8)$$

By inserting (1.2.5)-(1.2.8) into (1.2.4), under the assumption of constant viscosity μ one obtains:

$$\frac{\partial(\rho\mathbf{u})}{\partial t} + \nabla \cdot (\rho\mathbf{u}\mathbf{u}) = -\nabla p + \mu \left[\nabla^2 \mathbf{u} + \frac{1}{3} \nabla (\nabla \cdot \mathbf{u}) \right] + \rho\mathbf{g} \quad (1.2.9)$$

Equation (1.2.9) is generally known as the *Navier-Stokes* equation. It is easy to demonstrate that, by expanding the product derivatives and enforcing mass conservation (1.2.2) the left hand side of (1.2.9) becomes:

$$\rho \frac{\partial \mathbf{u}}{\partial t} + \rho \mathbf{u} \cdot \nabla \mathbf{u} = \rho \frac{D\mathbf{u}}{Dt} \quad (1.2.10)$$

The equivalence in (1.2.10) is more than a mere algebraic rework. It states that, in the momentum balance equation, the rate of change of momentum per unit volume is expressed by $\rho D\mathbf{u}/Dt$ rather than $D(\rho\mathbf{u})/Dt$. This result has a precise physical meaning [5]: the only reason why a particular bit of fluid is changing its momentum is that it is changing its velocity. If it is simultaneously changing its density, this is not because it is gaining or losing mass, but because it is changing the volume it occupies. The change in density is therefore irrelevant to the momentum change.

The Navier-Stokes equation can thus be modified in a more compact form, which stresses the contribution of each term to the total variation of momentum:

$$\rho \frac{D\mathbf{u}}{Dt} = \rho \left(\frac{\partial \mathbf{u}}{\partial t} + \mathbf{u} \cdot \nabla \mathbf{u} \right) = -\nabla p + \mu \left[\nabla^2 \mathbf{u} + \frac{1}{3} \nabla (\nabla \cdot \mathbf{u}) \right] + \rho \mathbf{g} \quad (1.2.11)$$

Terms in equation (1.2.11) have the dimensions of a force per unit volume, and they can be given the following physical meaning:

- $\mathbf{f}_i = \rho \frac{D\mathbf{u}}{Dt}$ inertial force
- $\mathbf{f}_p = -\nabla p$ pressure resultant
- $\mathbf{f}_v = \mu \nabla^2 \mathbf{u} + \frac{1}{3} \mu \nabla (\nabla \cdot \mathbf{u})$ viscous friction
- $\mathbf{f}_g = \rho \mathbf{g}$ gravity force

1.2.3 Energy equation

In analogy with equation (1.2.4) the energy balance on the unit volume is written as follows:

$$\frac{\partial(\rho e)}{\partial t} + \nabla \cdot (\rho \mathbf{u} e) = -\nabla \mathbf{q} + \nabla \cdot (\mathbf{u} \cdot \mathcal{T}) + \mathbf{u} \cdot \mathbf{f} + q_g \quad (1.2.12)$$

where the various terms have the following meaning:

- $\frac{\partial(\rho e)}{\partial t}$ time variation of energy in the unit volume
- $\nabla \cdot (\rho \mathbf{u} e)$ net energy advected by the flow across the unit volume boundary
- $-\nabla \mathbf{q}$ net transfer of heat by diffusion across the unit volume boundary
- $\nabla \cdot (\mathbf{u} \cdot \mathcal{T})$ total work of surface forces acting on the unit volume boundary
- $\mathbf{u} \cdot \mathbf{f}$ total work of body forces acting on the unit volume
- q_g heat generation per unit volume

By introducing the substantive derivative and enforcing (1.2.3), the left hand side of (1.2.12) is modified as follows:

$$\frac{\partial(\rho e)}{\partial t} + \nabla \cdot (\rho \mathbf{u} e) = \rho \frac{De}{Dt} \quad (1.2.13)$$

Energy e per unit mass is comprehensive of the contributions of both internal and kinetic energy:

$$e = e_{int} + e_{kin} = e_{int} + \frac{1}{2} \mathbf{u} \cdot \mathbf{u} \quad (1.2.14)$$

and, therefore, from (1.2.13) and (1.2.14), one easily obtains:

$$\rho \frac{De}{Dt} = \rho \frac{De_{int}}{Dt} + \rho \mathbf{u} \cdot \frac{D\mathbf{u}}{Dt} \quad (1.2.15)$$

The total work of surface forces on the unit volume can be decomposed as follows:

$$\nabla \cdot (\mathbf{u} \cdot \mathcal{T}) = \mathbf{u} \cdot (\nabla \cdot \mathcal{T}) + \mathcal{T} : \nabla \mathbf{u} \quad (1.2.16)$$

Equation (1.2.12) then becomes:

$$\rho \frac{De_{int}}{Dt} + \rho \mathbf{u} \cdot \frac{D\mathbf{u}}{Dt} = -\nabla \mathbf{q} + \mathbf{u} \cdot (\nabla \cdot \mathcal{T}) + \mathcal{T} : \nabla \mathbf{u} + \mathbf{u} \cdot \mathbf{f} + q_g \quad (1.2.17)$$

From the momentum balance equation (1.2.4), the following equation is easily derived:

$$\rho \mathbf{u} \cdot \frac{D\mathbf{u}}{Dt} = \mathbf{u} \cdot (\nabla \cdot \mathcal{T}) + \mathbf{u} \cdot \mathbf{f} \quad (1.2.18)$$

Equation (1.2.18) represents the balance of mechanical energy for a particle of fluid; such a balance can be subtracted entirely from (1.2.17), thus giving:

$$\rho \frac{De_{int}}{Dt} = -\nabla \mathbf{q} + \mathcal{T} : \nabla \mathbf{u} + q_g \quad (1.2.19)$$

The terms in (1.2.19) can be further specialized, in order to obtain the so called *temperature form* of the energy equation. First, it is convenient to express the whole balance in terms of enthalpy. By means of the thermodynamics definition of enthalpy:

$$h = e_{int} + \frac{p}{\rho} \quad (1.2.20)$$

one can write:

$$\rho \frac{De_{int}}{Dt} = \rho \frac{Dh}{Dt} - \frac{Dp}{Dt} + \frac{p}{\rho} \frac{D\rho}{Dt} \quad (1.2.21)$$

Then, it can be demonstrated [3] that the total variation of enthalpy for a single phase substance is expressed by the following:

$$\rho \frac{Dh}{Dt} = \rho c_p \frac{DT}{Dt} + (1 - \beta T) \frac{Dp}{Dt} \quad (1.2.22)$$

where β is the *thermal expansion coefficient*, whose definition is reported in Section 1.3.1. Hence, in terms of primitive variables, the total variation of energy can be expressed as:

$$\rho \frac{De_{int}}{Dt} = \rho c_p \frac{DT}{Dt} - \beta T \frac{Dp}{Dt} + \frac{p}{\rho} \frac{D\rho}{Dt} \quad (1.2.23)$$

The heat flux vector \mathbf{q} on the right hand side of equation (1.2.19) is defined by Fourier's law:

$$\mathbf{q} = -\lambda \nabla T \quad (1.2.24)$$

If the fluid thermal conductivity λ is constant, (1.2.24) gives:

$$-\nabla \cdot \mathbf{q} = \lambda \nabla^2 T \quad (1.2.25)$$

As for the surface forces contribution, according to (1.2.5) one has:

$$\mathcal{T} : \nabla \mathbf{u} = (-p\mathbf{I} + \mathbf{T}) : \nabla \mathbf{u} = -p\nabla \cdot \mathbf{u} + \mathbf{T} : \nabla \mathbf{u} \quad (1.2.26)$$

By substituting (1.2.23) and (1.2.26) into (1.2.19), and enforcing mass conservation (1.2.3), the energy equation becomes:

$$\rho c_p \frac{DT}{Dt} = \lambda \nabla^2 T + \beta T \frac{Dp}{Dt} + \mathbf{T} : \nabla \mathbf{u} + q_g \quad (1.2.27)$$

By plugging in the constitutive relationships (1.2.6) and (1.2.7), the remaining double inner tensor product is rewritten:

$$\mathbf{T} : \nabla \mathbf{u} = \mu \Phi \quad (1.2.28)$$

where Φ is the *viscous dissipation function*, whose complete expression is (making use of repeated indices):

$$\Phi = \left(1 - \frac{1}{2}\delta_{ij}\right) \left(\frac{\partial u_i}{\partial x_j} + \frac{\partial u_j}{\partial x_i}\right)^2 + \frac{2}{3} \left(\frac{\partial u_k}{\partial x_k}\right)^2 \quad (1.2.29)$$

Thus, the complete temperature form of the energy equation for a Newtonian fluid with constant viscosity and thermal conductivity reads as follows:

$$\rho c_p \frac{DT}{Dt} = \rho c_p \left(\frac{\partial T}{\partial t} + \mathbf{u} \cdot \nabla T \right) = \lambda \nabla^2 T + \beta T \frac{Dp}{Dt} + \mu \Phi + q_g \quad (1.2.30)$$

Terms in equation (1.2.30) are for unit volume and have the following meaning:

- $\rho c_p \mathbf{u} \cdot \nabla T$ thermal advection rate
- $\lambda \nabla^2 T$ thermal diffusion rate
- $\beta T \frac{Dp}{Dt}$ effect of compressibility on the rate of change of internal energy
- $\mu \Phi$ viscous dissipation rate
- q_g heat generation rate

It is important to observe that the balance of energy represented by equation (1.2.30) expresses, in its ultimate acceptance, the first principle of thermodynamics. In fact, it is also possible to derive it directly from the equation of the first principle itself [5], by already retaining the sole viscous dissipation term among the terms related to the work of surface and body forces. However, the present derivation has been preferred, for it clearly stresses the twofold role of the work of surface actions, represented by the decomposition in (1.2.16): one part of it ($\mathbf{u} \cdot (\nabla \cdot \mathcal{T})$) contributes to the dissipation/production of kinetic energy and the other ($\mathcal{T} : \nabla \mathbf{u}$) is dissipated into heat. Once again, such a distinction, which is rather physical, comes out naturally from the mathematical formulation of the problem.

1.3 The Boussinesq approximation

Equations (1.2.3), (1.2.11) and (1.2.30) are generally valid for any convection problem. The only hypotheses so far concern the nature of the working fluid, considered as Newtonian, and the fluid properties μ and λ , which were taken as constant for the sake of simplicity. For the study of convection and, especially, natural convection problems, it is common practice to adopt a convenient approximation of equations (1.2.2), (1.2.11) and (1.2.30), in order to reduce the amount of effort needed to tackle such a complex set of governing relationships.

The *Boussinesq approximation* consists in three fundamental assumptions:

- density is considered everywhere constant and equal to a reference value ρ_0 , except for the gravitational term in the Navier-Stokes equation (1.2.11), where the sole dependence of density on temperature is retained and assumed linear; ρ_0 is calculated at an appropriate reference state (T_0, p_0) ;
- all other fluid properties are considered constant;
- all terms at the right hand side in the energy equation are neglected, except for the diffusive term, and, in case, the source term.

1.3.1 Reformulation of the governing equations

Continuity equation

Under the hypotheses discussed above, equation (1.2.2) reduces to:

$$\nabla \cdot \mathbf{u} = 0 \quad (1.3.1)$$

which is the same as for incompressible flows. Hence, the disappearance of the inertial term transforms the mass conservation equation into a differential constraint for the velocity vector. In other words, in order to ensure mass conservation, the velocity field is bounded to be a solenoidal, *i.e.* divergence-free, vector field.

Navier-Stokes equation

Equation (1.2.11) is simplified as follows:

$$\rho_0 \frac{D\mathbf{u}}{Dt} = -\nabla p + \rho \mathbf{g} + \mu \nabla^2 \mathbf{u} \quad (1.3.2)$$

The gravitational term $\rho \mathbf{g}$ can be further reworked, given that the gravitational field is conservative, and therefore admits a potential:

$$\Psi = gz \quad (1.3.3)$$

Density can be expressed, in terms of variations from the reference state, in the form:

$$\rho = \rho_0 + \Delta\rho \quad (1.3.4)$$

The gravitational term is then modified:

$$\rho \mathbf{g} = -(\rho_0 + \Delta\rho) \nabla \Psi = -\nabla(\rho_0 \Psi) + \Delta\rho \mathbf{g} \quad (1.3.5)$$

By introducing the *piezometric pressure* P :

$$P = p + \rho_0 \Psi \quad (1.3.6)$$

the Navier-Stokes equation becomes:

$$\rho_0 \frac{D\mathbf{u}}{Dt} = -\nabla P + \mu \nabla^2 \mathbf{u} + \mathbf{g} \Delta \rho \quad (1.3.7)$$

where the term $\mathbf{f}_b = \mathbf{g} \Delta \rho$ represents the *buoyancy force*.

Equation (1.3.7) shows that, if density is considered everywhere uniform, the gravitational field has no influence on the flow. When, instead, $\Delta \rho \neq 0$, for example due to temperature variations, the term $\mathbf{g} \Delta \rho$ cannot be neglected, even if $\Delta \rho \ll \rho_0$. This is often the case in pure natural convection problems, where buoyancy is the only source of motion. In those cases, all the accelerations involved in the flow are small with respect to \mathbf{g} :

$$\left(\left| \frac{D\mathbf{u}}{Dt} \right| \ll |\mathbf{g}| \right) \quad (1.3.8)$$

For a given fluid, the value of density at a certain thermodynamic state, is always determined by an equation of state:

$$\rho = \rho(p, T) \quad (1.3.9)$$

The fractional variation of density is bound to the variation of pressure and temperature by the following:

$$\frac{d\rho}{\rho} = \frac{1}{\rho} \left(\frac{\partial \rho}{\partial p} \right)_T dp + \frac{1}{\rho} \left(\frac{\partial \rho}{\partial T} \right)_p dT \quad (1.3.10)$$

By defining the *isothermal compressibility coefficient*, χ , and the above-mentioned thermal expansion coefficient β :

$$\chi = \frac{1}{\rho} \left(\frac{\partial \rho}{\partial p} \right)_T \quad \beta = -\frac{1}{\rho} \left(\frac{\partial \rho}{\partial T} \right)_p \quad (1.3.11)$$

equation (1.3.10) can be rewritten as:

$$\frac{d\rho}{\rho} = \chi dp - \beta dT \quad (1.3.12)$$

The coefficients χ and β are fluid properties and, under the Boussinesq approximation, are designed to be constant. Hence, when density variations are only due to temperature gradients, the buoyancy term $\mathbf{g} \Delta \rho$ in equation (1.3.7) can be linearized as a function of temperature:

$$\Delta \rho = -\beta \rho_0 (T - T_0) = -\beta \rho_0 \Delta T \quad (1.3.13)$$

The classical form of the Navier-Stokes equation under the Boussinesq approximation is obtained by dividing each side of equation (1.3.7) by ρ_0 :

$$\frac{D\mathbf{u}}{Dt} = -\frac{\nabla P}{\rho_0} + \nu \nabla^2 \mathbf{u} - \mathbf{g} \beta \Delta T \quad (1.3.14)$$

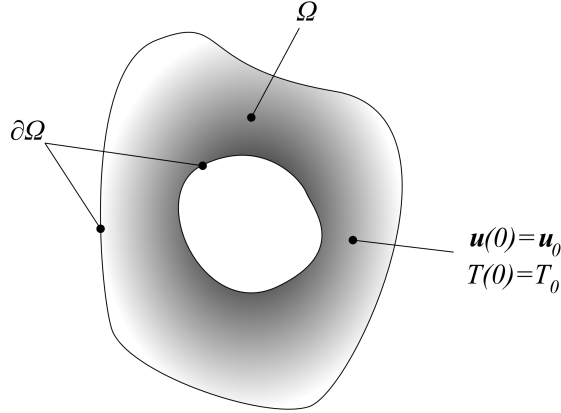


Figure 1.2: General spatial domain of integration for the governing equations of convection.

Energy equation

Applying the Boussinesq approximation and dividing each side of (1.2.30) by $\rho_0 c_p$, the energy equation becomes:

$$\frac{DT}{Dt} = \alpha \nabla^2 T + J \quad (1.3.15)$$

where:

$$J = \frac{q_g}{\rho_0 c_p} \quad (1.3.16)$$

1.3.2 Boundary conditions

The equations of convection under the Boussinesq approximation (1.3.1), (1.3.14), (1.3.15) admit solution in a given domain Ω (Figure 1.2) only if suitable initial and boundary conditions are imposed. First of all, the initial field of all time-dependent variables must be specified univocally:

$$\mathbf{u}(x, y, z, 0) = \mathbf{u}_0(x, y, z) \quad (1.3.17)$$

$$T(x, y, z, 0) = T_0(x, y, z) \quad (1.3.18)$$

where the functions \mathbf{u}_0 and T_0 represent the spatial distribution of velocity and temperature at the initial time. It must be stressed that pressure does not appear explicitly as a time-dependent variable of the problem, and therefore it does not require an initial condition.

In analogy with [8], the following general formulation of the dynamical conditions on the boundary $\partial\Omega$ is proposed:

- Dirichlet condition on velocity

$$\mathbf{u} = \bar{\mathbf{u}} \quad (1.3.19)$$

- Neumann condition on velocity

$$-P\hat{\mathbf{n}} + \mu \nabla \mathbf{u} = \bar{T} \quad (1.3.20)$$

where $\bar{\mathbf{T}} = (\bar{T}_\xi, \bar{T}_\eta, \bar{T}_\zeta)$ is the vector of boundary stresses. Condition (1.3.20) is expanded as follows:

$$-P + \mu \frac{\partial u_\eta}{\partial \eta} = \bar{T}_\eta \quad (1.3.21)$$

$$\mu \frac{\partial u_\xi}{\partial \eta} = \bar{T}_\xi \quad (1.3.22)$$

$$\mu \frac{\partial u_\zeta}{\partial \eta} = \bar{T}_\zeta \quad (1.3.23)$$

For natural convection cases, the boundary conditions on velocity are typically of two kinds. Zero velocity is prescribed either at solid walls or at far-field free boundaries:

$$\mathbf{u} = \mathbf{0} \quad (1.3.24)$$

For semi-confined flows, instead, the value of pressure must be specified:

$$P = \bar{P} \quad (1.3.25)$$

When condition (1.3.25) is enforced, it is usually assumed that also $\bar{\mathbf{T}} = 0$, and the relative boundary condition on the velocity components is easily recovered from (1.3.20).

As for the boundary conditions on temperature, they can be summarized by the following general form:

$$aT + b \frac{\partial T}{\partial \eta} = c \quad (1.3.26)$$

with coefficients a , b and c opportunely dimensioned for the equation to be homogeneous.

For natural convection cases, the fundamental boundary conditions at a solid wall are:

- *T condition* - imposed wall temperature (Dirichlet condition):

$$T = \bar{T} \quad (1.3.27)$$

- *Q condition* - imposed wall heat flux density (Neumann condition):

$$-\lambda \frac{\partial T}{\partial \eta} = q_w \quad (1.3.28)$$

Moreover, the homogeneous Neumann condition is used for adiabatic walls or for pressure boundaries:

$$\frac{\partial T}{\partial \eta} = 0 \quad (1.3.29)$$

More complex conditions, expressed in the form (1.3.26), may occur when treating conjugate heat transfer cases with conductive walls.

1.3.3 Considerations on the buoyancy force

Equation (1.3.7) identifies the buoyancy force as the driving force of natural convection. With reference to a fluid particle of volume ΔV , the buoyancy force is expressed:

$$\mathbf{F}_b = \mathbf{g}(\rho - \rho_0)\Delta V = \mathbf{g}\Delta\rho\Delta V \quad (1.3.30)$$

It can be observed that (1.3.30) does not express the Archimedes force acting on the particle, but the resultant (*weight - buoyancy*) for a particle with density ρ immersed in a hydrostatic field at constant density ρ_0 . This resultant is not at all related to the force actually acting on a fluid particle in a variable density field (this is always the case in natural convection problems).

If ρ varies spatially (and temporally) inside the domain of interest, the Archimedes force acting on the fluid element of volume ΔV is given by the local vertical gradient of the hydrostatic pressure p_h , which, in turn, depends on the instantaneous vertical density gradient:

$$\mathbf{F}_A = - \left(\frac{\partial p_h}{\partial z} \right) \Delta V \hat{\mathbf{k}} \quad (1.3.31)$$

The true *local* value of \mathbf{F}_b is the sum of \mathbf{F}_A and the weight force \mathbf{F}_g :

$$\mathbf{F}_g = \mathbf{g}\rho\Delta V \quad (1.3.32)$$

Hence, the definition (1.3.30) corresponds to a conventional estimate of the buoyancy force, where a reference value of the hydrostatic pressure gradient is substituted to the its actual value. This reference value has necessarily to be representative of the problem, and this makes the choice of the reference state (p_0, T_0) a crucial feature when addressing a natural convection problem.

On the other hand, formulation (1.3.30) of the buoyancy force has enormous practical utility, in that it is a premise for the successive linearization step (1.3.13), through which the variable density is replaced by temperature. Otherwise, a state equation should be added to the governing system of equations. This explains the universality of the Boussinesq approximation as a tool for the analysis of natural convection problems.

1.3.4 Conditions for the onset of buoyancy-induced flows

This section is dedicated to point out the rotational character of buoyant flows, following Tritton [5]. The vorticity, ω , of a fluid motion is defined as:

$$\omega = \nabla \times \mathbf{u} \quad (1.3.33)$$

It is thus a vector quantity defined at every point within the flow, and represents the rotation rate of a fluid particle. Applying the curl operation throughout equation (1.3.14), one obtains the *vorticity equation*:

$$\frac{D\omega}{Dt} = \omega \cdot \nabla \mathbf{u} + \nu \nabla^2 \omega - \beta \mathbf{g} \times \nabla(\Delta T) \quad (1.3.34)$$

Horizontal components of the temperature gradient contribute to the last term, representing vorticity generation. The vorticity so generated is also horizontal, but orthogonal to the temperature gradient. In other words, the torque associated with the tendency for a

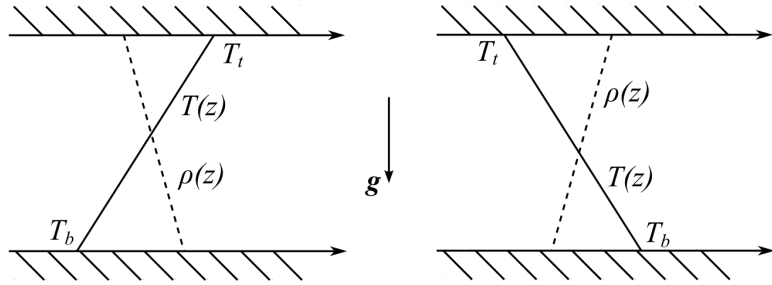


Figure 1.3: Density and temperature gradients in the Rayleigh-Bénard problem: stable (left) and inverse (right).

hotter fluid element to rise and a colder to fall, produces a rotation about a horizontal axis. Therefore, the presence of a horizontal temperature gradient does not allow any equilibrium condition with the fluid at rest, whereas, in situations where the temperature gradient is only vertical, equilibrium solutions are feasible, in that the vorticity generation term reduces to zero. Such equilibrium may be stable or unstable. The rest configuration is governed by equation (1.3.14), with terms involving velocity set to zero:

$$-\frac{\nabla P}{\rho_0} = g\beta\Delta T \quad (1.3.35)$$

Equation (1.3.35) is the hydrostatic balance equation for non-isothermal conditions and expresses a balance between pressure and buoyancy forces. Since the curl of a the pressure gradient is identically zero, it must be:

$$\nabla \times (\beta\mathbf{g}\Delta T) = \beta\mathbf{g} \times \nabla(\Delta T) = \mathbf{0} \quad (1.3.36)$$

Condition (1.3.36) is satisfied only when $\nabla(\Delta T)$ is vertical: this is the necessary condition for the hydrostatic equilibrium (1.3.35) to be verified.

In most of the elementary cases reviewed in Section 1.1.2, the onset of convection is not subject to any constraint. This is obvious for the vertical plate and for the side-heated enclosure, where the imposed temperature gradient is horizontal. Although with minor evidence, this is also the case for the line heat source, since in the immediate surroundings of the source itself, the conditions of non-zero horizontal gradient are verified.

On the contrary, an equilibrium state in the presence of a density gradient, satisfying (1.3.35) is represented by the solution of the Rayleigh-Bénard problem. With reference to Figure 1.3, if the temperature at the bottom T_b is lower than that at the top T_t , a stable density gradient is created, due to conduction, with linearly decreasing density with increasing height. However, even in case $T_t < T_b$, *i.e.* with *inverse* temperature and density gradients, a stable equilibrium solution may exist. This is justified by the above considerations.

1.3.5 Validity of the Boussinesq approximation

In this section, the conditions under which the Boussinesq approximation is valid are discussed, in the specific context of natural convection.

The Boussinesq approximation actually embodies several hypotheses not immediately evident. Therefore, the simplified forms of the governing equations (1.3.1)-(1.3.15) obtained under this approximation, although suitable for a significantly wide range of problems, may fail at times because of complexities related to the particular case studied (for example if the flow involves more than a single length scale). Even if this is not necessarily the case when dealing with laboratory experiences or standard engineering applications, to consider the various hypotheses subjacent to the Boussinesq approximation may become very useful in specific cases. Under those circumstances, the correct choice of the governing parameters can be driven by the following analysis, originally performed by Tritton [5]. In fact, as discussed later on in Section 1.4, the Boussinesq approximation underlies the statement that dynamical similarity of natural convective flows depends on two dimensionless parameters, the Grashof number and the Prandtl number. When the approximation fails, additional parameters should necessarily come into play.

It is assumed that, in a fluid system of length scale L , flow is produced by the introduction of temperature differences of order ΔT_{ref} . The principal criteria for the applicability of the Boussinesq approximation are [5]:

$$A = \beta \Delta T_{ref} \ll 1 \quad (1.3.37)$$

$$B = g \rho \chi L \ll 1 \quad (1.3.38)$$

$$C = \frac{g \beta L}{c_p} \ll 1 \quad (1.3.39)$$

$$D = \frac{g \beta L T_0}{c_p \Delta T_{ref}} \ll 1 \quad (1.3.40)$$

where T_0 is the absolute temperature at the reference state (T_0, p_0) . Supplementary criteria related to the assumption that the fluid properties $(\mu, \lambda, c_p, \beta)$ are constant will be discussed later. If conditions (1.3.37)-(1.3.40) are valid, the Boussinesq equations (1.3.1)-(1.3.15) apply directly.

In order to examine the significance of relationships (1.3.37)-(1.3.40) and their role in the frame of the Boussinesq approximation, it is convenient to choose pressure and temperature as the two independent thermodynamic variables, in terms of which other thermodynamic properties can be expressed. Restricting to steady-state conditions, pressure and temperature can be expressed in the form of sums:

$$p = p_0 + p_h + p' \quad (1.3.41)$$

$$T = T_0 + T' \quad (1.3.42)$$

where:

- p_0, T_0 absolute pressure and temperature values at a reference state
- p_h hydrostatic pressure variation, function of the vertical coordinate z only
- p', T' variations associated with flow, general functions of position

In particular, T' encompasses all variations in T , whether associated with the boundary conditions or arising from internal effects such as viscous dissipation or adiabatic compression-expansion.

The density can now be written:

$$\rho = \rho_0 + \rho_h + \rho' \quad (1.3.43)$$

where:

- ρ_0 density value at the reference state (p_0, T_0)
- ρ_h departure from ρ_0 due to variations of the hydrostatic pressure, $\rho_h = \rho_h(p_h)$
- ρ' further departure from ρ_0 associated with flow, $\rho' = \rho'(p', T')$

It will be shown how the general equations of motion, reduce to the Boussinesq approximation taking the continuity (1.2.2), Navier-Stokes (1.2.11) and energy (1.2.30) equations in turn.

For steady flows, the continuity equation (1.2.2) is:

$$\mathbf{u} \cdot \nabla \rho + \rho \nabla \cdot \mathbf{u} = 0 \quad (1.3.44)$$

by indicating with U a representative velocity scale, which is unknown *a priori*, the orders of magnitude of the two terms are:

$$\mathbf{u} \cdot \nabla \rho \approx \frac{(\rho_h + \rho')U}{L} \quad (1.3.45)$$

$$\rho \nabla \cdot \mathbf{u} \approx \frac{(\rho_0 + \rho_h + \rho')U}{L} \quad (1.3.46)$$

The approximation of (1.2.2) to the incompressible form (1.3.1) requires that:

$$\frac{\rho_h}{\rho} \ll 1, \quad \frac{\rho'}{\rho} \ll 1 \quad (1.3.47)$$

When these are true, the dependence of ρ on p and T can be linearized to give:

$$\rho_h = \rho_0 \chi p_h, \quad \rho' = \rho_0 (-\beta T' + \chi p') \quad (1.3.48)$$

and (1.3.47) is then equivalent to the following three conditions:

$$\chi p_h \ll 1 \quad (1.3.49)$$

$$\beta T' \ll 1 \quad (1.3.50)$$

$$\chi p' \ll 1 \quad (1.3.51)$$

Taking these in turn, condition (1.3.49) depends on the order of magnitude of p_h which can be estimated by the hydrostatic balance:

$$\nabla p_h = (\rho_0 + \rho_h) \mathbf{g} \simeq \rho_0 \mathbf{g} \Rightarrow p_h \approx \rho_0 g L \quad (1.3.52)$$

giving:

$$\chi p_h \approx \rho_0 g \chi L = B \ll 1 \quad (1.3.53)$$

As from (1.3.49) the condition $B \ll 1$ is fulfilled when the hydrostatic pressure p_h is assumed not to be dependent on the value of the absolute pressure.

The principal requirement for condition (1.3.50) is evidently that:

$$\beta T' \approx \beta \Delta T_{ref} = A \ll 1 \quad (1.3.54)$$

i.e. that the imposed temperature difference should not directly produce excessive density differences. This is valid either when the effects of temperature on density are fully neglected (forced convection) or when adopting the Boussinesq approximation. Flow-induced variations must also be subject to this restriction. The dimensionless parameter A is also designed *Gay-Lussac number*, Ga [9].

It will be shown below that being condition (1.3.51) much less restrictive than (1.3.49) and (1.3.50), it does not need separate consideration.

Turning to the Navier-Stokes equation (1.2.11), the conditions to put $\rho \cong \rho_0$ in the inertial term and to reduce the viscous term to $\mu \nabla^2 \mathbf{u}$ are again (1.3.47). Hence, for steady flows, subtracting out from (1.2.11) the hydrostatic balance (1.3.52), one has:

$$\rho_0 \mathbf{u} \cdot \nabla \mathbf{u} = -\nabla p' + \mu \nabla^2 \mathbf{u} - \rho' \mathbf{g} \quad (1.3.55)$$

The Boussinesq linearization also implies that:

$$\rho' = -\rho_0 \beta T' \quad (1.3.56)$$

which is valid if:

$$\chi p' \ll \beta T' \quad (1.3.57)$$

The order of magnitude of p' is indicated by equation (1.3.14); the second term in this will be, at most, of the same order as the largest of other terms. For natural convection cases, the buoyancy term is dominant:

$$\frac{p'}{L} \approx g \rho_0 \beta T' \Rightarrow \chi p' \approx \chi g \rho_0 \beta T' L \Rightarrow g \rho_0 \chi L = B \ll 1 \quad (1.3.58)$$

Hence, condition B (1.3.38) also implies that compressibility effects on density variations can be neglected with respect to temperature effects. Condition (1.3.51), whose consideration was postponed above, will then be automatically fulfilled if (1.3.57) is valid, in that the product $\beta T'$ is limited, in turn, by condition A (1.3.37).

Dividing the pressure variations into their hydrostatic and hydrodynamic parts, as in (1.3.41), the steady form of the energy equation (1.2.30) reads:

$$\rho c_p \mathbf{u} \cdot \nabla T = \lambda \nabla^2 T + \beta T \mathbf{u} \cdot \nabla p_h + \beta T \mathbf{u} \cdot \nabla p' + \mu \Phi + q_g \quad (1.3.59)$$

To obtain the Boussinesq form (1.3.15), the third, fourth and fifth term of (1.3.59) must be neglected. In the following, each term at the right hand side of (1.3.59) will be compared in turn with the advective term by order of magnitude.

Firstly:

$$\frac{\beta T \mathbf{u} \cdot \nabla p_h}{\rho c_p \mathbf{u} \cdot \nabla T} \approx \frac{\beta T_0 p_h}{\rho_0 c_p T'} \approx \frac{g \beta T_0 L}{c_p T'} \quad (1.3.60)$$

supposing that $T' = O(\Delta T_{ref})$, the criterion to neglect the third term of (1.3.59) is (1.3.40), *i.e.* that D is small.

As for the fourth term:

$$\frac{\beta T \mathbf{u} \cdot \nabla p'}{\rho c_p \mathbf{u} \cdot \nabla T} \approx \frac{\beta T_0 p'}{\rho_0 c_p T'} \quad (1.3.61)$$

The order of p' is given by (1.3.58). The criterion for the neglect of the fourth term in (1.3.59) is then:

$$\frac{\beta T_0}{c_p} g \beta L \ll 1 \quad (1.3.62)$$

Since the product βT_0 is of order 1 for gases and is $\ll 1$ for other fluids, (1.3.62) will be fulfilled whenever condition C (1.3.39) is fulfilled.

It is worthy to note that the above discussion provides a rigorous justification for the choice of c_p , in place of c_v , in the temperature form of the energy equation (1.2.30). In fact, by using the couple (T, v) as the independent thermodynamic variables, and then developing the internal energy, one could analogously formulate an equation for $c_v DT/Dt$, instead of $c_p DT/Dt$, but an extra term would arise, whose negligibility would be guaranteed only when the difference $(c_p - c_v)$ is itself negligible (*i.e.* only for liquids) [5].

Finally, the reduction of (1.2.30) to the Boussinesq form (1.3.15) requires the viscous dissipation term to be negligible. For a Newtonian, incompressible fluid with constant viscosity μ , such a term is expressed as:

$$\mu \Phi = \mu \frac{\partial u_i}{\partial x_j} \left(\frac{\partial u_i}{\partial x_j} + \frac{\partial u_j}{\partial x_i} \right) \quad (1.3.63)$$

its order of magnitude estimate being:

$$\mu \Phi \approx \mu \frac{U^2}{\delta^2} \quad (1.3.64)$$

where δ is the length scale appropriate to viscous effects. The distinction between δ and L is made so that the discussion applies either for viscous flow ($\delta \approx L$) or for boundary layer cases ($\delta \ll L$). In natural convection, the balance between the buoyancy force and the viscous force gives:

$$\mu \frac{U}{\delta^2} \approx \rho g \beta T' \quad (1.3.65)$$

Hence:

$$\frac{\Phi}{\rho c_p \mathbf{u} \cdot \nabla T} \approx \frac{\rho g \beta T' U L}{\rho_0 c_p T'} \approx \frac{g \beta L}{c_p} = C \ll 1 \quad (1.3.66)$$

The criterion for viscous dissipation to have a negligible effect on the thermal balance is that this is sufficiently small; *i.e.* it is relationship (1.3.39).

It is also useful to consider in which situations the source term q_g in equation (1.2.30) can be neglected, other than the trivial case for which there is no internal heat generation. Apparently, no simple and immediate criteria are available, and, moreover, a comparison between the generative term and the advective term would require the definition of an appropriate scale velocity (see Section 1.4.4). It is however reasonable to suppose that a neglect criterion for q_g could be based on the comparison between the term itself with the diffusive term of (1.2.30), in the sense that a possible neglect of localized heat generation with respect to conduction effects would include the neglect of the temperature gradients

associated with heat generation itself, and, consequently, of the buoyancy forces related to it. In this case, the criterion could be expressed as follows:

$$\frac{q_g}{\lambda \nabla^2 T} \approx \frac{q_g L^2}{\lambda T'} \approx \frac{q_g L^2}{\lambda \Delta T_{ref}} \ll 1 \quad (1.3.67)$$

Criterion (1.3.67) specifies that the characteristic temperature difference of the generative phenomenon, expressed by the ratio $q_g L^2 / \lambda$ is small compared to the reference temperature difference ΔT_{ref} based on boundary conditions. In case generative processes were dominant, significantly influencing the thermal asset of the system, the ratio (1.3.67) would be of order 1.

The physical meaning of conditions (1.3.37)-(1.3.40) is finally summarized.

- (A) The requirement $A \ll 1$ (1.3.37) states that the relative variation of ρ produced by the thermal expansion of the fluid is negligible in the continuity (1.2.2) equation and in the Navier-Stokes equation (1.2.11), let alone the buoyancy term. As previously mentioned, this implies that the imposed temperature differences must not be excessive, for either forced or natural convection cases under the Boussinesq approximation.

This also implies that the imposed restrictions on the energy equation (1.2.30) for its Boussinesq form to be valid include condition $A \ll 1$ (1.3.37), in that it limits the temperature variations T' associated with the flow, to be of order ΔT_{ref} .

- (B) Condition $B \ll 1$ (1.3.38) ensures that: (i) the relative variation of ρ produced by fluid compressibility under hydrostatic action is negligible in the continuity equation (1.2.2); (ii) compressibility effects are negligible with respect to the effects of temperature on density in the momentum equation (1.2.11).
- (C) Condition $C \ll 1$ (1.3.39) guarantees that: (i) the effect of flow-related pressure variations on the temperature field is negligible; (ii) viscous dissipation has little influence on the temperature field.
- (D) Condition $D \ll 1$ (1.3.40) ensures that the influence of hydrostatic effects on the temperature field can be neglected. If (1.3.37), (1.3.38), (1.3.39) are fulfilled, but not (1.3.40), the Boussinesq approximation still applies, but the variable T should be substituted with a “potential temperature”, the scale of variation of such a temperature then taking the place of ΔT_{ref} . This can be the case for many geophysical problems, where the hydrostatic pressure variation due to large height differences produces significant effects on density [5]. However, in such cases, it is very likely that also conditions (1.3.37)-(1.3.39) lose their validity; in particular, the parameters B and C may become not negligible in large-scale geophysical systems (atmospheric flows, flows inside stars and planets, etc.). Nevertheless, for laboratory scale systems, B , C and D are usually very small.

It is worthy to note that the parameters B and C are independent, but they tend to assume the same order of magnitude. For example, for an ideal gas:

$$\beta = \frac{1}{T}, \quad \chi = \frac{1}{\rho R_t T} \quad \Rightarrow \quad \frac{B}{C} = \frac{1}{G} \approx 1 \quad (1.3.68)$$

where G is the *Grüneisen ratio*.

In addition to the various effects considered so far, the Boussinesq approximation requires effective constancy of the physical properties of the fluid; that is of μ , λ , c_p and β . The temperature and pressure variations must not be so large as to produce large fractional changes in these quantities. Often the fulfillment of this requirement will go along with the fulfillment of the requirement of small fractional density changes. However, in principle, any parameter having a much larger temperature or pressure coefficient than density needs special consideration.

In this context, the work of Gray and Giorgini [10] stands out as a classical reference. From that study, it is inferred that constant property analyses are accurate only within a restricted range of temperature variations. For instance, in air at 15°C and at atmospheric pressure, ΔT_{max} should not exceed 28.6°C . Beyond that value, it is foreseen that the effects of the variability of thermophysical properties are not irrelevant.

In particular, for gases, β varies with T^{-1} , μ and λ with $T^{0.65}$. On the other hand, for water and most liquids, μ strongly depends on temperature.

In most of the cases, particular attention is given to the choice of an appropriate temperature T_{ref} , at which the physical properties are evaluated. When the temperature differences are small, the *film temperature* can be safely chosen as the reference:

$$T_{ref} = T_{film} = T_0 + 0.5\Delta T_{ref} \quad (1.3.69)$$

When the range of variability of temperature is greater, one may resort to different choices of T_{ref} other than T_{film} [2], or to the property ratio method [4]. A specific problem is that regarding water around its density maximum, which occurs at 4°C , at atmospheric pressure. In this case, the Boussinesq approximation does not apply.

1.4 Dimensional analysis and pure numbers

The study of thermofluids systems gains significant benefit from the theory of dimensional analysis. By applying dimensional analysis to the governing equations of a general physical problem, one can extract the dimensionless parameters (or *pure numbers*) which are most relevant to it. Such parameters provide a qualitative indication of the nature of the problem itself. Moreover, two problems that are *physically similar* [11], and are characterized by the same dimensionless numbers, are also governed by the same dimensionless equations, and can be studied in identical way.

If two systems are geometrically similar (*i.e.* have different spatial extension but identical proportions), kinematically similar (*i.e.* same ratio between velocity vectors in correspondent points of the domain), dynamically similar (*i.e.* parallelism and proportionality between force vectors in correspondent points), have thermal similarity (*i.e.* proportionality between thermal fields) and same initial and boundary conditions, they behave in a totally equivalent manner. From a mathematical standpoint, this implies the possibility to identify a number of characteristic quantities for the physical problem and, consequently, to perform a non-dimensionalization of the governing equations.

1.4.1 Non-dimensionalization of the governing equations.

For a given convection problem, the reference quantities are chosen as follows:

L characteristic length: it is a relevant linear dimension for the problem. Relevant means that the chosen quantity should correctly represent the dimension of the field of variability of the dependent variables;

U characteristic velocity: its value is known when dealing with forced and mixed convection problems, but not in pure natural convection cases;

ΔT_{ref} *characteristic temperature difference*: it is normally determined by thermal boundary conditions;

Δp_{ref} *characteristic pressure difference*: for incompressible flows, it can be arbitrarily chosen; the most common choice poses $\Delta p_{ref} = \rho_0 U^2$.

Each variable is divided by its reference quantity, thus obtaining different forms of the governing equations, where each dimensionless term is multiplied by a coefficient that, if the reference values are chosen correctly, provides an estimate of the order of magnitude of the term itself as a whole, contemporarily conserving dimensional consistency. The variable, dimensionless part of the terms results instead of order $O(1)$.

At this step of the process, equation (1.3.14) takes the form below:

$$\left[\rho_0 \frac{U^2}{L} \right] \left(\frac{\partial \mathbf{u}}{\partial t} + \mathbf{u} \cdot \nabla \mathbf{u} \right) = - \left[\rho_0 \frac{U^2}{L} \right] \nabla P + \left[\mu \frac{U}{L^2} \right] \nabla^2 \mathbf{u} - \left[\frac{\rho_0 g \beta \Delta T_{ref}}{L^2} \right] \hat{\mathbf{g}} T \quad (1.4.1)$$

where:

$$\hat{\mathbf{g}} = \frac{\mathbf{g}}{g} \quad (1.4.2)$$

represents the unit vector associated with gravity, and all the variables are to be intended as dimensional. In particular, it has been posed:

$$T = \frac{\Delta T}{\Delta T_{ref}} \quad (1.4.3)$$

The order of magnitude of the forces represented by equation (1.4.1) can be evaluated as follows:

- $f_i \approx \rho_0 \frac{U^2}{L}$ inertial force
- $f_p \approx \rho_0 \frac{U^2}{L}$ pressure resultant
- $f_v \approx \mu \frac{U}{L^2}$ viscous friction force
- $f_b \approx \frac{\rho_0 g \beta \Delta T_{ref}}{L^2}$ buoyancy force

Analogously, for the energy equation (1.3.15)

$$\left[\frac{\rho c_p U \Delta T_{ref}}{L} \right] \left(\frac{\partial T}{\partial t} + \mathbf{u} \cdot \nabla T \right) = \left[\frac{\lambda \Delta T_{ref}}{L^2} \right] \nabla^2 T \quad (1.4.4)$$

and the coefficients represent, respectively:

- $v_{ad} \approx \frac{\rho c_p U \Delta T_{ref}}{L}$ advective transport velocity
- $v_{cd} \approx \frac{\lambda \Delta T_{ref}}{L^2}$ conductive transport velocity

Finally, by dividing all terms by the coefficient of the left hand side (f_i , v_{ad}), completely dimensionless forms of the governing equations are obtained, where the numerical coefficients represent ratios between the intensities of the forces or processes listed above:

$$\nabla \cdot \mathbf{u} = 0 \quad (1.4.5)$$

$$\frac{\partial \mathbf{u}}{\partial t} + \mathbf{u} \cdot \nabla \mathbf{u} = -\nabla P + \frac{1}{Re} \nabla^2 \mathbf{u} - \frac{Gr}{Re^2} \hat{\mathbf{g}} T \quad (1.4.6)$$

$$\frac{\partial T}{\partial t} + \mathbf{u} \cdot \nabla T = \frac{1}{Pe} \nabla^2 T \quad (1.4.7)$$

The dimensionless parameters appearing in (1.4.6)-(1.4.7) are defined as follows:

- $Re = \frac{UL}{\nu}$ Reynolds number
- $Pr = \frac{\nu}{\alpha}$ Prandtl number
- $Pe = Re Pr = \frac{UL}{\alpha}$ Péclet number
- $Gr = \frac{g\beta \Delta T_{ref}}{\nu^2}$ Grashof number

As an alternative to Gr , one can employ the products:

- $Ra = Gr Pr = \frac{g\beta \Delta T_{ref}}{\nu \alpha}$ Rayleigh number
- $Bo = Ra Pr = \frac{g\beta \Delta T_{ref}}{\alpha^2}$ Boussinesq number

1.4.2 Role of pure numbers

Equations (1.4.5)-(1.4.7) do not differ from the dimensionless forms of the governing equations of forced convection, with the exception of the buoyancy term in (1.4.6). The parameters defined above can be given the meaning of ratios between orders of magnitude of forces or intensities of heat transport processes:

- $Re \approx \frac{f_i}{f_v}$ (inertia/viscous friction)
- $Pe \approx \frac{v_{ad}}{v_{cd}}$ (advection/diffusion)
- $\frac{Gr}{Re^2} \approx \frac{f_b}{f_i}$ (buoyancy/inertia)

Being defined by the ratio between two fluid properties, the Prandtl number is a fluid property as well, which can be interpreted as follows:

- $Pr = \frac{\nu}{\alpha}$ (momentum and vorticity diffusion rate/heat diffusion rate)

By estimating the orders of magnitude of the dimensionless parameters, it is possible to evaluate which terms of equations (1.4.5)-(1.4.7) are negligible.

The order of magnitude of the Reynolds number commonly discriminates between the following extremes:

- $Re \ll 1 \Rightarrow f_i \ll f_v$ viscous flow
- $Re \gg 1 \Rightarrow f_i \gg f_v$ potential flow

In the former case, the inertial term of (1.4.6) is negligible. In the latter case, the viscous term of equation (1.4.6) may be regarded as negligible in terms of bulk flow; however, the action of viscous friction can never be neglected in those zones adjacent to solid walls, named as *(dynamic) boundary layer* zones.

The coefficient of f_b , Gr/Re^2 , is also known as *Archimedes number (Ar)* or *Richardson number (Ri)*. It gives an indication on whether a given problem is in the limit of forced convection, belongs to the category of mixed convection or can be considered in the limit of natural convection (in cases where a forced component of the flow is anyway present):

- $\frac{Gr}{Re^2} \ll 1 \Rightarrow f_b \ll f_i$ forced convection
- $\frac{Gr}{Re^2} \approx 1 \Rightarrow f_b \approx f_i$ mixed convection
- $\frac{Gr}{Re^2} \gg 1 \Rightarrow f_b \gg f_i$ natural convection

In forced convection cases the buoyancy term of (1.4.6) is negligible. In all other cases, instead, no terms of equation (1.4.6) are negligible in principle; in particular, in the limit of natural convection, the action of buoyancy forces is predominant, as compared to the inertia of the forced flow. It is worthy to note that, in the latter case, the scale velocity U can not be defined *a priori*: in fact, it is rather pointless to choose as characteristic, a velocity that is related to a flow component (the forced one), whose contribution is deemed to be negligible.

The Péclet number provides an estimate of the relative entity of the advection and diffusion terms in the energy equation (1.4.7):

- $Pe \ll 1 \Rightarrow v_{ad} \ll v_{cd}$ purely diffusive heat transfer
- $Pe \gg 1 \Rightarrow v_{ad} \gg v_{cd}$ purely advective heat transfer

In the former case, the advection term of (1.4.7) is negligible. This means that the flow, if present, has little effect on the temperature distribution, which is, in practice, determined by the conduction equation. In the latter case, the diffusion term of the energy equation (1.4.7) is regarded as negligible. Heat is mainly advected by the flow, in the form of enthalpy, and the global temperature distribution is not affected by conduction; however, thermal diffusion can not be neglected in the vicinity of solid walls involved in heat transfer processes. Such regions are named as *(thermal) boundary layer* zones.

For steady state conditions, (1.4.7) becomes:

$$\mathbf{u} \cdot \nabla T = \frac{1}{Pe} \nabla^2 T \quad (1.4.8)$$

By neglecting the advection term, it reduces to:

$$\nabla^2 T = 0 \quad (1.4.9)$$

When, instead, the diffusion term is neglected, the bulk temperature distribution can be represented by the following equation:

$$\mathbf{u} \cdot \nabla T = 0 \quad (1.4.10)$$

As pointed out in [5], this kind of argument, when referred to equations containing only two terms as (1.4.8), may give rise to some perplexity. Equation (1.4.8) states that, at each point of the domain considered, advection exactly balances diffusion, but also that, in the meantime, Pe measures the relative entity of the two heat transfer mechanisms. The apparent contradiction emerges from the fact that the equation is exact, but, on the contrary, an order of magnitude analysis of the two terms may lead to establish that one is dominant over the other; however, this is true in the sense that one term prevails over the other in the determination of the distribution of the variable. For example, $Pe \gg 1$ implies that advection is the dominant process in the determination of the temperature field, whereas, diffusion has little influence on it. One can solve equation (1.4.10), thus obtaining a good approximation of the temperature field. It is important to point out that (advection term equal to zero) means the exact contrary of (negligible advection); to this point, the purely diffusive case is even clearer, since equation (1.4.9) undoubtedly governs steady state conduction.

1.4.3 The Nusselt number

The *convection heat transfer coefficient*, h , is defined by *Newton's law of cooling*:

$$q_w = h(T_w - T_0) = h\Delta T_{ref} \quad (1.4.11)$$

For the correlation of heat transfer data, it is useful to introduce the dimensionless formulation of h , expressed by the *Nusselt number*:

$$Nu = \frac{hL}{\lambda} = \frac{q_w L}{\lambda \Delta T_{ref}} \quad (1.4.12)$$

From the previous analysis, it can be inferred that, under the Boussinesq approximation, Nu can be a function of Gr (or, alternatively, Ra or Bo) or Re , depending on the flow regime considered. For a given problem, the value of Nu is also influenced by Pr , by the geometric characteristics of the problem itself, and by the type of thermal conditions imposed at the boundaries.

1.4.4 Scale velocities in natural convection

The definition of the scale velocity U represents the first step of the dimensional analysis of natural convection cases, since, as already mentioned, no reference velocity is associated *a priori* with such problems.

The choice of U is based, once again, on considerations upon the order of magnitude of the different terms of equations (1.3.14) [5] and (1.3.15).

Since the flow is originated by the buoyancy force f_b , it is safe to assume that $f_b = O(1)$. In (1.3.14), the contribution of f_b shall be balanced by either the inertial force f_i and/or the viscous force f_v , while neither f_i or f_v can be of a higher order than f_b . The hydrostatic case $f_b \approx f_p$ will be addressed later on.

I) Assuming that $f_b \approx f_i$, one obtains:

$$|\mathbf{u} \cdot \nabla \mathbf{u}| \approx |g\beta\Delta T| \quad (1.4.13)$$

that is, in terms of scales:

$$\frac{U^2}{L} \approx g\beta\Delta T_{ref} \quad (1.4.14)$$

This leads to the following scale velocity:

$$U \approx (g\beta\Delta T_{ref} L)^{\frac{1}{2}} \quad (1.4.15)$$

also called the *Brunt-Väisälä velocity*. The comparison between inertial and viscous forces produces the following equivalence between Re and Gr :

$$\frac{f_i}{f_v} \approx \frac{UL}{\nu} = Re \approx \left(\frac{g\beta\Delta T_{ref} L^3}{\nu^2} \right)^{\frac{1}{2}} = Gr^{\frac{1}{2}} \quad (1.4.16)$$

Since the initial assumption was that $f_g \approx f_i$, if $Gr \gg 1$, then $f_i \gg f_v$. Therefore, for values of the Grashof number much larger than unity, inertial forces are dominant over viscous friction forces. Viscous forces are not negligible in the vicinity of solid walls; given the complex relationship between dynamic and thermal processes in natural convection, the viscous term in equation (1.3.14) shall not be neglected.

II) If, on the contrary, it is assumed that $f_b \approx f_v$:

$$|\nu \nabla^2 \mathbf{u}| \approx |g\beta\Delta T| \quad (1.4.17)$$

that is:

$$\frac{\nu U}{L^2} \approx g\beta\Delta T_{ref} \quad (1.4.18)$$

The associated scale velocity is then:

$$U \approx \frac{g\beta\Delta T_{ref} L^2}{\nu} \quad (1.4.19)$$

By drawing the same comparison as in (1.4.16):

$$\frac{f_i}{f_v} \approx \frac{UL}{\nu} = Re \approx \frac{g\beta\Delta T_{ref} L^3}{\nu^2} = Gr \quad (1.4.20)$$

From (1.4.20) it can be inferred that, if $Gr \ll 1$, the inertial forces are negligible with respect to viscous friction.

It can be concluded that Gr always provides an evaluation of the ratio between the orders of magnitude of inertial and viscous forces in natural convection, in the majority of the cases ($Gr \gg 1$) through its square root. Moreover, in analogy with the role of Re for isothermal flows, the value of Gr also designates the laminar or turbulent character of the flow.

Concerning the intensity of the different heat transfer processes involved in natural convection, with reference to equation (1.3.15), one has:

I) for high Gr -values ($Gr \gg 1$)

$$\frac{v_{ad}}{v_{cd}} \approx \frac{UL}{\alpha} = Pe = Gr^{\frac{1}{2}} Pr = (RaPr)^{\frac{1}{2}} = Bo^{\frac{1}{2}} \quad (1.4.21)$$

therefore, for:

$Gr \gg 1$ and $Pr \geq 1$ advection dominates over conduction; the flow is typically of boundary layer type.

$Gr \gg 1$ and $Pr \ll 1$ the predominance of advection is ensured only if $Bo \gg 1$; otherwise, the boundary layer assumption is not necessarily fulfilled.

II) for low Gr -values ($Gr \ll 1$)

$$\frac{v_{ad}}{v_{cd}} \approx \frac{UL}{\alpha} = Pe = GrPr = Ra \quad (1.4.22)$$

therefore, for:

$Gr \ll 1$ and $Pr \leq 1$ the predominance of diffusive transport over advection produces low velocity viscous flows at a great distance, with rather small influence on the thermal field; the latter substantially coincides with a purely conductive temperature distribution. At comparable values of Gr , the extension of the flow region reduces with increasing Pr .

$Gr \ll 1$ and $Pr \gg 1$ the predominance of diffusive transport is ensured only if $Ra \ll 1$; otherwise, at comparable values of Gr , the flow originates from near-wall advective/diffusive processes and propagates throughout the domain by viscous shear.

Hence, it shall be observed that, in general, if $Pr \approx 1$, as for gases, the predominance of advection in equation (1.3.15) corresponds to the predominance of inertial forces in the momentum equation (1.3.14). In such circumstances, it can be safely assumed that the flow has a boundary layer character. Moreover, for $Pr \approx 1$, when thermal diffusion represents the greater contribution in (1.3.15), viscous diffusion governs the dynamic balance (1.3.14), and, with the same degree of confidence, one could conclude that the flow has not boundary layer character. In high- Pr (water, oils, etc.) and low- Pr fluids (liquid metals), such correspondences do not subsist.

The fact that diffusive terms in equations (1.3.14) and (1.3.15) are not negligible even if the values of $Gr^{\frac{1}{2}}$ and $Gr^{\frac{1}{2}}Pr$ are high, comes from a rather simple consideration: for free convection, conduction is always the first process giving rise to temperature gradients, and, in turn, to the flow; therefore, to neglect everywhere its effect, means to eliminate the problem of natural convection itself. On the contrary, as it will be shown in Section 1.5.1, the equilibrium conditions $f_i \approx f_v$ and $v_{ad} \approx v_{cd}$, within the boundary layer, allow the boundary layer thickness to be chosen as the characteristic linear dimension for the viscous and thermal diffusion terms.

III) When both f_i and f_v are much smaller than f_b , the hydrostatic balance $f_b \approx f_p$ applies; however, this does not provide any information on the velocity scale, since, in this cases, the circulation is very weak and the overall flow has little influence on the dynamic asset of the system. Anyway, a suitable velocity scale (although presumably small) can be predicted by means of considerations on the relative intensity of the heat transfer processes. Assuming $v_{ad} \approx v_{cd}$ in equation (1.3.15), one has:

$$|\mathbf{u} \cdot \nabla T| \approx |\alpha \nabla^2 T| \quad (1.4.23)$$

that is:

$$\frac{U \Delta T_{ref}}{L} \approx \frac{\alpha \Delta T_{ref}}{L^2} \quad (1.4.24)$$

The associated scale velocity is then:

$$U \approx \frac{\alpha}{L} \quad (1.4.25)$$

which is also called the *diffusive velocity* scale. Although the contribution of both f_i and f_v is small, it can be still inferred that:

$$\frac{f_i}{f_v} \approx \frac{UL}{\nu} = Re \approx \frac{\alpha}{\nu} = Pr^{-1} \quad (1.4.26)$$

while the heat transfer balance returns, obviously:

$$\frac{v_{ad}}{v_{cd}} = Pe \approx 1 \quad (1.4.27)$$

It is then evident that, in these cases, the relative importance of inertial and viscous effects is governed by the diffusive properties of the fluid.

In general, the choice of (1.4.25) is well suited either for cases that are characterised by very small temperature differences (*pseudo-conductive* or *pseudo-diffusive* cases) [12, 13], or for cases where the direction of the density gradient is parallel to that of the hydrostatic

pressure gradient, as it is for Rayleigh-Bénard convection. As mentioned in Section 1.3.4, in such situations the onset of convection is often bound to a stability condition, the hydrostatic balance being a stable solution of (1.3.14) for a wide range of Gr -values.

Ostrach [14] reports two more velocity scales, which may be seen as variants of the diffusive scale (1.4.25). The former is the following:

$$U \approx \frac{\nu}{L} \quad (1.4.28)$$

and it expresses a balance between inertia and viscous forces in the momentum equation (1.3.14). In fact, it is:

$$\frac{f_i}{f_v} \approx \frac{UL}{\nu} = Re \approx 1 \quad (1.4.29)$$

Moreover, the heat transfer balance:

$$\frac{v_{ad}}{v_{cd}} = Pe \approx \frac{\alpha}{\nu} = Pr^{-1} \quad (1.4.30)$$

states that, in practice, the scale (1.4.28) is the dual of the scale (1.4.25) and that, in the frame of an inertia-friction balance, the relative importance of convective and conductive effects is ruled by Pr .

The latter is a sort of “hybrid” diffusive scale:

$$U \approx \frac{(\nu\alpha)^{\frac{1}{2}}}{L} \quad (1.4.31)$$

whose real physical meaning is however unclear.

Obviously, the three scales (1.4.25), (1.4.28) and (1.4.31) coincide for $Pr \approx 1$.

1.4.5 Ostrach’s velocity scale

For cases respecting the boundary layer conditions, *i.e.*, in light of the above considerations, for $Gr \gg 1$ and $Pr \geq 1$ Ostrach [15] proposes the following scale velocity, alternative to (1.4.15):

$$U \approx \left(\frac{g\beta\Delta T_{ref}L}{Pr} \right)^{\frac{1}{2}} \quad (1.4.32)$$

Ostrach starts from observing that, for a correct scaling of all terms in the governing equations, the reference length of the derivatives in the direction orthogonal to the flow in the diffusive term should not be L , but the thermal boundary layer thickness δ_T , since the temperature variations due to thermal diffusion are confined in that region. In the example above, this implies:

$$\frac{\partial^2 u_z}{\partial x^2} \approx \frac{U}{\delta_T^2}; \quad \frac{\partial^2 T}{\partial x^2} \approx \frac{T}{\delta_T^2} \quad (1.4.33)$$

At the same time, within the thermal boundary layer, the advective and diffusive terms in equation (1.4.7) must be of equal order:

$$\mathbf{u} \cdot \nabla T \approx \nabla^2 T = O(1) \quad (1.4.34)$$

Hence, the coefficient of the right hand side of (1.4.7) has to be redefined, so as to become $O(1)$. From (1.4.7), and taking into account (1.4.33):

$$\mathbf{u} \cdot \nabla T \approx \frac{1}{Pe} \left(\frac{\delta_T}{L} \right)^2 \nabla^{*2} T \quad (1.4.35)$$

where ∇^{*2} indicates that the coordinates are non-dimensionalized with respect to the unknown boundary layer thickness δ_T . It must then be:

$$\frac{1}{Pe} \left(\frac{\delta_T}{L} \right)^2 \approx 1 \quad (1.4.36)$$

From (1.4.36) one obtains the following estimate of δ_T , as a function of the unknown reference velocity U :

$$\delta_T \approx \left(\frac{UL^3}{\alpha} \right)^{\frac{1}{2}} \quad (1.4.37)$$

For steady state conditions, and according to the boundary layer assumption (1.4.33), equation (1.4.6) is rewritten as:

$$\mathbf{u} \cdot \nabla \mathbf{u} = -\nabla P + \frac{1}{Re} \left(\frac{\delta_T}{L} \right)^2 \nabla^{*2} \mathbf{u} - \frac{Gr}{Re^2} \hat{\mathbf{g}} T \quad (1.4.38)$$

The scale velocity (1.4.32) is then derived by assuming that $f_b \approx f_v$. This is equivalent to assume:

$$Re^2 = \frac{Gr}{Pr} \quad (1.4.39)$$

It should be noted that, if one assumes instead $f_b \approx f_i$, the scale velocity (1.4.15) is recovered, and δ_T should be evaluated according to that scale.

1.4.6 Dimensionless equations of natural convection

The dimensionless equations of natural convection assume different forms, depending on the choice of the reference velocity. Starting from the governing set of equations for convection (1.4.5)-(1.4.7), and choosing the Brunt-Väisälä velocity (1.4.15) as the scale velocity (*i.e.* assuming $Gr \gg 1$), one has:

$$\nabla \cdot \mathbf{u} = 0 \quad (1.4.40)$$

$$\frac{\partial \mathbf{u}}{\partial t} + \mathbf{u} \cdot \nabla \mathbf{u} = -\nabla P + \frac{1}{Gr^{\frac{1}{2}}} \nabla^2 \mathbf{u} - \hat{\mathbf{g}} T \quad (1.4.41)$$

$$\frac{\partial T}{\partial t} + \mathbf{u} \cdot \nabla T = \frac{1}{Gr^{\frac{1}{2}} Pr} \nabla^2 T \quad (1.4.42)$$

High values of Gr are encountered much more frequently than lower ones. Rather vigorous natural convection flows set on very easily inside large volumes of fluid, even under the action of very low temperature differences. For example, with $\Delta T = 1^\circ C$ and $L = 1cm$, one has $Gr \approx 10^3$ for water and $Gr \approx 10^2$ if the working fluid is air. Hence, cases characterized by high Gr -values have much greater practical interest, as compared to cases for which $Gr \ll 1$.

Anyway, the Navier-Stokes and energy equations for the latter cases are also reported, for which the reference velocity is given by (1.4.19):

$$\frac{\partial \mathbf{u}}{\partial t} + \mathbf{u} \cdot \nabla \mathbf{u} = -\nabla P + \frac{1}{Gr} \nabla^2 \mathbf{u} - \frac{1}{Gr} \hat{\mathbf{g}} T \quad (1.4.43)$$

$$\frac{\partial T}{\partial t} + \mathbf{u} \cdot \nabla T = \frac{1}{Gr Pr} \nabla^2 T \quad (1.4.44)$$

If the diffusive velocity (1.4.25) is chosen as the reference one, equations (1.4.6)-(1.4.7) are modified as follows:

$$\frac{\partial \mathbf{u}}{\partial t} + \mathbf{u} \cdot \nabla \mathbf{u} = -\nabla P + Pr \nabla^2 \mathbf{u} - Gr Pr^2 \hat{\mathbf{g}} T \quad (1.4.45)$$

$$\frac{\partial T}{\partial t} + \mathbf{u} \cdot \nabla T = \nabla^2 T \quad (1.4.46)$$

If finally the Ostrach velocity scale is chosen (1.4.32), with δ_T as the reference length for the non-dimensionalization of the orthogonal diffusive terms, the equations become:

$$\frac{\partial \mathbf{u}}{\partial t} + \mathbf{u} \cdot \nabla \mathbf{u} = -\nabla P + Pr \nabla^{*2} \mathbf{u} - Gr Pr^2 \hat{\mathbf{g}} T \quad (1.4.47)$$

$$\frac{\partial T}{\partial t} + \mathbf{u} \cdot \nabla T = \nabla^{*2} T \quad (1.4.48)$$

Switching back to the usual dimensionless coordinates, (1.4.47)-(1.4.48) read as:

$$\frac{\partial \mathbf{u}}{\partial t} + \mathbf{u} \cdot \nabla \mathbf{u} = -\nabla P + \frac{Pr^{\frac{1}{2}}}{Gr^{\frac{1}{2}}} \nabla^2 \mathbf{u} - Gr Pr^2 \quad (1.4.49)$$

$$\mathbf{u} \cdot \nabla T = \frac{1}{Gr^{\frac{1}{2}} Pr^{\frac{1}{2}}} \nabla^2 T \quad (1.4.50)$$

Equations (1.4.41)-(1.4.42) clearly indicate that, due to the coupling between velocity and temperature imposed by the buoyancy term, the conditions for dynamical similarity (and energetic similarity) are granted by the identity of a pair of independent parameters, (Gr, Pr), or, alternatively, (Ra, Pr).

For boundary layer cases, Gr does not appear explicitly in equations (1.4.47)-(1.4.48), but it is implicitly included in the non-dimensionalization of the x^* coordinate, orthogonal to the main flow. It is also observed that (1.4.47) implies the dominance of viscous friction over inertial forces for $Pr \gg 1$, thus shedding light onto a new interpretation of the Prandtl number, seen as the ratio between the orders of magnitude of friction forces and inertial forces for boundary layer conditions in natural convection. Hence, the option (1.4.32) is preferable over (1.4.15) for the determination of the characteristic velocity under boundary layer conditions. Obviously, the two options coincide for $Pr \approx 1$.

1.5 Some classical scaling arguments

Scale analysis stands as a particularly efficient tool for the preliminary investigation of a specific problem, and for the control *a posteriori* of the results obtained by experimental,

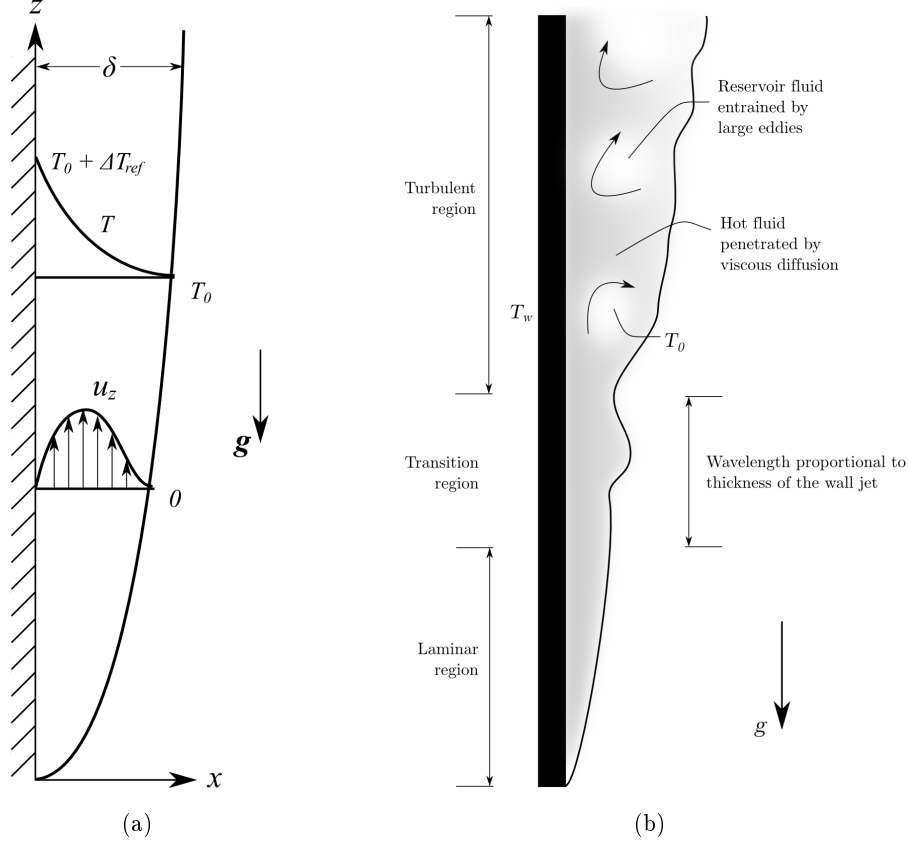


Figure 1.4: Boundary layer flow along a vertical plate: (a) schematic of the problem; (b) qualitative description of transition to turbulence.

numerical and analytic means. In fact, this method allows a considerable quantity of information on the problem to be extracted with comparatively little effort.

The technique is based upon the selection of suitable reference quantities (lengths, time intervals, etc.), whose value, initially unknown, is sized as a function of the characteristic known parameters of the problem, in order to obtain general correlations of interdependency between them.

A summary of the main rules of scale analysis is found in Appendix A. Here, the scale analyses of two cases of external natural convection are reported, namely the boundary layer flow along a vertical plate (Figure 1.4(a)), following Bejan [3], and the buoyant plume arising from a horizontal line heat source (Figure 1.10(a)), following Tritton [5], to illustrate in semi-quantitative terms the phenomenology of those basic cases.

1.5.1 Boundary layer along a vertical plate

With reference to Figure 1.4(a), let a vertical plate of temperature T_w and height H be immersed in an initially quiescent fluid of temperature T_0 , for sufficiently high values of $Gr^{\frac{1}{2}}$ and $Gr^{\frac{1}{2}}Pr$.

The fluid, heated at the wall by conduction, rises along it. At the same time, the heated fluid, advected by the flow, reaches a general height z . In the steady state, the process can

be described as follows: at z , the heat conducted from the wall horizontally into the fluid is swept and carried upwards by the ascending stream.

Heat transfer is confined in the thermal boundary layer region adjacent to the wall. Outside that region, the fluid temperature is T_0 everywhere. The flow is equally confined into a thin layer, the dynamic boundary layer, outside of which the velocity is almost zero. The boundary layer itself creates a suction effect, which drives fluid from the bulk to the wall, thus producing a progressive increase of the fluid quantity entrained in the boundary layer itself, and, therefore, the growth of its thickness with increasing z .

For the purposes of the scale analysis, the governing equations are written in dimensional, steady-state form. By extending the dimensional considerations of Section 1.4.5, it is possible to obtain a simplified set of equations for the boundary layer case, starting from (1.2.2), (1.3.14) and (1.3.15). A complete demonstration [4] is omitted for the sake of brevity. With reference to the coordinate system of Figure 1.4(a):

$$\frac{\partial u_x}{\partial x} + \frac{\partial u_z}{\partial z} = 0 \quad (1.5.1)$$

$$u_x \frac{\partial u_z}{\partial x} + u_z \frac{\partial u_z}{\partial z} = \nu \frac{\partial^2 u_z}{\partial x^2} + g\beta(T - T_0) \quad (1.5.2)$$

$$u_x \frac{\partial T}{\partial x} + u_z \frac{\partial T}{\partial z} = \alpha \frac{\partial^2 T}{\partial x^2} \quad (1.5.3)$$

It is worthy to point out that, physically, equations (1.5.1)-(1.5.2) have the following implications:

- (i) the piezometric pressure within the boundary layer is identical to the pressure at the border of the boundary layer;
- (ii) the velocity component orthogonal to the wall is much smaller than the parallel component, and, therefore, it is determined only on the basis of continuity;
- (iii) in the boundary layer, streamwise momentum and thermal energy diffusion is negligible.

Conditions (i)-(iii) have no chance to be verified for $Gr \ll 1$; instead, as anticipated in Section 1.4, it may be inferred that, in natural convection, such conditions are safely fulfilled for all cases with $Gr \gg 1$ and $Pr \leq 1$. Cases with $Gr \gg 1$ and $Pr \ll 1$ are more difficult to be interpreted. In fact, one may expect that thermal diffusion produces alterations in the temperature field, and, therefore, buoyancy-induced currents, already upstream of the heat source. At least, in the onset zone of the flow, diffusive terms prevail and, for sure, condition (iii) is not verified.

The scales of maximum variation of the variables are defined as follows:

$$\Delta x_{max} \approx \delta_T; \quad \Delta z_{max} \approx H; \quad \Delta T_{max} \approx \Delta T_{ref} = T_w - T_0 \quad (1.5.4)$$

The analysis starts from the assumption that, within the thermal boundary layer of thickness δ_T , the thermal advection velocity v_{ad} must balance the thermal diffusion velocity v_{cd} , $v_{ad} \approx v_{cd}$. From equation (1.5.3), in terms of orders of magnitude, one has:

$$u_x \frac{\Delta T_{ref}}{\delta_T} + u_z \frac{\Delta T_{ref}}{H} \approx \alpha \frac{\Delta T_{ref}}{\delta_T^2} \quad (1.5.5)$$

The continuity equation (1.5.1) indicates that:

$$\frac{u_x}{\delta_T} \approx \frac{u_z}{H} \quad (1.5.6)$$

Hence, advective terms turn out to be of the same order, so that:

$$u_z \frac{\Delta T_{ref}}{H} \approx \alpha \frac{\Delta T_{ref}}{\delta_T^2} \Rightarrow u_z \approx \alpha \frac{H}{\delta_T^2} \quad (1.5.7)$$

The inertial, friction, and buoyancy terms in the z -component of the Navier-Stokes equation (1.5.2) are respectively of order:

$$f_i \approx \frac{u_z^2}{H}; \quad f_v \approx \nu \frac{u_z}{\delta_T^2}; \quad f_b \approx g\beta \Delta T_{ref} \quad (1.5.8)$$

It is essential to evaluate whether, within the thermal boundary layer, the dynamic and thermal processes are conditioned by the force balances $f_i \approx f_b$ or $f_v \approx f_b$.

From the ratios between orders of magnitude, one obtains:

$$\frac{f_i}{f_b} \approx \left(\frac{H}{\delta_T} \right)^4 Ra_H^{-1} Pr^{-1}; \quad \frac{f_a}{f_b} \approx \left(\frac{H}{\delta_T} \right)^4 Ra_H^{-1}; \quad \frac{f_a}{f_i} \approx Pr \quad (1.5.9)$$

In this case, the Grashof number is replaced by the Rayleigh number, based on the wall height, H :

$$Ra_H = \frac{g\beta \Delta T_{ref} H^3}{\nu \alpha} \quad (1.5.10)$$

From expression (1.5.9) it is clear that the competition between inertial and friction forces in boundary layer problems is decided by a fluid property, the Prandtl number, as already observed in equation (1.4.47) after Ostrach [15].

The evaluation of the order of magnitude of q_w is based on (1.3.28):

$$q_w = -\lambda \left(\frac{\partial T}{\partial n} \right)_w \approx \lambda \frac{\Delta T_{ref}}{\delta_T} \quad (1.5.11)$$

and, therefore:

$$Nu_H = \frac{hH}{\lambda} \approx \frac{H}{\delta_T} \quad (1.5.12)$$

The three cases are examined in the following.

Pr $\gg 1$ The case is representative of the majority of liquids with small thermal conductivity. The variations of T are confined within the thickness δ_T , whilst the variations of u_z are restricted to a layer of thickness $\delta > \delta_T$, as shown in Figure 1.5.

For $Pr \gg 1$, the relationships (1.5.9) indicate that the friction-buoyancy balance is dominant inside δ_T :

$$\frac{f_v}{f_b} \approx \left(\frac{H}{\delta_T} \right)^4 Ra_H^{-1} = O(1) \quad (1.5.13)$$

From (1.5.13), it is immediate to extract the dimensional scales for δ_T and u_z , and, on the basis of (1.5.12), the order of magnitude of Nu_H :

$$\delta_T \approx H Ra_H^{-\frac{1}{4}}; \quad u_z \approx \frac{\alpha}{H} Ra_H^{\frac{1}{2}}; \quad Nu_H \approx Ra_H^{\frac{1}{4}}; \quad (1.5.14)$$

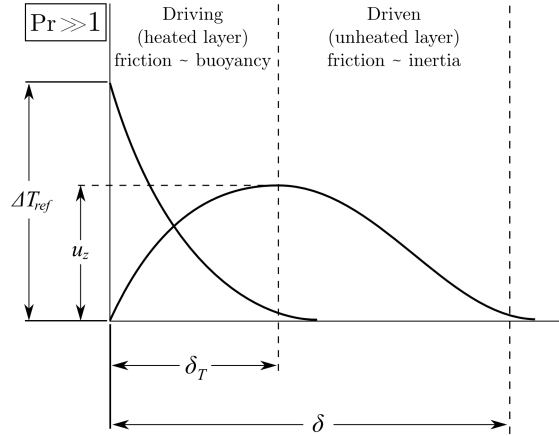


Figure 1.5: Boundary layer length scales for $Pr \gg 1$.

As for the evaluation of δ , it should be noted that, for $x > \delta_T$, $f_g \approx 0$ and $f_i \approx f_a$. By scaling the variations of u_z by δ and not by δ_T :

$$\frac{u_z^2}{H} \approx \nu \frac{u_z}{\delta^2} \quad (1.5.15)$$

therefore:

$$u_z \approx \nu \frac{H}{\delta^2} \quad (1.5.16)$$

It is reasonable to admit that the range of variability of u_z is of the same order within δ and δ_T . Then, one has:

$$\delta \approx HRa_H^{-\frac{1}{4}} Pr^{\frac{1}{2}}; \quad \frac{\delta}{\delta_T} \approx Pr^{\frac{1}{2}} \quad (1.5.17)$$

With reference to Figure 1.5 the boundary layer model for $Pr \gg 1$ can be summarized as follows:

- the boundary layer has two different length scales, δ_T and δ ;
- the action of buoyancy forces ensues the flow within δ_T and determines its intensity;
- velocity progressively decays to zero in the zone between δ_T and δ , where isothermal fluid is dragged by viscous shear;
- the extension of the viscous layer δ grows with the square root of Pr .

Pr ≈ 1 The case is representative of gases, for which, typically, $Pr \simeq 0.7$. It is substantially analogous to the case $Pr \gg 1$. Being also $Pr \approx 1$, the length scales δ_T and δ practically coincide; thus, the effect of viscous drag does not propagate outside the thermal boundary layer. In other words, the velocity decay due to viscous friction is accompanied by the progressive reduction of the intensity of buoyancy forces within the thermal boundary layer, with increasing x . Obviously, in this case, it is $Ra_H \approx Gr_H$.

The case is represented in Figure 1.6

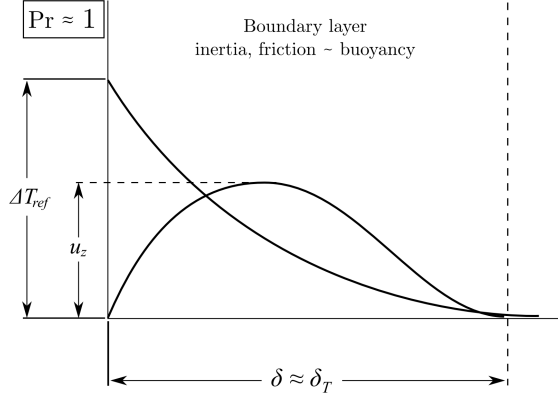


Figure 1.6: Boundary layer length scales for $Pr \approx 1$.

Pr ≪ 1 The case is representative of the behaviour of liquid metals. From (1.5.9), it can be observed that, within the thermal boundary layer δ_T , inertia prevails over friction and balances the action of buoyancy, so that $f_i \approx f_b$:

$$\frac{f_i}{f_b} \approx \left(\frac{H}{\delta_T} \right)^4 Ra_H^{-1} Pr^{-1} = O(1) \quad (1.5.18)$$

The following scales can then be extracted:

$$\delta_T \approx H (Ra_H Pr)^{-\frac{1}{4}} \quad u_z \approx \frac{\alpha}{H} (Ra_H Pr)^{\frac{1}{4}} \quad Nu_H \approx (Ra_H Pr)^{\frac{1}{4}} = Bo_H^{\frac{1}{4}} \quad (1.5.19)$$

where Bo_H is the Boussinesq number, based on H :

$$Bo_H = \frac{g\beta\Delta T_{ref}H^3}{\alpha^2} = Gr Pr^2 \quad (1.5.20)$$

It is worthy to note that the definition of Bo recalls closely that of Gr , from which it differs only for the substitution of the kinematic viscosity ν with the thermal diffusivity α , thus indicating the dominant role of α for low- Pr fluids.

With reference to Figure 1.7 the boundary layer model for $Pr \ll 1$ is summarized as follows:

- the action of buoyancy causes the flow within δ_T and is balanced by inertia;
- the flow is confined within the thermal boundary layer, since the momentum diffusion rate is low compared to the heat diffusion rate;
- the length scales δ_T and δ coincide;
- the decay of the flow in the outer part of the layer δ_T is mainly due to the decay of the buoyancy force.

A second length scale can be identified in the case $Pr \ll 1$ [3]. Such a scale consists in the location of maximum vertical velocity, δ_u . The entity of the scale can be evaluated

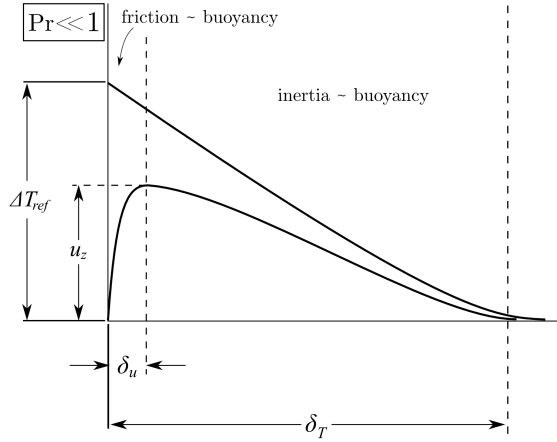


Figure 1.7: Boundary layer length scales for $Pr \ll 1$.

assuming that, in the thin layer of thickness δ_u , the dynamic asset is governed by the viscous forces, and, therefore $f_v \approx f_b$:

$$\frac{f_v}{f_b} \approx \frac{\nu u_z}{\delta_u^2 (g \beta \Delta T_{ref})} = O(1) \quad (1.5.21)$$

from which one has:

$$\delta_u \approx H \left(\frac{Ra_H}{Pr} \right)^{-\frac{1}{4}} = H Gr^{-\frac{1}{4}}; \quad \frac{\delta_u}{\delta_T} \approx Pr^{\frac{1}{2}} \quad (1.5.22)$$

It should be pointed out that this scale analysis is only valid for $Pr \ll 1$, leading to an inconsistent result ($\delta_u \approx \delta_T$) in the limit $Pr \approx 1$.

Summarizing the results of the scale analysis of free convection boundary layer flows over a vertical flat plate, the role of the product $HRa_H^{1/4}$ has to be stressed [3], in that it emerges as the fundamental length scale for the boundary layer itself. On such a scale, all other characteristic dimensions of the problem, δ_T , δ_u , δ can be derived, by means of a coefficient depending on Pr only. The relative orders of magnitude of all linear scales can then be represented as a function of $HRa_H^{1/4}$ and Pr , as in Figure 1.8.

The previous scale analysis provides also an alternative interpretation of the pure numbers Ra , Bo , Gr , or, more precisely, of their fourth roots [3], to be intended not as representative of ratios between forces or process intensities, but rather as geometrical ratios, according to the following scheme:

- $Ra_H^{\frac{1}{4}} \approx \frac{H}{\delta_T}$ for $Pr \gg 1$
- $Bo_H^{\frac{1}{4}} \approx \frac{H}{\delta_T}$ for $Pr \ll 1$
- $Gr_H^{\frac{1}{4}} \approx \frac{H}{\delta_u}$ for $Pr \ll 1$

Although such an interpretation is correct and convincing, it is appropriate to recall that:

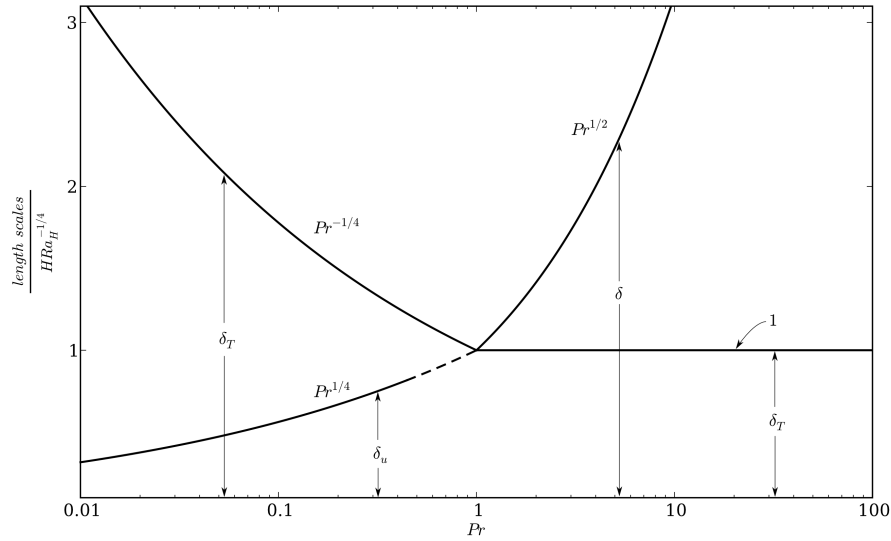


Figure 1.8: Length scales of natural convection boundary layers.

- it is limited to external flow cases with boundary layer characteristics, and these, in turn, are determined by the value of Gr or Ra , as previously discussed;
- it does not invalidate the general conclusions on the role and the meaning of the dimensionless groups drawn in the Section 1.4.

The uniform heat flux condition When the heat flux q_w is assumed constant at the wall (Q-condition) of the vertical plate, the wall temperature T_w varies locally with the vertical coordinate, $T_w = T_w(z)$. The scale analysis now brings:

$$q_w \approx \lambda \frac{T_w - T_0}{\delta_T}$$

The Rayleigh number for the Q-condition is redefined as follows:

$$Ra_{qH} = \frac{g\beta q_w H^4}{\lambda \alpha \nu} \quad (1.5.23)$$

For $Pr \gg 1$, the equilibrium between inertia and buoyancy forces provides again the expressions (1.5.14). By employing (1.5.23) to eliminate the characteristic temperature difference, now unknown:

$$\delta_T \approx H Ra_{qH}^{-\frac{1}{5}}; \quad T_w - T_0 \approx \frac{q_w}{\lambda} H Ra_{qH}^{\frac{1}{5}}; \quad Nu_H \approx Ra_{qH}^{\frac{1}{5}} \quad (1.5.24)$$

Analogously, for $Pr \ll 1$:

$$\delta_T \approx H Bo_{qH}^{-\frac{1}{5}} \quad T_w - T_0 \approx \frac{q_w}{\lambda} H Bo_{qH}^{\frac{1}{5}} \quad Nu_H \approx Bo_{qH}^{\frac{1}{5}} \quad (1.5.25)$$

with $Bo_{qH} = Ra_{qH} Pr$.

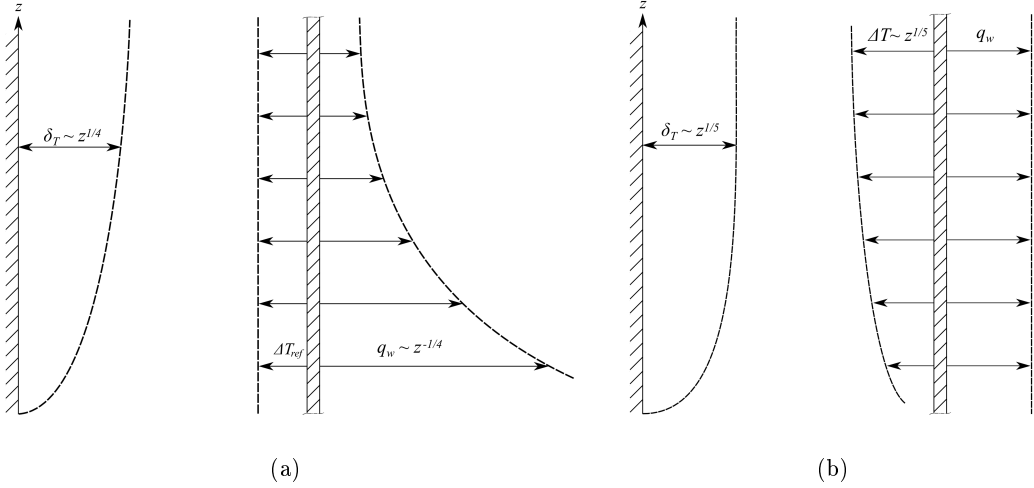


Figure 1.9: Effect of the thermal boundary condition on the natural convection boundary layer along a vertical wall: (a) isothermal wall; (b) uniform heat flux.

It is useful to stress the relationship between the definitions of Ra and Ra_q :

$$Ra_q = \frac{Ra}{Nu} \quad (1.5.26)$$

The definition (1.5.26) indicates that Ra_q is then lower than Ra by at least one order of magnitude. Analogous expressions subsist between Gr_q and Gr , and between Bo_q and Bo .

The qualitative trends of temperature and heat flux in the isothermal and isoflux cases are represented in Figures 1.9(a) and 1.9(b).

Transition and turbulent boundary layer As for forced boundary layer flows [4], also thermal boundary layers are subject to hydrodynamic instability, *i.e.* the amplification of small random disturbances, which originates turbulent flows. According to Bejan [3], the transition from laminar and turbulent flow has universal features, since it always starts with an oscillation whose wavelength is directly related to the characteristic dimension of the flow. In the present case, this dimension is the boundary layer thickness. The general conclusion of the analysis is that the transition is universally defined by a local Reynolds number, based on the characteristic velocity and the length scale of the section of the viscous region close to the transition points; such value of Re results of order 10^2 , with a range of variation mainly determined by the degree of confinement of the flow itself (the more the flow interacts with solid boundaries, the higher is the critical Re -value).

On such a basis, the following criterion for the transition of the free convection boundary layer over a flat plate is set, with reference to the local value of the Grashof number, Gr_z :

$$Gr_{z,tr} = \frac{g\beta\Delta T_{ref}z_{tr}^3}{\nu^2} \approx 10^9 \quad (1.5.27)$$

From (1.5.27) it is possible to extract the height at which it is likely for the laminar boundary layer to become unstable, according to the scheme of Figure 1.4(b). The criterion is fairly validated by the available experimental data, and, as opposed to what is commonly

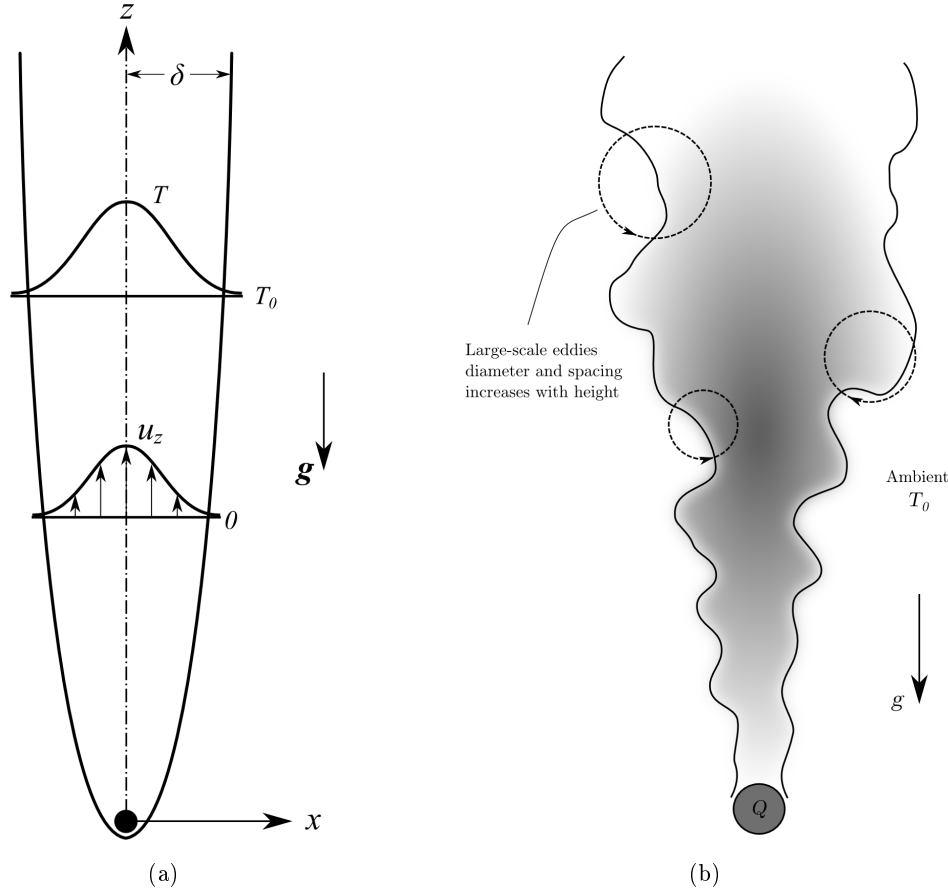


Figure 1.10: Buoyant plume from a line heat source: (a) schematic of the problem; (b) qualitative description of transition to turbulence.

reported in literature (see *e.g.* [1]), it excludes any dependence of the transition height on the Prandtl number. However, it must also be pointed out that, according to linear stability theory, the frequency of maximum amplification of the disturbances is dependent on Pr [2]. This seems to leave open the question of the effect of Pr on transition.

For the case of a fully turbulent boundary layer, the power law dependence $Nu(Ra)$ or $Nu(Ra, Pr)$ is generally estimated with higher values of the exponent than those related to the laminar regime (0.25 and 0.2, respectively, for the isothermal and isoflux cases). Most of the literature agrees on an estimate of the order of 0.33 [16] for the isothermal case, and for values between 0.22 and 0.25 [2] for the isoflux case.

1.5.2 Buoyant plume from a line heat source

The flow originated by a horizontal line heat source, dissipating a constant heat power to the surrounding, initially quiescent fluid has already been generally described in Section 1.1.2. With reference to Figure 1.10(a), let T_0 be the bulk fluid temperature, and Q the total power dissipated by the source per unit length.

The thermal jet rising from the source, at least in its initial stages, remains laminar. As for forced jets [3], the plume becomes unstable, and attains a fully turbulent structure much

more quickly than boundary layers. The qualitative evolution of the system is depicted in Figure 1.10(b).

Although the laminar zone of the flow may often be very limited, scale analysis provides useful information as well. Assuming the flow as two-dimensional, the governing equations of the problem are identical to the ones for the boundary layer (1.5.1)-(1.5.3). It is easy to infer that the boundary layer hypotheses are fulfilled also in this case.

The analysis [5] starts considering that, for the buoyant jet, the total heat being transported vertically by the plume is conserved. The energy flux advected at the height z is then subject to the constraint:

$$\int_{-\infty}^{+\infty} \rho_0 c_p u_z (T - T_0) dx = Q \quad (1.5.28)$$

What distinguishes substantially the buoyant plume and the boundary layer over a vertical plate is the fact that, for the plume, both maximum velocity and temperature are located on the centerline. The scales of maximum variation of the variables can be defined as power law functions of the height z :

$$\Delta x_{max} = \delta_p \propto z^k; \quad u_{z,max} \propto z^m; \quad \Delta T_{max} = T_{max} - T_0 \propto z^n \quad (1.5.29)$$

where δ_p is the half-width of the buoyant plume. Hence, in scaling terms, the inertial and buoyancy term of the z -momentum equation (1.5.2) obey the following proportionalities:

$$u_z \frac{\partial u_z}{\partial z} \propto z^{2m-1}; \quad g\beta(T - T_0) \propto z^n \quad (1.5.30)$$

Assuming that the balance between inertia and buoyancy holds at a certain height z , it must be:

$$2m - 1 = n \quad (1.5.31)$$

Analogous considerations are drawn for the advection and diffusion terms in the energy equation (1.5.3):

$$u_z \frac{\partial T}{\partial z} \propto z^{m+n-1}; \quad \alpha \frac{\partial^2 T}{\partial x^2} \approx \alpha \frac{\Delta T_{max}}{\delta_p^2} \propto z^{n-2k} \quad (1.5.32)$$

thus giving:

$$m + n - 1 = n - 2k \quad (1.5.33)$$

The constraint expressed by (1.5.28) provides the third condition for the determination of the exponents k, m, n :

$$Q \propto u_{z,max} \Delta T_{max} \delta_p \propto z^{k+m+n} \quad (1.5.34)$$

Since Q does not depend on z , it must be:

$$k + m + n = 0 \quad (1.5.35)$$

By putting together the three conditions (1.5.31), (1.5.33) and (1.5.35), the following estimates are finally obtained:

$$\delta_p \propto z^{\frac{2}{5}} \quad u_{z,max} \propto z^{\frac{1}{5}} \quad (T_{max} - T_0) \propto z^{-\frac{3}{5}} \quad (1.5.36)$$

The vertical mass and momentum fluxes can be respectively expressed by orders of magnitude:

$$\int_{-\infty}^{+\infty} \rho_0 u_z dx \propto \rho_0 u_{z,max} \delta_p \propto z^{-\frac{3}{5}} \quad (1.5.37)$$

$$\int_{-\infty}^{+\infty} \rho_0 u_z^2 dx \propto \rho_0 u_{z,max}^2 \delta_p \propto z^{-\frac{4}{5}} \quad (1.5.38)$$

Relation (1.5.37) indicates that the plume entrains ambient fluid, just as a forced jet does [5], thus enlarging with z . The increasing momentum of the fluid with height (1.5.38) is due to acceleration by the buoyancy force, whilst (1.5.36) shows that the maximum temperature progressively decreases.

A local Grashof number is usually defined on the basis of the source power Q :

$$Gr_{Q,z} = \frac{g\beta Q z^3}{\alpha\nu\lambda} \quad (1.5.39)$$

It is worthy to report some approximate estimates on the development of the buoyant jet beyond the laminar zone, according to the literature results summarized in [2]. In particular, the height at which the plume undergoes transition corresponds to the value:

$$Gr_{Q,z,tr} \approx 10^9 \quad (1.5.40)$$

while the jet becomes fully turbulent for

$$Gr_{Q,z,turb} \approx 10^{10} \quad (1.5.41)$$

Moreover, in the transition zone, it is:

$$(T_{max} - T_0) \propto z^{-\frac{3}{4}} \quad (1.5.42)$$

and in the fully turbulent zone:

$$(T_{max} - T_0) \propto z^{-\frac{3}{2}} \quad (1.5.43)$$

Hence, transition to turbulence corresponds to a rapid enlargement of the jet section and to a drastic reduction of the temperature contrast ($T_{max} - T_0$), anticipating the subsequent extinction of the jet itself.

1.6 Summary

In this chapter, the main aspects of thermally induced natural convection have been reviewed. Five examples of natural convection have been described in Section 1.1.2. Heuristically speaking, such cases contain most of the basic phenomenology of buoyancy-induced flows. Boundary layers, thermal jets, Rayleigh-Bénard-like structures, enclosed or semi-enclosed circulations are encountered in any heat exchanging system with a superior degree of complexity, including the ones considered in the following chapters.

The derivation of the equations of convection (Section 1.2) and the successive application of the Boussinesq approximation (Section 1.3) have led to the complete formulation

of the mathematical background for the development of the present work. Moreover, in Section 1.4, the dimensionless parameters governing similarity in convection have been defined with the aid of dimensional analysis, and the choice of the appropriate reference velocities in natural convection has been discussed.

Finally, in Section 1.5, two examples of scale analysis on the fundamental cases of external buoyancy-induced flows have been reported, in order to illustrate the potentialities of the method of scale analysis itself, and to introduce some fundamental scaling rules of natural convection.

Chapter 2

Background and literature review

2.1 Introduction

The study of transitional natural convection flows in enclosures represents a significant branch of the research on hydrodynamic stability and transition to turbulence. In the present work, various aspects of this topic are addressed, ranging from the onset of convection out of diffusion-driven regimes to the approach to two-dimensional unsteady chaotic flows. The task of determining the nature of transitions and the asymptotic flow regimes is mainly tackled by numerical means. In this view, Direct Numerical Simulations can be thought of as numerical experiments, whose results are analysed in light of the theory of dynamical systems.

In particular, the theories of bifurcation and chaos provide a convenient framework for the qualitative interpretation of the early phases of transition to turbulence. Such a framework can be used, together with physical arguments of the mechanics of transition, to understand the essence of flow instabilities, especially in cases where a solution is not immediately at hand, if not, precisely, in numerical terms.

2.1.1 The equations of convection as a dynamical system

In Chapter 1, the governing equations of natural convection have been derived from the general equations of fluid motion, in their dimensionless forms. Among the possible choices of the scale velocity (see Section 1.4.4), the Brunt-Väisälä definition (1.4.15) has been preferred throughout the major part of this work, since many significant features of transitional free convection occur for high- Gr flows. Equations (1.4.40)-(1.4.42) are then assumed as the system of PDEs to be solved numerically. The numerical methodology is described in Chapter 3. The equations are repeated here for convenience:

$$\nabla \cdot \mathbf{u} = 0 \quad (2.1.1)$$

$$\frac{\partial \mathbf{u}}{\partial t} + \mathbf{u} \cdot \nabla \mathbf{u} = -\nabla P + \frac{1}{Gr^{\frac{1}{2}}} \nabla^2 \mathbf{u} - \hat{\mathbf{g}} T \quad (2.1.2)$$

$$\frac{\partial T}{\partial t} + \mathbf{u} \cdot \nabla T = \frac{1}{Gr^{\frac{1}{2}} Pr} \nabla^2 T \quad (2.1.3)$$

From the point of view of dynamical systems, the evolution of the system (2.1.1)-(2.1.3), on a given domain Ω and under a given set of initial and boundary conditions, can be

described as follows:

$$\dot{\mathbf{S}} = \Theta_\gamma(\mathbf{S}) \quad (2.1.4)$$

Equation (2.1.4) defines a *continuous time dynamical system*; such a system is also commonly labeled as a *flow*.

Phase space. In the definition (2.1.4), \mathbf{S} is a vector representing the *unknown variable fields*. In this case, \mathbf{S} is a set of observables of a continuous medium, $\mathbf{S} = (u_x, u_y, u_z, T)^T$, which are functions of time and physical space. In this set, pressure does not appear, since, for incompressible flows, it acts as a Lagrangian multiplier [17].

Thus, equation (2.1.4) defines a *dynamical system* whose *phase space* is of functional nature, and, therefore, infinite-dimensional. This means that its trajectories, *i.e.* all the solutions of equation (2.1.4), belong to an ∞ -dimensional space.

To this end, it is important to remark that a solution of equations (2.1.1)-(2.1.3) can always be approximated asymptotically by an element of a low-dimensional phase space. In other words, a solution can be approximated by an infinite spectral expansion, such as Fourier series, over space, and approximated asymptotically by a truncation of such expansion, retaining only a finite number of its components. The amplitudes of such components satisfy an ordinary differential system of low order in time [18].

To take the concept even further, it can be stated that, by means of *any* space discretization, the infinite-dimensional system (2.1.4) can always be reduced to a finite-dimensional approximation. The latter is usually much easier to handle than its infinite-dimensional counterpart, from the point of view of the system dynamics.

Features of the system. The operator Θ_γ defines an abstract *vector field* on the phase space, which characterises the flow itself. In this case, Θ_γ is representative of the various terms in the system (2.1.1)-(2.1.3), summing up to balance the time variations of the observables. The general shape of Θ_γ determines the dynamical properties of (2.1.4). In particular, the dynamical system (2.1.4) is:

- *autonomous*, since Θ_γ does not depend explicitly on time, unless time-dependent boundary conditions are imposed (this is not the case in the present context);
- *nonlinear*, for it contains the convective terms $\mathbf{u} \cdot \nabla \mathbf{u}$ and $\mathbf{u} \cdot \nabla T$, which are the strongly nonlinear terms coupling the unknown variable fields;
- *dissipative*, due to the presence of diffusive terms in equations (2.1.1)-(2.1.3); in fact, from a physical standpoint, such terms account for dissipation of momentum and heat, as already mentioned in Chapter 1.

The above definition of dissipativity requires greater care, when intended in mathematical terms, and especially when dealing with infinite-dimensional dynamical systems represented by partial differential equations. For ODE-based systems, a condition for dissipativity is that the divergence of the vector field defining the system itself be everywhere negative (See Appendix B). In fact, according to the Liouville theorem [19], this implies that the phase space volume is always decreasing with time; such a property can be assumed as a definition of dissipativity. For example, it can be demonstrated [18], that flows resulting from truncated spectral expansions of the Navier-Stokes equations (1.2.3)-(1.2.11) are rigorously dissipative.

In the case of PDEs, for infinite-dimensional phase spaces, the Liouville theorem does not hold, and even the definition of divergence is problematic. The definition of dissipativity is bound to the existence of an *absorbing* subset of the phase space, where any trajectory of the system enters after some time. For the Navier-Stokes equations (1.2.3)-(1.2.11), the existence of such a set is demonstrated only for the two-dimensional case. The study of the three-dimensional case is even more complicated, due the absence of an existence and uniqueness theorem for the equations themselves. Similar considerations can reasonably be extended to equations (2.1.1)-(2.1.3). Hence, it is evident that a complete proof of the dissipativity of (2.1.4) cannot be given, but, for the scope of the present work, the arguments provided seem sufficient to take it as valid.

Parameters. In equation (2.1.4), the subscript γ denotes the set of control parameters, or coordinates, in the relevant *parameter space*. In the present case, $\gamma = (Gr, Pr, A)$, where A represents a geometric aspect ratio, characterising the domain Ω where the variables in \mathbf{S} are defined.

As pointed out in Chapter 1, in natural convection, the dominant parameter is the Grashof number Gr . In fact, if dimensional analysis is correctly performed, Gr (or, alternatively, Ra or Bo) is a measure of the magnitude of buoyancy in the global force balance represented by the Navier-Stokes equation (2.1.2). Dimensional analysis (Section 1.4) shows that, Gr plays the same role of the Reynolds number Re for forced flows.

The study of dynamical systems is already very complex, even when considering the effect of just two parameters. For this reason, the analyses presented in the following chapters focus on the evolution of the system as a function of Gr , for a limited, but nevertheless representative set of values of Pr and A .

2.1.2 Stability and bifurcations in transitional convection problems

In its most general meaning, the term *transition* indicates the passage from one flow regime to another one, which differs from the previous by some definite and distinguishable character. The ways in which a flow undergoes transition can however be extremely diverse, and due to different causes. The classical acception of this concept is represented, undoubtedly, by the transition from steady-state laminar regimes to time-dependent flows and, ultimately, turbulence.

With little exception, the occurence of transition for a given flow is linked to the concepts of flow *stability* and of *bifurcation*. These “keywords” frequently recur throughout the study of transitional flows. It is useful, in this context, to provide an overview of their meaning, through a more precise set of definitions, in order to fix the background for the analyses that follow.

Attractor. The main characteristic of dissipative dynamical systems, such as (2.1.4), is that of being driven, after a certain time, to settle onto an asymptotic state of motion that satisfies the dynamical equations. For a given set of initial conditions, the trajectories of the system tend to draw infinitely closer to a definite region of phase space, called *attractor*.

An attractor is an *invariant* set in phase space, *i.e.* a set evolving into itself under the effect of the system dynamics. Hence, the attractor represents in itself a particular solution of the system, on which all trajectories starting from a given set of initial conditions (named the *basin of attraction*), tend to arrive asymptotically. Geometrically, an attractor can be

a *point*, a *curve*, a *manifold*, or even a complicated set with a fractal structure known as a *strange attractor*. The main types of attractors are described in Appendix B.

Stability. For the same values of the parameters γ and of the boundary conditions, a system may admit a multiplicity of invariant solutions, some of which are attractors, and others which are called *repellers*. The difference between attractors and repellers lies in their *stability* properties.

Attractors are *stable*, *i.e.* robust to perturbations. Not only all the initial conditions inside the basin of attraction tend to reach the attractor after a certain transient, but, if a trajectory lying on the attractor is perturbed, the system dynamics tend to damp the disturbances asymptotically. Repellers are, instead, *unstable* invariant solutions of the systems. This means that any disturbance, no matter how small, causes the dynamic on the repeller to be inevitably disrupted.

Physically, the distinction between stable and unstable solutions reflects in the actual feasibility of the solution itself. In fact, even if exact, an unstable solution cannot be observed, because the occurrence of perturbations is unavoidable in nature.

Not all the solutions reaching an attractor have the same degree of stability. For the system under consideration (2.1.4), and, more generally, for all fluid flow problems, if sufficiently low values of the main parameter R (Gr , Ra or Bo for natural convection, Re for forced flows) are taken, the system is always attracted to a steady-state solution, the *base flow*, which is *unconditionally stable* [7, 20]. Unconditional (or *global*) stability implies that *any* finite disturbance, no matter how large, vanishes asymptotically. Moreover, if the disturbances decrease monotonically in time, the state is said to be *monotonically stable*. Otherwise, transient growth of the disturbances may be observed, yet those disturbances will ultimately decay as time proceeds to infinity.

The critical value of the main parameter that marks the separation between monotonic and non-monotonic unconditional stability is called the *energy stability limit*, R_E . The energy limit owes its name to the class of theoretical methods that can be used for its estimation, the *energy methods*, [20]. Such methods are based on a variational formulation of the stability problem, and lead to the definition of a sufficient condition for the stability of the base flow. A complete explanation of the main features of energy methods is found in [20].

In convection problems, the existence of an unconditionally stable state is bound to the presence of the diffusive terms in the governing equations (2.1.1)-(2.1.3). As shown by the dimensional analysis (Section 1.4.4), if the leading parameter is sufficiently low, such (linear) terms dominate the momentum and energy balance, overcoming the effect of (nonlinear) convective terms.

Above a certain value of the main parameter, equation (2.1.4) might admit a multiplicity of attractors, alongside the base flow, representing different possible asymptotic flow behaviours. Both the base flow and these other solutions are labeled as *conditionally stable*, in that there always exists a critical, finite amplitude of disturbances, which can cause the perturbed flow to stray from its initial state, and approach another stable configuration. The value of R marking the passage from unconditional to conditional stability is called *global stability limit*, $R_G \geq R_E$. Such a limit can be viewed as the threshold which ultimately separates stability from instability, and its determination is the main goal of any stability analysis [20]. Unfortunately, there is no theory capable of predicting such a result.

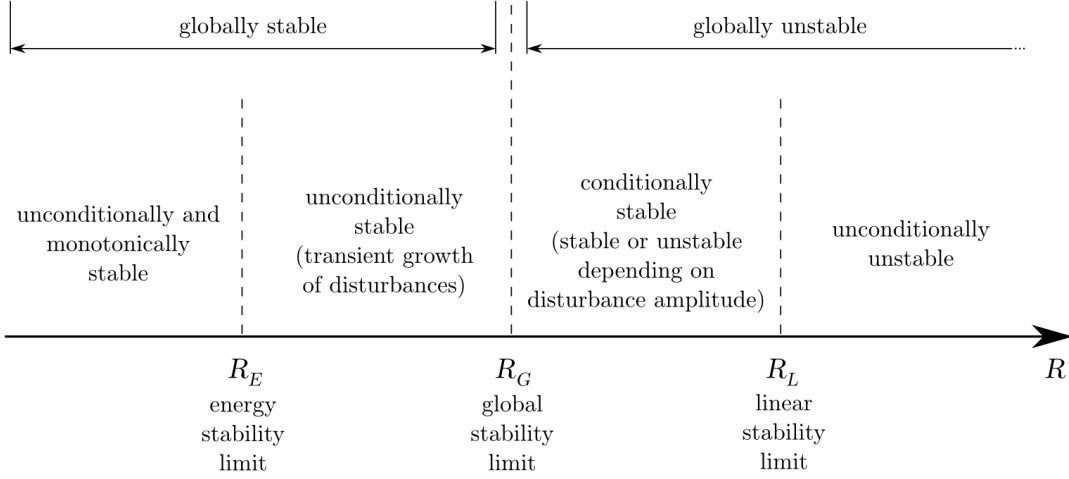


Figure 2.1: Stability limits for the base flow

Finally, there exists another critical value of R above which the base flow definitely loses its stability, turning from an attractor into a repeller, and becoming thus *unconditionally unstable*. This value is called the *linear stability limit*, $R_L \leq R_G$, for it is predictable by means of *linear stability theory*. An outline of the linear stability analysis process for a thermo-fluid system of the type described by (2.1.4) is given in Appendix C.

The sequence of stability limits for the base flow is summarized in the scheme of Figure 2.1. Despite the lack of an exact theory for the prediction of R_G , the stability features of the base flow in the range $R_G < R < R_L$ can be explored using *weakly nonlinear theories*. Moreover, it can be noted that R_G is bounded from below and from above by R_E and R_L , respectively. Therefore, for those cases for which R_E and R_L are reasonably close one to another, a good approximation of the global limit can be obtained [20].

Bifurcation. The loss of stability of the base flow is linked to the occurrence of a *bifurcation*. A bifurcation can be defined as a sudden qualitative or topological change in the behaviour of a system, caused by the variation of one of the governing parameters [21]. A point of the parameter space where a bifurcation takes place is called a *bifurcation point*; from a bifurcation point, a number of solution *branches* usually emerge, either stable or unstable. The dynamical characteristics of the branching solutions are determined by the type of bifurcation occurring.

Typically, a solution which is stable before undergoing a bifurcation, becomes unstable after the bifurcation point, and the corresponding attractor turns into a repeller. The representation of any significant property of the system as a function of the bifurcation parameter is called a *bifurcation diagram*. The main types of possible bifurcations, of a dissipative dynamical system, with the related bifurcation diagrams, are reviewed in Appendix B.

Some of the above considerations on the stability of the base flow can be read in terms of bifurcation theory. A meaningful example can be drawn. Figures 2.2 and 2.3(a) report the bifurcation diagrams for two types of *pitchfork* bifurcation, one of the most common

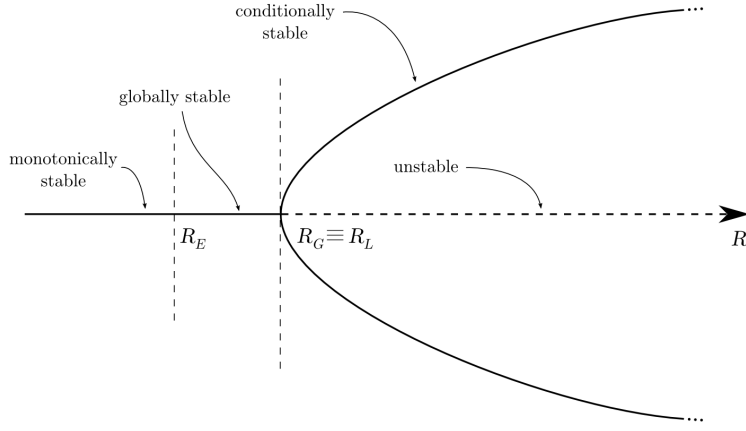


Figure 2.2: Stability and bifurcations of the base flow: supercritical (or direct) bifurcation.

kinds of bifurcations of a buoyancy-driven base flow. In both diagrams, the degree of stability of the base flow can be followed by moving in the positive direction of the leading parameter R . A solid line indicates a stable state, and a dashed line an unstable one.

In the case represented in Figure 2.2, known as a *supercritical* or *direct bifurcation*, for lower values of R , the solid line represents the only possible state, the base flow, which remains stable regardless of the disturbance amplitude. Then, at a given point, the line becomes dashed, indicating instability, while two solid lines depart continuously from this point in the direction of increasing R . Such lines represent two new solution branches, which are supercritical, in that they exist only beyond the bifurcation point, and conditionally stable, because they may lose their stability if subject to perturbations of sufficient intensity. Hence, for flows undergoing supercritical bifurcations, it is $R_L = R_G$.

The situation depicted in Figure 2.3(a) is quite different. There, a *subcritical* or *inverse bifurcation* is represented. Beyond the limit R_G , two conditionally stable branches appear alongside the base flow in the bifurcation diagram. At the bifurcation point, where the base flow becomes unstable, the solution deviates abruptly on one or the other attractor. In this case, $R_L \neq R_G$, since the base flow admits a window of conditional stability.

This type of bifurcation also indicates the existence of *hysteresis*, as shown in Figure 2.3(b): if the value of R is increased beyond the threshold R_L , the solution “jumps” on one of the two stable branches born after the bifurcation. But, if R is then decreased back to a value smaller than R_L , the solution remains on the branch, until, when $R = R_G$ again, it returns on the base flow attractor. Such a phenomenon is not uncommon in natural convection problems.

Analogous considerations apply also to other types of bifurcations. For example, a similar situation is found when a Hopf bifurcation is encountered; a Hopf bifurcation (see Appendix B) marks the passage from steady-state to periodic flow. Both sub- and supercritical Hopf bifurcations frequently recur in hydrodynamic stability problems as well.

Chaos and Turbulence. When the value of the leading parameter is increased further beyond the stability limits of the base flow, the system (2.1.4) undergoes a sequence of

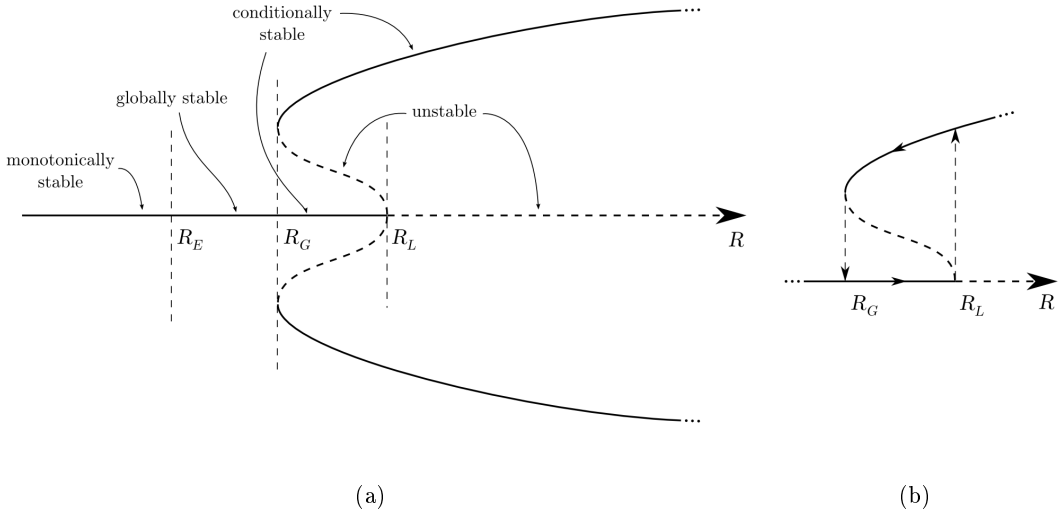


Figure 2.3: Stability and bifurcations of the base flow: (a) subcritical (or inverse) bifurcation; (b) hysteresis.

bifurcations, leading to an ever-increasing variety of the flow configurations. Such bifurcations represent the various stages of the process of *transition*. The process is initially triggered by the birth of time-dependent, oscillatory flows out of steady-state solutions, and its ultimate endpoint is the attainment of *turbulence*.

Turbulence is usually understood as a highly fluctuating flow regime, characterized by enhanced mixing and transfer properties. The question of its origin raises the important problem of the emergence of *stochasticity* out of a *deterministic* evolution. This matter can now be viewed as solved [5], thanks to the notion of *chaos*.

Chaos is one of the possible dynamical behaviours of dissipative, nonlinear dynamical systems. A particularly fitting “pseudo-definition” of chaos is the one given in [21]. There, it is observed that the characteristic property of a chaotic behaviour is that of being substantially not predictable, even if originated by a set of deterministic equations. In other words, the knowledge of the state of the system for an arbitrarily long time span does not allow any prediction on the further evolution of the system itself to be made. In phase space, a chaotic behaviour is represented by the appearance of a *strange attractor* (See Appendix B).

A first deterministic interpretation of transition to turbulence was provided by Landau [22]. He presented transition as an indefinite cascade of instabilities introducing new scales of motion, whose superimposition resulted in an apparently randomly fluctuating regime. The scenario is schematised in Figure 2.4(a), where oscillatory motions are represented by nested ellipses. Ruelle and Takens [23] corrected this picture by remarking that the notion of superimposition was somehow too linear, and that nonlinear interaction, intrinsic to the equations of thermo-fluid dynamics, could yield the appearance of a chaotic behaviour already with a few interacting oscillatory modes. The scheme of Figure 2.4(b) represents the appearance of chaos by means of a miniature of the Lorenz attractor [24]. An entire body of research on hydrodynamic stability and transition to turbulence has confirmed that the intuition of Ruelle and Takens is correct: turbulent flow can be seen as an example of

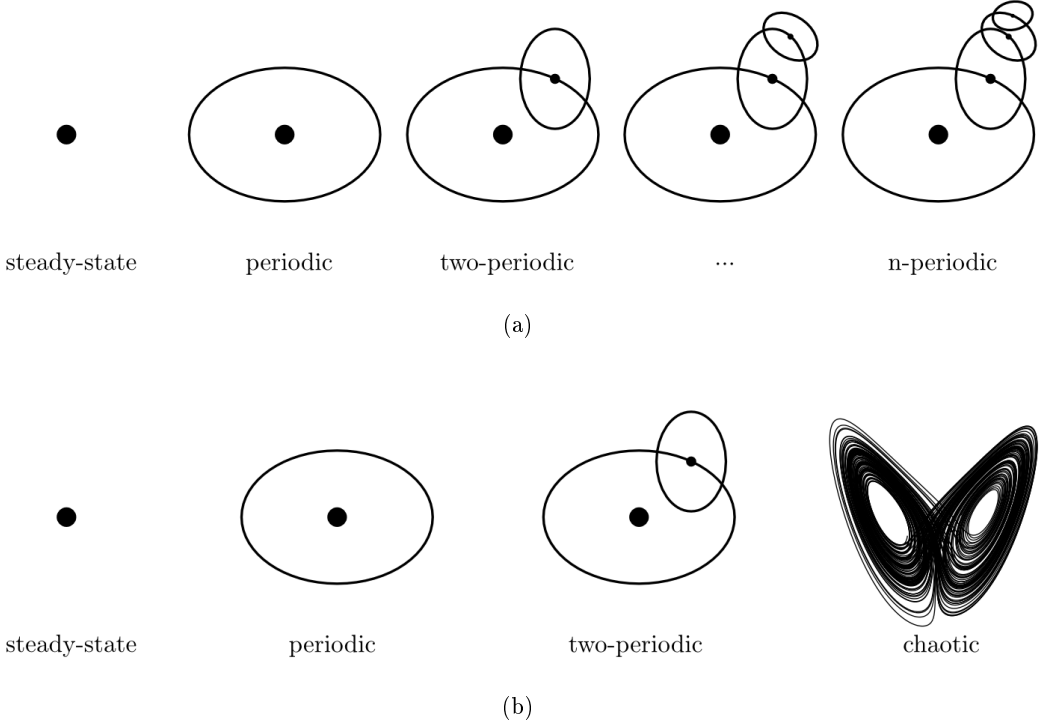


Figure 2.4: Landau (a) and Ruelle-Takens (b) scenarios of transition to turbulence

chaotic behaviour [25], not implying the failure of the deterministic set of equations from which it originates (and of which it is a solution).

The details of transition to turbulence are very complicated, and also vary greatly from flow to flow. There is a number of established *routes to chaos*, whose validity is supported by a strong body of theory [21], and which are found to be common to many types of dissipative dynamical systems. The main examples of such routes are reviewed in Appendix B. Several routes have been identified to recur in flow transition problems, even though the physical mechanisms of the same route may differ from one flow to another; also, in general, the occurrence of a certain route in place of another cannot be predicted *a priori*. Moreover, many critical issues concerning the correspondence between turbulence and chaos, still remain unresolved. Some of these arguments are hinted at and discussed in [5].

The main focus of the present work is the investigation of the scenarios of transition, and the identification of the possible routes to chaos for some selected cases in the domain of buoyancy-driven confined flows. While some elements of the classical routes to chaos, described in Appendix B, have already been observed experimentally and predicted numerically, the real phenomena associated with buoyant flows are considerably more complex. The strong nonlinearity of convective terms, the infinite number of degrees of freedom, and the interdependence between velocity and temperature fields, suggest that a variety of dynamical behaviours is implied in the system 2.1.4, and this is expected to reflect on transition scenarios.

For this reason, a comprehensive review of the main results concerning transition to chaos and turbulence for some of the most representative enclosure configurations is pre-

sented in the following sections.

2.1.3 Brief systematic of flow regimes

When reviewing the work on confined buoyant flows, several types of flow regimes are encountered, of which a qualitative classification can be given. It is useful to introduce a simple set of acronyms and abbreviations, in order to facilitate the description of such flows and the explanation of the global patterns of transition associated with them. The notation of Gollub and Benson [26] is followed and properly extended where necessary. For each flow regime, the indication of the corresponding attractor is also given.

C will indicate the *pure conduction regime*, typical of the Rayleigh-Bénard problem at low values of the Rayleigh number. In this case, there is no flow, since the buoyancy forces induced by density variations inside the fluid are balanced by hydrostatic pressure gradients (see also Section 1.3.4), and the temperature field is purely conductive. Such a state represents the base flow of Rayleigh-Bénard convection, and it is represented by a fixed-point attractor.

PD indicates a *pseudo-diffusive* flow [12, 13], typical of low-*Ra* natural convection in vertical enclosures. Pseudo-diffusive flow regimes are characterised by very weak, shear-driven circulations (also labeled *creeping flows* [27]), and by a diffusion-dominated temperature field. In phase space, they are represented by a fixed point.

S denotes a generic *steady-state* convective flow, driven by a buoyancy-inertia balance, and normally organized in a number of circulation cells. In this case, the nature of the underlying temperature patterns strongly depends on *Pr*: in particular, a diffusive temperature field can still coexist with convective circulations for very low values of *Pr*, while, for high *Pr*-values, convective transport dominates. Steady-state conduction regimes are fixed-points in phase space.

NS indicates a *non symmetric*, steady-state flow, with the same characteristics of the *S*-type flow, but with the particular feature of presenting asymmetries in an otherwise symmetric problem. Typically, when a *NS* flow is observed, it is very likely that its symmetric counterpart exists, with respect to the symmetry plane of the system. The dynamics of *NS* flows are represented once again by fixed-points, which are likely to appear after a pitchfork bifurcation of a *S*-type flow.

P denotes a time-dependent, *periodic* flow, represented by a closed orbit in phase space, and typically originated by a Hopf bifurcation of a *S*- or *NS*-type flow

P_n indicates another periodic state, emerging after a series of *period doublings* of a *P*-type flow. Its corresponding attractor is again a closed orbit.

QP_n denotes a *quasi-periodic* flow, characterised by oscillation presenting *n* independent, incommensurable frequencies. In phase space, the trajectory associated with a quasi-periodic flow lies on the surface of a torus.

L indicates a periodic flow with a number frequencies locked, by twos, to a rational ratio (*phase locking*). In this case, the flow regime is represented by a closed orbit on a torus.

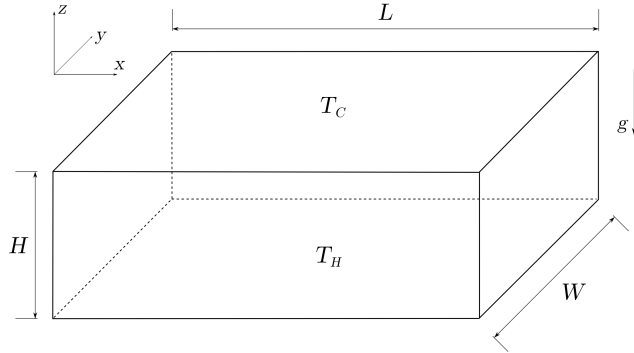


Figure 2.5: Schematic of the Rayleigh-Bénard enclosure problem.

I denotes an *intermittent* flow regime, *i.e.* a regime characterised by alternating periodic phases and chaotic “bursts”, whose representation in phase space is a strange attractor.

N indicates a non-periodic, chaotic flow, represented by a strange attractor as well.

2.2 Rayleigh-Bénard convection

As anticipated in Chapter 1, Rayleigh-Bénard convection consists in the buoyancy-induced flow originating within a layer of fluid enclosed between two parallel, differentially heated horizontal surfaces.

The problem is schematised in Figure 2.5. A parallelepiped enclosure, of height H , length L and width W , with its dimensions aligned with the Cartesian axes, is filled with a fluid whose Prandtl number (Pr) is fixed. The top and bottom walls are isothermal, and maintained at T_H and T_C respectively, with $T_C < T_H$; hence, an inverse vertical temperature gradient is established. The side walls are typically adiabatic. The governing parameter of the system is the Rayleigh number Ra_H , based on the fluid layer thickness H , and on the temperature difference ($T_H - T_C$).

Two aspect ratios A_x and A_y can be defined:

$$A_x = \frac{L}{H}, \quad A_y = \frac{W}{H} \quad (2.2.1)$$

The limit $A_x \rightarrow \infty$, $A_y \rightarrow \infty$ represents the *infinite fluid layer* Rayleigh-Bénard problem, whose results can be conveniently used as reference to examine the effects of lateral confinement.

The body of research associated with Rayleigh-Bénard convection is separate, and a complete review of all the works related to this problem would require a monograph. An interesting review of the main physical aspects of the Rayleigh-Bénard problem is given by Bergé and Dubois [28]. The present section will rather focus on the main results relevant to flow stability issues and transition scenarios. These have been reviewed only by Catton [29] and by Yang [30].

2.2.1 Onset of convection

The linear stability analysis of the infinite layer Rayleigh-Bénard problem, based on the set of governing equations (2.1.1)-(2.1.3), is well documented [7]. The base flow is the conduction regime (C). The main outcome of the analysis is the critical value of the Rayleigh number $Ra_{H,c}$, for which the buoyant flow sets on. For rigid top and bottom surface, it is $Ra_{H,c} = 1707.76$, and the corresponding dimensionless wave number marking instability is $a_c = 3.117$. The stable convective mode is given by long rolls of almost square cross-section. The spacing between rolls is given by the wave number a_c itself.

Both $Ra_{H,c}$ and a_c are independent of Pr , and have been experimentally verified for a wide range of Pr -values [31, 32]. However, the planforms of the convection rolls appear to be somewhat irregular in experiments, as opposed to the predictions of the stability analyses.

Several causes can be identified as the origin of these differences. From a theoretical standpoint, the eigenvalue problem for the prediction of the onset of convection is a degenerate one [7] and, thus, there are many possible solutions at $Ra_{H,c}$. More practically, the roll planforms are very sensitive to defects such as nonuniformities in the boundary temperatures and geometric irregularities, which frequently arise in experimental conditions. Then, fluid layers in experiments must necessarily be of finite extent and enclosed, and, consequently, the effect of the presence of side walls on the final flow asset is inevitable.

Moreover, nonlinear stability theories reveal the admissibility of multiple convective roll planforms with different wave numbers, while the planforms obtained experimentally are, essentially, of a unique nature. Hence, the determination of an additional crieterion for the wave number selection is one of the central issues of nonlinear Rayleigh-Bénard convection problems. To this aim, various criteria were proposed and reviewed by Catton [29, 33] and Catton and Buell [34], who also provide a review of several numerical works on the topic, and conclude that the wave number selection problem is still not closed.

Another closely related issue is the variation of the preferred wave numbers with Ra_H in the near supercritical region. While experimental data [31, 35, 36] have consistently shown that the wave number decreases as Ra_H increases beyond $Ra_{H,c}$, several early theoretical studies predict the opposite behaviour [37]. However, more recent theories showed that the reduction in the wave number for increasing Ra_H (also referred to as the *loss of convection rolls*) is either caused by three-dimensional instabilities [38, 39, 40] or by the presence of the vertical side walls [41, 42, 43].

2.2.2 Instability of convection rolls

Linear stability analysis can also be used to investigate the stability regions of two-dimensional convection rolls. Since the wave number selection problem is not solved, the wave number a remains as a parameter in the results. The analyses, reviewed by Busse [38], follow the same scheme given in Appendix C, and yield, as a main result, the eigenvalue of the growth rate $\lambda = \lambda(Ra_H, Pr, a, a_x, a_y)$, where a_x and a_y are the wave numbers of the disturbances applied to the flow.

The resulting stability diagram is reported in Figure 2.6(a), showing also a variety of instability types, denoted by proper abbreviations. The *zig-zag instability* (ZZ) consists in a steady bending of the rolls into wavy patterns, and normally occurs at low wave numbers and moderate to high Prandtl numbers. The *cross-roll instability* (CR) consists in the appearance of additional new rolls at right angles with respect to the base rolls. The *Eckhaus*

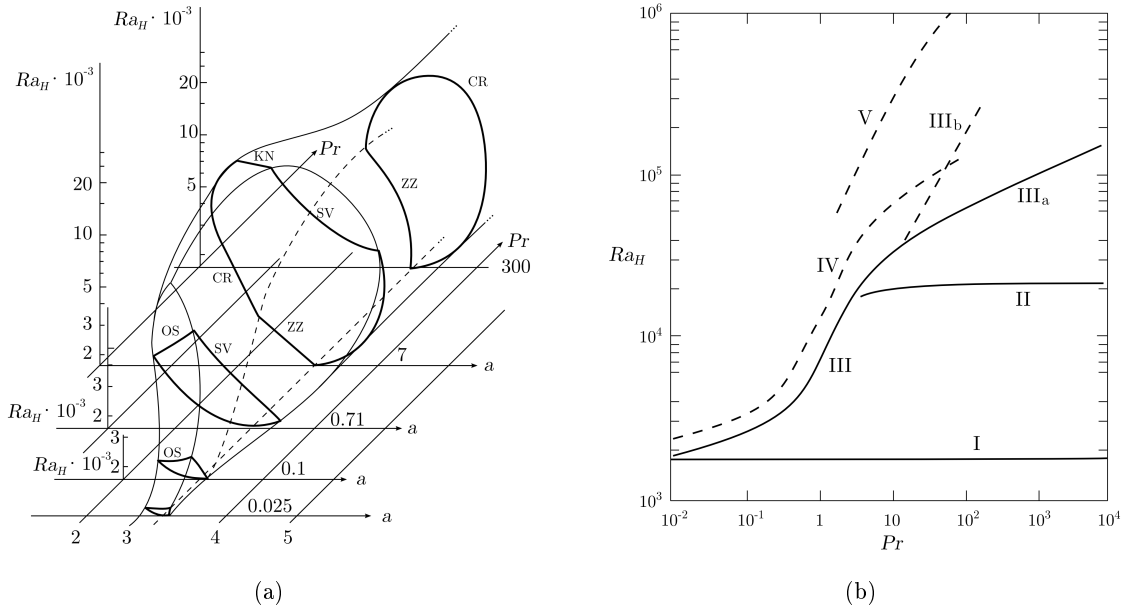


Figure 2.6: Instabilities and bifurcations in Rayleigh - Bénard convection: (a) stability diagram of stable two-dimensional convection rolls in an infinite fluid layer [38]; (b) experimental bifurcation patterns as a function of Ra_H and Pr : (I) onset of two-dimensional steady rolls; (II) three-dimensional convection; (III) time dependent convection (a) in isolated spots, (b) uniformly throughout the layer; (IV,V) nonperiodic flow [38].

instability (E) usually occurs for small Pr -values, and consists in a two-dimensional sideband phenomenon with $a_y = 0$. The *oscillatory instability* (OS) is the only temporally periodic instability found in the linear analysis, and the oscillations represent translational waves traveling along the roll axes. The critical Ra_H for this instability increases strongly with Pr . At intermediate Pr -values, the *knot instability* (KN) is observed, which may be regarded as a modified CR-instability with small a_y , resulting in the appearance of large scale cells with a knot-like structure. Finally, the *skewed varicose instability* (SV) also occurs at moderately high Prandtl numbers and is characterized by finite, nonzero values of a_x and a_y . Such an instability is responsible for the increase in the wavelengths of the convecton rolls with increasing Ra_H , resulting in a skewing distortion of the roll patterns.

This strong dependence of the instabilities on Pr , emerging from the linear analyses abridged in Figure 2.6(a) is confirmed by the comparison with earlier experimental observations [38, 44], as shown in Figure 2.6(b). It is particularly worthy to note that, despite the limitations of linear stability analyses, especially in the supercritical regions, many of the instabilities detected in such analyses have also been found in experiments as well as in numerical simulations, even for values of Ra_H well beyond the range where the analysis is expected to be valid.

2.2.3 Effect of lateral confinement

Results for the infinite layer case are expected to be good approximations to those of confined enclosures of large aspect ratios, and *vice versa*. As the aspect ratios are reduced,

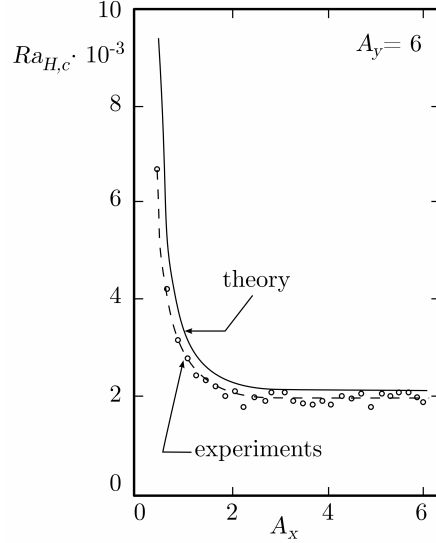


Figure 2.7: Effect of adiabatic confining walls on the critical Rayleigh number $Ra_{H,c}$ for the onset of convection [45].

the effect of lateral confinement becomes significant. The thermal boundary conditions at the side walls are also expected to have an influence on the transition mechanisms of the whole system. Moreover, the effect of Pr on the instability patterns detected for the infinite layer case can be altered by the presence of the vertical walls.

Although the physical phenomena for the confined enclosure case are much more complex than those occurring for infinite fluid layers, it is possible to single out a number of different mechanisms linked to the effect of confinement, and to analyze them in detail.

The first effect of lateral confinement is on the minimum critical Rayleigh number $Ra_{H,c}$. In view of the increased drag caused by presence of the side walls, $Ra_{H,c}$ is expected to increase, as compared to the infinite layer case. However, the determination of $Ra_{H,c}$ as a function of the aspect ratio is no longer simple, due to the impossibility of separating variables in the linear stability analysis; in order to solve the stability problem, it is then necessary to resort to numerical means.

Calculations for the cases of adiabatic and perfectly conducting side walls have been carried out by Davis [46] and Catton [47]. The comparison between the calculated data and the experimental results by Müller [45], reported in Figure 2.7, reveal that the linear theory slightly overestimates the value of $Ra_{H,c}$ as a function of the aspect ratio A_x . A complete summary of all the calculated and measured values of $Ra_{H,c}$ is provided by Raithby and Hollands [48]. Overall, the increase in $Ra_{H,c}$ with decreasing A is evident, as confirmed by the trends shown in Figure 2.7.

In the supercritical region, the presence of side walls determines a modification in the structure of the convective rolls forming the basic state for the infinite layer case. In the enclosed case, convection is always three-dimensional, and the characteristics of the flow structures depend on the aspect ratios, on Pr , and on the thermal boundary conditions at the side walls.

For large and moderate-size enclosures ($A_x \gtrsim 10$, $A_y \gtrsim 4$), the influence of the vertical walls extends only over one unit of H -size into the enclosure, with a very slight modulation

Author	$A_x \times A_y$	Pr	$Ra_{H,o}$
Kessler [50]	4×2	0.71	$3.34 \times 10^4 \pm 50$
		7	$3.9 \times 10^4 \pm 100$
Jäger [51]	4×2	0.71	3.4×10^4
Gollub and Benson [26]	3.5×2.1	2.5	$2.9 \times 10^4 \pm 1700$
Maurer and Libchaber [52]	3.5×1.9	0.71	2.35×10^4

Table 2.1: Critical Rayleigh number values for the bifurcation to oscillatory flow in enclosed Rayleigh-Bénard convection, according to various authors.

along the axis of other rolls in the enclosure middle [49]. For smaller enclosures, such an influence becomes much more complex.

Concerning this issue, the three-dimensional numerical study of Kessler [50] is particularly relevant. A small enclosure with $A_x = 4$, $A_y = 2$ is treated, for $Pr = 0.71$ and $Pr = 7$, with either adiabatic or conductive side walls. For $Pr = 0.71$ and for both types of wall boundary conditions, the convective rolls have a fully three-dimensional structure, up to $Ra_H = 3 \times 10^4$. Such rolls are not closed, in that there is a mechanism of mass exchange between the rolls. Moreover, for the case of conductive walls, small vortices form at the corners of the enclosure. The appearance of corner vortices is confirmed by experimental evidence, as reviewed by Yang [30]. On the contrary, the three-dimensionality of the flow for $Pr = 7$ is essentially limited to the wall region, while the flow remains two-dimensional in the central region of the enclosure.

The effects of lateral confinement become much more evident when Ra_H increases in the supercritical region. The mechanisms of convective rolls instability reviewed above, undergo significant modifications. In particular, the increase of the roll wavelength with Ra_H is no more continuous and driven by the SV-type instability [38], but occurs through successive discrete steps, each of which is actually a bifurcation from a stable state to another, with progressive a decrease in the number of rolls. This is confirmed by a number of studies concerning enclosures characterised by different values of A_x and A_y , and abridged by Yang [30]. What clearly appears from the overall picture, is that, for enclosures with small or moderate aspect ratios, only a few bifurcations are observed, and oscillatory motions set in only for high Ra_H values, of order $Ra_H \approx 10^5$. On the other hand, several bifurcations may occur for enclosures with large aspect ratios, before oscillations appear, for lower values of Ra_H ($Ra_H \approx 10^4$). However, the phenomena of the loss of rolls seem to be not fully understood yet for the enclosed case, and may have multiple causes. Some of them are reviewed and discussed by Pomeau and Manneville [41] and Cross *et al.* [43].

2.2.4 Oscillatory behaviours

As already shown in Figure 2.6(b), flow oscillations lie beyond the region of stable three-dimensional stationary flow for the infinite-layer case, regardless of Pr . This is also the case if the layer is confined by lateral walls. However, the aspect ratios play a significant role in the determination of the dynamics of such oscillations. When A_x and A_y are small, the oscillatory behaviour consists of traveling waves along the roll axis [40]. For enclosures characterised by large values of A_x and A_y , complex three-dimensional orientations of the rolls may occur, leading to a variety oscillation modes [49].

The critical values $Ra_{H,o}$ at which the bifurcations to oscillatory flow occur can be

influenced either by the enclosure size, by Pr , or by the boundary conditions at the side walls. The numerical results of Kessler [50] show that the difference between the bifurcation points for conductive and adiabatic walls is minimum and contained within one percentage point.

The effect on $Ra_{H,o}$ of the remaining parameters is summarized in Table 2.1, where the available results for a number of different enclosures and Pr -values have been collected. The values of $Ra_{H,o}$ provided by Kessler [50] are fairly consistent with the experimental observations of Jäger [51] for the same case. Moreover, it can be generally observed that a smaller A_x might produce a decrease in $Ra_{H,o}$ [26, 52], whilst higher Pr -values enlarge the stability range of the steady convective rolls.

Even though the thermal boundary conditions at the side walls apparently have no influence on the bifurcation point for the onset of the oscillatory behaviour, they do have non negligible effects on the subsequent bifurcations at higher Ra -values, as demonstrated again by Kessler [50], for the case of an enclosure with $A_x = 4$, $A_y = 2$, and for $Pr = 0.71$. Under adiabatic conditions, the oscillatory flow remains stable up to $Ra_H = 6 \times 10^4$, whilst, for conductive walls, a period doubling (P_2) occurs slightly beyond $Ra_H = 3.8 \times 10^4$ and remains stable until $Ra_H = 5.6 \times 10^4$, where a two-frequency, quasi-periodic flow (QP_2) sets on. A detailed analysis of the results reveals that the occurrence of a period doubling in the conductive cases, is caused by the presence of corner vortices.

2.2.5 Routes to chaos

The subject of transition to chaos of Rayleigh-Bénard convection is deeply entwined with the history of bifurcation and chaos theory since the meteorologist Edward N. Lorenz [24] witnessed for the first time the occurrence of deterministic, but nevertheless unpredictable behaviours out of the numerical analysis of a dynamical system. Such a system was a model problem directly derived from the equations of an infinite layer of fluid heated from below, and consisted of three equations, representing a truncation of a spectral expansion of equations (2.1.1)-(2.1.3). His analysis proved that complex chaotic dynamics could be reproduced even by a low-dimensional system, and later observations [30] confirmed that analogous dynamics can be recovered in the study of real cases, although the Lorenz model is not at all representative of the real Rayleigh-Bénard problem. It is also worthy to mention that the Lorenz model problem has been reprised in a number of analytical and numerical studies, aiming at characterising in greater detail its dynamical features. Among these studies is the outstanding analytical work by Vadasz [53, 54].

Turning to the analysis of the complete Rayleigh-Bénard enclosure problem, all the most relevant studies are experimental and deal with systems with small aspect ratios ($A \lesssim 4$). For such configurations, the transition to chaos generally consists of just a few, well defined bifurcations. Table 2.1(a) summarizes the results of a number of experimental studies, carried out for a wide range of enclosure sizings, and of Pr -values.

Maurer and Libchaber [52, 55] performed measurements on enclosures with variable A_x , filled with liquid helium at Prandtl number ranging between 0.4 and 0.8. All the transition scenarios detected present a cascade of Hopf bifurcations, leading to the onset of nonperiodic flow out of phase-locked or quasi-periodic states. In particular, in the case $A_x = 2.24$, $A_y = 1.88$, $Pr = 0.59$, the general picture of the Ruelle-Takens scenario (see Appendix B), is reproduced, with a QP_2 state bifurcating to a T^3 torus, before chaos appears; for slightly greater values of A_x and Pr , the occurrence of intermittency is also

(a)

Maurer and Libchaber [52, 55]		
$A_x \times A_y$	Pr	Route to chaos
2.24×1.88	0.59	$S \rightarrow P \rightarrow QP_2 \rightarrow QP_3 \rightarrow L \rightarrow N$
2.32×1.88	0.62	$S \rightarrow P \rightarrow QP_2 \rightarrow I \rightarrow N$
2.73×1.88		
3.29×1.88	$0.4 \div 0.8$	$S \rightarrow P \rightarrow QP_2 \rightarrow L_I \rightarrow L_{II} \rightarrow P_2 \rightarrow P_4 \rightarrow N$
3.49×1.88		

Gollub and Benson [26]		
$A_x \times A_y$	Pr	Route to chaos
2.42×1.23	5	$S_I \rightarrow P \rightarrow I \rightarrow N$
3.51×2.08	2.5	$S_{II} \rightarrow P \rightarrow P_2, P_4 \rightarrow N$
3.51×2.08	5	$S_I \rightarrow P \rightarrow QP_3 \rightarrow N$ or $S_{II} \rightarrow P \rightarrow QP_2 \rightarrow L \rightarrow N$

Berge <i>et al.</i> [56]		
$A_x \times A_y$	Pr	Route to chaos
2×1.2	130	$S_I \rightarrow P \rightarrow QP_2 (L, P, P_2) \rightarrow N$ or $S_{II} \rightarrow P \rightarrow P_2 \rightarrow I \rightarrow N$ or $S_{II_s} \rightarrow P \rightarrow QP_2 \rightarrow L \rightarrow N$ or $S_{III} \rightarrow P \rightarrow QP_2 \rightarrow L \rightarrow N$ or $S_{IV} \rightarrow N$

(b)

Bifurcation	Ra_H	Notes
$S \rightarrow P$	2×10^4	$f_1 = 0.55\text{Hz}$
$P \rightarrow QP_2$	2.7×10^4	$f_2 = 0.09\text{Hz}$
$QP_2 \rightarrow L_I$	3.2×10^4	$f_1/f_2 = 0.65$
$L_I \rightarrow L_{II}$		$f_1/f_2 = 0.7$
$L_{II} \rightarrow P_2, P_4$	3.38×10^4	doublings of f_2
$P_2, P_4 \rightarrow N$	$\geq 3.38 \times 10^4$	nonperiodic flow

Table 2.2: Rayleigh-Bénard convection in low aspect ratio enclosures: (a) known routes to chaos, as carried out by various authors; (b) detail of the bifurcations for the case $A_x = 3.29$, $A_y = 1.88$, $Pr = 0.5$, following Maurer and Libchaber [55].

observed.

For even larger values of A_x and for all Pr -values, the scenario looks more complex. Two phase locking states L_I and L_{II} , with different ratios between the frequencies, follow a QP_2 flow. It is important to note that hysteresis exists between the phase locking states. Then, the L_{II} state undergoes period doubling until chaos is reached. In Table 2.1(b), the detail of the critical Ra_H -values for this route are reported, for the case $A_x = 3.29$, $A_y = 1.88$, $Pr = 0.5$.

Gollub and Benson [26] identified four different routes to the onset of chaos, based on Laser-Doppler measurements on two different enclosures filled with water at two different Prandtl numbers, $Pr = 2.5$ and 5.0 . All of the four scenarios start from a steady-state flow, consisting either of three rolls of irregular shape (S_I) or two stable, symmetric counter-rotating rolls (S_{II}), and pass through a periodic state P . For the smaller enclosure, transition is characterised by intermittency, much alike to what observed by Maurer and Libchaber [52]; for the larger one, the value of Pr discriminates between two different kinds of scenario. At $Pr = 2.5$, the period doubling route cascade (see Appendix B) is detected, starting from the (S_{II}) state, whilst at $Pr = 5$, the transition scenarios are once again comparable to the Ruelle-Takens route, and the occurrence of QP_2 or QP_3 states is strictly related to the initial structure of the steady-state flow.

Bergé *et al.* [57, 56] observed transition to chaos in a small enclosure with aspect ratios $A_x = 2$ and $A_y = 1.2$, with adiabatic side walls, and filled with silicone oil at $Pr = 130$. Multiple spatial organizations of steady-state circulations were detected in this case, namely structure S_I , with three rolls aligned along the x direction, structures S_{II} and S_{II_s} , with four cells, one for each quadrant of the enclosure, and structures S_{III} and S_{IV} , consisting of six and eight cells respectively, arranged in rows of two along the x -axis.

Each of these structures gives rise to a different transition scenario, as summarized in Table 2.1(a). In particular, structures S_I , S_{II_s} and S_{III} evolve in a manner similar to the Ruelle-Takens route, whilst, from S_{II} , chaotic behaviour is reached through states of intermittency [57]. The transition to nonperiodic flow of the S_{IV} asset appears rather sudden, although intermediate states are likely to exist.

It shall also be reported that the more complex organizations (S_{II_s} , S_{III} and S_{IV}) remain stable for a much wider range of Ra_H (up to 700 times the value of $Ra_{H,c}$ for S_{IV}), if compared to the simpler ones (S_I and S_{II}), which undergo transition for $Ra_H \simeq 250R_{H,c}$.

Complete numerical studies of transition to chaos for the three-dimensional Rayleigh-Bénard problem are much rarer, mainly due to the computational resource limits of the years when the maximum research efforts on the subject were carried out [30]. On the other hand, more recent numerical studies on transitional natural convection have often been aimed at analyzing different configurations, or tackled the problem only partially.

Zienicke *et al.* [58] analyzed numerically the bifurcations in a two-dimensional enclosure with $A_x = 2.83$ and $Pr = 6.8$, by means of spectral decomposition, and imposing stress-free conditions at the boundaries of the domain. Quite interestingly, their analysis reproduces a dynamics that does not attain chaotic conditions, but shows the occurrence of a cascade of Hopf bifurcations of tori. The first bifurcation, from a S -type state to a P -state, occurs at $Ra_H = 3 \times 10^4$, while a second Hopf bifurcations at $Ra_H = 4.5 \times 10^4$ gives rise to T^2 torus (QP_2). By the appearance of traveling waves at $Ra_H = 8.5 \times 10^4$, the T^2 torus bifurcates in a T^3 torus (QP_3). At $Ra_H = 2.3 \times 10^5$, no chaos is detected, but the solution lies on a T^4 torus, with 4 incommensurate frequencies (QP_4).

Finally, some numerical studies also dealt with enclosures of aspect ratios $A_x, A_y \leq 1$.

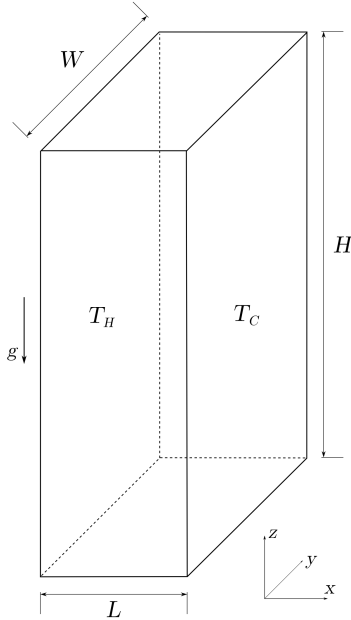


Figure 2.8: Schematic of the side-heated enclosure problem.

Pallares *et al.* [59] considered the case of a cubical cavity ($A_x = A_y = 1$), for three values of the Prandtl number, $Pr = 0.7, 10, 130$, and in the range $10^4 \leq Ra_H \leq 6 \times 10^4$, finding seven different types of steady flows, bifurcating into each other for varying Ra_H and Pr . Moreover, Cappelli D’Orazio *et al.* [60] recently carried out an analysis of a two-dimensional enclosure heated from below, with $0.17 \leq A_x \leq 0.5$, and for $10^3 \leq Ra_H \leq 2 \times 10^6$ and detected the occurrence of pitchfork and Hopf bifurcations with hysteresis in that range, the flow being still periodic for the highest Ra_H -value.

2.3 Side-heated enclosure

The so-called “vertical cavity” is the second fundamental geometry for confined buoyant flows: a parallelepiped enclosure to which a differential heating is applied on one pair of opposite vertical walls. The schematic of the problem, shown in Figure 2.8, uses the symbols already defined for the Rayleigh-Bénard case (see Section 2.2). The thickness L of the vertical heated layer becomes the reference distance for the definition of the aspect ratios A_x and A_y , since the overall transfer of heat between the two walls is directed in the x -direction:

$$A_x = \frac{H}{L}, \quad A_y = \frac{W}{L} \quad (2.3.1)$$

Nevertheless, it is more appropriate to adopt the vertical extension of the enclosure as the characteristic length of the system [3], and, therefore the system is again governed by the Rayleigh number Ra_H , based on the enclosure height H . The reason for this choice is that many remarkable features of the flow induced by the differential heating are common to the case of a free boundary layer on a vertical plate.

As compared to the Rayleigh-Bénard problem, the subject of natural convection in side-heated enclosures is much younger, although it has received a great deal of attention by the scientific community in the last three decades. The first prominent theoretical study on the case is due to Batchelor [61]. Reviews of the main literature results have been provided by Catton [29, 32], Hoogendorn [62] and Ostrach [14, 15]. Yang [30] and Le Quéré [63] specifically addressed the topic of flow transition and are particularly significant in the present context.

2.3.1 Main flow characteristics

As opposed to the Rayleigh-Bénard case, in the system of Figure 2.8 fluid motion starts immediately after imposing a temperature difference between the walls. This is due to the fact that the gravity vector is orthogonal to the imposed density gradient (see Section 1.3.4). The characteristics of the resulting flow strongly depend on the values of the aspect ratios and of Pr , other than Ra_H .

The scale analysis performed by Patterson and Imberger [64], and successively reprised by Bejan [3], provides a broad, but nevertheless effective distinction of the main flow characteristics for a two-dimensional enclosure heated from the side and with adiabatic end walls. It covers fluids with $Pr \gtrsim 1$, and the role of Ra_H and the aspect ratio A_x are highlighted. Based on considerations upon the scalings of the thermal boundary layer, the $A_x - Ra_H$ plane is divided into four sectors, each corresponding to a distinct flow and heat transfer regime [3]:

- *Regime I: pseudo-diffusive regime*: for $Ra_H \lesssim 1$, regardless of the value of A_x , the circulation is slow and mainly driven by shear. Heat is transferred by conduction from the heated to the cooled wall, and the temperature varies linearly across the enclosure.
- *Regime II: tall enclosure limit*: if $A_x \gtrsim Ra_H^{1/4}$, the transfer of heat across the enclosure is still dominated by conduction, whilst the flow is characterised by the presence of two distinct thermal layers in the vicinity of the top and bottom walls.
- *Regime III: boundary layer regime*: when $Ra_H^{-1/4} \lesssim A_x \lesssim Ra_H^{1/4}$, the flow is characterised by two vertical boundary layers along the differentially heated side walls, and the adiabatic horizontal walls are lined by distinct thermal layers. Most of the fluid in the core region of the enclosure is relatively stagnant and vertically stratified.
- *Regime IV: shallow enclosure limit*: if $A_x \gtrsim Ra_H^{-1/4}$, the heat transfer mechanism is again dominated by the presence of vertical thermal layers. In the long horizontal core of the cavity, two counterflowing horizontal streams are formed, which, in turn, exchange heat one to the other.

The $Ra_H - A_x$ plane subdivision is shown in Figure 2.9. No similar analyses considering Pr -values of order less than unity are available. However, it may be inferred that the relevant types of flow are still those depicted by the above systematic, even if the interplay between the thermal and dynamic fields is substantially different from the case $Pr \gtrsim 1$, and may lead to the formation of more complex intermediate flow structures.

The occurrence of the flow patterns sketched above has been confirmed by several experimental studies. Extensive observations of the flow structures were carried out by

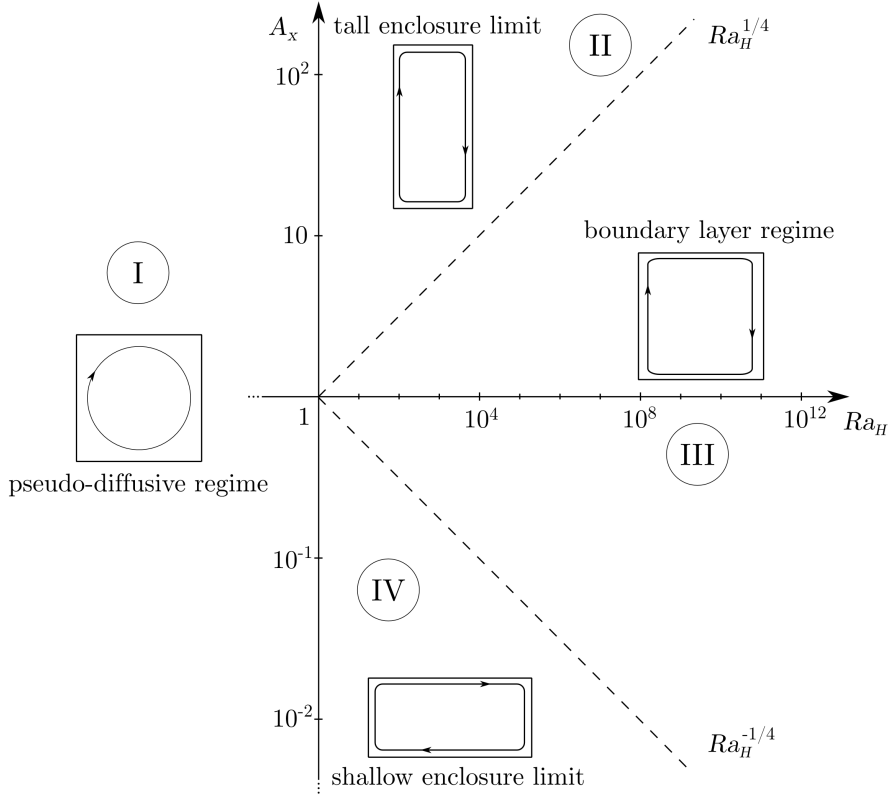


Figure 2.9: Main types of flow regimes for natural convection in an enclosure heated from the side, following [3] and [64]

Elder [65, 66], for essentially two-dimensional vertical enclosures filled with water, and for a wide range of aspect ratios ($1 \leq A_x \leq 60$, large A_y). The problem was later analyzed by Ayyaswamy (see [32, 29]). Such analyses revealed that, in tall enclosures, the pseudo-diffusive regime can hold up to $Ra_H \approx 10^3$. In the range $10^3 \lesssim Ra_H \lesssim 10^5$, the flow and temperature fields become of boundary layer type. The birth of secondary and tertiary circulations is observed, respectively, for $Ra_H \approx 10^5$ and $Ra_H \approx 10^6$. At $Ra_H \approx 10^7$, the boundary layers become unstable, and turbulent flow is attained for $Ra_H \approx 10^9$.

The case of a two-dimensional shallow enclosure was treated analytically and numerically by Cormack *et al.* [67, 68] and experimentally by Imberger [69], in a joint study. In the analytical work [67], the problem was tackled by means of matched asymptotic expansions in the limit $A_x \rightarrow 0$ and fixed Ra_H . The analysis confirmed the existence of the parallel counterflow pattern described above, and issued a criterion stating that, for $Ra_H^2 A_x^3 \leq 10^5$, the dominant mode of heat transfer is conduction. Moreover, for $Ra_H \rightarrow \infty$ and A_x fixed, the boundary layer pattern was shown to prevail. Such theoretical predictions were in excellent agreement with the numerical results in [67]. Most of the flow features indicated by the numerical work were qualitatively observed in the experimental work [69]. Experiments for $Ra_H A^3 \approx 10^{11}$ indicate that the mid-depth of the cavity becomes isothermal, and that there is a slow central circulation throughout the entire enclosure. Such a behavior marks a strong difference with the case of tall enclosures, where, instead, the core

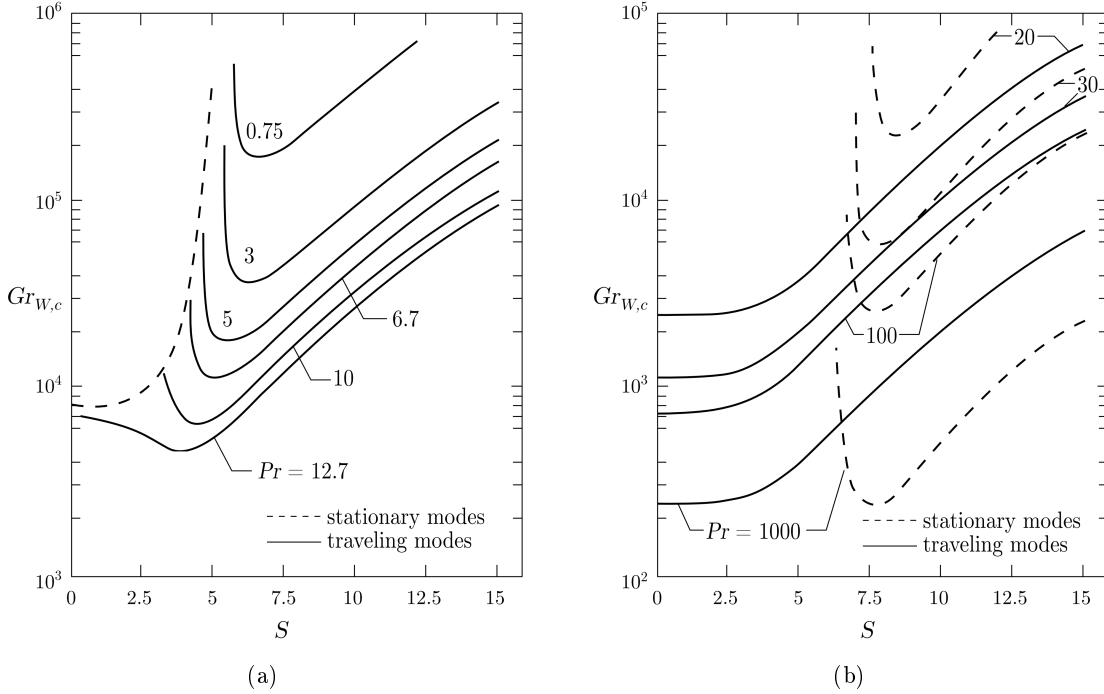


Figure 2.10: Critical Grashof number curves for the stability of natural convection in a differentially heated vertical layer [72]: (a) $Pr = 0.75 \div 12.7$; (b) $Pr = 20 \div 1000$.

remains stagnant.

In contrast to the Rayleigh-Bénard case, the effects of the third dimension on the general flow characteristics in side-heated enclosures are much less substantial, especially when the flow is steady, and at moderate values of A_x . The numerical analyses of Mallinson and De Vahl Davis [70] and Janssen *et al.* [71] provide detailed insight of the three-dimensional thermal and flow fields. However, as reported in the following, the presence of the lateral bounding walls has a non-negligible effect on the system stability and on transition to unsteady flow.

2.3.2 Stability of steady-state regimes

Stability analyses for the side-heated enclosure are hard to perform, due to the difficulties arising in determining the base flow inside the domain. Vest and Arpaci [73], and, successively, Bergholz [72] carried out linear stability analyses of the flow within a differentially heated vertical fluid layer, corresponding to the case of an enclosure with $A_x \rightarrow \infty$, for both the pseudo-diffusive and the boundary layer regimes. For the purposes of the analyses, the base flow and temperature profiles were taken as functions of the sole vertical coordinate z , with the additional assumption that, in the boundary layer case, the stratification in the core is linear with z , and can be incorporated in the boundary conditions. A dimensionless stratification parameter S is defined as:

$$S = \left[\frac{Ra_H}{4} \frac{|\partial T / \partial x|}{T_H - T_C} \right]^{\frac{1}{4}} \quad (2.3.2)$$

This had to be prescribed in the eigenvalue problem (see Appendix C), to encompass the stability of both flow regimes in one single analysis. The results show that two distinct instability mechanisms can take place, one in the form of secondary steady circulations, and the other in the form of traveling periodic waves. Figures 2.10(a) and 2.10(b) show that the curves of marginal stability, presented in terms of the critical Grashof number $Gr_{W,c}$, based on the gap width W between the vertical walls, are complex functions of S and Pr . For the conduction regime, for which $S = 0$, it is seen that the preferred instability is that of multicells for $Pr \leq 12.7$, while, as Pr is increased beyond $Pr = 12.7$, traveling waves determine the loss of stability. In the boundary layer regime ($S > 0$), and up to $Pr \approx 30$, instability always occurs in the form of traveling waves. A more recent analysis [74] performed by means of weakly non-linear theories, substantially confirmed Bergholz's results [72].

Numerical predictions have been subsequently brought forth for comparison with the results of the stability analysis. Korpela *et al.* [75] and Lee and Korpela [76] performed detailed two-dimensional calculations of the flow in an air-filled enclosure in the range $10 < A_x < 40$. According to Lee and Korpela [76], for $A_x = 20$, the bifurcation to multicellular flow occurs within $10^4 < Gr_{W,c} < 1.1 \times 10^4$; such a result compares well with the experimental data of Hollands and Konicek [77]. Moreover, in accordance to Figure 2.10(a), the stability analysis [72] predicts a value of $Gr_{W,c} = 0.804 \times 10^4$, for vanishing S ; the slight discrepancy with the above numerical result [76] is due to the fact that, in the real case, S is not identically zero and A_x has a large but finite value.

The numerical analyses of Lee and Korpela [76] also showed that the bifurcation to multicellular flow takes place only for $A_x \leq 10 \div 12.5$, depending on Pr . Up to those critical values, the steady-state flow is essentially of unicellular structure, and the critical Gr_W -value for the traveling wave instability to occur increases with Pr (as opposed to the predictions of the linear theory for $A_x \rightarrow \infty$) and decreases with increasing A_x .

Concerning enclosures with moderate aspect ratios ($1 \leq A_x \leq 10$), similar conclusions are drawn by Le Quéré [63] both for air and water. The cases of adiabatic and conductive horizontal walls are considered, and, for $Pr = 0.71$, a stability diagram representing the critical Rayleigh number, based on the enclosure width, $Ra_{W,c}$, is extracted from various studies (Figure 2.11). The choice of W as the characteristic dimension is somewhat in contrast with proper scaling arguments [3], but is appropriate for a comparison with the results for $A_x \rightarrow \infty$. The general trends of Figure 2.11 confirm that the $Ra_{W,c}$ decreases for increasing A_x , and indicate that instabilities take place for lower Ra_W -values if the top and bottom walls are conductive. The stability threshold is found to be generally higher for water, $Pr \approx 7$, and practically independent of the aspect ratio, since, for $Pr \gg 1$, the flow exhibits very thin thermal boundary layers: for $A_x = 10$, Le Quéré [78] predicts a value of $Ra_{W,c}$ in the range $8 \times 10^9 \leq Ra_{W,c} \leq 9 \times 10^9$; for $A_x = 1$, Henkes [79] proposes $4 \times 10^9 \leq Ra_{W,c} \leq 5 \times 10^9$. Both results consider adiabatic end walls.

The stability of natural convection regimes in an air-filled square enclosure ($A_x = 1$, $Pr = 0.71$) with periodic boundary conditions in the third dimension, was investigated by Henkes and Le Quéré [80], with respect to two- and three-dimensional perturbations, and for both the cases of conducting and adiabatic top and bottom walls. In contrast to the assumption of 2D flow, they proved that perturbations in the third dimension are less stable than those in the enclosure cross section. Hence, lower critical values were predicted for the onset of time-dependent flows: for conducting horizontal walls, $1.8 \times 10^6 < Ra_{W,c,2D} < 2.3 \times 10^6$ while $10^6 < Ra_{W,c,3D} < 1.8 \times 10^6$; for adiabatic horizontal walls

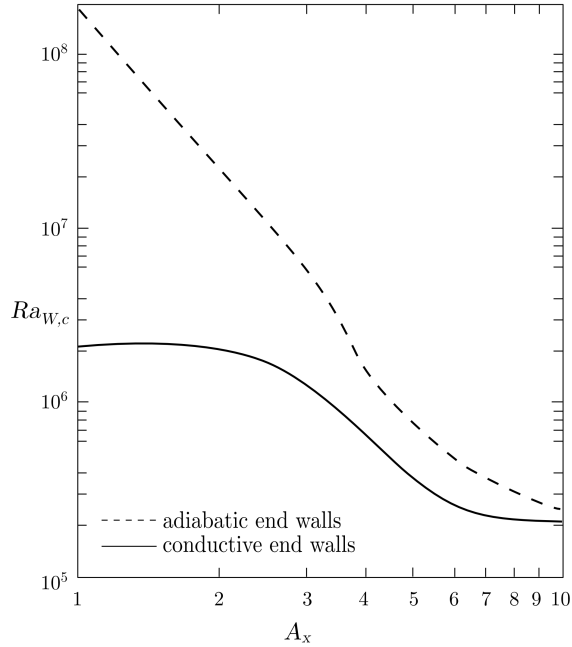


Figure 2.11: Critical Rayleigh number curves for the stability of natural convection in a differentially heated enclosure with $1 \leq A_x \leq 10$ and $Pr = 0.71$ [63].

$10^8 < Ra_{W,c,2D} < 2 \times 10^8$ while $10^7 < Ra_{W,c,3D} < 10^8$. Such a trend was successively confirmed by a more detailed analysis by Xin and Le Quéré, over a wider range of Pr -values [81].

A stability study of the limit for shallow enclosures $A_x \rightarrow 0$ has not been performed so far, probably because, with such an assumption, it might be impossible to derive a reasonable expression of the base flow. The work of Wakitani [82] is however worth of mention in this frame. By means of numerical simulations, he traced the general trends of for the critical Grashof number $Gr_{H,c}$ marking the onset of oscillatory flow, in three-dimensional side-heated shallow enclosures with $0.25 \leq A_x \leq 0.5$ and $0.24 \leq A_y \leq 2$, for very low values of Pr , $Pr = 0 \div 0.027$. The results indicate that, in the range of Pr considered, the most influential parameters for transition are A_x and A_y . In particular, it is seen that $Gr_{H,c}$ generally decreases when either A_x or A_y decrease. Such a result is in opposition to the trends depicted for tall enclosures [63].

2.3.3 Transition to chaotic flow

In view of the prominence of the traveling-wave instabilities, and due to the fact that the flow, for a wide range of the aspect ratios, is of boundary layer type, many of the transition scenarios in a side-heated enclosure are alike to those of external buoyant flow over vertical surfaces [30]. Hence, one might not expect to encounter the diversity of routes witnessed in Rayleigh-Bénard convection (Section 2.2.5).

In his review, Le Quéré [63] presents the routes to chaos for two 2D air-filled enclosures respectively with $A_x = 4$ and adiabatic end walls, and $A_x = 1$ and conductive floor and ceiling. In both cases, various solution branches were detected, but, substantially, with

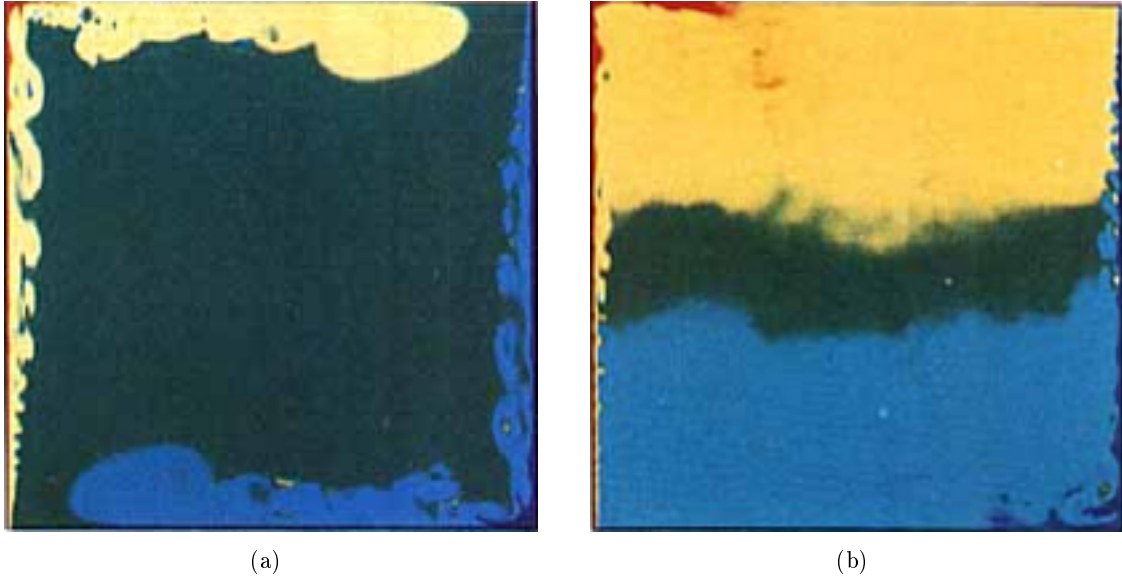


Figure 2.12: Snapshots of the temperature field in a side-heated square enclosure, $Ra_H = 2 \times 10^{10}$ and $Pr = 0.71$, taken from [83]: a) thermal boundary layer transition; b) asymptotic stratification.

only one way of approaching chaos. The instability of the steady state regime S always leads to a periodic state P . All transition scenarios invariably pass through a QP_2 state before attaining a nonperiodic flow N . The occurrence of intermittency is signalled for the case $A_x = 4$, while one period doubling is detected on a solution branch for $A_x = 1$.

The time evolution of a two-dimensional, nonperiodic flow of air ($Pr = 0.71$) at $Ra_H = 2 \times 10^{10}$, in a square-sectioned enclosure ($A_x = 1$) was described by Paolucci [83] by means of DNS calculations. In Figures 2.12(a) and 2.12(b), two instantaneous snapshots of the temperature field are reported. Figure 2.12(a) shows the transition of the vertical boundary layers, which undergo a Tollmien-Schlichting-type instability [4], with the appearance of typical “hook” thermal structures; moreover, along the top and bottom walls, two horizontal jets intrude the quiescent fluid, and slowly diffuse into the enclosure core, while approaching the opposite vertical boundary. In Figure 2.12(b), a statistically steady state is reproduced; the core is nearly quiescent, and is characterised by a complete vertical temperature stratification. The full development of the thermal boundary layers at each vertical wall can also be appreciated in the figure.

2.4 The horizontal annulus

A third fundamental case of confined free convection is the flow originating in the annular region between two concentric circular horizontal cylinders. A cross section of the system is schematised in Figure 2.13. Different temperatures are imposed at the surfaces of the inner and outer cylinders, respectively T_H and T_C , with $T_H > T_C$.

The geometry can be characterized by means of three possible length scales, namely the inner diameter of the cavity, $D_i = 2r_i$, the outer diameter $D_o = 2r_o$, or the radial gap spacing $H = r_o - r_i$.

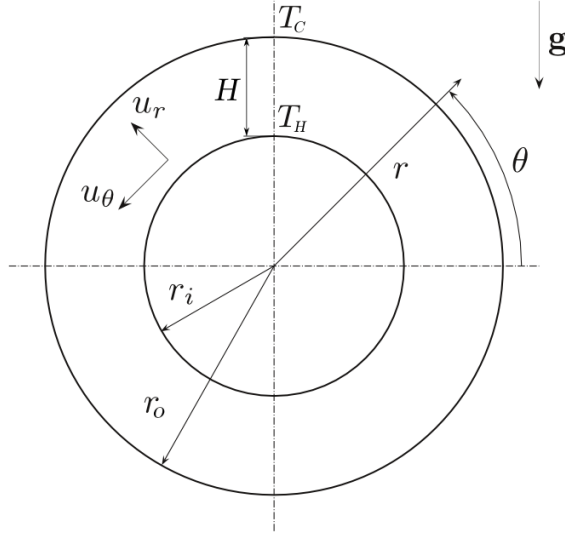


Figure 2.13: Schematic of the cross-section of the horizontal annulus.

Each length scale is representative for a different feature of the system. The choice of δ seems the most reasonable, in that it often has the advantage of reducing the dependence of the solution on the aspect ratio R . This, for instance, is shown to facilitate, the fitting of heat transfer data, relative to different configurations, with a single curve [84]. However, in the limiting case of large aspect ratio, $r_o \gg r_i$, the solution is expected to approach that of an isolated isothermal cylinder, or of an enclosed line heat source. These cases are treated correctly only choosing either D_i or D_o as the reference length, depending on which of the two lengths is finite, compared to the other. Moreover, D_o represents the vertical extent of the enclosure, and, for some authors [3], it stands as the correct scale for the evaluation of the magnitude of buoyancy forces.

In all cases, in order to give a complete geometrical definition of the problem, the aspect ratio R has also to be defined:

$$R = \frac{r_o}{r_i}, \quad 1 < R < \infty \quad (2.4.1)$$

In most of the theoretical approaches reviewed in the following, the annulus axial length is assumed to be very large, in comparison to the outer diameter, so that flow and heat transfer effects in the axial direction are be neglected. This assumption is of course limitative when investigating inherently three-dimensional flows, as the ones occurring for supercritical values of the governing parameters.

2.4.1 General characteristics of the flow

The horizontal annulus is an interesting convective system, since, due to the curvature of the cylindrical differentially heated surfaces, its phenomenology encompasses the features of both the Rayleigh-Bénard and the vertical enclosure systems. Once the temperature of the inner cylinder is increased, a fluid motion ensues immediately in the vicinity of the horizontal midplane, where the cylindrical walls are substantially vertical. On the other hand, the fluid in the top part of the annulus is subject to an unstable vertical gradient,

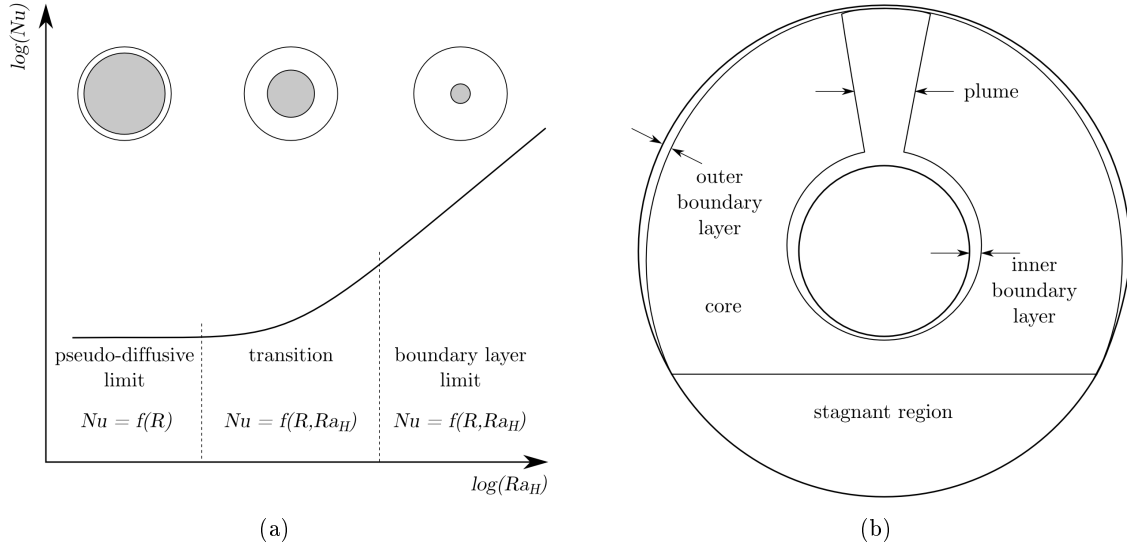


Figure 2.14: Flow regimes in the horizontal annulus: a) sketch of the flow and heat transfer characteristics as a function of R and Ra_H [84]; b) flow regions in the boundary layer limit [85].

as in the Rayleigh-Bénard problem. The combination of these two situations in a single problem produces a variety of flow configurations and transition phenomena: in the lateral regions, $\theta \simeq 0, \pi$, the flow is likely to undergo instabilities of hydrodynamic type, as described by Bergholz [72] for a vertical, differentially heated infinite fluid layer; on the contrary, in the upper regions, $\theta \simeq 90$, instabilities are mainly thermally driven, of the types analyzed by Busse [38] for an unstably heated horizontal layer.

The general characters of the possibly expected flow regimes are broadly schematised in Figure 2.14(a), associated to the sketch of the typical trend of the average Nusselt number as a function of Ra_H . For very low Ra_H -values, the regime is pseudo-diffusive (*PD*), and the heat transfer is conduction-dominated and is function only of R . Such a regime persists as long as the annular gap H and/or the temperature difference ($T_H - T_C$) are sufficiently small. The slow circulation induced by the feeble temperature gradient is characterised by two symmetric, counter-rotating cells, whose shape varies according to the value of R : for small R -values (narrow annuli) the cells have the shape of a crescent, while for large aspect ratios they assume the typical kidney shape.

At the opposite limit, for high Ra_H -values, the flow is of boundary layer type. As depicted in Figure 2.14(b), the boundary layer regime can be subdivided into five different flow regions: a thin boundary layer develops around the inner cylinder, giving rise to a buoyant plume in the top region of the annulus; for large values of R , the dynamics of the plume are the leading phenomenon for transition to turbulent flow.

Along the cooler, outer cylinder walls, the fluid redescends, forming a second, downward boundary layer. The core region between the two boundary layers is characterised by fluid recirculation, while below the cylinder the fluid is stably stratified and mainly stagnant. For this flow regime, the average heat transfer rate is a function of both Ra_H and R .

In the intermediate region between the pseudo-diffusive and boundary layer regimes, the flow is a strong function of both Ra_H and R . As Ra_H increases, the steady cellular

patterns of the pseudo-diffusive regime change into various types of flow, depending on the aspect ratio R , and also on the Prandtl number. The identification of the possible flow regimes in this “transition region” is a major issue in the study of buoyant flow in a horizontal annulus. Such issue has been addressed by many authors so far, and the main outcomes of the research addressing this particular topic are be surveyed in the following.

General correlations for the average Nusselt number at the inner and outer cylinder surfaces, for the complete range of Ra , R and Pr , are due to Raithby and Hollands [86] and Kuehn and Goldstein [87]. It is important to note that, for $R \gtrsim 10$, the heat transfer rate approaches that of a single cylinder in an infinite medium [88, 89], thus indicating that the presence of the outer bounding surface does no longer affect heat transfer.

2.4.2 Fundamental studies

Most of the early works on the horizontal annulus mainly dealt with the hear transfer characteristics of the systems. A thorough review of those works is provided by Teertstra and Yovanovich [84]. The first experimental study on horizontal annular enclosures was presented by Beckmann [90] in 1931, while the first numerical predictions were provided by Crawford and Lemlich [91] and Abbott [92], using of finite difference schemes.

As shown in Figure 2.13, the annular domain is conveniently parametrized in cylindrical coordinates, and the an analytical resolution of cylindrical form of the governing equations (2.1.1)-(2.1.3) can be afforded. To this aim, Crawford and Lemlich [91] first presented an analytical expression for the 2D flow and temperature fields in the pseudo-diffusive limit. Successively, Mack and Bishop [93] and Huetz and Petit [94] developed analytical solutions for the stream function and temperature fields, for low values of the Rayleigh (or Grashof) numbers, by means of the *perturbation method*, and for the cases of isothermal and uniformly heated inner surfaces, respectively. The solutions were expressed in infinite power series of Ra_{D_i} (or Gr_{D_i}), and validated against previous experimental data. Estimates of the limits of validity of the solutions, *i.e.* of the limiting values of Ra_{D_i} (or Gr_{D_i}) for which the series converge, are also provided. Both solutions were recast in the form of double perturbation series in Gr_{D_o} and Pr by Custer and Shaugnessy [95], with the aim of exploring the low- Pr range.

Approximate analytical studies have also been performed. A complete solution of the steady laminar boundary layer regime in a horizontal annulus is due to Jischke and Farshchi [85]. Recently, an expression for the flow and temperature fields was derived by Desrayaud *et al.* [12], for the pseudo-diffusive regime in the limit $R \rightarrow 1$, for pure fluids and binary mixtures.

2.4.3 Flow regimes in the transition region

Powe *et al.* [96], in their outstanding work, identified the flow regimes and spatial patterns as a function of the radius ratio R and the Rayleigh number Ra_H , for air-filled annuli with a finite axial extension. Based on flow visualization experiments, results were summarized in the flow pattern map reproduced in Figure 2.15(a), where the abscissa is a modified version of the radius ratio, $2/(R-1)$. The chart depicts regions where different flow transitions take place. In particular, for wide gap annuli, *i.e.* for $R > 1.71$, a direct transition was observed from the two-dimensional, steady unicellular flow, to an oscillatory flow. For moderate gap annuli, $1.24 < R < 1.71$, a three-dimensional spiral flow was detected past the transition point; the spiralling movement of fluid particles was the result of the combination of

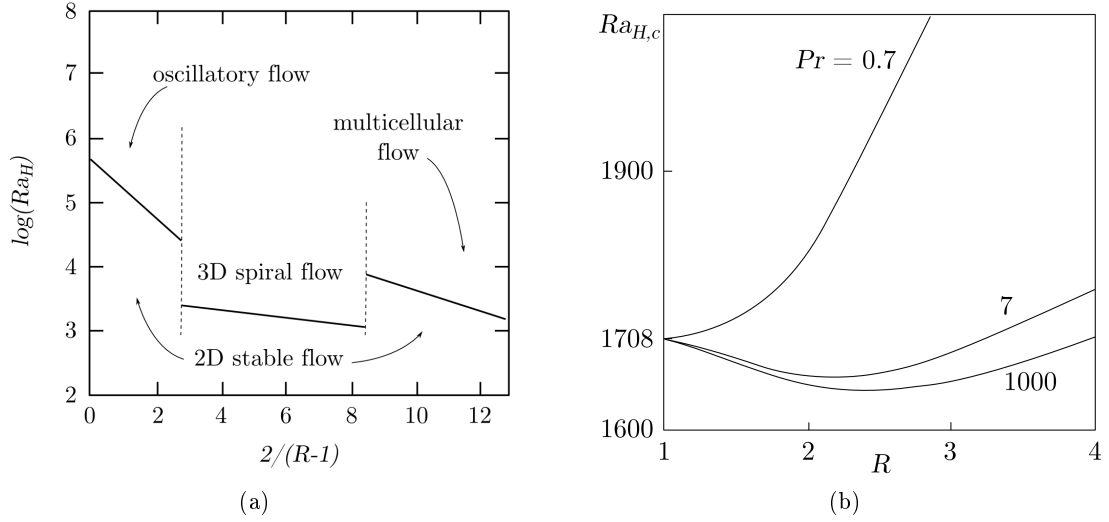


Figure 2.15: Flow patterns and stability in horizontal annuli: a) experimental map of the flow regimes as reported by Powe *et al.* [96]; b) marginal stability curves as a function of Pr [97].

the crescent-shaped eddies on the transversal plane, with a set of counterrotating rolls developing in the axial direction, generated by a Rayleigh-Bénard-like instability. Finally, for the narrowest annuli, $R < 1.24$, the basic unicellular flow was observed to change into several multicellular 2D flows.

Experimental and numerical studies were later conducted by Rao *et al.* [98], yielding results in fair qualitative agreement with Powe's experimental map, especially for the cases of moderate and narrow-gap annuli. The chart in Figure 2.15(a) is still an absolute reference for the study of flow transition in buoyant horizontal annuli.

The first stability analyses of the 2D flow with respect to 3D disturbances, in annuli of infinite length, were performed by Mojtabi and Caltagirone, by means of linear [97] and energy methods [99]. A first-order truncation of the perturbation solution by Mack and Bishop [93] was used as the base flow, and perturbed with axisymmetric disturbances. The marginal stability curves were obtained analytically as functions of Ra_H , R , Pr and the wave number a . Three different curves from the linear analysis, corresponding to three Pr -values, are reported in Figure 2.15(b). It is seen that the stability thresholds, in the parallel plate limit, $R \rightarrow 1$, tend to the critical value $Ra_{H,c} = 1708$, typical of Rayleigh-Bénard convection. Such a result was confirmed also by the energy analyses [99].

Subsequent studies were aimed at clarifying the nature of the instabilities and the resulting flow regimes. Focusing on air flows, $Pr = 0.7$, the occurrence of multiple solutions was detected experimentally and numerically by Cheddadi *et al.*, [100] for moderately narrow annuli, under the two-dimensional assumption. The authors showed that two different regimes could coexist for a wide range of Ra_H , namely, the basic crescent-shaped unicellular flow, and a bicellular flow with a pair of thermally-driven counterrotating rolls in the top part of the annulus. A similar result, showing fair agreement with the analyses of Cheddadi *et al.*, [100] was recovered later by Cadiou *et al.* [101], who analyzed the flow in very narrow annuli ($R < 1.24$). They were the first to postulate the dual solutions to be originated existence of an imperfect bifurcation with two stable branches. Moreover, they

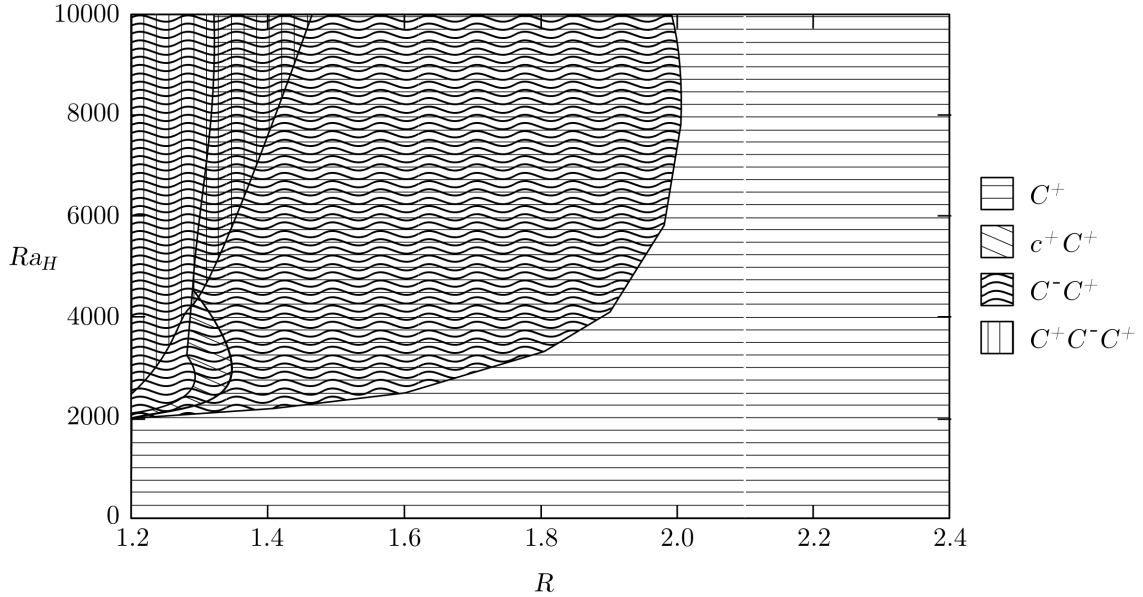


Figure 2.16: Chart of the two-dimensional flow patterns in the (R, Ra_H) plane, reproduced from [102].

found out that the number of multiple solutions and cells increased for decreasing R , and that for $R < 1.15$ and increasing Ra_H , shear-driven instabilities may give birth to small co-rotating cells, shaped like the eyes of a cat.

Analogous results were provided later by Chung *et al.* [103], Yoo [104, 105, 106], and Desrayaud *et al.*. Mizushima *et al.* [107] were the first to attempt a rigorous determination of the behaviour of the system near the bifurcation point, confirming that the dual solutions were due to an imperfect transcritical bifurcation. Petrone *et al.* [108, 102], performed a stability analysis of the steady-state solutions obtained numerically, and concluded that, in the limit $R \rightarrow 1$, the imperfect transcritical bifurcation closes into the pitchfork bifurcation of the onset of Rayleigh-Bénard convection, leading once again to the same threshold value, $Ra_{H,c} = 1708$.

Petrone *et al.* [102] ultimately determined the possible steady flow patterns in two-dimensional, air-filled annuli for a wide range of R and Ra_H -values. They showed also that not only dual but also triple solutions can be stable for certain values of the parameter. The chart in Figure 2.16 summarizes the results of their stability analyses, and reveal that four different configurations are essentially possible for $R > 1.2$, namely the basic unicellular flow, two kinds of bicellular flows, and a tricellular flow. The symbols C^+ and C^- respectively indicate anticlockwise and clockwise rotating cells extending over the entire annular gap, while c^+ indicates a smaller, co-rotating cell which eventually grows aside of the main C^+ circulation. The chart also indicates that, for $Pr = 0.7$ multiple solutions can occur only for $R \leq 2$, a result which agrees fairly with Powe's *et al.* experimental findings [96] (see Figure 2.15(a)).

After the stability analyses of Mojtabi and Caltagirone [97, 99], different authors addressed the effect of three-dimensional perturbations on the stability of the two-dimensional base flow. Choi and Kim [109] performed a linear stability analysis for air-filled annuli of infinite length, in the range $1.2 \leq R \leq 2$. They demonstrated a weak dependence of the

$Ra_{H,c}$ threshold on the radius ratio ($1714 \leq Ra_{H,c} \leq 2514$), and, on the basis of numerical simulations for supercritical Ra_H -values, witnessed that the instabilities were due to the formation of transverse rolls in the upper part of the annulus, giving rise to the spiral flow already detected by Powe *et al.* [96]. Once again, the agreement between analytical [109] and experimental results [96] was very satisfactory. Similar instability mechanisms were also observed by Dyko *et al.* [110], who provided a thorough description of the flow patterns in three-dimensional annuli, characterised by moderate and large gap widths, by means of accurate numerical simulations and flow visualizations. The linear and energy analyses [97, 99] were extended to the case of non-axisymmetric perturbations and finite length annuli, showing, in particular, that instabilities are more likely to occur for axisymmetric disturbances. The flow in a large gap annulus ($R = 2.1$) was also investigated in [110], for a fluid with $Pr = 100$, and it was observed that, with increasing Ra_H , the center of the crescent-shaped base circulation shifts to the top part of the annulus, before undergoing transition to oscillatory flow.

Subsequently, Dyko and Vafai [111] considered air-filled narrow gap annuli ($R \leq 1.15$), detecting that the possible flow structures consisted either in transverse rolls or in a combination of longitudinal counterrotating cells (as observed for 2D flows, [102]) and transverse rolls.

After performing further three-dimensional linear stability analyses, Petrone *et al.* [112, 113] concluded that natural convection flows in air-filled horizontal annuli can be classified into three categories according to the value of the radius ratio R . Transverse, steady roll perturbations are amplified at $Ra_{H,c} \approx 2000$ in narrow-gap annuli with $R \leq 1.5$. Moderate-gap annuli are defined by radius ratios at which multiple transitions, with dual solutions, occur for the two-dimensional flows, namely, for $1.5 \leq R \leq 2$. Large-gap annuli, $R \geq 2$, are associated with the onset of oscillatory disturbances for $2 \leq R \leq 2.24$ ($Ra_{H,c} \approx 10^4$) and with steady, symmetry-breaking disturbances for $R \geq 2.24$ ($Ra_{H,c} \approx 10^5$).

2.4.4 The low Prandtl number range

A considerable amount of numerical work has been also performed in order to clarify the flow regimes in the transition region for low Pr fluids, and in particular to assess the extent to which the occurrence of dual solutions is common also to cases with $Pr < 0.7$. Such an issue is addressed in the studies of Yoo *et al.* [114], Yoo [105, 106, 115, 116], and Mizushima and Hayashi [117]. Even if the results cover a wide range of values of Pr and R , they remain very fragmentary, and fail to provide a complete characterisation of the case. However, a general conclusion can already be extracted, *i.e.* that dual solutions are possible down to Pr -values of order $Pr \approx 10^{-1}$. It is also seen that multiple solutions always show up in the form of counterrotating vortices in the top part of the annulus, suggesting that their admissibility is strictly linked to the occurrence of Rayleigh-Bénard-like thermal instabilities [105, 106, 115, 116]. Again, Mizushima and Hayashi [117] confirmed that the underlying bifurcation is an imperfect transcritical one. Moreover, the range of R -values up to which multiple solutions are possible, is likely to extend with decreasing Pr , since Yoo [105] reports that dual steady states coexist in annuli with $R = 5$ for $Pr = 0.3$.

For even lower Pr -values, the flow characteristics are quite different. Since, in the energy balance, thermal diffusion predominates over convection, the temperature field remains almost purely conductive for a wide range of Ra_H -values [114], until instabilities of hydrodynamic nature set on, consisting either in the birth of co-rotating steady cells, or

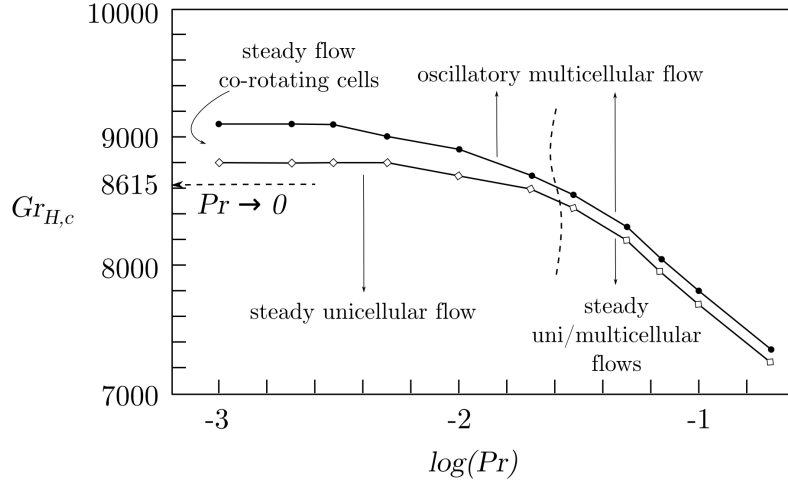


Figure 2.17: Critical Gr_H -values for the transition to multicellular and oscillatory flow of low Pr fluids in an annulus with $R = 1.17$. Numerical data by Yoo [115] are compared with the asymptotic stability condition by Rothmayer and Fant [118] for $Pr \rightarrow 0$.

in the insurgence of traveling wave oscillations. Fant *et al.* [119, 120] performed stability analyses of the flow in a two-dimensional annulus in the limit $Pr \rightarrow 0$, where convective effects become negligible in the energy equation. Numerical solutions of both the boundary layer equations, and the full Navier-Stokes equations were used for linear analyses. As a final result, Rothmayer and Fant [118] issued a stability condition relating the normalized gap spacing, H/r_i , and the critical Grashof number, based on the inner radius Gr_{r_i} :

$$\frac{H}{r_i} \simeq 20.5 Gr_{r_i}^{-\frac{1}{3}} \quad (2.4.2)$$

If equation (2.4.2) is re-scaled according to the gap width H , a stability threshold is found for the critical Grashof number, based on the gap width, $Gr_{H,c} \simeq 8615$. For $Pr \rightarrow 0$, such a value is insensitive to the radius ratio.

The diagram of Figure 2.17 reports the trends of $Gr_{H,c}$ as a function of Pr , as obtained numerically by Yoo [115] for a 2D annulus with $R = 1.17$. The chart shows that, as Pr decreases, the critical Grashof number for which the unicellular steady flow becomes unstable tends to an asymptotic value. Such a value is fairly close to the stability threshold predicted by Rothmayer and Fant [118] (within 3%). Moreover, it confirms that, for Pr -values of order 10^{-2} and lower, the primary instability mechanism is characterised by the birth of secondary, co-rotating cells aside of the main circulation.

2.4.5 Routes to chaos

Despite the great amount of published work on instabilities and bifurcative behaviours of the buoyancy-induced flows in a horizontal annulus, very few complete studies of the transition to chaos of such flows have been carried out so far.

In this context, the numerical work of Yoo *et al.* [114] is of particular interest, although limited to 2D systems. They considered the case of a very low- Pr fluid, $Pr = 0.02$, and constructed the flow pattern chart reported in Figure 2.18, describing the influence of R on the different steps of the transition from steady-state to unsteady, chaotic behaviours, and

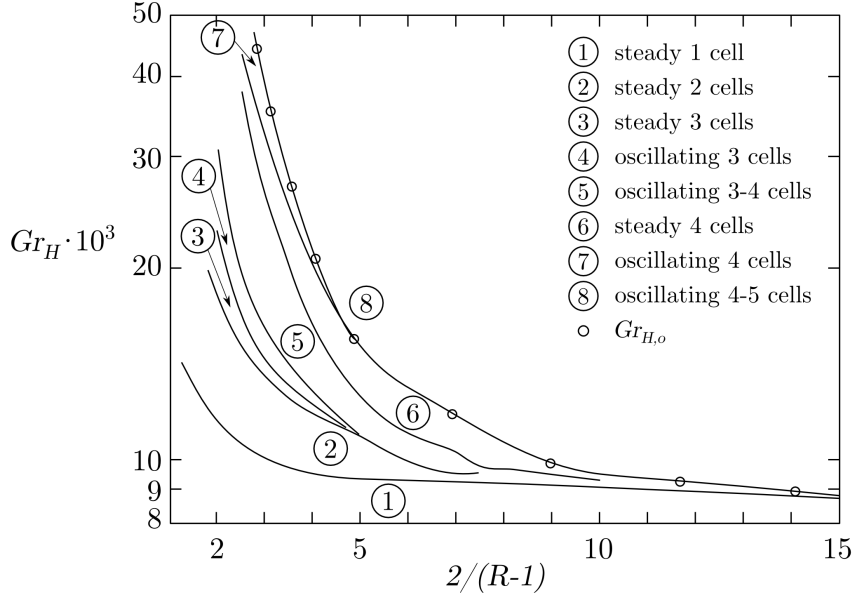


Figure 2.18: Transition patterns and critical Gr_H -curves as a function of the inverse radius ratio, $2/(R-1)$, for the buoyant flow in a horizontal annulus filled with a fluid at $Pr = 0.02$, as obtained by Yoo *et al.* [114]. Circles indicate the computed values $Gr_{H,o}$ above which the flow is always oscillatory.

Yoo and Han [121]			2D, $R = 2$, $Pr = 0.1$
Route to chaos: $S \rightarrow P \rightarrow P_3 \rightarrow QP_2 \rightarrow P_3 \rightarrow P_6 \rightarrow P_{12} \rightarrow N_I \rightarrow P_4 \rightarrow N_{II}$			
Bifurcation	Ra_H	Notes	
$S \rightarrow P$	1.7×10^3	$f = 0.816$ (dimensionless)	
$P \rightarrow P_3$	$3 \div 3.1 \times 10^4$		period-tripling
$P_3 \rightarrow QP_2$	3.8×10^4	$f_1 = 6.71$, $f_2 = 4.39$	
$QP_2 \rightarrow P_3$	5×10^4		$f_1/f_2/f_3 = 1/2/3$
$P_3 \rightarrow P_6, P_{12}$	$5.5 \div 6.3 \times 10^4$	$f_1/f_2/f_3 = 1/2/3$	period doublings
$P_{12} \rightarrow N_I$	$6.3 \div 6.4 \times 10^4$		nonperiodic flow
$N \rightarrow P_4$	7.4×10^4	$f = f_1/4$	
$P_4 \rightarrow N_{II}$	8×10^4		final transition to chaos

Labonia and Guj [122]			3D, $R = 2.36$, $A = 6.68$, $Pr \simeq 0.7$
Route to chaos: $S \rightarrow P \rightarrow QP_2 \rightarrow P \rightarrow QP_3 \rightarrow N$			
Observed regime	Ra_H	Frequencies (Hz)	
P	1.82×10^5	$f_1 = 0.0166$	
QP_2	2.13×10^5		$f_1 = 0.0049$, $f_2 \simeq 128f_1$
P	2.36×10^5		$f_1 = 0.665$
QP_3	2.84×10^5		$f_1 = 0.048$, $f_2 = 0.736$, $f_3 = 0.394$
N	3.37×10^5		(chaotic flow)

Table 2.3: Routes to chaos for the horizontal annulus, [122, 121].

on the spatial structure of the flow. Little detail is provided on the precise dynamical nature of the predicted flows. However, it is noteworthy that, for narrow gap annuli ($R \leq 1.2$), the transition to chaotic flow appears to occur through the breaking of a quasi-periodic orbit. Such an interpretation is suggested by the presence of sharp, almost impulsive peaks in some of the time-series plots reported in [114], which might correspond to a loss of regularity of the related Poincaré section curve (see Appendix B).

Later, Yoo and Han [121] investigated the case of a large-gap annulus ($R = 2$), for a slightly larger value of Pr , $Pr = 0.1$, and performed computations in the range $10^4 \leq Ra_H \leq 9 \times 10^4$, following an entire route to chaos, whose main features are summarized in Table 2.3. Quite interestingly, the occurrence of a period-tripling bifurcation is observed after the transition to oscillatory flow. The three-period phase (P_3) is interrupted by a window of quasi-periodicity (QP_2); subsequently, a period-doubling cascade (P_6, P_{12}) leads to a first nonperiodic phase (N_1). Before the final transition to chaos N_{II} , a relaminarisation phase is observed, consisting in a small window of periodicity (P_4) whose frequency is related with the fundamental frequency of the first periodic regime by a factor 4.

A very thorough experimental analysis of the transition to chaos in an annulus with $R = 2.36$ was provided by Labonia and Guj [122]. The test section was characterised by an axial length-to-gap ratio $A = L/H = 6.68$, and was filled with a gas $Pr \simeq 0.7$. Quantitative and qualitative measurements were performed by interferometry, smoke visualizations and hot wire anemometry. The results reported in Table 2.3 refer to single experiments, each representing a sample of the various stages of transition. In this case, the route to chaos appears to be characterised by a sequence of Hopf transitions, once again very similar to the Ruelle-Takens scenario.

2.5 Enclosures containing heat sources

In the present work, natural convection from a horizontal cylindrical source centred into a two-dimensional square cavity is mainly addressed. In terms of complexity, such a geometry might be placed halfways between the fundamental cases reviewed in the previous sections, and more advanced configurations which better represent practical applications. For instance, a complete analytical treatment of the case might be possible only by means of approximate representation methods [123, 124], since the domain cannot be easily defined in a suitable coordinate system.

On the other hand, the study of natural convection from enclosed thermal sources is of great importance in a variety of technological applications. However, the established literature on this topic is still scarce, and mainly focuses on heat transfer performances [125]; the most significant results are summarized in heat transfer handbooks [16].

Nevertheless, it is useful to provide a short review of relevant literature, and to mention, in particular, the studies encompassing the issues of flow stability and bifurcations.

The thermal interaction between a cylindrical source and a rectangular enclosure was first investigated by Ghaddar [126]: a uniformly heated 2D circular source in a rectangular cavity was considered numerically, using a spectral element method. Flow patterns and heat transfer rates were predicted for air over a wide range of Ra -values. The case of an isothermal cylinder in a rectangular cavity was investigated by Cesini et al. [127] by both experiments and numerical modelling. Results were presented in terms of the local and averaged Nusselt numbers, for different values of the cavity aspect ratio.

The work of Moukalled and Acharya [128] is of primary concern here, since they were the first to bring forth a numerical analysis of the convective annulus created by a inner circular cylinder and a outer square cylinder. Numerical simulations were performed for three values of the ratio between the cylinder radius and the cavity side, and five values of the Rayleigh number. The finite-volume method adopted involved the use of structured boundary-fitted curvilinear meshes, to solve the momentum and energy equations in their steady-state formulation. Flow patterns and thermal fields in all configurations were presented, alongside with profiles of the local Nusselt number on both the enclosure walls and the cylinder surface. An asymptotic correlation for the averaged Nusselt number was proposed, including the effect of both parameters. Results in [128] were recently used by Shu and Zhu [124], and by Peng et al. [129] for the sake of validation of their numerical procedures. In the former case a numerical approach based on the differential quadrature method was used. The technique allowed accurate solutions to be obtained while adopting relatively coarse grids. Peng et al. [129] employed a Lattice-Boltzmann method, and estimated its accuracy and suitability to the simulation of buoyancy-driven flows. The addition of fresh quantitative data was scarce in that case.

The effect of the positioning of a circular source inside a 2D square cavity was investigated by Shu *et al.* [130], again by means of differential quadrature methods, and, later, by Tasnim *et al.* [131] and Kim *et al.* [132]. A similar study, by experimental means, was also performed by Ekundayo *et al.* [133], for a small cylinder in a cubical enclosure. For all these works, the main focus was again the determination of the flow patterns in the steady-state laminar regime and of the heat transfer rate.

To date, the most important study upon time-dependent, bifurcative buoyant flows induced by an enclosed thermal source is due to Desrayaud and Lauriat [134]. They investigated very thoroughly the dynamical behaviour of the buoyant plume arising from a horizontal line source, modeled as a point source in a 2D rectangular cavity. The analyses were performed taking air as the heat carrier fluid ($Pr = 0.71$), for several values of the enclosure aspect ratio A , and for various depths of immersion H_s of the source along the vertical axis of the cavity. The leading parameter of the system was the Rayleigh number based on the cavity width W , Raw .

Depending on the depth of immersion H_s , various dynamics were detected. In particular, for cases characterised by $A = 1$ and moderate H_s -values, the onset of unsteadiness occurred by the subcritical transition from steady-state to a periodic swaying motion of the buoyant plume, whose spatial extent encompassed the whole depth H_s . The critical values of Raw for which the transition occurred were of order $O(10^6) \div O(10^7)$, as illustrated in Figure 2.19. As reported in Table 2.4, the correspondent route to chaos passed through phase-locking and intermittency states. The progressive increase of the dimensionless dominant frequency appeared to be fairly resolved, thus demonstrating the overall consistency of the results.

For higher values of A and H_s the scenario changed dramatically. Above the thermal plume, an unstably stratified region was maintained at rest thanks to the hydrostatic gradient, until, for $Ra \simeq 6 \times 10^3$, a pitchfork bifurcation occurred, leading to a non-symmetric bending of the plume, which entrained the above fluid layer. The subsequent bifurcation to oscillatory flow was characterised by lower values of the critical Raw , as shown in Figure 2.19. Moreover, hysteresis phenomena were detected for the case $A = 2$, revealing the occurrence of subcritical Hopf bifurcations for the highest values of H_s .

Later, Deschamps and Desrayaud [135] highlighted the substantial concordance between

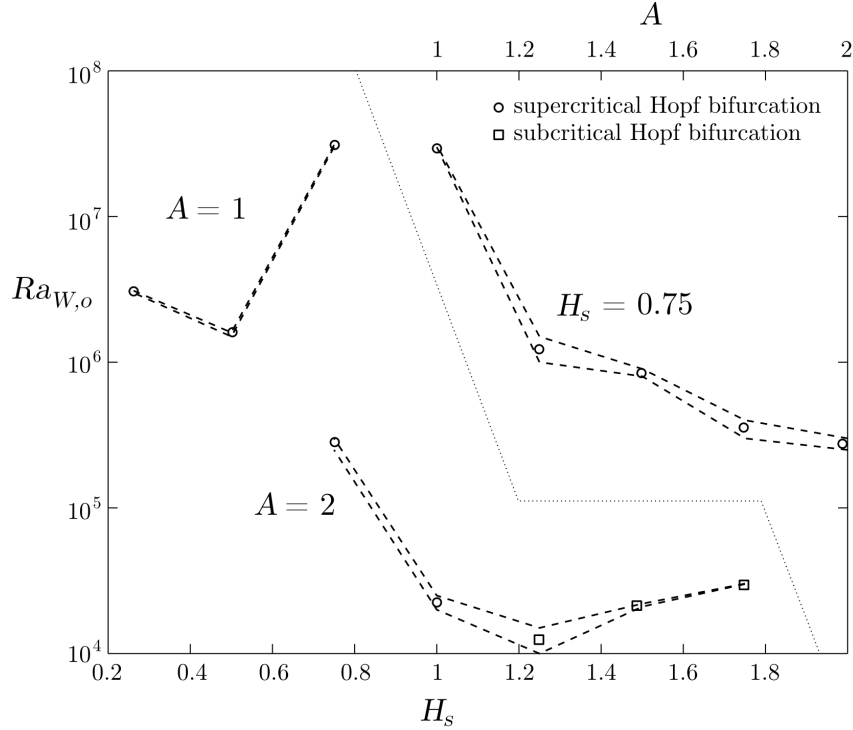


Figure 2.19: Critical $Ra_{W,o}$ -ranges (within the dashed lines) for which a Hopf bifurcation occurs in the buoyancy-induced flow from an enclosed line heat source, as a function of the enclosure aspect ratio A and depth of immersion H_s . The chart is extracted from the data available in [134].

$A = 1, H_s = 0.75, Pr = 0.71$		
Route to chaos: $S \rightarrow P \rightarrow L \rightarrow I \rightarrow$		
Bifurcation	Ra_L	Notes
$S \rightarrow P$	$3 \div 3.1 \times 10^7$	$f_1 = 294.2$ (dimensionless)
$P \rightarrow L$	$3.6 \div 3.7 \times 10^7$	$f_1 = 294.2, f_2 = 99.2$
$L \rightarrow I$	$3.8 \div 3.85 \times 10^7$	intermittency

$A = 2, H_s = 1.75, Pr = 0.71$		
Route to chaos: $S \rightarrow NS \rightarrow P \rightarrow \dots \rightarrow N$		
Bifurcation	Ra_L	Notes
$S \rightarrow NS$	6×10^3	pitchfork bifurcation
$NS \rightarrow P$	$3 \div 3.02 \times 10^4$	$f_1 = 0.2$, subcritical Hopf
$\dots \rightarrow N$	8×10^5	chaotic flow

Table 2.4: Routes to chaos for an enclosed line heat source, as carried out by Desrayaud and Lauriat [134].

results for wires of small diameter and line heat sources [134]. The results of both studies were later summarized by Lauriat and Desrayaud [136].

The case was later addressed by Barozzi and Corticelli [137], who achieved the simulation of a periodic regime, for the following set of parameters: $A = 1$, $H_s = 0.5$, $Pr = 0.71$, $Raw = 1.6 \times 10^6$. For that regime, the value of the dimensionless frequency was in excellent agreement (within 2%) with that of Desrayaud and Lauriat, but the analyses weren't carried any further, due to computational limitations.

2.6 Summary

In this chapter, the theoretical framework for the analysis of transitional natural convection regimes in enclosures has been outlined, by introducing a set of basic concepts of dynamical systems theory and stability theory, applied to thermo-fluid dynamics problems.

Moreover, a detailed review of the main results concerning transition has been provided, for three fundamental enclosure systems, namely a horizontal fluid layer heated from below (Rayleigh-Bénard convection) and bounded by vertical side walls, the differentially heated vertical enclosure and the annulus between two horizontal circular cylinders.

Finally, an overview of some relevant studies on buoyancy-induced flows arising from enclosed thermal sources has been given, in order to define the state-of-the-art for the present analyses.

Chapter 3

Numerical methods

3.1 Introduction

In order to properly resolve the problem of fluid flow in natural convection regimes, it is essential to provide a classification of its governing equations.

The relations (2.1.1)-(2.1.3), from a strictly mathematical standpoint, form a system of nonlinear, inhomogeneous partial differential equations. Because of this nonlinearity, the character of these equations strongly depends on the conditions of motion and can not be identified *a priori*.

Moreover, as a consequence of the incompressibility assumption, the continuity equation (2.1.1), has no direct dependence on the time variable, and, as already mentioned in Section 1.3.1, becomes a differential constraint, in addition to the boundary and initial conditions. Such a constraint does not provide any information on the time evolution of the variables, but, on the contrary, it represents a condition to be fulfilled at each instant.

The numerical resolution of (2.1.1), for which specific techniques must be employed, will be considered in the following section.

Turning now to the momentum and energy equations (2.1.2)-(2.1.3), it can be noted that the following common structure can be identified [138]:

$$\frac{\partial \varphi}{\partial t} + \mathbf{u} \cdot \nabla \varphi = \Gamma \nabla^2 \varphi + \sigma_V \quad (3.1.1)$$

Here φ represents a generic field variable, and the terms of equation (3.1.1), can be interpreted as follows:

- $\frac{\partial \varphi}{\partial t}$ is the *inertial term*
- $\mathbf{u} \cdot \nabla \varphi$ is the *convective transport term*
- $\Gamma \nabla^2 \varphi$ is the *diffusive term*, where Γ is a generic *diffusivity*.
- σ_V is the *volumetric source term*.

The mathematical nature of a problem depends on the properties of the independent variables (or *coordinates*) that govern such a problem: as already mentioned, in the case of fluid dynamics, they are the spatial coordinates x , y and z , and time t . The coordinates of a given PDE system can be either *one-way* or *two-way* [138].

A *one-way* coordinate is such that the value of the dependent variables defined for some value of this coordinate, is influenced by the changes in the same variables, only in one of the two directions of variation of the coordinate itself. A *two-way* coordinate, instead, is such that the changes in the dependent variables in a given point, are influenced by changes in the coordinate itself, in both its directions of variation.

From the definitions introduced above, it is immediately understood that time t is always a one-way coordinate, and that spatial coordinates are in general two-way. However, a spatial coordinate may be regarded as one-way, because of the action of a strongly unidirectional fluid flow (in the direction of that coordinate); in such a case, conditions in a given point are strongly influenced by upstream conditions and very weakly by downstream conditions. The one-way nature of a spatial coordinate is an approximation; in fact, even if convection is a unidirectional process, diffusion, which is always present, is inherently a two-way process (and this is the case with natural convection, where some part of the domain is always affected by diffusive processes). However, when convection predominates over diffusion, the spatial coordinates assume an almost one-way behaviour. The presence of a one-way coordinate is very advantageous from the computational standpoint, since it reduces computational times and data storage demands.

The concepts of one-way and two-way coordinates is connected to the classification of PDEs into *parabolic*, *elliptic* and *hyperbolic* equations [138]. With reference to equation (3.1.1), if the solution of a pure diffusion problem is sought after, in the absence of internal sources, the inertial and convective terms vanish, giving rise to a transport equation of the following type:

$$\nabla^2 \varphi = 0 \quad (3.1.2)$$

Equation (3.1.2) belongs to the category of elliptic PDEs, for it contains fully two-way spatial coordinates, and does not depend on time. If the transient solution of the same problem is sought after, the inertial term should also be taken into account:

$$\frac{\partial \varphi}{\partial t} = \Gamma \nabla^2 \varphi \quad (3.1.3)$$

Unlike (3.1.2), equation (3.1.3) belongs to the category of parabolic PDEs; this is due to the introduction of a one-way coordinate, as time t is. A third case is represented by purely convective transport, *i.e.* when the transport of the variable takes place in the absence of diffusion. In the absence of internal sources, one has:

$$\frac{\partial \varphi}{\partial t} + \mathbf{u} \cdot \nabla \varphi = 0 \quad (3.1.4)$$

Equation (3.1.4) is representative of hyperbolic PDEs. The category of hyperbolic equations is representative of particular problems which preserve a one-way character, not on the coordinate directions but on a set of lines called the *characteristic lines*.

The mathematical problem associated with equation (3.1.1), includes aspects from all the three types of equations introduced presented above. Generally, in buoyancy-induced flows, there is an initial phase in which the transport of heat takes place only by diffusion, and the problem is essentially parabolic. When the density gradient becomes large enough to ensue convective currents, the contribution of convective terms becomes no longer negligible. The flow moves then to a phase in which the modes of transport of thermal energy are overlap and interact.

In cases where the thermal gradient is particularly high (or, conversely, the fluid has very low viscosity), the system can reach at a situation where transport is almost entirely convective (hyperbolic problem). Otherwise, in the presence of a small thermal gradients, the solution may attain a condition of stagnation, where heat transfer is predominantly diffusive (elliptic problem).

For this reason, the models and algorithms employed for the numerical resolution of the equations of natural convection must be able to deal adequately with different types of differential equations, related to the different modes of transport that may occur.

3.2 Pressure-Velocity coupling

As already mentioned, the hypothesis of incompressibility involves a substantial change in the nature of the continuity equation. As a matter of fact, in the case of compressible flow, the density of the fluid is an unknown of the problem, and its temporal evolution is determined through equation 1.2.2. Pressure, density and temperature are also related one to another by the equation of state of the fluid (1.3.9); hence, pressure can be derived from the other two variables at each time. Usually the so-called *coupled* solvers are used in this case; such procedures solve directly, for each time step, equations (1.2.2), (1.2.11) and (1.2.30) and, subsequently, derive the pressure.

By contrast, in the case of incompressible flow, density loses its dependence on pressure, and pressure is related solely to the velocity field through the Navier-Stokes equation (1.2.11). The continuity equation, in addition, reduces itself to a constraint for the components of the velocity vector. In this case, the coupled solution of the system of equations remains possible, but it is expensive and rarely used. Methods allowing a decoupling of pressure and velocity are preferred, where the two variables are calculated separately.

In that frame, a class of numerical algorithms is introduced, identified in the literature with the name of *Projection Methods*, which provide an approximate solution to the Navier-Stokes equation. These algorithms allow the pressure to be considered as constant in the single calculation step, and to be resolved afterwards by correcting its value iteratively until convergence. Following the approach outlined by these methods [139, 140], the momentum equation (2.1.2) is recast in alternative form:

$$\frac{\partial \mathbf{u}}{\partial t} + \nabla P = \mathbf{G}(\mathbf{u}) \quad (3.2.1)$$

where:

$$\mathbf{G}(\mathbf{u}) = \frac{1}{Gr^{\frac{1}{2}}} \nabla^2 \mathbf{u} - \hat{\mathbf{g}} T - \mathbf{u} \cdot \nabla \mathbf{u} \quad (3.2.2)$$

In general, the vector $\mathbf{G}(\mathbf{u})$ is a functional of velocity, which is neither solenoidal (*i.e.* with zero divergence), nor irrotational (zero curl). However, it is reasonable to assume that, given the velocity vector \mathbf{u} , the vector $\mathbf{G}(\mathbf{u})$ can be considered as known. $\mathbf{G}(\mathbf{u})$ is projected into two vector subspaces, the space of solenoidal vectors and the space of irrotational vectors. According to the continuity equation (2.1.1), it is:

$$\frac{\partial \mathbf{u}}{\partial t} = \Sigma(\mathbf{G}(\mathbf{u})) \quad (3.2.3)$$

and, since the curl of a gradient is always zero:

$$\nabla P = I(\mathbf{G}(\mathbf{u})) \quad (3.2.4)$$

where Σ and I are the projection operators. One may also observe that Σ projects any vector in the kernel of the vector space of divergence, while I projects any vector in the kernel of the vector space of curl.

The exact value of pressure being generally unknown, equation (3.2.1) assumes the form:

$$\frac{\partial \tilde{\mathbf{u}}}{\partial t} + \nabla \tilde{P} = \mathbf{G}(\tilde{\mathbf{u}}) \quad (3.2.5)$$

where the terms \tilde{P} and $\tilde{\mathbf{u}}$ represent initial guesses for pressure and velocity. Although the values of \tilde{P} and $\tilde{\mathbf{u}}$ satisfy equation (3.2.5), this does not necessarily mean that $\tilde{\mathbf{u}}$ is divergence-free, since $P \neq \tilde{P}$. Such a condition would be guaranteed only if the continuity equation (2.1.1) were verified. However, it is possible to iteratively correct the values of velocity and pressure, until equations (2.1.1) and (3.2.1) are simultaneously verified. When the value of $\nabla \cdot \mathbf{u}$ is close enough to zero (*i.e.* when the continuity equation is verified within a pre-definite limit), the procedure ends.

Leaving aside the mathematical discussion which defines such iterative procedure (this is deferred to the literature [139, 140, 141]), attention is now focused on the procedure itself [141] which is one of the bases of the entire resolution procedure.

It is supposed that, at a given instant of time n , the values of velocity components and pressure are known. By definition, such values satisfy the continuity equation 2.1.1. The values of pressure and velocity at the time step $n+1$ are sought for. At first, an estimate of velocity must be provided, based on available data, to be used as an initial guess for equation (3.2.5). In particular, since the procedure has to be decoupled, it is necessary to employ known values of pressure and temperature. The approximate velocity is then calculated according to the following equation:

$$\frac{\partial \tilde{\mathbf{u}}}{\partial t} + \tilde{\mathbf{u}} \cdot \nabla \tilde{\mathbf{u}} = -\nabla \tilde{P} + \frac{1}{Gr^{\frac{1}{2}}} \nabla^2 \tilde{\mathbf{u}} - \hat{\mathbf{g}} T \quad (3.2.6)$$

Once the approximate velocity field $\tilde{\mathbf{u}}$ is determined, a new variable ϕ is derived, called pseudo-pressure, which represents a Lagrange multiplier related to the projection of $\tilde{\mathbf{u}}$, and whose Laplacian is, consequently, the error committed with respect to the hypothesis of zero divergence:

$$\nabla^2 \phi = \nabla \cdot \tilde{\mathbf{u}} \quad (3.2.7)$$

Equation (3.2.7) is a Poisson equation, belonging to the class of elliptical PDSS. As such, it requires the imposition of suitable boundary conditions for the variable ϕ . For a closed system, the basic theory of Projection Methods [8] suggests the adoption of a Neumann condition over the entire boundary of the domain of integration:

$$\frac{\partial \phi}{\partial \eta} = 0 \quad (3.2.8)$$

Here η is a general normal to a solid boundary. The estimate of the pseudo-pressure ϕ provides a correction to the initial guess for velocity, $\tilde{\mathbf{u}}$:

$$\mathbf{v} = \tilde{\mathbf{u}} - \nabla \phi \quad (3.2.9)$$

Through simple steps, it is possible to verify that the vector field \mathbf{v} is divergence-free, thus satisfying the continuity equation (2.1.1). Hence, \mathbf{v} represents the real velocity vector \mathbf{u} at time step $n+1$.

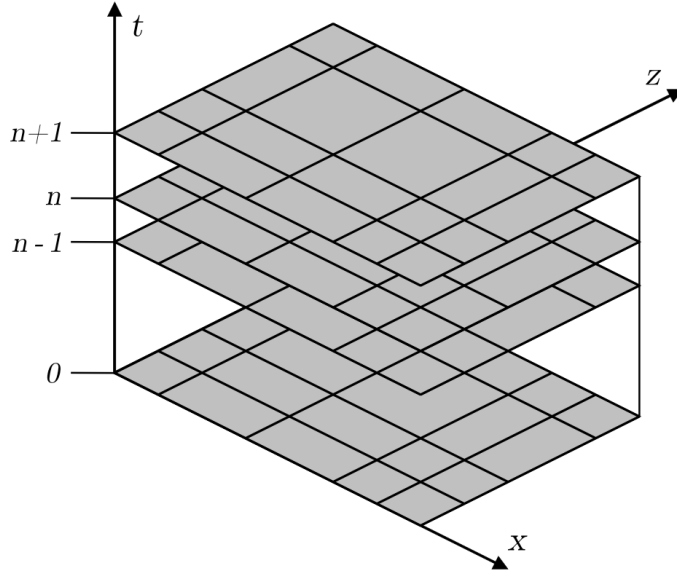


Figure 3.1: Discretization grids.

The pressure value is finally updated as follows:

$$P^{n+1} = P^n + 2 \frac{\phi}{\delta t} \quad (3.2.10)$$

The procedure outlined above conveniently separates the calculation of \mathbf{u} from that of P , thus removing the need for resolving the continuity and momentum equations simultaneously. However, the numerical resolution of the Poisson equation (3.2.7) implies an additional computational cost, which is so high to overwhelm any possible advantage. This dictated the use of the *Fast Poisson Solver*, based on the *Matrix Decomposition* method for the solution of block tridiagonal systems. The details of the discretization procedure for the Poisson equation, and of the Matrix decomposition method are omitted here for brevity. However, a thorough description of both methodologies can be found in [142].

3.3 Time discretization

In order to perform the numerical integration of the equations of motion, (2.1.1)-(2.1.3), it is necessary to reformulate them in a discrete form. To this aim, a general discrete grid is introduced, formed by a succession of non-uniform spatial grids, placed at different time steps, distributed, in turn, along a sequence of non-uniform time intervals. Such a grid is shown in Figure 3.1.

As pointed out above, time is typically a one-way variable. Hence, it can be assumed that the solution at the generic time step $n + 1$, depends only on the states assumed by the system from the initial step 0, at which the start of the time evolution is fixed, up to the time step n , and on the boundary conditions. It is supposed, in particular, that the value of the general variable φ at the time step $n + 1$ can be calculated as:

$$\varphi^{n+1} = \varphi^n + \left(\frac{\partial \varphi}{\partial t} \right)^{n+\frac{1}{2}} \Delta t^n \quad (3.3.1)$$

where superscripts designate time steps, and the following convention is applied for the differences:

$$\Delta(\cdot)^n = (\cdot)^{n+1} - (\cdot)^n \quad (3.3.2)$$

It is now necessary to express the different terms of equation (3.1.1), in terms of the states of the system at $t = 0, \dots, n + 1$.

For the discretization of the *inertial term*, a two-level scheme has been employed, expressing the time derivative of the variable φ as a linear combination of the differences calculated at time-steps n and $n - 1$ [143]:

$$\frac{\partial \varphi}{\partial t} \simeq (1 + \gamma) \frac{\Delta \varphi^n}{\Delta t^n} - \gamma \frac{\Delta \varphi^{n-1}}{\Delta t^{n-1}} \quad (3.3.3)$$

It is also necessary to identify suitable schemes for the temporal discretization of the diffusive and convective terms. In fact, the spatial partial derivatives (the gradient and Laplacian operators) should be calculated at an intermediate time between n and $n - 1$.

The *convective term* has the particularity of being inherently non-linear, since it contains the velocity \mathbf{u} , one of the unknowns of the problem, as a multiplicative factor. For this reason, the adoption of an implicit discretization of the convective term would imply the solution of a system of non-linear algebraic equations. Hence, an explicit scheme is adopted here, namely a version of the three-level Adams-Basforth scheme [143], characterized by second order accuracy.

In view of the continuity equation, the convective term can be conveniently reformulated in its conservative form:

$$\mathbf{u} \cdot \nabla \varphi + \varphi \nabla \cdot \mathbf{u} = \nabla(\mathbf{u}\varphi) \quad (3.3.4)$$

The discretization of the convective term, in its conservative form, turns out to be:

$$\nabla(\mathbf{u}\varphi) \simeq \left(1 + \frac{1}{2} \frac{\Delta t^n}{\Delta t^{n-1}}\right) (\nabla(\mathbf{u}\varphi))^n - \frac{1}{2} \frac{\Delta t^n}{\Delta t^{n-1}} (\nabla(\mathbf{u}\varphi))^{n-1} \quad (3.3.5)$$

The explicit nature of the scheme requires the imposition of a constraint on the time step size, ensuring the stability of the scheme itself. The following constraint is used:

$$\Delta t = \frac{\min(\Delta x, \Delta z)}{\|\mathbf{u}\|} \quad (3.3.6)$$

where Δx and Δz are the characteristic dimensions of the single computational cell, and $\|\mathbf{u}\|$ is the standard Euclidean norm of the vector velocity in such cell.

A different approach is needed for the *diffusive term*. Equation (3.1.1) shows that, unlike the convective term, the diffusive operator does not present any non-linearity associated with it. Furthermore, the diffusive term contains a second-order spatial derivative, and this would entail the presence of a constraint on the time-step size, proportional to the square of the characteristic grid size [143], in case an explicit scheme were adopted. In this framework, a two-level implicit Crank-Nicolson scheme [143] is used. In its generalized form, this is expressed:

$$\Gamma \nabla^2 \varphi \simeq \Gamma \left[(1 - \beta) (\nabla^2 \varphi)^n + \beta (\nabla^2 \varphi)^{n-1} \right] \quad (3.3.7)$$

The coefficient β represents the relative weight to be attributed to the unknown variable, (*i.e.* the variable at the step $n + 1$) in the estimate of the diffusive term. The adoption of a

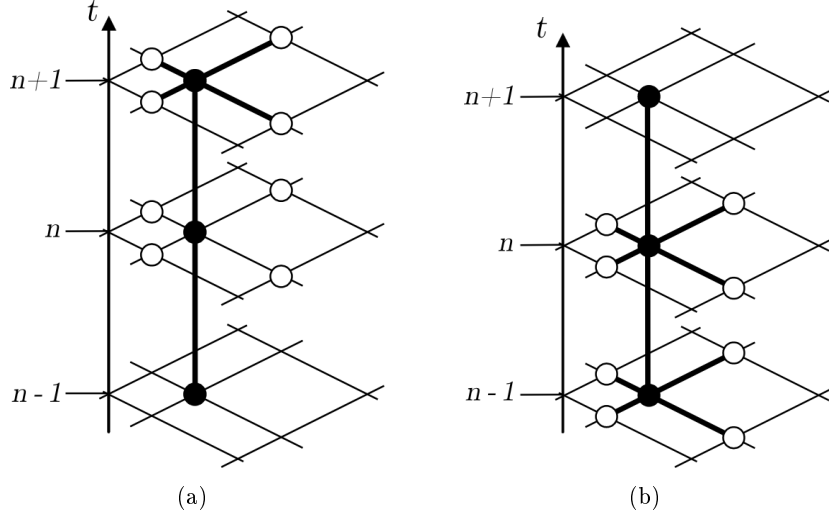


Figure 3.2: Discretization stencils for the diffusive (a) and convective (b) terms.

value of β equal to $\beta = 0$ makes the scheme (3.3.7) coincident with a second-order explicit scheme, while if β takes the value $\beta = 1$, a second-order implicit scheme is obtained. The choice of β is then crucial for the scheme to be stable and accurate. For the numerical method described here, the values of the two parameters γ and β were chosen as:

$$\gamma = \frac{1}{2} \quad \text{and} \quad \beta = 1 \quad (3.3.8)$$

Such values ensure second-order accuracy for the discretization of the diffusive operator and, contextually, the unconditional stability of the resolution algorithm.

The time discretization adopted is, then, a *three-level, second-order* accurate discretization, *implicit* for the diffusive term and *explicit* for the convective term. The semi-discrete form of equation (3.1.1) is now written:

$$(1 + \gamma) \frac{\Delta\varphi^n}{\Delta t^n} - \gamma \frac{\Delta\varphi^{n-1}}{\Delta t^{n-1}} + \left(1 + \frac{1}{2} \frac{\Delta t^n}{\Delta t^{n-1}}\right) (\nabla(\mathbf{u}\varphi))^n - \frac{1}{2} \frac{\Delta t^n}{\Delta t^{n-1}} (\nabla(\mathbf{u}\varphi))^{n-1} \\ = \Gamma \left[(1 - \beta) (\nabla^2 \varphi)^n + \beta (\nabla^2 \varphi)^{n-1} \right] + \sigma_V \quad (3.3.9)$$

with $\gamma = 0.5$ and $\beta = 1$. Such a form is applied to the resolution of equations (2.1.2)-(2.1.3).

The computational stencils associated with the two integration schemes for the diffusive and convective terms are represented in Figure 3.2(a) and 3.2(b), respectively.

3.4 Space discretization on Cartesian grids

The numerical solution of the equations of motion requires the identification of a finite number of unknowns, in order to represent the spatial distribution of the variables of interest correctly. Hence, the equations must be properly discretized in a given set of points in space, where the unknowns of the problem will be located. To this aim, the *Finite Volume method* has been chosen for the spatial discretization of the transport equations.

3.4.1 The Finite Volume method

Among the possible discretization methods commonly used for the study of thermo-fluid problems, the *Finite Volume method* [144] is of special importance. The main features of the technique are:

- the *grid* (or *mesh*) of points, at which the approximate solution shall be calculated;
- the subdivision of the spatial domain of integration into a set of non-overlapping cells, the *control volumes*. Each control volume contains a node of the computational grid;
- the integration of the generic differential equation on each control volume;
- the use of a piecewise function to estimate the values of the generic variable φ between the grid points. The nature of this function determines the order of accuracy of the discretization chosen.

The general integral form of the balance equations is obtained by integrating equation (3.1.1) on the control volume V , whose boundary is labeled S :

$$\int_V \left(\frac{\partial \varphi}{\partial t} + \mathbf{u} \cdot \nabla \varphi \right) dV = \int_V (\Gamma \nabla^2 \varphi + \sigma_V) dV \quad (3.4.1)$$

By expressing the convective term in its equivalent conservative form (3.3.4) and invoking the Gauss-Green theorem, an analogous form of (3.4.1) is obtained:

$$\int_V \left(\frac{\partial \varphi}{\partial t} \right) dV + \int_S (\mathbf{u} \varphi) \cdot \hat{\mathbf{n}} dS = \int_S \Gamma (\nabla \varphi \cdot \hat{\mathbf{n}}) dS + \int_V \sigma_V dV \quad (3.4.2)$$

Equation 3.4.2 represents well the relationship linking the temporal variation and the internal generation of the unknown quantity within the control volume V , with the convective and diffusive fluxes crossing the boundary S of the volume itself.

3.4.2 Computational grids

The choice of the geometry and structure of the computational grids significantly affects the accuracy of a numerical calculation. As shown in Figure 3.3, the technique enforced here is based on staggered, two-dimensional Cartesian grids. Such an approach is based on the adoption of three Cartesian lattices, aligned with the coordinate axes x and z , on which the nodal values of the scalar variables and the two velocity components are located, respectively.

The regular geometry of the grid makes it somewhat easier to discretize the differential operators, while its structure enables the use of fast solvers. Moreover, the use of different grids for scalars and velocity components allows for a straightforward evaluation of the momentum and energy fluxes crossing the control volume boundary; at the same time, it avoids the occurrence of the so-called “checkerboarding” effect [144] on the variable distributions, which typically arises when a unique grid is used. Finally, the regular grid structure lends itself to an easy subdivision of the domain in regular subsets of cells, and, therefore, to the parallelization of the solution procedure.

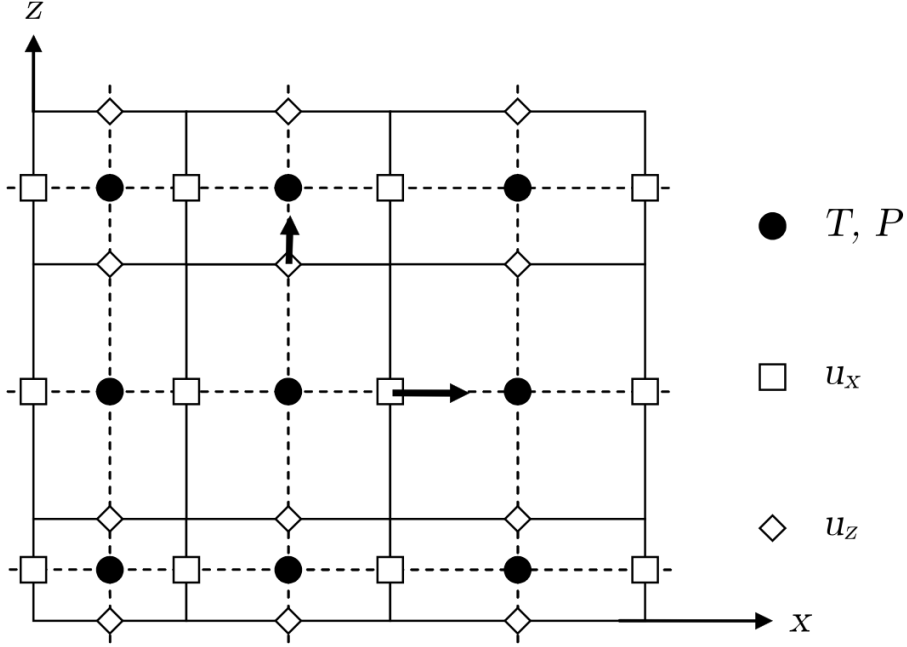


Figure 3.3: Computational grids for scalars and velocity components.

The main drawback of the Cartesian approach is, however, its inherent difficulty in treating geometries whose contours are not aligned with the coordinate. Unless appropriate modeling schemes are adopted, the accuracy of the solution is compromised, thus vanishing the above-mentioned advantages. It is mainly for this reason that, throughout the years, the Cartesian approach has been progressively supplanted by the use of unstructured or conformal structured grids, for the study of fluid dynamics problems.

However, the use of Cartesian grids has been recently rediscovered, and many research efforts have been devoted to the study of suitable techniques for the modeling of irregular geometries. The method adopted here will be outlined in Section 3.6.

3.4.3 Discretization of the generic transport equation

The spatial discretization of equation (3.1.1) is described in this section. Figure 3.4 represents the generic control volume V on which the equation is integrated, according to equation (3.4.2). It may be assumed that, to a first approximation, the values of the velocity components are known on the control volume boundary.

The discretization of the *inertial term* is carried out by assuming that the integral mean value of φ be equal to the value of the function in the central point of the control volume. To this aim, it is important to note that the concept of central point is not uniquely defined, in the case of staggered grids. With reference to Figure 3.5, the central point coincides with the centroid of the control volume for the scalar quantities, while for the grids associated with the velocity components, it coincides with the midpoint of the side of the associated scalar cell. As it will be seen in the following, the latter hypothesis allows for a straightforward approximation of the convective fluxes related to the scalar cells.

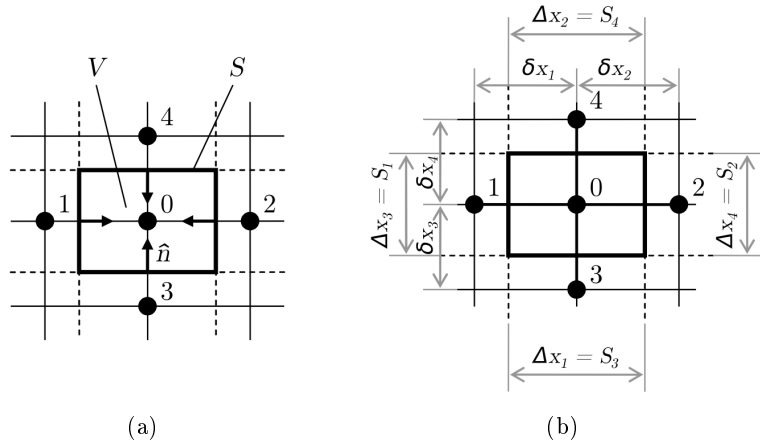


Figure 3.4: Topology (a) and relevant sizes (b) of a generic control volume in a 2D Cartesian discretization.

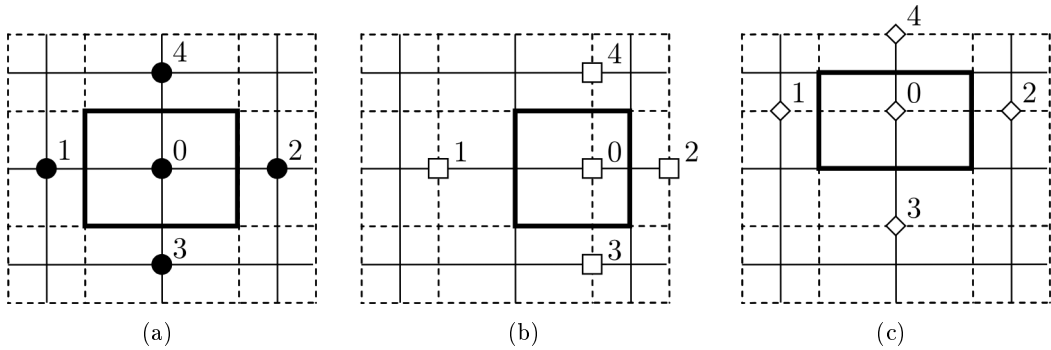


Figure 3.5: Control volumes for scalars (a) and velocity components (b,c), for staggered 2D Cartesian grids.

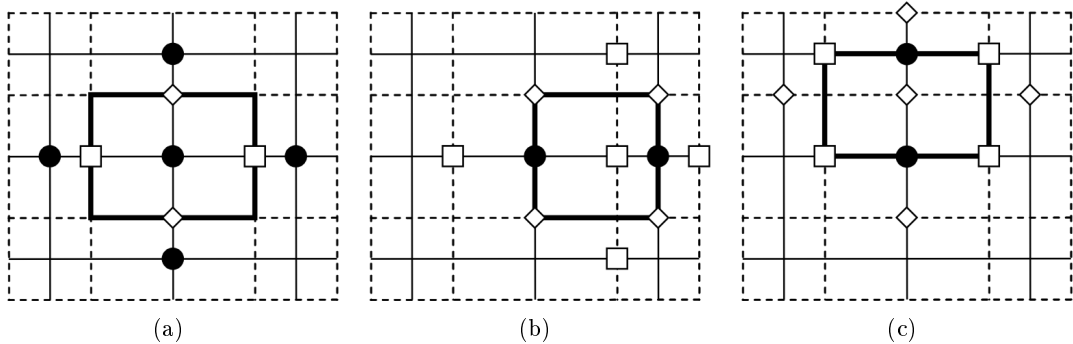


Figure 3.6: Computational stencils for scalars (a) and velocity components (b,c), for staggered 2D Cartesian grids.

In discrete form, the inertial term can be written as follows:

$$\int_V \left(\frac{\partial \varphi}{\partial t} \right) dV \simeq \Delta x_1 \Delta x_3 \frac{\partial \varphi_0}{\partial t} \quad (3.4.3)$$

where the subscript next to the variable φ identifies its location within the computational stencil.

The discrete *convective term* is represented as the sum of the fluxes crossing the control volume sides:

$$\int_S \mathbf{u} \cdot \hat{\mathbf{n}} dS \simeq \sum_{k=1}^4 \check{u}_k \check{\varphi}_k S_k \quad (3.4.4)$$

where \check{u}_k denotes the velocity component normal to the cell boundary, while the variable $\check{\varphi}_k$ represents an estimate of the unknown on the boundary itself. By assuming the unknown function to vary linearly in the interval between the center of two adjacent cells, one has:

$$\sum_{k=1}^4 \check{u}_k \check{\varphi}_k S_k = \sum_{k=1}^4 \check{u}_k \frac{\Delta x_k^{(k)} \varphi_0 + \Delta x_k^{(0)} \varphi_k}{\Delta x_k^{(k)} + \Delta x_k^{(0)}} S_k \quad (3.4.5)$$

where superscripts (O) and (k) respectively denote the characteristic dimensions of the cell itself and of the adjacent cell in the direction of the k -th stencil arm.

Analogously, the *diffusive term* can be expressed as the sum of the fluxes crossing the cell boundaries. If the above linearity hypothesis holds, one has:

$$\int_S \Gamma (\nabla \varphi \cdot \hat{\mathbf{n}}) dS \simeq \sum_{k=1}^4 \frac{\varphi_k - \varphi_0}{\delta x_k} S_k \quad (3.4.6)$$

The discretization of the *source term* is analogous to that of the inertial term:

$$\int_V \sigma_V dV \simeq \Delta x_1 \Delta x_3 \sigma_V \quad (3.4.7)$$

Hence, equation (3.4.2) can now be rewritten in the following discrete form:

$$\Delta x_1 \Delta x_3 \frac{\partial \varphi_0}{\partial t} + \sum_{k=1}^4 \check{u}_k \frac{\Delta x_k^{(k)} \varphi_0 + \Delta x_k^{(0)} \varphi_k}{\Delta x_k^{(k)} + \Delta x_k^{(0)}} S_k = \sum_{k=1}^4 \frac{\varphi_k - \varphi_0}{\delta x_k} S_k + \Delta x_1 \Delta x_3 \sigma_V \quad (3.4.8)$$

Some observations on equation (3.4.8) are in order. First, the velocity \check{u}_k is to be determined at the control volume boundary. With reference to Figure 3.6, one can easily notice, that, when considering the grids associated to the velocity components, the normal component \check{u}_k is, in general, not available on the perimeter of the volume. It is then necessary to reconstruct these components in order to calculate the convective fluxes in the momentum equation.

For faces normal to direction of the unknown velocity component, a linear interpolation can be performed. Much alike to equation (3.4.5), one has:

$$\check{u}_k \equiv \check{\varphi}_k = \frac{\Delta x_k^{(k)} \varphi_0 + \Delta x_k^{(0)} \varphi_k}{\Delta x_k^{(k)} + \Delta x_k^{(0)}} S_k \quad (3.4.9)$$

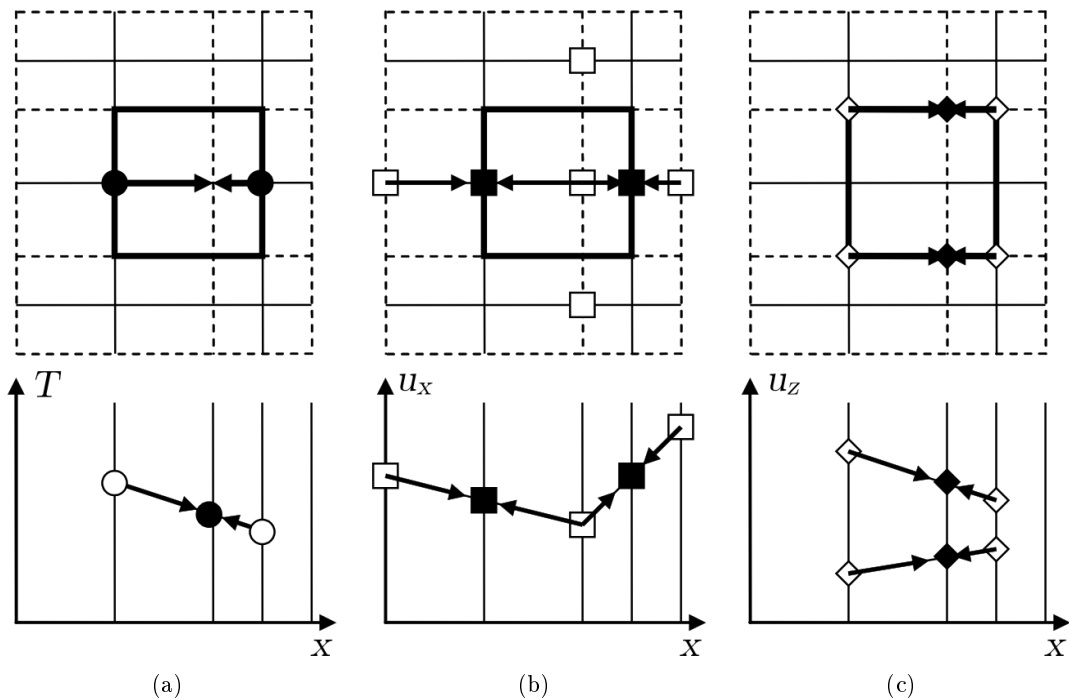


Figure 3.7: Reconstruction of temperature (a) and normal velocity components (b,c) for the x -velocity grid.

A similar procedure is repeated in the reconstruction of the fluxes across faces parallel to the direction of the unknown velocity components: in this case the φ -values are available at the vertices of the control volume.

Moreover, the source term in (3.4.8), takes on different formats, depending on the equation to which it refers. In the energy equation 2.1.3, the source terms have been neglected, and, therefore, it is $\sigma_V = 0$. As for the momentum equation, instead, one has:

- momentum equation - x -direction $\sigma_V = -\frac{\partial P}{\partial x} - T \cos \theta$
 - momentum equation - z -direction $\sigma_V = -\frac{\partial P}{\partial y} - T \sin \theta$

where θ is the angle between the gravitational versor $\hat{\mathbf{g}}$ and the positive x -direction. Hence, the value of σ_V must be reconstructed from the values of the scalar variables. Such reconstruction is easy if it is assumed again that both temperature and pressure vary linearly between the nodes of the grid for scalars.

The interpolation procedures outlined above, are schematised in Figure 3.7 for the unit cell of the grid for the x -velocity component. For the z -component of the momentum equation, such procedures are completely analogous.

3.5 Approximate Factorization

The algorithm for the numerical integration of the general transport equation (3.1.1) is now described. It is recalled first that the chosen time discretization schemes for the diffusive

and convective terms are an implicit scheme and an explicit scheme, respectively. Hence, the only unknowns to be derived at each time step are contained within the inertial and diffusive terms. It is therefore useful to introduce an alternative form of equation (3.3.9), referring to the temporal variations of the unknown quantities:

$$\Delta\varphi^n - \Delta t^n \frac{\beta}{1+\gamma} \Gamma \nabla^2 (\Delta\varphi)^n = rhs^n \quad (3.5.1)$$

where:

$$\begin{aligned} rhs^n &= \frac{\Delta t^n}{1+\gamma} \left[- \left(1 + \frac{1}{2} \frac{\Delta t^n}{\Delta t^{n-1}} \right) (\nabla(\mathbf{u}\varphi))^n + \frac{1}{2} \frac{\Delta t^n}{\Delta t^{n-1}} (\nabla(\mathbf{u}\varphi))^{n-1} \right] \\ &\quad + \Gamma \nabla^2 \varphi^n + \gamma \frac{\Delta \varphi^{n-1}}{\Delta t^{n-1}} + \sigma_V \end{aligned} \quad (3.5.2)$$

The formulation (3.5.1) has the advantage of separating the unknown terms from the right-hand-side expression rhs^n , which is known at each time step. It also shows that the choice of an implicit scheme for the time discretization of the diffusive term involves a coupling between the unknowns associated with different nodes of the computational grid. Mathematically, this means that the matrix of the resolving linear system is not diagonal; nevertheless, thanks to the regular structure of the Cartesian grid, such a matrix has a fairly regular structure (block tridiagonal), which greatly facilitates the numerical resolution procedure.

To this end, the *Approximate Factorization* technique [138] is introduced, through which the solution of equation (3.5.1) can be further simplified. The left-hand side term is decomposed in the product of two factors, associated to the directions of the Cartesian axes:

$$\left[1 - \Delta t^n \frac{\beta}{1+\gamma} \Gamma \frac{\partial^2}{\partial x^2} \right] \left[1 - \Delta t^n \frac{\beta}{1+\gamma} \Gamma \frac{\partial^2}{\partial z^2} \right] \Delta\varphi^n = rhs^n \quad (3.5.3)$$

With simple algebraic steps, it is shown that the product at the left-hand-side of equation (3.5.3) *does not coincide* with the left-hand-side of (3.5.1), from which it was derived. However, the error induced by this approximation is proportional to $(\Delta t^n)^2$, and this is the same order of the error introduced by the time discretization schemes. What varies, when passing from (3.5.1) to (3.5.3) is the truncation term, but not the overall accuracy of the solution. Equation (3.5.3) can be further decomposed along the Cartesian directions, by introducing a simple change of variable:

$$\begin{cases} \left[1 - \Delta t^n \frac{\beta}{1+\gamma} \Gamma \frac{\partial^2}{\partial x^2} \right] \Delta\tilde{\varphi}^n = rhs^n \\ \left[1 - \Delta t^n \frac{\beta}{1+\gamma} \Gamma \frac{\partial^2}{\partial z^2} \right] \Delta\varphi^n = \Delta\tilde{\varphi}^n \end{cases} \quad (3.5.4)$$

The resolution of system (3.5.4) leads to the determination of the value of φ at time step $n+1$. Thanks to the factorization, the differential operators have been splitted along the Cartesian directions, so that, once the spatial discretization is performed, each equation gives rise to a tridiagonal linear system, whose resolution is computationally cheap. The description of the details of the solution of the discrete equations is postponed, since such procedure is intimately linked with the modeling of irregular boundaries.

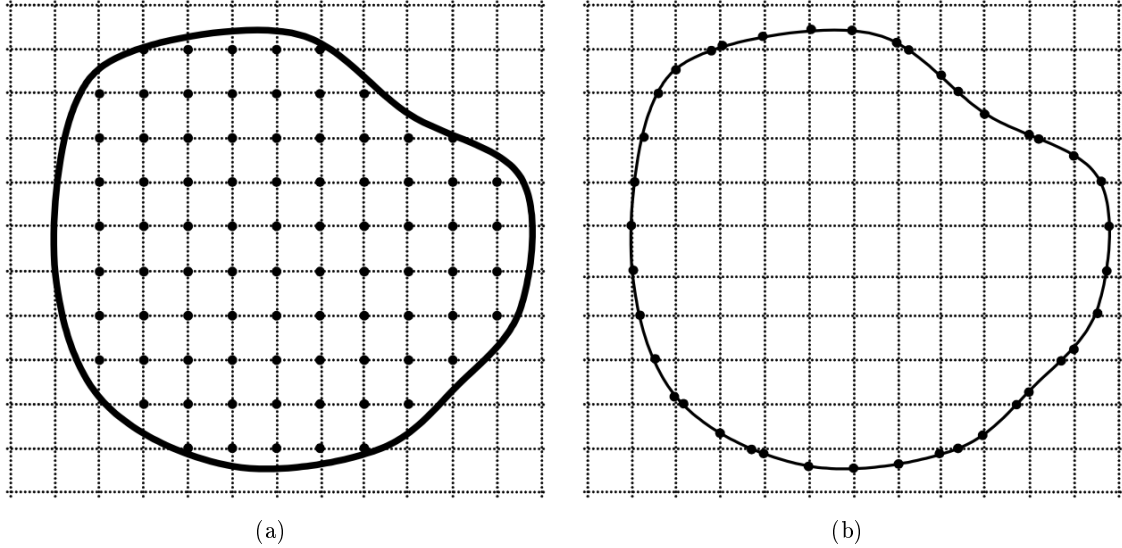


Figure 3.8: Computational grid \mathcal{G} (a) and set of intersection points \mathcal{B} (b).

3.6 Treatment of irregular boundaries

The methodology employed for the modeling of boundaries non-aligned with the Cartesian grid represents an extension to convection problems of a methodology originally developed for thermal diffusion problems [145]. The method and its extension to natural convection problems is described here in its main characteristics.

3.6.1 Computational grids, local stencils, control volumes

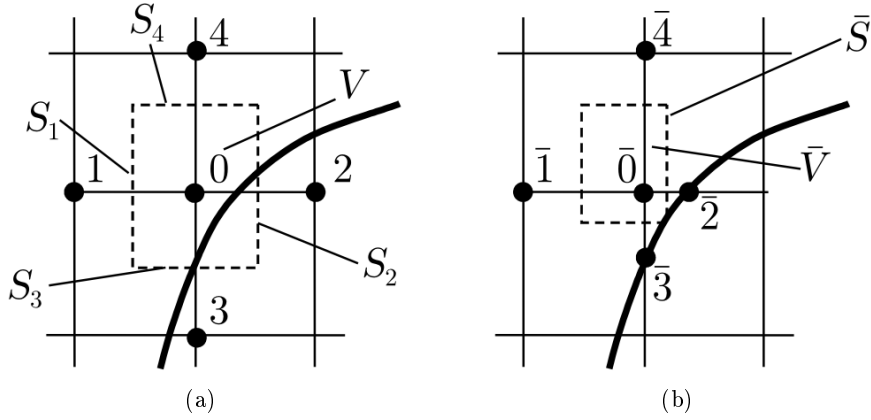
In order to achieve a good level of accuracy without penalizing computational efficiency, the process of approximation of the equations of motion (discretization) and resolution of the associated algebraic system (computing) are treated separately.

Three mathematical entities are now defined, namely the *discretization grid* \mathcal{D} , the *computational grid* \mathcal{G} and the set of *intersection points* \mathcal{B} . The last two sets are represented in Figures 3.8(a) and 3.8(b), respectively, and, as it can be seen, they result from the superimposition of a Cartesian grid to the geometry of an arbitrarily shaped domain.

The computational grid \mathcal{G} is defined as the grid formed by the nodes that lie within the physical domain; the unknown functions must necessarily be defined at those points. The grid \mathcal{G} is characterized by an incomplete two-dimensional topological structure, whose exploitation would bring significant benefits to the computational procedure. However such a grid does not carry any useful information on the real geometry of the domain, nor on boundary conditions.

The set \mathcal{B} is also defined, as the set formed by the intersection points between the Cartesian grid and the boundary of the domain of integration. Unlike the grid \mathcal{G} , the set \mathcal{B} has a one-dimensional topological structure, and is not linked to the unknowns of the problem; on the contrary, it contains the missing information concerning the boundary conditions.

To provide a support for the approximation of the equations, the set $\mathcal{D} = \mathcal{G} \cup \mathcal{B}$ is

Figure 3.9: Local stencils g (a) and d (b).

considered. \mathcal{D} has, as of \mathcal{B} , a one-dimensional structure, and, therefore, does not provide an useful support to the resolution of the equations. The set \mathcal{D} , on the other hand, contains information related to both the field (interior nodes) and the boundary conditions (intersection points). The resolute procedure passes through the construction of a linear mapping between the grids \mathcal{G} and \mathcal{D} , with the aim of expressing the equations discretized on \mathcal{D} as a function of the nodal unknowns of \mathcal{G} , so that the computational advantages of Cartesian grids can be preserved.

Grids \mathcal{G} and \mathcal{D} can be thought of as a union of a finite number of the local stencils represented in Figures 3.9(a) and 3.9(b), designated as g and d respectively. The g stencil is complete only when all its nodes lie inside the domain, otherwise it cannot provide a complete support to the discretization of the equations, because of the "lack" of some of its nodes.

Stencil d instead is always complete, since it replaces the missing nodes with the intersection points of the boundary with the grid. If all the nodes of g are internal to the domain, the two stencils coincide. Hence, the set \mathcal{D} is, in general, capable of providing a full support to the discretization, but it can not be conveniently assembled within a full two-dimensional structure.

Two distinct control volumes are identified for the two stencils. The cell V is related to the computational stencil g ; V is independent of the presence and the relative position of the boundary: its size depends only on the structure of the grid to which it refers. On the contrary, the size of the discretization cell \bar{V} , linked to the d -stencil, must be defined coherently with the presence of the geometric boundary. In the method outlined in [145], the geometry of the cell \bar{V} is maintained rectangular. In this way, the union of all the cells \bar{V} does not coincide with the whole domain of integration, thus implying a lack of accuracy in the approximation of the physical domain. However, from a mathematical standpoint, such a choice does not affect the achievement of second-order accuracy.

The size of the cell \bar{V} is defined on the basis of the relative positioning of the intersection point and the computational stencil. Consistently with the discretization adopted, in case the boundary intersects the stencil on one of its end points, the cell \bar{V} coincides with V . In the standard case, the lengths of the half-sides of \bar{V} are sized as proportional to those of V , by the ratio between the distance of the cell center from the intersection point, and the length of the associated stencil arm.

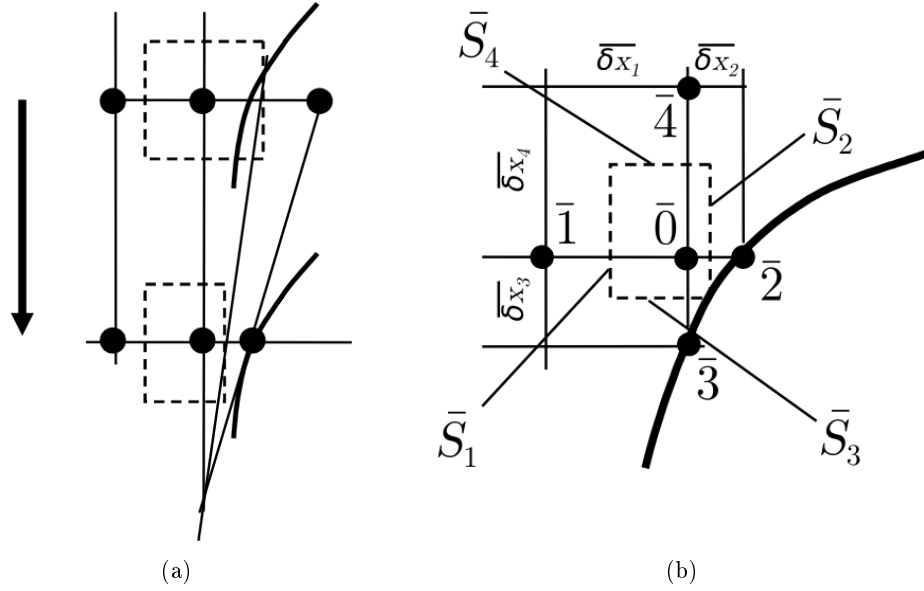


Figure 3.10: Resizing (a) and geometry of the discretization cell (b).

The resizing procedure is schematised in Figure 3.10(a), while the measures of the sides \bar{S} of the modified cell are displayed in Figure 3.10(b).

3.6.2 Discretization of the equations on the boundary cell

The generic transport equation 3.1.1 can be rewritten in integral form on the unit cell \bar{V} . From equation (3.4.2), one has:

$$\int_{\bar{V}} \left(\frac{\partial \varphi}{\partial t} \right) d\bar{V} + \int_{\bar{S}} (\mathbf{u}\varphi) \cdot \hat{\mathbf{n}} d\bar{S} = \int_{\bar{S}} \Gamma (\nabla \varphi \cdot \hat{\mathbf{n}}) d\bar{S} + \int_{\bar{V}} \sigma_V d\bar{V} \quad (3.6.1)$$

In analogy with the discretization procedure introduced in Section 3.4.3, for the volumetric terms, one can write:

$$\int_{\bar{V}} \left(\frac{\partial \varphi}{\partial t} \right) d\bar{V} \simeq \bar{S}_1 \bar{S}_3 \frac{\partial \varphi_0}{\partial t} \quad (3.6.2)$$

$$\int_{\bar{V}} \sigma_V d\bar{V} \simeq \bar{S}_1 \bar{S}_3 \sigma_{V,0} \quad (3.6.3)$$

Similarly, it is possible to introduce the discrete forms of the diffusive and convective terms:

$$\int_{\bar{S}} \Gamma (\nabla \varphi \cdot \hat{\mathbf{n}}) d\bar{S} \simeq \sum_{k=1}^4 \Gamma \frac{\partial \phi}{\partial n_k} = \sum_{k=1}^4 \frac{\bar{\varphi}_k - \bar{\varphi}_0}{\delta x_k} \bar{S}_k \quad (3.6.4)$$

$$\int_{\bar{S}} (\mathbf{u}\varphi) \cdot \hat{\mathbf{n}} d\bar{S} \simeq \sum_{k=1}^4 \check{u}_k \check{\varphi}_k \bar{S}_k \quad (3.6.5)$$

Equations (3.6.4) and (3.6.5) can be effectively represented in vector notation, as functions of the nodal unknowns on the discretization stencil:

$$\sum_{k=1}^4 \frac{\bar{\varphi}_k - \bar{\varphi}_0}{\delta x_k} \bar{S}_k = \Gamma \sum_{k=1}^4 \frac{\bar{S}_k}{\delta x_k} (\bar{\varphi}_k - \bar{\varphi}_0) \equiv \Gamma \mathbf{s}^T \cdot \bar{\mathbf{f}} \quad (3.6.6)$$

$$\sum_{k=1}^4 \check{u}_k \check{\varphi}_k \bar{S}_k \equiv \mathbf{h}^T \cdot \check{\mathbf{f}} \quad (3.6.7)$$

In equation (3.6.6), the vector $\mathbf{s} \equiv (s_0 \dots s_4)$ contains the metric coefficients, while the vector $\bar{\mathbf{f}} \equiv (\bar{f}_0 \dots \bar{f}_4)$ contains the nodal unknowns. In equation (3.6.7) the vector $\mathbf{h} \equiv (h_0 \dots h_4)$ represents the product between velocity and the side lengths at the interfaces of \bar{V} ; the vector $\check{\mathbf{f}} \equiv (\check{f}_0 \dots \check{f}_4)$ contains the interface values of the unknown. The components of the above vectors are defined as follows:

$$s_k = \frac{\bar{S}_k}{\delta x_k} \quad k = 1 \dots 4, \quad s_0 = - \sum_{k=1}^4 s_k \quad (3.6.8)$$

$$\bar{f}_k = \bar{\varphi}_k \quad k = 1 \dots 4, \quad f_0 = \bar{\varphi}_0 \equiv \varphi_0 \quad (3.6.9)$$

$$h_k = \check{u}_k \bar{S}_k \quad k = 1 \dots 4 \quad (3.6.10)$$

$$\check{f}_k = \check{\varphi}_k \quad k = 1 \dots 4 \quad (3.6.11)$$

An important aspect of the discretization is that, while the metric coefficients s_k of the discrete diffusive term (3.6.6) can be calculated in a pre-processing phase, once the topology of the discretization grid \mathcal{D} is determined, the convective term (3.6.7) contains an explicit reference to the velocity components normal to the cell boundaries, gathered in vector \mathbf{h} . Such components must be accurately determined at each step of the calculation procedure. For this reason, the procedure to be implemented is not trivial and, most importantly, it must be adapted to the variable being considered. This issue will be addressed further, and discussed in full detail.

A semi-discrete form of the generic transport equation (3.1.1) can now be written for each discretization cell \bar{V} :

$$\frac{\partial \bar{f}_0}{\partial t} \bar{V} + \mathbf{h}^T \cdot \check{\mathbf{f}} = \Gamma \mathbf{s}^T \cdot \bar{\mathbf{f}} + \sigma_V \bar{V} \quad (3.6.12)$$

From equation (3.6.12), one can switch to a fully discrete form by applying the temporal discretization introduced in Section 3.3, and expressing it as a function of the temporal variations of the unknown variable:

$$\Delta \bar{f}_0^n \bar{V} - \Delta t^n \frac{\beta}{1 + \gamma} \Gamma \mathbf{s}^T \cdot \Delta \bar{\mathbf{f}}^n = rhs^n \quad (3.6.13)$$

where:

$$\begin{aligned} rhs^n &= \frac{\Delta t^n}{1 + \gamma} \left[- \left(1 + \frac{1}{2} \frac{\Delta t^n}{\Delta t^{n-1}} \right) (\mathbf{h}^T)^n \cdot \check{\mathbf{f}}^n + \left(\frac{1}{2} \frac{\Delta t^n}{\Delta t^{n-1}} \right) (\mathbf{h}^T)^{n-1} \cdot \check{\mathbf{f}}^{n-1} \right. \\ &\quad \left. + \Gamma \mathbf{s}^T \cdot \bar{\mathbf{f}}^n + \left(\gamma \frac{\Delta \bar{f}_0^{n-1}}{\Delta t^{n-1}} + \sigma_{V,0} \right) \bar{V} \right] \end{aligned} \quad (3.6.14)$$

Equations (3.6.13) and (3.6.14) represent a completely discrete form of the differential equation (3.1.1) on the grid \mathcal{D} .

As mentioned above, however, the distribution of the nodes of the grid \mathcal{D} does not allow for a global reconstruction on the two-dimensional computational domain. For this reason, a link is to be established between the variables \bar{f}_k on the discretization grid and the nodal unknowns f_k . This is achieved by constructing a linear transformation that allows to switch from the equations on the grid \mathcal{D} to those on the computational grid \mathcal{G} .

In general, the value of the unknown in the generic node of the stencil d can be expressed as a linear combination of the values of the unknown in the nodes of the stencil g , plus a non-homogeneous term accounting for the boundary conditions. Hence, in vector notation, one can write:

$$\bar{\mathbf{f}} = \mathbf{E} \cdot \mathbf{f} + \mathbf{g} \quad (3.6.15)$$

The coefficients of the matrix \mathbf{E} and the vector \mathbf{g} are defined on the basis of the possible intersections of the computational stencil g and the boundary of the domain. The boundary conditions associated with those intersections also define the terms of \mathbf{E} and \mathbf{g} . If the stencil is completely contained within the domain, one has:

$$\bar{\mathbf{f}} = \mathbf{f} \quad \Rightarrow \mathbf{E} = \mathbf{I}, \mathbf{g} = \mathbf{0} \quad (3.6.16)$$

The analytical expressions of \mathbf{E} and \mathbf{g} are discussed below. Equations (3.6.13) and (3.6.14) are now transformed according to the definition (3.6.15). Before doing this, it is necessary to reformat equation (3.6.15) for the temporal changes of the unknown. This is done here under the assumptions of fixed boundaries and stationary boundary conditions. In this case, the matrix \mathbf{E} and the vector \mathbf{g} are constant, and the following relationship holds:

$$\Delta \bar{\mathbf{f}} = \Delta (\mathbf{E} \cdot \mathbf{f} + \mathbf{g}) = \Delta (\mathbf{E} \cdot \mathbf{f}) + \mathbf{g} = \mathbf{E} \cdot \Delta \mathbf{f} \quad (3.6.17)$$

Hence, by operating the appropriate substitutions, a general expression of equations (3.6.13) and (3.6.14) on the computational stencil g is obtained:

$$\Delta f_0^n \bar{V} - \Delta t^n \frac{\beta}{1+\gamma} \Gamma \mathbf{s}^T \cdot \mathbf{E} \cdot \Delta \mathbf{f}^n = rhs^n \quad (3.6.18)$$

where:

$$\begin{aligned} rhs^n &= \frac{\Delta t^n}{1+\gamma} \left[- \left(1 + \frac{1}{2} \frac{\Delta t^n}{\Delta t^{n-1}} \right) (\mathbf{h}^T)^n \cdot \check{\mathbf{f}}^n + \left(\frac{1}{2} \frac{\Delta t^n}{\Delta t^{n-1}} \right) (\mathbf{h}^T)^{n-1} \cdot \check{\mathbf{f}}^{n-1} \right. \\ &\quad \left. + \Gamma \mathbf{s}^T \cdot (\mathbf{E} \cdot \mathbf{f}^n + \mathbf{g}) + \left(\gamma \frac{\Delta f_0^{n-1}}{\Delta t^{n-1}} + \sigma_{V,0} \right) \bar{V} \right] \end{aligned} \quad (3.6.19)$$

3.6.3 Boundary conditions

The procedure for determining the coefficients of \mathbf{E} and \mathbf{g} is described. At the generic intersection node k , the boundary condition for the unknown f_k is expressed by the following general form:

$$a_k f_k + b_k \frac{\partial f_k}{\partial \eta_k} = c_k \quad (3.6.20)$$

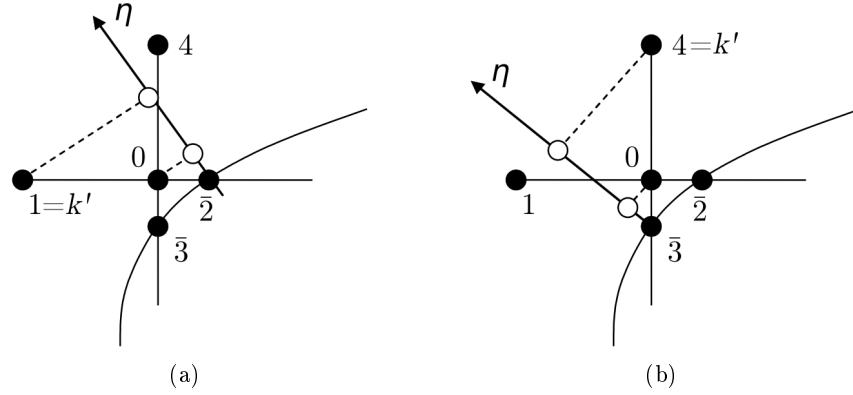


Figure 3.11: Local discretization stencils for intersections with $k = 2$ (a) and $k = 3$ (b).

where η_k denotes the direction normal to the boundary at node k . With reference to Figures 3.11(a) and 3.11(b), the index k' , identifying the symmetric of node k with respect to the center of the stencil, is defined as follows:

$$\begin{cases} k' = 3 - k & k = 1, 2 \\ k' = 7 - k & k = 3, 4 \end{cases} \quad (3.6.21)$$

It is assumed that the nodes $0, k, k'$ provide the basis for a reasonable estimate of the normal derivative, in that its value is moderately affected by the distortive effect of the misalignment of the grid and the normal direction η . By performing a second-order Taylor expansion of φ around k , along the direction η , one can write:

$$\varphi(\eta) \simeq \varphi_{\eta=0} + \left(\frac{\partial \varphi}{\partial \eta} \right)_{\eta=0} \eta + \left(\frac{\partial^2 \varphi}{\partial \eta^2} \right)_{\eta=0} \eta^2 \quad (3.6.22)$$

Here, the node k is taken as the origin of the η axis. The expression (3.6.22) holds for any point in the vicinity of k , and, therefore, it can be applied to all the three points $0, k, k'$ chosen for the approximation of the normal derivative:

$$f_l \simeq f_k + \left(\frac{\partial \varphi}{\partial \eta} \right)_{\eta=0} \eta_l + \left(\frac{\partial^2 \varphi}{\partial \eta^2} \right)_{\eta=0} \eta_l^2 \quad l = 0, k, k' \quad (3.6.23)$$

On the basis of the relationship (3.6.23), the normal derivative of the variable φ at the boundary can be expressed as a linear combination of the nodal values of the variable itself in the points $0, k, k'$ of the stencil:

$$\left(\frac{\partial \varphi}{\partial \eta} \right)_{\eta=0} = p_{k,0} \bar{f}_0 + p_{k,k} \bar{f}_k + p_{k,k'} \bar{f}_{k'} = \sum_l p_{k,l} \bar{f}_l, \quad l = 0, k, k' \quad (3.6.24)$$

The coefficients $p_{k,l}$ of the linear combination are unknown. In order to determine them, equation (3.6.23) is substituted into equation (3.6.24), yielding:

$$\left(\frac{\partial \varphi}{\partial \eta} \right)_{\eta=0} = \sum_l p_{k,l} \bar{f}_l \simeq \sum_l \left[f_k + \left(\frac{\partial \varphi}{\partial \eta} \right)_{\eta=0} \eta_l + \left(\frac{\partial^2 \varphi}{\partial \eta^2} \right)_{\eta=0} \eta_l^2 \right] \quad l = 0, k, k' \quad (3.6.25)$$

By enforcing congruence between the members of equation (3.6.25), the following conditions arise:

$$0 = \sum_l p_{k,l}, \quad 1 = \sum_l p_{k,l} \eta_l, \quad 0 = \sum_l p_{k,l} \eta_l^2, \quad l = 0, k, k' \quad (3.6.26)$$

The following 3×3 linear system is then obtained for the generic intersection node k :

$$\begin{pmatrix} 1 & 1 & 1 \\ \eta_0 & 0 & \eta_{k'} \\ \eta_0^2 & 0 & \eta_{k'}^2 \end{pmatrix} \begin{pmatrix} p_{k,0} \\ p_{k,k} \\ p_{k,k'} \end{pmatrix} = \begin{pmatrix} 0 \\ 1 \\ 0 \end{pmatrix} \quad (3.6.27)$$

where the central column of the coefficients matrix of coefficients contains null values, since k has been taken as the origin for η -coordinate.

Once the coefficients $p_{k,l}$ have been calculated, it is possible to insert the expression (3.6.24) for the normal derivative of φ into the generic boundary condition (3.6.20), thus obtaining:

$$a_k \bar{f}_k + b_k \sum_l p_{k,l} \bar{f}_l = c_k, \quad l = 0, k, k' \quad (3.6.28)$$

Equation (3.6.28) expresses a useful constraint to determine the value of f_k , when point k lies on the boundary. If, on the contrary, the computational stencil is completely contained within the domain, the link between the values associated with the discretization and computational stencils will simply be:

$$\bar{f}_k = f_k \quad (3.6.29)$$

Hence, a general equation can be written, in order to establish a relationship between vector $\bar{\mathbf{f}}$ and vector \mathbf{f} , simultaneously satisfying the boundary conditions:

$$(a_k + b_k p_{k,k}) \bar{f}_k + b_k \sum_{l=0, l \neq k}^4 p_{k,l} \bar{f}_l = c_k + d_k f_k \quad (3.6.30)$$

According to the above approximation, in the sum at the left-hand-side of equation (3.6.30), the coefficients $p_{k,l} = 0$ for $l \neq 0, k'$. The coefficients d_k allow the relation itself to hold also for internal cells. More specifically, $d_k = 1$ if the associated node is inside the domain, while $d_k = 0$ if the node lies on the boundary.

Equation (3.6.30) can be reformulated in matrix notation as:

$$\mathbf{A} \cdot \bar{\mathbf{f}} = \mathbf{D} \cdot \mathbf{f} + \mathbf{c} \quad (3.6.31)$$

where:

$$\mathbf{A} = \begin{pmatrix} 1 & 0 & 0 & 0 & 0 \\ b_1 p_{10} & a_1 + b_1 p_{11} & b_1 p_{12} & b_1 p_{13} & b_1 p_{14} \\ b_2 p_{20} & b_1 p_{21} & a_2 + b_2 p_{22} & b_2 p_{23} & b_2 p_{24} \\ b_1 p_{30} & b_1 p_{31} & b_1 p_{32} & a_3 + b_3 p_{33} & b_3 p_{34} \\ b_1 p_{40} & b_1 p_{41} & b_1 p_{42} & b_4 p_{43} & a_4 + b_4 p_{44} \end{pmatrix} \quad (3.6.32)$$

$$\mathbf{D} = \begin{pmatrix} 1 & & & & \\ & d_1 & & & \\ & & d_2 & & \\ & & & d_3 & \\ & & & & d_4 \end{pmatrix} \quad (3.6.33)$$

$$\mathbf{c} = (c_0, \dots, c_k) \quad (3.6.34)$$

For instance, in the case $k = 2$ (Figure 3.11(a)):

$$\mathbf{A} = \begin{pmatrix} 1 & 0 & 0 & 0 & 0 \\ 0 & 1 & 0 & 0 & 0 \\ b_2 p_{20} & b_1 p_{21} & a_2 + b_2 p_{22} & b_2 p_{23} & b_2 p_{24} \\ 0 & 0 & 0 & 1 & 0 \\ 0 & 0 & 0 & 0 & 1 \end{pmatrix} \quad (3.6.35)$$

$$\mathbf{D} = \begin{pmatrix} 1 & & & & \\ & 1 & & & \\ & & 0 & & \\ & & & 1 & \\ & & & & 1 \end{pmatrix} \quad (3.6.36)$$

$$\mathbf{c}^T = (0, 0, c_2, 0, 0) \quad (3.6.37)$$

It is now possible to formulate the expressions for \mathbf{E} and \mathbf{g} introduced by the definition (3.6.15):

$$\mathbf{E} = \mathbf{A}^{-1} \cdot \mathbf{D}, \quad \mathbf{g} = \mathbf{A}^{-1} \cdot \mathbf{c} \quad (3.6.38)$$

It should be noted that the values of \mathbf{E} and \mathbf{g} depend only on the coefficients of equation (3.6.20) and on the boundary geometry and, therefore, they can be calculated once for all in the pre-processing phase of the numerical procedure.

3.6.4 Reconstruction of convective fluxes and source terms

In order to complete the reformulation of the discrete equation (3.6.18) for the generic boundary cell \bar{V} , two elements must be further addressed.

One is the determination of vectors \mathbf{h} and \mathbf{f} , accounting for the convective fluxes across the boundary cell interface, which contains explicit references to the velocity components normal to the cell sides, and to the value of the variable at the interface itself. Such quantities depend not only on the boundary conditions, but also on the values assumed by the variable at each time-step. Moreover, their format varies according to the equation to be considered.

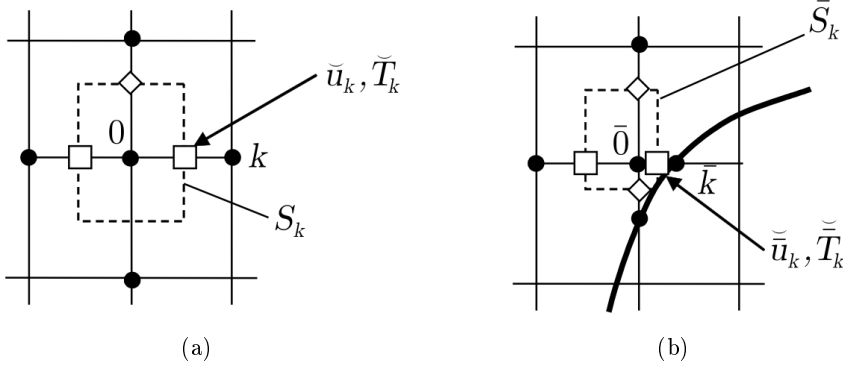


Figure 3.12: Computational (a) and discretization (b) stencils for the energy equation.

The other issue concerns the estimate of the source terms in the Navier-Stokes equations, already addressed in Section 3.4.3. This depends on scalar quantities (temperature and pressure) and its reconstruction process must be reformulated for the boundary cell \bar{V} . Such procedures will be briefly described in the following, by treating each equation separately.

Energy equation

The energy equation (2.1.3) is repeated here for the sake of clarity:

$$\frac{\partial T}{\partial t} + \mathbf{u} \cdot \nabla T = \frac{1}{Gr^{\frac{1}{2}} Pr} \nabla^2 T \quad (3.6.39)$$

In analogy with equation (3.6.5) and with reference to Figure 3.12, the convective term in equation (3.6.39) can be integrated on the generic control volume associated with the discretization grid, thus obtaining the following discrete form:

$$\int_{\bar{S}} (\mathbf{u}T) \cdot \hat{\mathbf{n}} d\bar{S} \simeq \sum_{k=1}^4 \check{u}_k \check{T}_k \bar{S}_k \quad (3.6.40)$$

It is then necessary to determine the quantities \check{T}_k and \check{u}_k . As for the former, it can be expressed as a function of the value on the centroid of the cell, \bar{T}_0 , and the value at the k -th node of the discretization stencil, \bar{T}_0 . Linearly interpolating between the two quantities, one can write:

$$\check{T}_k = \frac{\Delta x_k^{(k)} \bar{T}_0 + \Delta x_k^{(0)} \bar{T}_k}{\Delta x_k^{(k)} + \Delta x_k^{(0)}} S_k \quad (3.6.41)$$

It should be noted that the weights of the interpolation coincide with those in equation (3.4.5), since the relationship between the length of the k -th stencil arm and the distance of the centroid from the k -th cell side is invariant with respect to the deformation due to the presence of the boundary.

The determination of the normal velocity at the interface, \check{u}_k , is slightly more complex, in that, it requires information related to a variable that lies on a different grid. Depending on the relative distance between the centroid of the cell and the intersection point k , one might experience the three situations represented in Figure 3.13

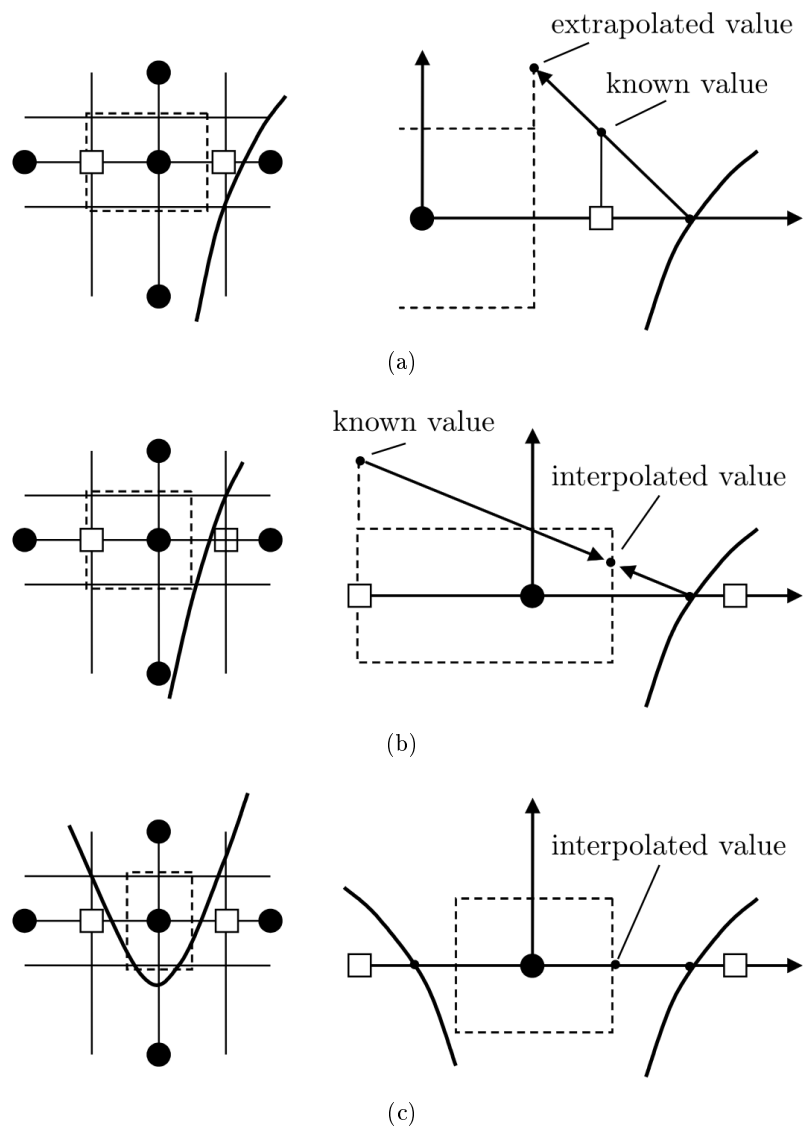


Figure 3.13: Procedure for the estimate of the normal velocity component near the boundary for the energy equation.

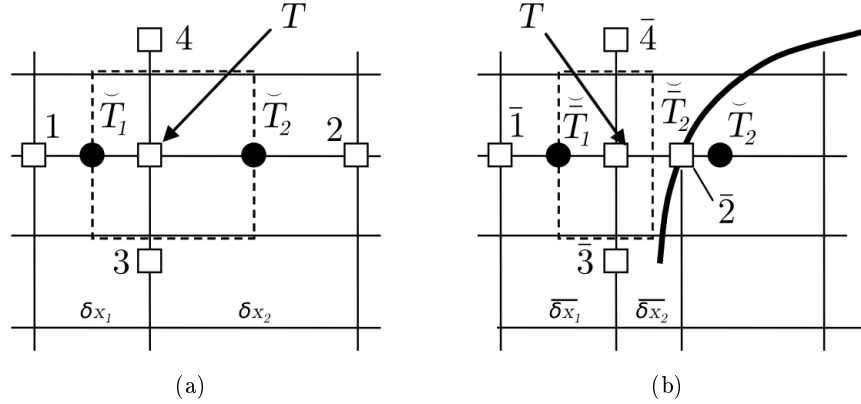


Figure 3.14: Computational (a) and discretization (b) cells and stencils for the reconstruction of source terms in the Navier-Stokes equation.

In case (a), the node containing the required value of velocity lies within the domain. Although this node is no longer located on the cell boundary, due to the deformation induced by the presence of the boundary itself, it can nevertheless be used to determine the value of the normal velocity component \bar{u}_k . Such an estimation can be performed by linear extrapolation from the value of the node itself and the value at the intersection point k (which is always zero for a closed domain).

In case (b), the node containing the required velocity value lies outside the domain and is therefore excluded from the calculations. In this situation, a linear interpolation must be performed between the value at the symmetric node of the velocity grid, with respect to the centroid, and the value at the boundary. Such a procedure is valid, however, only when at least one of the two nodes associated with the stencil direction is contained within the domain of integration.

Otherwise, a situation similar to that represented by case (c) arises: the normal flux on the cell side can not be determined from the nodal values of the velocity grid, since no “active” node falls in the vicinity of the cell itself. The calculation of the normal velocity at the interface is then operated from the only information available, *i.e.* the values at the intersection nodes. In the case of a closed domain, this corresponds to impose zero velocity on the cell side.

The reconstruction procedures described above are to be carried out for each of the four directions of the stencil.

Navier-Stokes equation

The discretization of convective fluxes and source terms in the Navier-Stokes equation involves the introduction of a set of more complex approximation techniques, as compared to those seen for the energy equation. On the one hand, this is due to the presence of a greater number of terms for which a numerical reconstruction is needed; on the other hand, an additional difficulty is inherent in the determination of the normal velocity components for the convective term.

For simplicity, the procedure is outlined for the sole $x-$ component of the Navier-Stokes

equation (2.1.2):

$$\frac{\partial u_x}{\partial t} + \mathbf{u} \cdot \nabla u_x = -\frac{\partial P}{\partial x} + \frac{1}{Gr^{\frac{1}{2}}} \nabla^2 u_x - T \cos \theta \quad (3.6.42)$$

First, the determination of temperature at the cell center is addressed, necessary for the estimate of the source term $T \cos \theta$. According to the finite volume discretization, such a value is expected to coincide with the integral mean value over the whole cell. With reference to Figure 3.14, one has that, for an internal cell, the temperature value on the centroid can be calculated by linear interpolation of the two T -values available at the cell interface:

$$T = \frac{\delta x_2 \check{T}_1 + \delta x_1 \check{T}_2}{\delta x_1 + \delta x_2} \quad (3.6.43)$$

Equation (3.6.43) is valid even if the stencil intersects the boundary. The change in the geometry of the cell does not affect the centroid, so the point where the temperature must be calculated remains the same. If, however the intersection with the contour excludes one of the two nodes used in equation (3.6.43), the information carried by the boundary condition at the intersection point must be used. In the limiting case where both nodes lie outside the domain, the temperature at the cell center shall be determined solely from boundary conditions. Hence, in general, it is:

$$T = \frac{\overline{\delta x_2} \check{T}_1 + \overline{\delta x_1} \check{T}_2}{\overline{\delta x_1} + \overline{\delta x_2}} \quad (3.6.44)$$

It must be observed that, regardless of the type of boundary condition, the boundary values of temperature for the convective term are known from the preceeding time-step.

The discretization of the spatial derivative of pressure is addressed now. Like T , pressure P is calculated on the scalar grid; therefore, the problems associated with the position of the nodes with respect to the domain of integration are identical to those encountered for the calculation of the buoyancy term. In this case, however, the quantity to be determined is a derivative. If the stencil lies inside the domain, one can write:

$$\frac{\partial P}{\partial x} \simeq 2 \frac{\check{P}_2 - \check{P}_1}{\delta x_1 + \delta x_2} \quad (3.6.45)$$

Once again, the intersection between the stencil and the boundary could make unavailable one of two pressure values in (3.6.45). The expression of the discrete first derivative is then corrected by enforcing the related boundary condition. For a closed domain, a Neumann boundary condition is always imposed on pressure:

$$\frac{\partial P}{\partial \eta} = 0 \quad (3.6.46)$$

Hence, in case one of the two points required for the calculation lies outside the domain, (3.6.45) will degenerate in the following approximate form:

$$\frac{\partial P}{\partial x} \simeq \frac{\partial P}{\partial \eta} = 0 \quad (3.6.47)$$

The discretization of equation (3.6.42) is completed by the approximation procedure for the convective term $\mathbf{u} \cdot \nabla u_x$. This term can be expressed in conservative form, and expanded along the grid directions:

$$\mathbf{u} \cdot \nabla u_x = \nabla \cdot (\mathbf{u} u_x) = \frac{\partial}{\partial x} (u_x^2) + \frac{\partial}{\partial z} (u_x u_z) \quad (3.6.48)$$

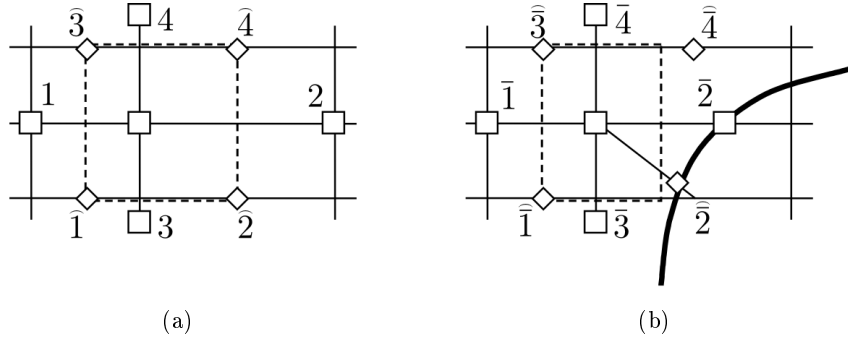


Figure 3.15: Computational (a) and discretization (b) cells and stencils for the reconstruction of convective fluxes in the Navier-Stokes equation.

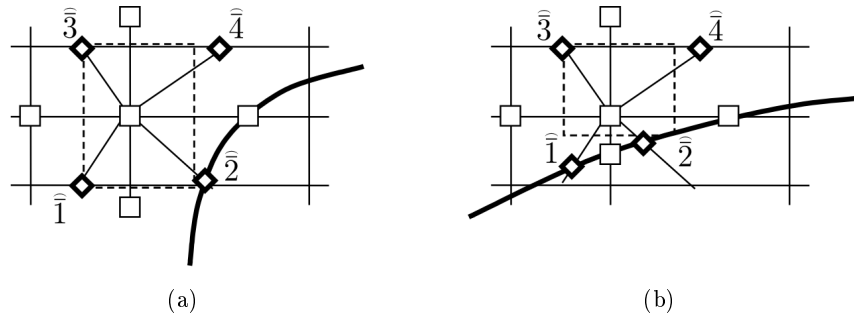


Figure 3.16: Discretization stencils for the reconstruction of the normal velocity components: diagonal intersections.

With reference to Figure 3.15(a), it is possible to obtain the following discrete form for the integration of (3.6.48) on the generic control volume:

$$\frac{\partial}{\partial x} (u_x^2) + \frac{\partial}{\partial z} (u_x u_z) \simeq \check{u}_{x,2}^2 S_2 - \check{u}_{x,1}^2 S_1 + \check{u}_{x,4} \check{u}_{z,4} S_4 - \check{u}_{x,3} \check{u}_{z,3} S_3 \quad (3.6.49)$$

The evaluation of (3.6.49) requires the interpolation of the normal velocity components. The terms containing only values of u_x are easily derived from the available node values:

$$\check{u}_{x,k} = \frac{u_{x,k} + u_{x,0}}{2} \quad (3.6.50)$$

In case the stencil intersects the boundary of the domain (Figure 3.15(b)), one can easily rewrite equation (3.6.50), given the available information:

$$\bar{u}_{x,k} = \frac{\bar{u}_{x,k} + \bar{u}_{x,0}}{2} \quad (3.6.51)$$

For the mixed terms in (3.6.49), however, information from a different grid is required. The following interpolations for \tilde{u}_z is performed:

$$\ddot{u}_{z,3} = \frac{\delta x_2 \hat{u}_{z,1} + \delta x_1 \hat{u}_{z,2}}{\delta x_1 + \delta x_2} \quad (3.6.52)$$

$$\ddot{u}_{z,3} = \frac{\delta x_2 \hat{u}_{z,3} + \delta x_1 \hat{u}_{z,4}}{\delta x_1 + \delta x_2} \quad (3.6.53)$$

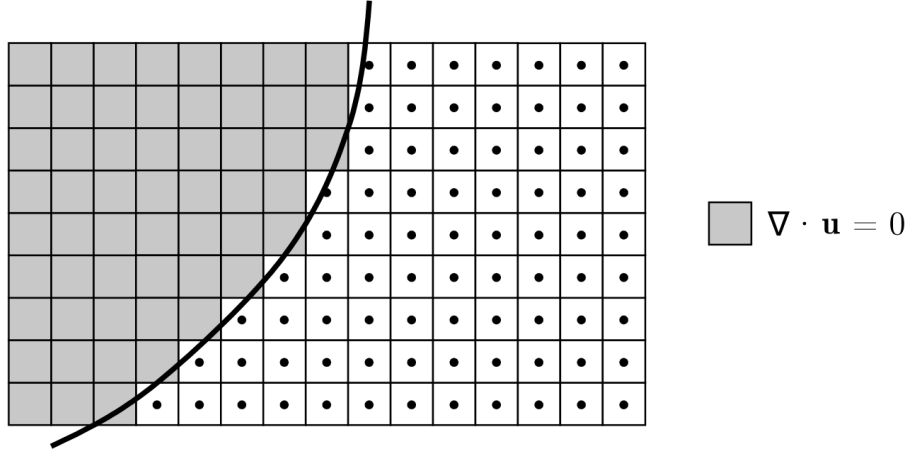


Figure 3.17: Adaptation of the Matrix Decomposition approach to irregular domains.

The above relations require a more complex treatment, in the case of intersection of the stencil with the geometric boundary. In fact, depending on the position of the boundary itself, it might be that one or more nodes, necessary for the evaluation of the vertical velocity component u_z , fall outside the domain.

Therefore, the nodes for the calculation of the normal velocity components are defined on the basis of the intersections of the boundary with the segments $O\hat{k}$, connecting the center of the stencil with the nodes \hat{k} (Figure 3.16).

Since the vertices \hat{k} , in general, do not lie on the grid directions, a bilinear function must be introduced, whose support is formed by the set of vertices \hat{k} . The coefficients of this function can be computed in the pre-processing phase, since they only depend on the geometry.

The definition of such a function and the description of the subsequent calculation of such coefficients is omitted here for the sake of brevity. The procedure leading to the discretization of convective and source terms for the z -component of the Navier-Stokes equations is also omitted, being completely analogous to that presented for equation (3.6.42).

3.6.5 Pressure-velocity coupling

The technique for the modeling of irregular domains on Cartesian grids allows all the terms in the momentum and energy equations to recast in discrete form. As premised, the resolution of the transport equations requires an additional calculation step, *i.e.* the resolution of a Poisson problem for the correction of pressure. Equation (3.2.7) for pseudo-pressure should be modified in order to extend its validity to irregular domains. In particular, the zero-flux condition (3.2.8) should be enforced at the geometric boundary, rather than on the sides of the computational cells.

The numerical algorithm adopted, based on the Matrix Decomposition approach [142] is however not suitable for an adaptation to the presence of irregularly shaped boundaries. Its structure, particularly advantageous for computations on Cartesian grids, requires the metric coefficients on the grid to be homogeneous along each grid direction [146]. An appropriate perturbation of the coefficients on the local stencils would then vanish all the computational benefits deriving from the methodology adopted.

For this reason, the Matrix Decomposition Method was retained in its original version. It is clear that such an approach is not strictly correct. In fact, instead of the zero-flux assumption at the boundary, it is assumed that the Laplacian of the pseudo-pressure be zero in the regions outside the domain, as shown in Figure 3.17. This will allow the function ϕ to have non-zero normal gradient near the solid wall, as opposed to the theoretical requirements of the Projection Methods. Nevertheless, as shown in the following chapters, such a practice is justified *a posteriori* by accuracy tests. It is seen that the error committed in the correction of velocity neither influences the overall solution, nor leads to a divergence of the calculation procedure. Moreover, the computational advantages ensured by the procedure are preserved.

3.7 Summary

The main features of the numerical procedure employed, have been outlined in this chapter. These are:

- (i.) a Projection Method [8] for the decoupling of the continuity and Navier-Stokes equations;
- (ii.) three-level, second-order explicit and implicit time discretization schemes for the energy and Navier-Stokes equations;
- (iii.) second-order Finite-Volume schemes for the discretization of the transport equations on two-dimensional Cartesian grids;
- (iv.) an original treatment [145, 142] of irregularly shaped boundaries on Cartesian grids.

The resolution procedure of the governing equations (2.1.1)-(2.1.3) at each time step, as implemented in the numerical code employed in the present study, is now briefly reviewed.

At time t^{n+1} , the system state is calculated starting from the known values of the variables at times t^n and t^{n-1} , since the discretization is based on a three-level stencil. Energy equation is solved first, for it has the particular feature of not including any reference to the values of velocity and pressure at time t^{n+1} , thanks to the explicit discretization of the convective term. The temperature variation is ΔT^n is determined over the whole computational domain through the application of the Approximate Factorization method, adapted to the case of irregular domains.

Once the temperature T^{n+1} is known, the approximate velocity $\tilde{\mathbf{u}}$ is computed by the resolution of the x - and z - components of the momentum equations. It is pointed out that, in the source term, the temperature value T^n is advantageously substituted by T^{n+1} . Such a practice allows a greater accuracy in time to be achieved.

The last steps of the procedure consist in the resolution of the Poisson equation for pseudo-pressure ϕ , and in the subsequent correction of the velocity and pressure fields.

Chapter 4

Square enclosure containing a horizontal cylinder

4.1 Introduction

Various aspects are addressed concerning buoyancy-induced flows from a horizontal cylindrical source centred into a two-dimensional square cavity. The goals of the research are to characterize the case in terms of its relevant flow features, to analyze the variety of transitional behaviours occurring for different combinations of the main parameters, and to provide fresh heat transfer results.

4.1.1 Statement of the problem

The system considered is sketched in Figure 4.1. A horizontal cylinder of diameter D , is centred into an enclosure of square cross section. The y -axis of the coordinate system coincides with the cylinder longitudinal axis, the x -axis is horizontal, while the z -axis is parallel and opposed to the gravitational field. The cavity extension along y is assumed to prevail over L , the cavity side length; therefore, the three-dimensional system is reduced to its 2D feature, represented as a square section containing a circular heat source. Attention is thereby restricted to the (x, z) plane in Figure 4.1. The temperature of the enclosure walls is uniform, $T = T_C$; the cylindrical source is treated either as an isothermal surface, $T = T_H$, with $T_H > T_C$, or an isoflux boundary, $q = q_s$.

4.1.2 Non-dimensionalization

The analyses have been performed in dimensionless terms. Suitable reference quantities were chosen, in order to derive meaningful dimensionless results.

Characteristic length. The geometry under consideration can also be referred to as the annulus between a square outer cylinder and an inner circular cylinder [128]. As pointed out in Section 2.4, the most representative length scale for buoyancy-induced flows within an annulus between two horizontal, concentric circular cylinders, is the measure H of the gap between the cylinders (see Figure 2.13).

For the system in Figure (4.1), three length scales are eligible as reference. These are: the gap width H , the cylinder diameter D , and the enclosure side length L . In the early

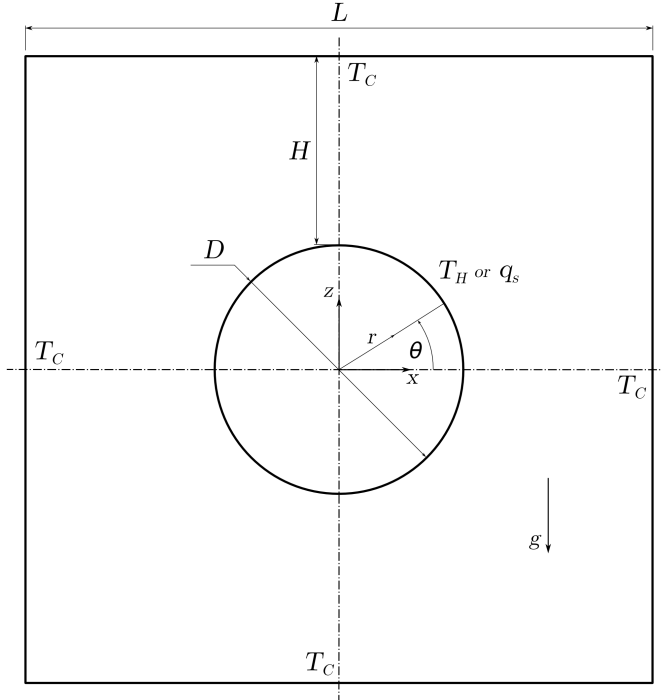


Figure 4.1: Schematic of the problem.

stages of the present analyses, the suitability of these scales was investigated, leading to the choice of H as the characteristic length. Such a choice, as identified by Teertstra and Yovanovich [84], allows a consistent representation of the case to be performed, by separating the influence of the aspect ratio and the Rayleigh number on both the flow asset and the overall heat transfer characteristics.

Characteristic temperature difference. Since the influence of the boundary conditions imposed at the source wall is one of the features under investigation, the choice of the reference temperature difference ΔT_{ref} is a crucial issue in the non-dimensionalization of the problem.

If a T condition (fixed temperature) is enforced at the source wall, the scaling temperature difference is straightforwardly defined:

$$\Delta T_{ref,T} = T_H - T_C \quad (4.1.1)$$

In case a Q condition (fixed wall heat flux density) is imposed, the reference temperature difference is defined:

$$\Delta T_{ref,Q} = \frac{q_s D}{\lambda} \quad (4.1.2)$$

It will be observed later, that such a choice gives rise to an alternative definition of the Rayleigh and Grashof numbers.

Characteristic velocity As already mentioned in Section (2.1), the Brunt-Väisälä velocity scale (1.4.15) was taken as reference throughout the major part of this work.

Definition	Range	h	d	R	A	σ	v
$h = \frac{H}{D}$	$0 < h < \infty$	1	$\frac{1-d}{2d}$	$\frac{R-1}{2}$	$\frac{1}{A-2}$	$\frac{1}{\sigma}$	$\frac{v}{1+2v}$
$d = \frac{D}{L}$	$0 < d < 1$	$\frac{1}{1+2h}$	1	$\frac{1}{R}$	$\frac{A-2}{A}$	$\frac{\sigma}{\sigma+2}$	$1+2v$
$R = \frac{L}{D}$	$1 < R < \infty$	$1+2h$	$\frac{1}{d}$	1	$\frac{A}{A-2}$	$\frac{\sigma+2}{\sigma}$	$\frac{1}{1+2v}$
$A = \frac{L}{H}$	$2 < A < \infty$	$\frac{1+2h}{h}$	$\frac{2}{1-d}$	$\frac{2R}{R-1}$	1	$\sigma+2$	$\frac{1}{v}$
$\sigma = \frac{D}{H}$	$0 < \sigma < \infty$	$\frac{1}{h}$	$\frac{2d}{1-d}$	$\frac{2}{R-1}$	$A-2$	1	$\frac{1+2v}{v}$
$v = \frac{H}{L}$	$0 < v < \frac{1}{2}$	$\frac{h}{1+2h}$	$\frac{1-d}{2}$	$\frac{R-1}{2R}$	$\frac{1}{A}$	$\frac{1}{\sigma+2}$	1

Table 4.1: Possible aspect ratios for the system under consideration, and their cross-relationships.

However, in order to present the results related to the pseudo-diffusive *PD* regime, (see Chapter 5), the diffusive velocity scale (1.4.25) appears to be the most appropriate, also considering that it is the reference velocity used for analytical solutions, to be used for comparison with the numerical predictions.

Dimensionless boundary conditions. With reference to Figure 4.1, the imposed boundary conditions are recast as follows, in dimensionless terms. At the enclosure walls:

$$T = 0, \quad \mathbf{u} = \mathbf{0} \quad (4.1.3)$$

On the cylinder surface, Dirichlet or Neumann boundary conditions were alternatively applied for temperature, while enforcing the no-slip condition:

$$T = 1, \quad \mathbf{u} = \mathbf{0} \quad (4.1.4)$$

$$\frac{\partial T}{\partial r} = 1, \quad \mathbf{u} = \mathbf{0} \quad (4.1.5)$$

4.1.3 Governing parameters

Three leading dimensionless parameters are recognized in the problem: the Rayleigh number Ra_H , based on H , the Prandtl number Pr , and a suitably chosen aspect ratio representing the system geometry.

The aspect ratio. The six possible aspect ratios for the present geometry are listed in Table 4.1, where a matrix of the cross-relations linking each definition to the other is also provided. These, in turn, are based on the relation between the three main lengths of the system:

$$H = \frac{L-D}{2} \quad (4.1.6)$$

Although the choice of the aspect ratio is less crucial than that of the characteristic length, some considerations upon it are in order:

- as already pointed out, the spatial extent of the system is suitably parametrized by choosing H as the reference length. Hence, the aspect ratio can be chosen as that ratio expressing one of the remaining lengths in dimensionless terms. To this aim, the choices of A and σ appear as the most appropriate. A is indeed the most representative of the two, in that, for $A \rightarrow \infty$, it tends to coincide with the aspect ratio of the horizontal, Rayleigh-Bénard-type layer formed by the cylinder wall and the enclosure ceiling, in the top part of the enclosure;
- although the choice of A formally appears as the most correct, the diameter to cavity side ratio d , or the gap width to diameter ratio h remain valid options anyway. Such parameters were alternatively considered while performing a consistent part of the analyses presented here, and, in particular, h turned out to be the best suited choice for the comprehensive correlation of heat transfer data, derived for the case $Pr = 0.7$ [13];
- in order to bring forth a parallel between the present case and the horizontal annulus, it is straightforward to adopt R as the aspect ratio. In fact, R can be seen as the ratio between the “radius” of the outer square cylinder ($L/2$) and the radius of the inner circular cylinder ($D/2$);
- among the six aspect ratios, v appears as the less significant, and, so far, has never been employed for the study of the system of Figure 4.1.

In the following, results will be presented in terms of A where possible, unless where otherwise specified. In particular, both d and h will be extensively used throughout the discussion of results related to the heat transfer characteristics of the system.

By employing the different aspect ratios listed in Table 4.1, it is possible to provide cross-relations between alternative definitions of the Rayleigh and Nusselt numbers, based on the three length scales of the problem of interest, H , D and L .

$$Ra_D = h^{-3} Ra_H = \sigma^3 Ra_H \quad (4.1.7)$$

$$Ra_L = A^{-3} Ra_H = v^3 Ra_H \quad (4.1.8)$$

$$Ra_L = d^{-3} Ra_D = R^3 Ra_D \quad (4.1.9)$$

$$Nu_D = h^{-1} Nu_H = \sigma Nu_H \quad (4.1.10)$$

$$Nu_L = A^{-1} Nu_H = v Nu_H \quad (4.1.11)$$

$$Nu_L = d^{-1} Nu_D = R Nu_D \quad (4.1.12)$$

The above relations (4.1.7)-(4.1.12) are useful to facilitate comparisons with the available literature data.

Heat transfer quantities. Throughout the following chapters, heat transfer results are always presented in terms of the Nusselt number, based on H , Nu_H , as defined by equation

1.4.12. Nu_H is the dimensionless measure of either the local or global heat transfer rate, as discussed in Section 1.4.3, and it assumes different forms, depending on the heat transfer feature to be quantified.

With reference to the angular coordinate system (r, θ) reported in the scheme of Figure 4.1, the local Nusselt number on the surface of the cylindrical source, can be defined as:

$$Nu_{H,\theta,s} = - \left(\frac{\partial T(r, \theta)}{\partial r} \right)_{r=\frac{\sigma}{2}} \quad (4.1.13)$$

By integrating along θ , one obtains the average Nusselt number on the cylinder surface:

$$Nu_{H,s} = \frac{1}{2\pi} \int_0^{2\pi} Nu_{H,\theta,s} d\theta \quad (4.1.14)$$

Analogous definitions can be given for the local and average Nusselt numbers at the enclosure walls; the related expressions will be recalled where needed, and, specifically, when presenting the results of the grid sensitivity analysis (see Section 4.3).

Rayleigh and Grashof number definition accounting for the boundary conditions. The Grashof number Gr and, consequently, the Rayleigh number, Ra , change in nature if either equation (4.1.1) or (4.1.2) are considered as the reference temperature for the non-dimensionalization of equations(2.1.1-2.1.3). Coherently with the notation of Section 1.5.1, the Rayleigh number defined with $T_{ref} = T_{ref,T}$ will be denoted Ra , while the modified Rayleigh number, based on $T_{ref} = T_{ref,Q}$, will be marked Ra_q . Enforcing the definition of the Nusselt number (1.4.12), the following relation holds between Ra_q and Ra [89]:

$$Ra^* = Ra \cdot Nu \quad (4.1.15)$$

It is important to point out that equation(4.1.15) turns out to be valid only under certain assumptions. When $T_{ref} = T_{ref,Q}$, it means that an equivalent Ra can be defined if the average temperature along the cylinder equals $T_{ref,T}$. On the contrary, when $T_{ref} = T_{ref,T}$, the relation is valid only if the average heat flux on the source equals q_s . Therefore, the equivalence in (4.1.15) provides a term of comparison between the two boundary conditions: once the value of the Nusselt number (*i.e.* the average temperature) at the source wall is established, results obtained in the isothermal case can be compared to those obtained under isoflux conditions, and *vice versa*, using (4.1.15).

4.2 Construction of the computational grids

The numerical predictions presented in the following chapters were carried out in different moments in time. For each group of computations, different types of grids were therefore constructed, characterised either by constant or variable spacing in both Cartesian directions. In all cases, the grid sizings were chosen very conservatively, and a number of criteria were been established, by enforcing scale analysis, in order to achieve the required computational accuracy.

Wall layers. In the near-wall regions, the cell size was chosen so as to have a sufficient number of cells inside the smallest diffusive wall layer. The dimensionless length scale of the latter may be estimated by means of the relations below, which have been derived starting from the scale analyses proposed by Bejan for the cases of a heated wall and of horizontal annulus [3]. For $Pr \ll 1$, the viscous forces balance buoyancy only across a limited portion of the thermal layer, thus creating a thin viscous wall layer. Along the heated surface of the cylinder, one obtains:

$$\delta_{v,s} \approx \left(h \frac{Ra_H}{Pr} \right)^{-\frac{1}{4}} \quad (4.2.1)$$

whilst at the lateral enclosure walls:

$$\delta_{v,w} \approx \left(\frac{h}{2h+1} \frac{Ra_H}{Pr} \right)^{-\frac{1}{4}} \quad (4.2.2)$$

For $Pr \gg 1$, instead, the formation of a viscous layer is driven by the much thinner thermal layer, that ensues fluid motion in the interior of the enclosure. Along the cylinder, the thermal layer scales as:

$$\delta_{T,s} \approx (h Ra_H)^{-\frac{1}{4}} \quad (4.2.3)$$

and at the enclosure walls:

$$\delta_{T,w} \approx \left(\frac{h}{2h+1} Ra_H \right)^{-\frac{1}{4}} \quad (4.2.4)$$

Core regions. As for the internal regions, an approach adopted by Di Piazza and Ciofalo [147] was used as a criterion to determine the order of magnitude of the maximum cell spacing. Since the main goal pursued here is to detect the occurrence of non-linear and, eventually, chaotic dynamical behaviours, the main criterion for the choice of the computational grids is that all relevant (energy-containing) time-dependent flow structures should be properly resolved. This requires the mesh size to be of the same order as the Kolmogorov scale Λ_K of dissipative eddies. This can be expressed [148] as:

$$\Lambda_K \approx \left(\frac{\nu^3}{\varepsilon} \right)^{\frac{1}{4}} \quad (4.2.5)$$

where ε is the rate of turbulent kinetic energy dissipation per unit mass. The total rate of dissipation per unit mass of mechanical energy in the cavity can be viewed as the product of the buoyancy acceleration, scaling as $g\beta\Delta T_{ref}$, by the buoyant velocity, see equation 1.4.15. In fully turbulent flows, *i.e.* in flows presenting high-dimensional chaos, it can be assumed that most of the dissipation occurs through a cascade of turbulent structures. Thus, it is possible to write:

$$\varepsilon \approx (g\beta\Delta T_{ref})^{\frac{3}{2}} H^{\frac{1}{2}} \quad (4.2.6)$$

By substituting equation (4.2.6) for ε into equation (4.2.5) and taking into account the definition of Gr_H , the following expression can be derived for the dimensionless dissipative scale $\delta_k = \Lambda_K/H$:

$$\lambda_K \approx Gr^{-\frac{3}{8}} \quad (4.2.7)$$

which can be used as an estimate of the maximum dimensionless mesh size Δx_i .

Grid	Relative error $\epsilon(\%)$		
n.° of elements	$\bar{N}u_{H,rw}$	f	X
212×212	0.01	0.61	0.45
106×106	0.34	1.57	3.44
53×53	8.71	4.06	26.49
s	4.67	1.37	2.95

Table 4.2: Results of the grid sensitivity analysis for the numerical procedure, $Ra_H = 8 \times 10^4$, $A = 2.5$, $Pr = 0.7$.

For the purposes of the present study, such an estimate appeared to be highly conservative. Therefore, a less restrictive criterion was adopted, namely the one established by Di Piazza and Ciofalo [147], who propose a slightly different result for λ_K :

$$\lambda_K \approx (32\pi\sqrt{2})^{\frac{1}{4}} Gr^{-\frac{3}{8}} \quad (4.2.8)$$

This is based on an alternative definition for the reference velocity U . The two estimates, (4.2.7) and (4.2.8), are the same order of magnitude, and it was assumed that the latter was suitable for the present simulations, either providing enough accuracy and allowing for long-term computations in a relatively short time.

Time discretization. As for the time-step size, the choice of an implicit scheme for the diffusive terms removes the stability constraint on the time-step width. This remains bound to the Courant-Friedrichs-Levy (CFL) condition, which accounts for the stability of the convective term, treated as explicit. At each cycle, the next time-step is computed by calculating the Courant number in each cell:

$$CFL_{i,j} = \frac{\| \mathbf{u}_{i,k} \| \Delta \tilde{t}}{\Delta \tilde{x}} \quad (4.2.9)$$

where Δt is the $(n+1)$ -th time-step, $\Delta x_{i,k}$ the dimensionless cell size, and i, k are the grid indices. The CFL condition implies that:

$$\max(CFL_{i,k}) \leq \tau \quad (4.2.10)$$

where $\tau \leq 1$. Throughout all the analyses, the maximum value of τ adopted was $\tau = 0.5$, *i.e.* half of the minimal constraint on the time step. Such a conservative choice is justified by the need to ensure the stability of the pressure correction computation, which had been recognized to be the less robust phase of the Projection Method employed.

4.3 Grid sensitivity analysis

In order to provide a validation of the computational procedure for the simulation of transitional, time-dependent regimes, a grid sensitivity analysis was carried out by means of Richardson extrapolation [149], for the case $A = 2.5$, $Ra_H = 8 \times 10^4$, $Pr = 0.7$, where the flow regime turned out to be periodic (P), and characterised by a single, well-defined

oscillation frequency. Spatial convergence was examined by taking the average Nusselt number at the right vertical wall of the enclosure as the reference quantity. This is defined as:

$$Nu_{H,rw} = \frac{1}{A} \int_{-\frac{A}{2}}^{\frac{A}{2}} \left(\frac{\partial T}{\partial x} \right)_{x=\frac{A}{2}} dz \quad (4.3.1)$$

To check grid-dependency of unsteady solutions, three alternative indices were tried. These are: the dimensionless fundamental frequency of the system, f ; the oscillation amplitude, X ; and the time-averaged heat flux over one oscillation period, $\bar{N}u_{H,rw}$. For all quantities, the order of convergence s is given by the following equation:

$$s = \frac{\ln \left(\frac{\varphi_3 - \varphi_2}{\varphi_2 - \varphi_1} \right)}{\ln(k)} \quad (4.3.2)$$

where φ is the test quantity, and subscripts 1 to 3 indicate values of the quantity obtained with three grids of constant refinement ratio k , progressively numbered from the finest (1) up to the coarsest (3) [149]. The value of s is used to obtain the Richardson extrapolation of the continuum value (value at zero grid spacing):

$$\varphi_{\Delta x=0} = \varphi_1 + \frac{\varphi_1 - \varphi_2}{k^s - 1} \quad (4.3.3)$$

The relative error ϵ between a discrete solution φ_i , and the continuum value is defined:

$$\epsilon = \left| \frac{\varphi_{\Delta x=0} - \varphi_i}{\varphi_{\Delta x=0}} \right| \quad i = 1, 2, 3 \quad (4.3.4)$$

Results of the analysis are summarized in Table 4.2. The finest (212×212) grid was halved once and twice ($k = 2$), while the Courant condition was inversely restricted, to keep the same time-step adaption rule throughout the different computation.

It is pointed out that even the coarsest grid (53×53) correctly captured the periodic nature of the flow, although the solution was affected by severe quantitative errors. From Table 4.2, the oscillation amplitude, X , emerges as the most grid-sensitive of the three indices. The small relative errors produced by the finest grid support the adoption of over-refined grids of that size, to ensure a satisfactory accuracy in the prediction of the asymptotic flows. Moreover, second-order accuracy of the computational method is assessed by the values of the order of convergence s reported in Table 4.2.

4.4 Overview of the simulations

Table 4.3 provides a summary of the simulations performed for the present work. Four different values of the Prandtl number, $Pr = 0.07, 0.7, 7, 70$, are considered. Those values are intended to be representative of liquid metals, air, water and oils, respectively. Four values of the aspect ratio A are considered as well, as reported in Table 4.3. For each of the 16 (Pr, A) couples, numerical predictions were carried out for values of the Rayleigh number encompassing the range $0 < Ra_H < Ra_{H,max}$. Such a range also includes the values of Ra_q considered to investigate the effect of the uniform heat flux condition at the source wall.

A	d	h	R	$Ra_{H,max}$	
				$Pr = 0.7$	$Pr = 0.07, 7, 70$
2.5	0.2	2	5	8×10^5	10^4
3.3	0.4	0.75	2.5	2.11×10^6	10^4
5	0.6	0.3	1.6	1.852×10^5	10^4
10	0.8	0.125	1.25	2.1×10^4	10^4

Table 4.3: Summary of the parameter ranges investigated

It shall be noted that a major part of the analyses, and especially of those aimed at detecting supercritical transitional behaviours, were performed for $Pr = 0.7$, which corresponds to air at environmental conditions. Such a choice is well justified, both from a theoretical and practical standpoint: on one hand, because, as reported in Section 4.2, the temporal and spatial scales of the thermal and viscous wall layers do not differ much one from the other [3], thus yielding flows whose character is simpler to identify; on the other hand, because air (and gases in general) is the working fluid in a relevant part of the possible applications involving natural convection as the main heat transfer mode. For this reason, the values of $Ra_{H,max}$ listed in Table 4.3 are higher for $Pr = 0.7$ than for the other Pr -values.

Each run was initialized either with a pseudo-diffusive temperature and flow field, as obtained by a preliminary simulation, or with a zero-field initialization. All the simulations were protracted either until the steady-state or, when unsteady flows were detected, until the system completed a sufficient number of time steps so as to allow the asymptotic flow character to be identified. The stop criterion for steady-state was based on the absolute residual ϱ , defined as:

$$\varrho(\varphi) = \frac{\sum_{i,k} |\varphi_{i,k}^{n+1} - \varphi_{i,k}^n| V_{i,k}}{\sum_{i,k} V_{i,k}} \quad (4.4.1)$$

where φ represents the generic variable, and $V_{i,k}$ is the volume of the cell (i,k) . The simulations were stopped when the residuals of all variables were less than 10^{-8} .

Time histories of the dimensionless temperature T , and the velocity components along x and z directions, were tracked for several locations within the enclosure. Values of the variables were interpolated from adjacent cell centers, and time series were resampled with a constant time step, in order to use discrete Fourier transforms for time series analysis. Thanks to the high degree of spatial and temporal resolution adopted for the computations, this double resampling operation is intended to avoid the data to be altered during post-processing. The time evolution of the average Nusselt number at the enclosure and source walls was also recorded. The averaged quantities were obtained by means of second order quadrature of the local values at the intersection nodes between the boundary segments and the Cartesian grids.

4.5 Results and discussion

The main results of the analysis are presented in the sequence: flow and temperature patterns for $Pr = 0.7$ are described first, focusing on the influence of the aspect ratio A ;

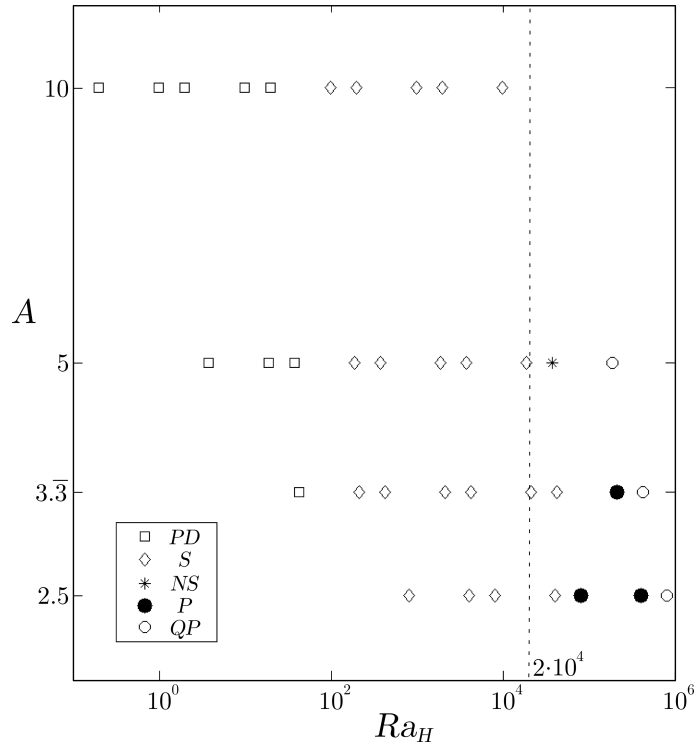


Figure 4.2: Overview of asymptotic flow regimes for $Pr = 0.7$ in the (Ra_H, A) plane.

the effect of the thermal boundary condition at the source walls is discussed, for the same value of Pr ; the influence of the third parameter, Pr , is finally envisaged, thus completing the general characterisation of the case.

The end section is dedicated to the analysis of the heat transfer performance of the system for steady regimes. A general heat transfer correlation is derived, encompassing the effect of the Rayleigh and Prandtl numbers, and the aspect ratio.

4.5.1 Steady-state regimes and transitional behaviour for $Pr = 0.7$

A qualitative overview of the long-term scenarios encountered for $Pr = 0.7$ is given in the chart of Figure 4.2. Such a diagram was carried out after a first group of simulations had been performed on the case. The labeling of different flow regimes follows the systematic of buoyant flows brought forth in Section 2.1.3. Results indicate that transitions of various type occur for different values of A . As it might have been expected, the geometry is found to have a crucial effect on the transition patterns and on the character of the supercritical flow regimes. This is particularly evident when comparing results for $A = 3.3$ and $A = 5$. In the former case, a periodic regime is encountered after the first critical Ra_H -value, then followed by a more complex flow. For $A = 5$, on the contrary, a steady non-symmetric configuration preceeds the transition to unsteady flow. Figure 4.2 bears evidence that, consistently, the minimum gap between the confining walls and the source, H , is the significant length of the problem, in that:

- (i.) it characterises the regions of potentially maximum temperature gradients;
- (ii.) the lateral gaps, where no stability constraint exists, are the initial flow promoters;

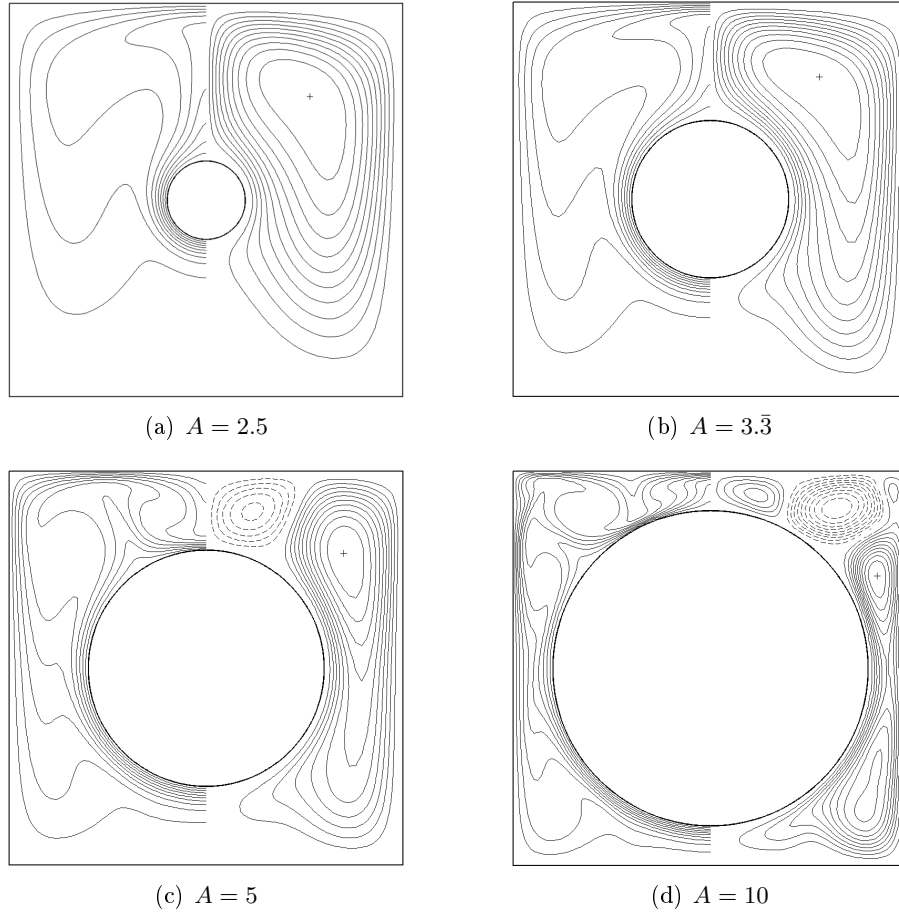


Figure 4.3: Isotherms ($0.1 \leq T \leq 0.9$) (left) and streamlines (right) of the *S*-type flow for four A -values, and for $Ra_H = 2 \times 10^4$.

- (iii.) the upper gap is a site of unstable thermal stratification;
- (iv). the regions associated with different long-term flow regimes are fairly aligned on the Ra_H -axis.

Results in Figure 4.2, allow a common threshold for steady-state regimes to be broadly identified. As a conservative estimate, the limit below which the asymptotic flow regimes can be assumed to be stable steady-state (*S*) is $Ra_H \leq 2 \times 10^4$, for $A \geq 2.5$.

Pseudo-diffusive and steady-state flows

For all the A -values, and for sufficiently low Ra_H , a purely diffusive thermal field and a very weak double-cell circulation is found, corresponding to a pseudo-diffusive flow (*PD*). The flow is generated within the lateral gaps and propagates throughout the domain by viscous shear, as documented by the symmetry of the circulation cells towards the horizontal midplane. Fluid velocity remains however too low for the temperature distribution to be affected, and the thermal field does not deviate from a purely conductive one.

At higher Rayleigh numbers, laminar steady-state convection prevails. Figure 4.3

demonstrates the influence of geometry on the general flow patterns and the thermal fields at steady-state. For each A -value, this Ra_H -value was elected as a first guess stability threshold, common to all A -values, $Ra_H = 2 \times 10^4$.

As reported by either Moukalled and Acharya [128] or Shu and Zhu [124], lower A -ratios (Figures 4.3(a) and 4.3(b)) exhibit a common structure, characterized by the presence of a vertical thermal plume rising from the cylinder top and impacting the upper side of the cavity, with two big symmetrical and counter-rotating vortices dragging upwards fresh air from the bulk of fluid placed below the cylinder. The flow radically changes when increasing A up to $A = 5$ (Figure 4.3(c)): in place of a single thermal plume, two smaller lateral plumes are now formed, while the fluid above the cylinder remains colder. The main circulations are pushed aside by the birth of two small counter-rotating secondary cells, which provide heat removal from the cylinder top. The above observations agree with previous findings in [128, 124].

For $A = 10$, the flow field becomes even more complex (Figure 4.3(d)). The interchanges between the upper and the lower part of the cavity are strongly reduced. This is due to the development of a co-rotating cell in the lower part of the enclosure, while complex four-cell architectures appear in the upper part of the cavity. Besides the twin thermal plumes already observed for $A = 5$, the thermal boundary layer along the cylinder surface is perturbed in three more points: two small symmetrical temperature lumps are present just below the lateral gap narrowing, and a short plume reappears at the top of the cylinder. The former are due to a partial detachment of the main vortices, forced by the reduced space beside the cylinder at $\theta = 0$. As a secondary effect, the circulation below the cylinder is strengthened. The latter effect is linked to the formation of a tertiary pair of cells above the cylinder, pushing aside the secondary vortices. Two smaller co-rotating vortices also appear at the upper corners of the enclosure.

Transition scenarios

When Ra_H is increased up to values high enough to break the steady symmetric patterns, substantial differences in the behaviour of the four geometrical configurations appear. For $A = 2.5$, the first transition is characterised by the occurrence of a supercritical Hopf bifurcation. For $Ra_H = 8 \times 10^4$ the flow is periodic (P). The power spectrum of the average Nusselt number at the enclosure upper wall exhibits a very neat peak at a dimensionless frequency $f = 0.667$.

Figure 4.4 reports a general description of the convective dynamics inside the cavity for $Ra_H = 2 \times 10^5$. Figure 4.4(b) and 4.4(c) show the numerical attractors describing the system dynamics in points $(0, 0.5)$ and $(0.5, 0)$, respectively. Both attractors show the existence of a well defined and closed two-period limit cycle, which can be assumed to represent the high amplitude-low frequency dynamical patterns. Moreover, the attractor present smaller scale and higher frequency ripples. These ripples can be observed clearly in Figure 4.4(b), but are less evident in Figure 4.4(c). This is only marginally due to the different angle chosen for the projection of the plots, whilst it depends mainly on the different positioning of the two observation points, and, hence, on the relative importance of the low and high frequency dynamics in different locations of the domain.

The system dynamics for $Ra_H = 2 \times 10^5$, $A = 2.5$ can thus be identified as periodic, the oscillating flow corresponding to the regular swaying motion of the central plume with respect to the vertical mid-plane. Such a periodic nature is confirmed by the analysis in

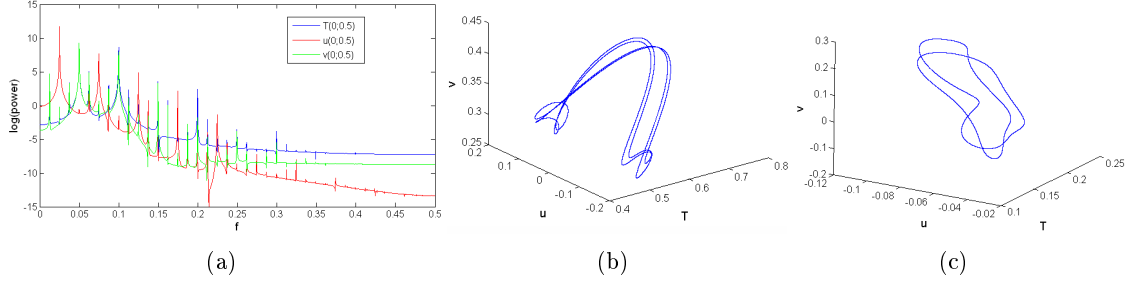


Figure 4.4: Numerical results for $A = 2.5$, $Ra_H = 2 \times 10^5$: (a) power spectral density; 3D attractor in phase space $T-u_x-u_z$ (referred to as $T-u-v$) at: (b) $(0, 0.5)$; (c) $(0.5, 0)$.

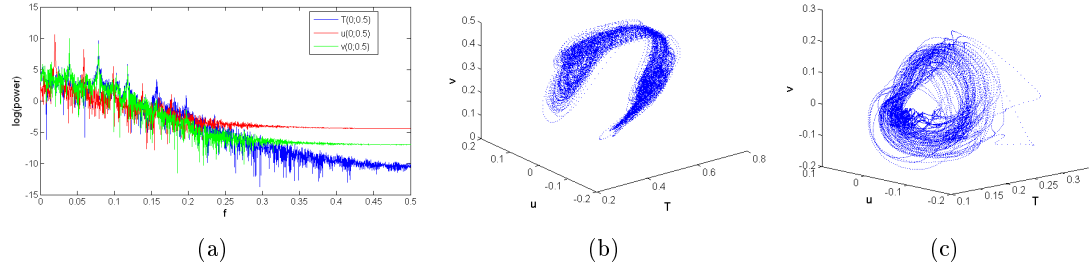


Figure 4.5: Numerical results for $A = 2.5$, $Ra_H = 4 \times 10^5$: (a) power spectral density; 3D attractor in phase space $T-u_x-u_z$ (referred to as $T-u-v$) at: (b) $(0, 0.5)$; (c) $(0.5, 0)$.

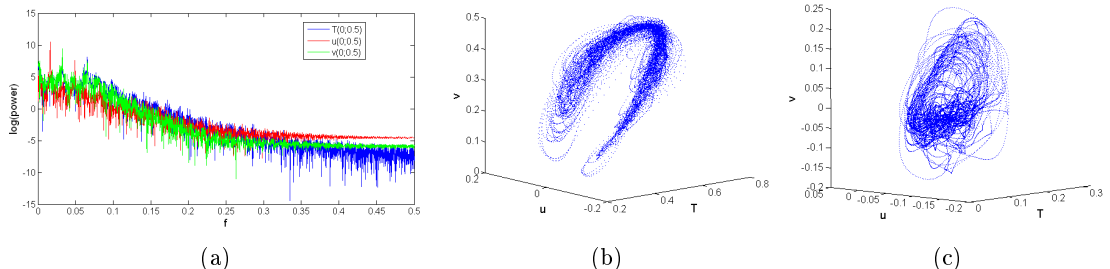


Figure 4.6: Numerical results for $A = 2.5$, $Ra_H = 6 \times 10^5$: (a) power spectral density; 3D attractor in phase space $T-u_x-u_z$ (referred to as $T-u-v$) at: (b) $(0, 0.5)$; (c) $(0.5, 0)$.

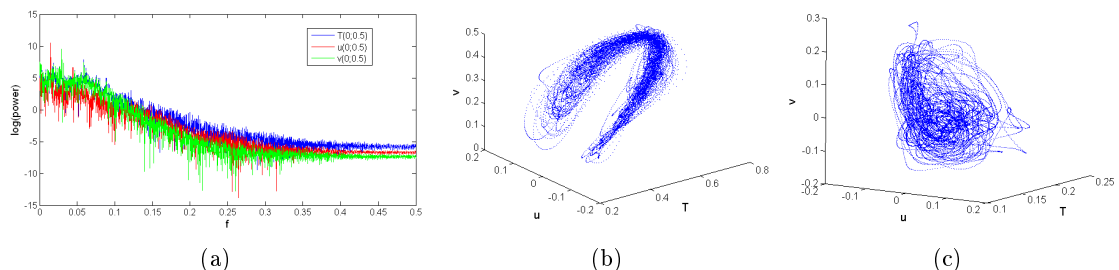


Figure 4.7: Numerical results for $A = 2.5$, $Ra_H = 8 \times 10^5$: (a) power spectral density; 3D attractor in state space $T-u_x-u_z$ (referred to as $T-u-v$) at: (b) $(0, 0.5)$; (c) $(0.5, 0)$.

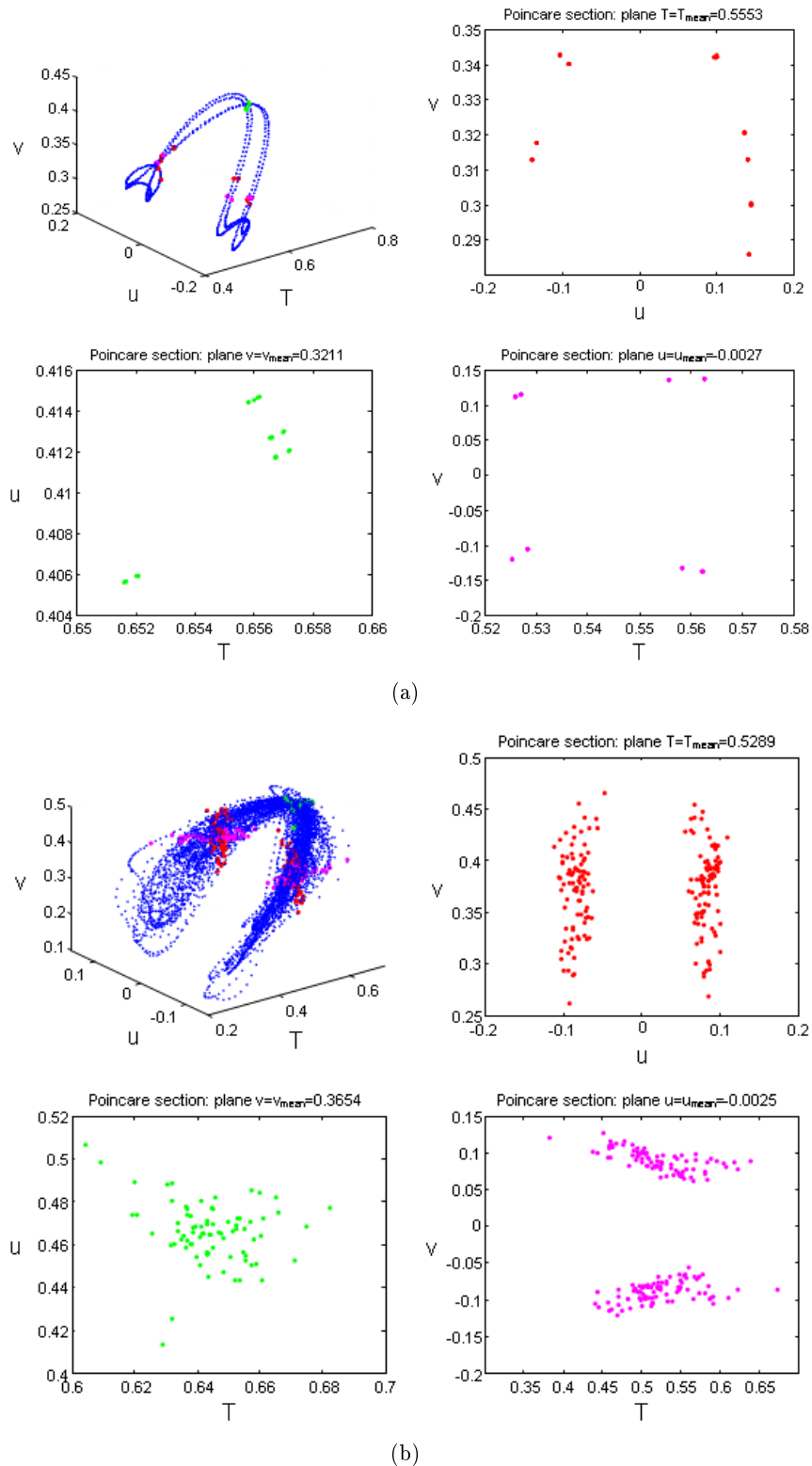


Figure 4.8: Poincaré maps $(0, 0.5)$ at point for $A = 2.5$ and: (a) $Ra_H = 2 \times 10^5$; (b) $Ra_H = 8 \times 10^5$

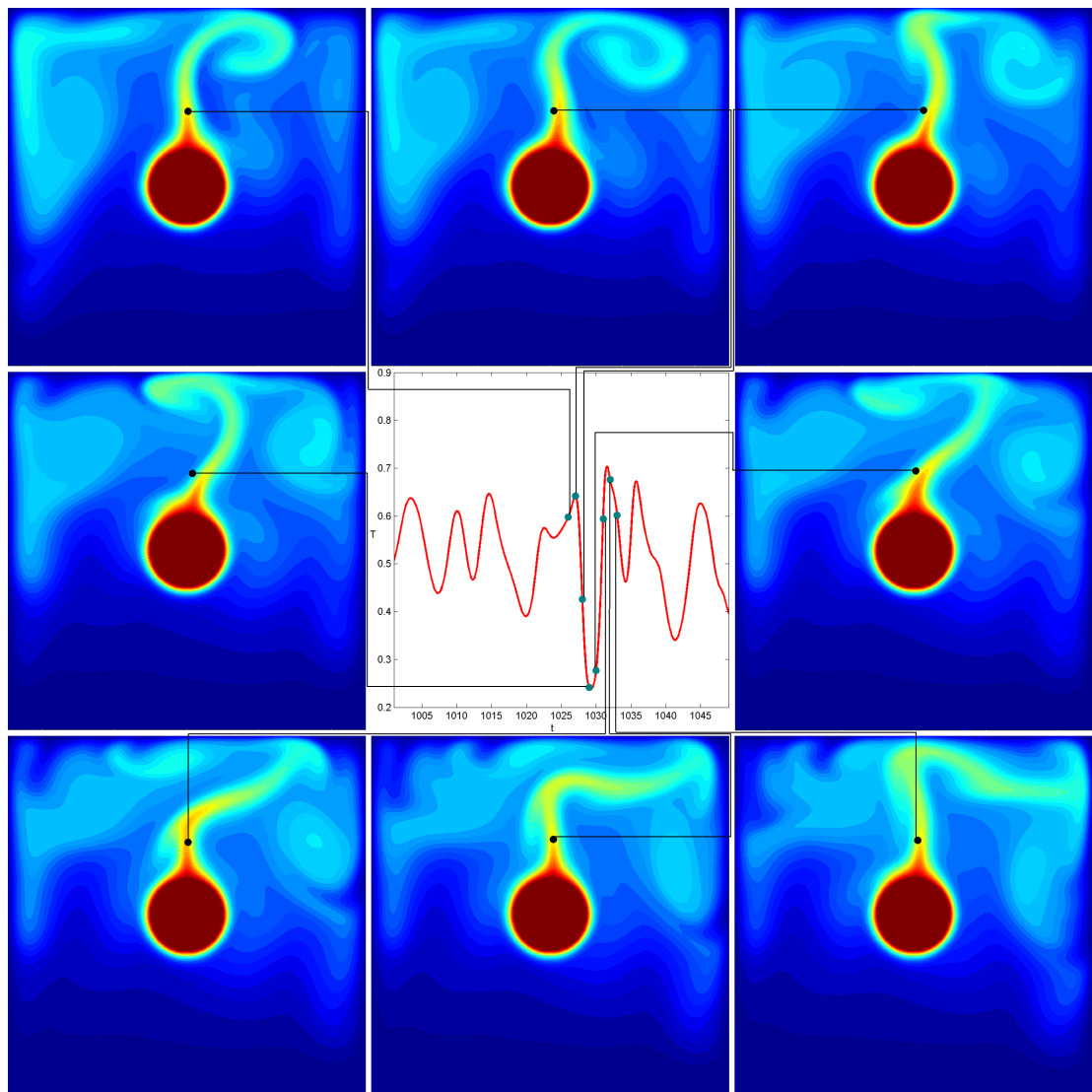


Figure 4.9: Sequence of isotherm contours associated with the time series of $T(0, 0.5)$ for $A = 2.5$, $Ra_H = 8 \times 10^5$.

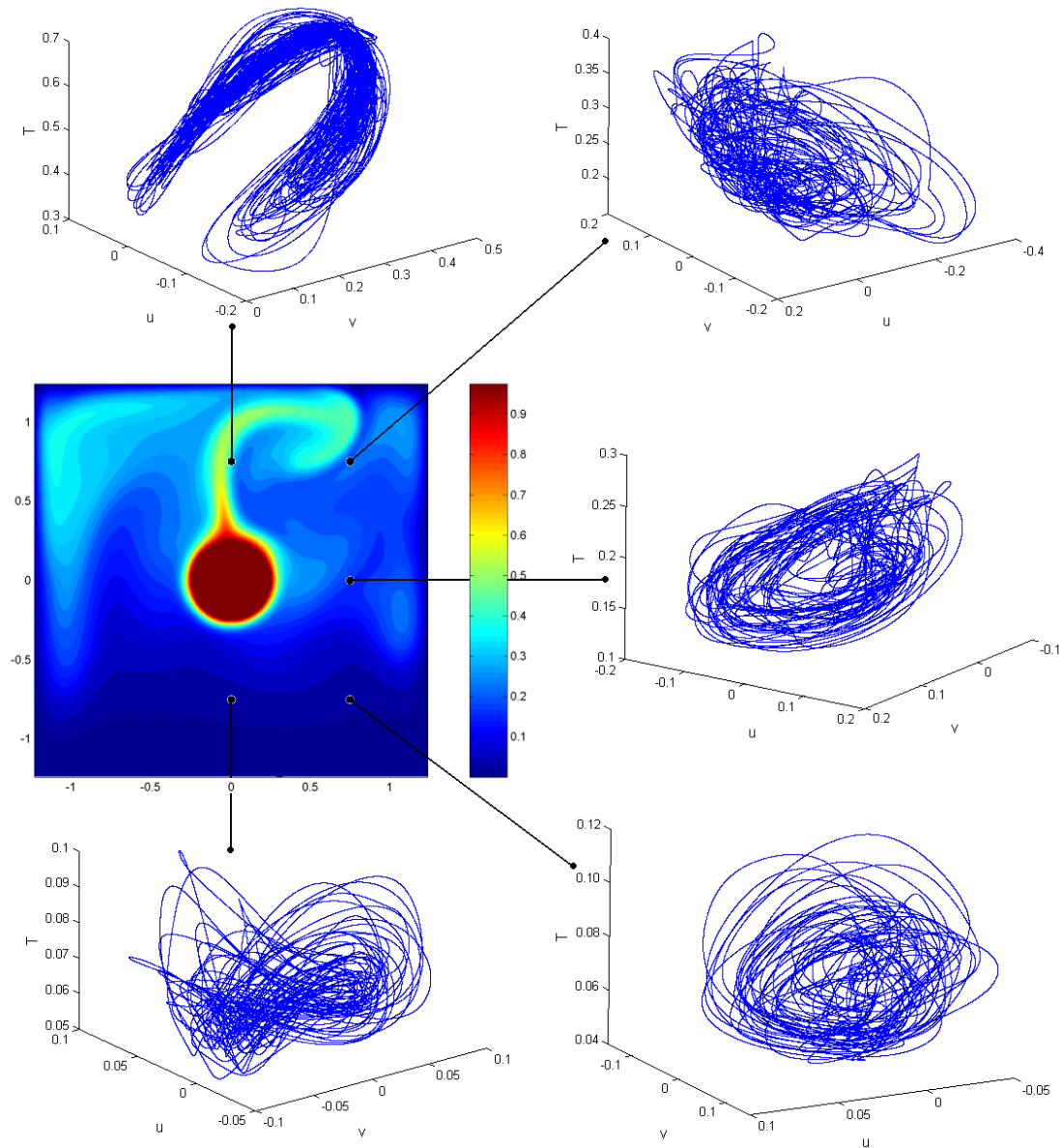


Figure 4.10: Visualization of 3D attractors in phase space $T-u_x-u_z$ (referred to as $T-u-v$) at various locations, for $A = 2.5$, $Ra_H = 8 \times 10^5$.

the frequency domain. In fact, power spectra of the variables T , u_x and u_z at the location $(0, 0.5)$, displayed in Figure 4.4(a), show a typical periodic behaviour. It is observed that the spectra of T and u_z are almost overlapped in the low frequency range, where the dominant dynamical features are contained; this is in fair accordance with the observation of almost parallel trajectories describing the corresponding limit cycle in the phase space $T-u_x-u_z$, as reported in Figure 4.4(b). On the other hand, the power spectrum of the horizontal velocity u_x at $(0, 0.5)$ is characterised by a higher amplitude and a lower dominant frequency, with respect to the other two variables. This means that the oscillation of the plume in the horizontal direction indeed represents the main dominant pattern, from a dynamical standpoint. Moreover, the dynamics of the three variables being interrelated with each other, the harmonics and sub-harmonics of the dominant frequencies detected in power spectra are reciprocally bound by rational ratios.

The effect of increasing the Rayleigh number can be observed by spanning Figure 4.5 to Figure 4.7. In particular, it can be inferred that the periodic flow detected for $Ra_H = 2 \times 10^5$, and illustrated in Figure 4.4, bifurcates to a quasi-periodic flow at $Ra_H = 4 \times 10^5$.

By comparing Figure 4.4 and Figure 4.5, it is possible to observe a broadening of the range of the excited frequencies in the power spectra of the three variables, where, nevertheless, dominant features can be still singled out. This is due to the raising of frequency bands, typical of quasi-periodic dynamics (*QP*), revealing that the motion is driven by incommensurate frequencies. The presence of rationally independent frequencies in the spectrum is reflected by the higher complexity of the quasi-periodic attractors at points $(0, 0.5)$ and $(0.5, 0)$, each of them generated by an open trajectory lying on a torus in phase space. Coherently, dense regions of trajectories are visible in Figures 4.5(b) and 4.5(c).

The numerical attractors as well as the power spectra obtained for $Ra_H = 6 \times 10^5$ (Figure 4.6) are, in general, comparable with those reported for $Ra_H = 4 \times 10^5$, although they show a further broadening of the quasi-periodic frequency sidebands occurs, as well as a slight increase in the attractor complexity.

Finally, the system behaviour at $Ra_H = 8 \times 10^5$ (Figure 4.7) can be considered as a limiting case of quasi-periodic dynamics; in fact, such a case is characterised by a broadband power spectrum where the frequency bands of the quasi-periodic flow can be hardly distinguished from the background. In other words, a further increase in the Rayleigh number is expected to cause a transition to a different kind of dynamical behaviour. In particular, an occasional spreading of trajectories can be observed already at $Ra_H = 8 \times 10^5$. This indicates that chaotic dynamics are likely to appear when increasing Ra_H further, possibly determining an enlargement of the phase space region occupied by the attractor (*i.e.* of the attractor global dimension) and the spreading of the attractor trajectories within this region.

Poincaré maps were also used to analyze the system dynamics for $A = 2.5$. In Figure 4.8, maps obtained by sectioning the attractors with the planes at the average values of T , u_x and u_z are shown for $Ra_H = 2 \times 10^5$ (Figure 4.8(a)) and $Ra_H = 8 \times 10^5$ (Figure 4.8(b)), respectively. The above considerations are corroborated by the observation of the maps. In fact, it is seen that for $Ra_H = 2 \times 10^5$ (Figure 4.8(a)), *i.e.* when flow is periodic, the points in the map are generated by the intersections of the stable limit cycle with the sectioning planes. On the contrary, for $Ra_H = 8 \times 10^5$ (Figure 4.8(b)), dense and aligned groups of points form the Poincaré sections, due to the higher complexity of the attractor. Such a finding is consistent with the above interpretation of the case, for which the dynamics are

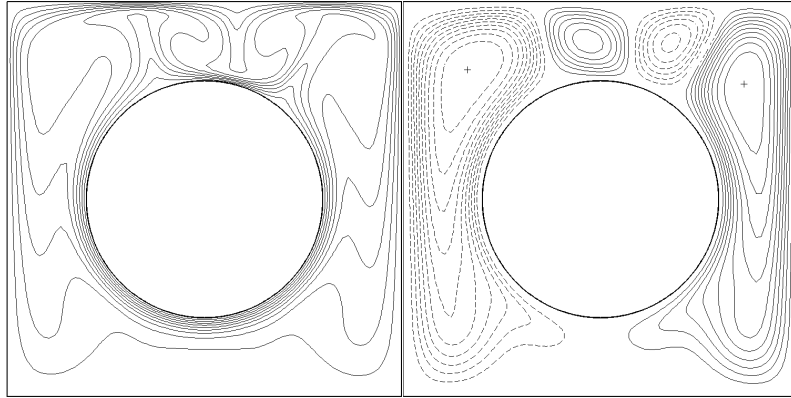


Figure 4.11: Isotherms ($0.1 \leq T \leq 0.9$) (left) and streamlines (right) of the NS -type flow for $A = 5$ and $Ra_H = 3.704 \times 10^4$.

deemed to be around the limit between quasi-periodic flow (QP) and chaotic flow (N).

Finally, the phenomenology of the case $Ra_H = 8 \times 10^5$ can be appreciated in Figure 4.9, where a sequence of instantaneous snapshots of the temperature fields over one oscillation are associated with the time series of temperature T at the point $(0, 0.5)$, and in Figure 4.10, where five different attractors are visualized in the phase space formed by T , u_x and u_z are depicted.

All in all, it is important to note, that the overall scenario depicted insofar stands in satisfactory agreement with the results reported by Desrayaud and Lauriat for the case of very small cylinders and horizontal line heat sources immersed in air-filled rectangular vessels [134, 136].

The transition scenario remains similar for $A = 3.3$, where the first unsteady flow is predicted to occur for a slightly higher value of Ra_H . Instead, the route to unsteadiness is radically different for $A = 5$. At $Ra_H = 3.704 \times 10^4$, the long-term prediction is still steady-state, but non-symmetric (NS), as shown in Figure 4.11. The transient behaviour of this case was monitored by a frame-by-frame display and a time-series analysis, leading to the conclusion that the non-symmetric pattern is formed by the progressive degeneration of a symmetric unstable configuration, through which the solution invariably passes. This symmetry-breaking pattern is typical of pitchfork bifurcations. Such an occurrence is not uncommon in confined buoyant flows [134].

For $Ra_H = 1.852 \times 10^5$, the circulation within the cavity becomes unsteady, and exhibits a multiple periodicity. Figure 4.12 reports time-series for the average Nusselt number based on D , Nu_D , on the two vertical sides of the cavity: the two quantities are found to oscillate around different time-averaged values. This seems to indicate that the periodic flow originates from one of the branches of the above pitchfork bifurcation. In particular, the case shown in Figure 4.12 falls on the same branch of the non-symmetric steady solution in Figure 4.11. An asymptotic time-averaged solution is likely to lie upon it, as demonstrated by Desrayaud and Lauriat [134] for an enclosed line source. In that case a pitchfork branching was found to be followed by a subcritical Hopf bifurcation.

For $A = 10$ the solution strays from a symmetric steady-state configuration only for 2×10^4 , where a non-symmetric (NS) flow is detected, much similar to that depicted in Figure 4.11.

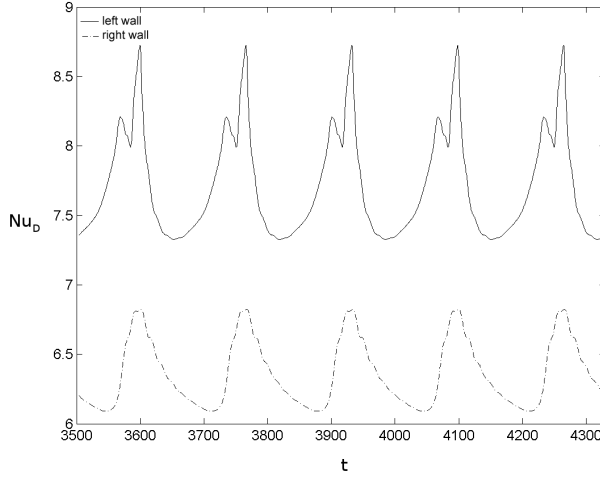


Figure 4.12: Time histories of the average Nusselt number, Nu_D , at the left and right walls: $A = 5$ and $Ra_H = 1.852 \times 10^5$

The issue of flow transition for the present geometry had not been discussed in previous work [124, 128, 129]. However, an estimate of the critical Ra-value can be inferred from Desrayaud and Lauriat [134], who detected a supercritical Hopf bifurcation at $Ra_L = 1.5 \div 1.6 \times 10^6$, for a line heat source centred in a square cavity. For the smallest cylinder size considered here, *i.e.* for $A = 2.5$, the first Ra_H -value associated with a periodic flow corresponds to $Ra_L = 1.25 \times 10^6$. Such a value compares very favourably with the stability threshold in [134], in view of the significant differences in the source size and the thermal boundary conditions at the enclosure walls.

It can also be inferred that, between $A = 3\bar{.}3$ and $A = 5$, a critical A -value exists, marking the passage between two different transition modes, one characterised by the oscillation of the thermal plume above the cylindrical source, and by a cascade of Hopf bifurcations, with the occasional appearance of intermittency, and the other characterised by the formation of Rayleigh-Bénard rolls in the region above the cylindrical source, which undergo a symmetry-breaking process before an oscillatory motion sets on.

A	Isothermal		Isoflux	
	Ra_H	Flow regime	Ra_{qH}	Flow regime
2.5	8×10^4	Periodic	4×10^5	Periodic
3.3	2.11×10^5	Periodic	4.2×10^5	Periodic
5	3.704×10^4	Non-symmetric	-	-
10	2×10^4	Non-symmetric	-	-

Table 4.4: Breaking of the steady symmetric patterns: Ra_H -values and flow regimes encountered for each A -value and for both the isothermal and iso flux case.

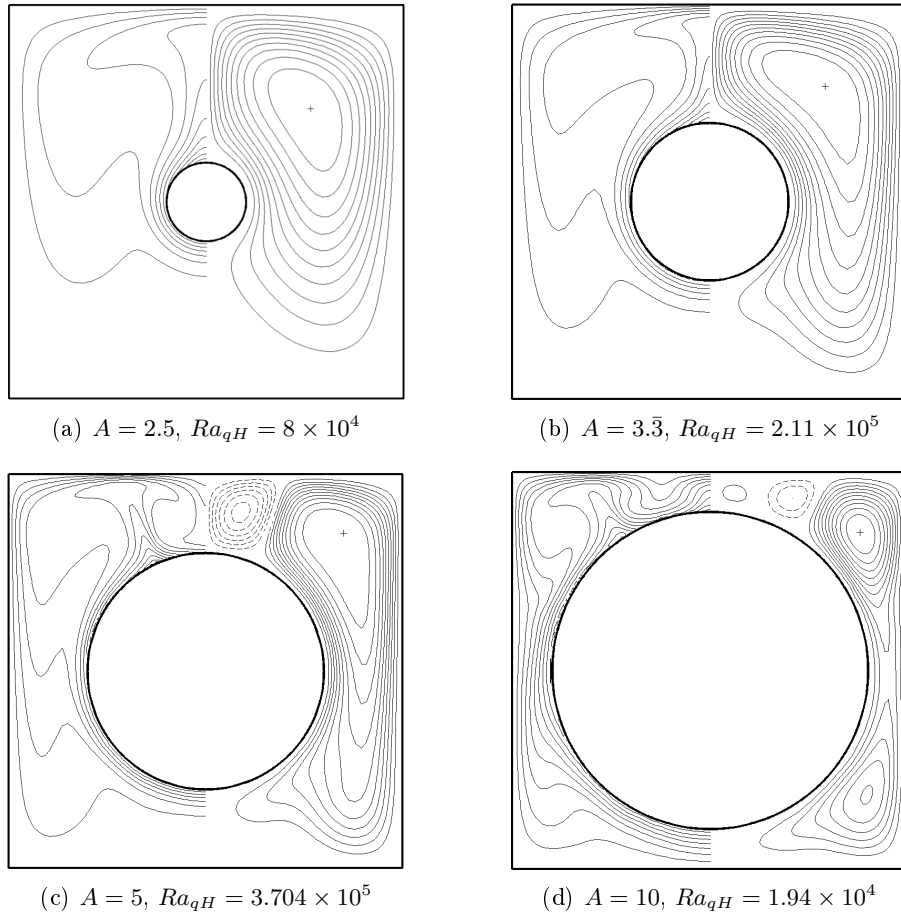


Figure 4.13: Isotherms ($0.1 \leq T \leq 0.9$ (left) and streamlines (right) of the S -type flow for four A -values, and for $Ra_{qH} = 2 \times 10^4$.

Effect of the thermal condition at the cylinder wall

For the four A -values considered here, and $Pr = 0.7$, additional computations were carried out in order to clarify the influence of the imposition of the two different boundary conditions on the cylinder surface, namely condition T and Q .

Figure 4.13 reports a snapshot of the temperature fields and the streamlines obtained in the isoflux case, for all A -values considered, and the maximum Ra_{qH} for which a steady symmetric thermal-flow asset was found. By comparing Figure 4.13 with its counterpart for the isothermal case 4.3, one may observe that the flow and thermal characters at steady-state are rather insensitive to the boundary condition imposed.

The values of Ra_{qH} at which transitional regimes were detected, are listed in Table 4.4. As in the isothermal case, for $A = 2.5$ and $A = 3.\bar{3}$, unsteady periodic flows are encountered. It should however be noted that the estimate of the critical Rayleigh number shifts upwards either when passing from $A = 2.5$ to $A = 3.\bar{3}$, or from the isothermal to the isoflux case.

For the two ratios $A = 5$ and $A = 10$, in the range of Ra_{qH} considered, none of the computations carried out under isoflux conditions revealed the occurrence of transitional

characteristics.

4.5.2 Influence of the Prandtl number

The results of the above data collection considered the variation of two of the three governing parameters of the problem under consideration, thus fixing the third parameter, Pr . Numerical results are presented in the following, for four values of the Prandtl number, namely $Pr = 0.07, 0.7, 7, 70$. Those values are intended to be representative of liquid metals, water, air and oils, respectively. For each of the 16 (Pr, A) couples, numerical predictions are carried out for the four values of the Rayleigh number $Ra_H = 10, 10^2, 10^3, 10^4$. The range of Ra_H -values covered by the analysis is entirely contained within the stability threshold proposed above for $Pr = 0.7$, $Ra_H \approx 2 \times 10^4$.

Steady flows and transitional behaviours

In all the simulations carried out for $A = 2.5$, a steady symmetric thermal-flow asset was found. For that geometry, the dependence of the asymptotic state on both Ra_H and Pr is portrayed in Figure 4.14. The *PD-S* transition for increasing Ra_H is recovered for all the four Pr -values considered, although the way in which this passage occurs for the case $Pr = 0.07$ is quite different from the one common to higher values of the Prandtl number. In the former case, by increasing Ra from 10^2 to 10^3 , the main recirculation is constrained in the lower part of the enclosure, whilst the inversely stratified bulk of fluid occupying the gap between the cylinder and the top wall remains substantially motionless. For $Ra_H = 10^4$, instead, the fluid dragged upwards along the heated sides of the cylinder has entrained such a layer, and a typical convection plume develops in the upper part of the cavity. For $Pr = 0.7$ and higher, the transition to steady laminar convection is much smoother, and the sole effect of increasing Pr is a slight shift upwards of the center of the lung-shaped side eddies (Figure 4.14).

For $A = 3.3$, the main flow characteristics are very similar to those observed for $A = 2.5$.

For A -values higher than $A = 2.5$, unsteady flows were encountered for $Pr = 0.07$, while for $Pr = 0.7, 7, 70$, the predicted flows evolve asymptotically to a fixed-point solution. Exemplary snapshots of the steady-state solutions are reported in Figure 4.15. Differences between the flow characters at $Ra_H = 10^4$, $Pr = 0.7$ and $Pr = 7$ can be appreciated in Figure 4.15(a) and 4.15(b), for $A = 5$. In the first case (Figure 4.15(a)), heat is removed from the top of the cylinder by a pair of secondary, Rayleigh-Bénard-like rolls, which push aside the main lateral circulations; consequently, a pair of symmetric plumes rise from the upper half of the cylinder, at $\theta \simeq \pi/4$. For $Pr = 7$ (Figure 4.15(b)), instead, the rolls disappear, and a single plume is formed on the top of the cylinder. This suggests the possible occurrence of a pitchfork bifurcation for increasing Pr , with the critical Pr -value ranging between $Pr = 0.7$ and $Pr = 7$.

A similar scenario is reproduced also for $A = 10$ (Figure 4.15(c) and 4.15(d)). The streamlines and isotherms for $Pr = 0.7$ are analogous to those reported in Figure 4.3(d), the circulation inside the enclosure consisting in a set of counter-rotating rolls in the upper part, and in a pair of slower, co-rotating cells along the sidewalls. When Pr is increased to $Pr = 7$, the rolls above the cylinder do not subside this time, but they reduce in number, from 4 to 2.

All the simulations performed for $Ra_H \leq 10^4$ and $0.7 \leq Pr \leq 70$ approached a steady symmetric flow configuration. This supports the idea that the overall stability threshold

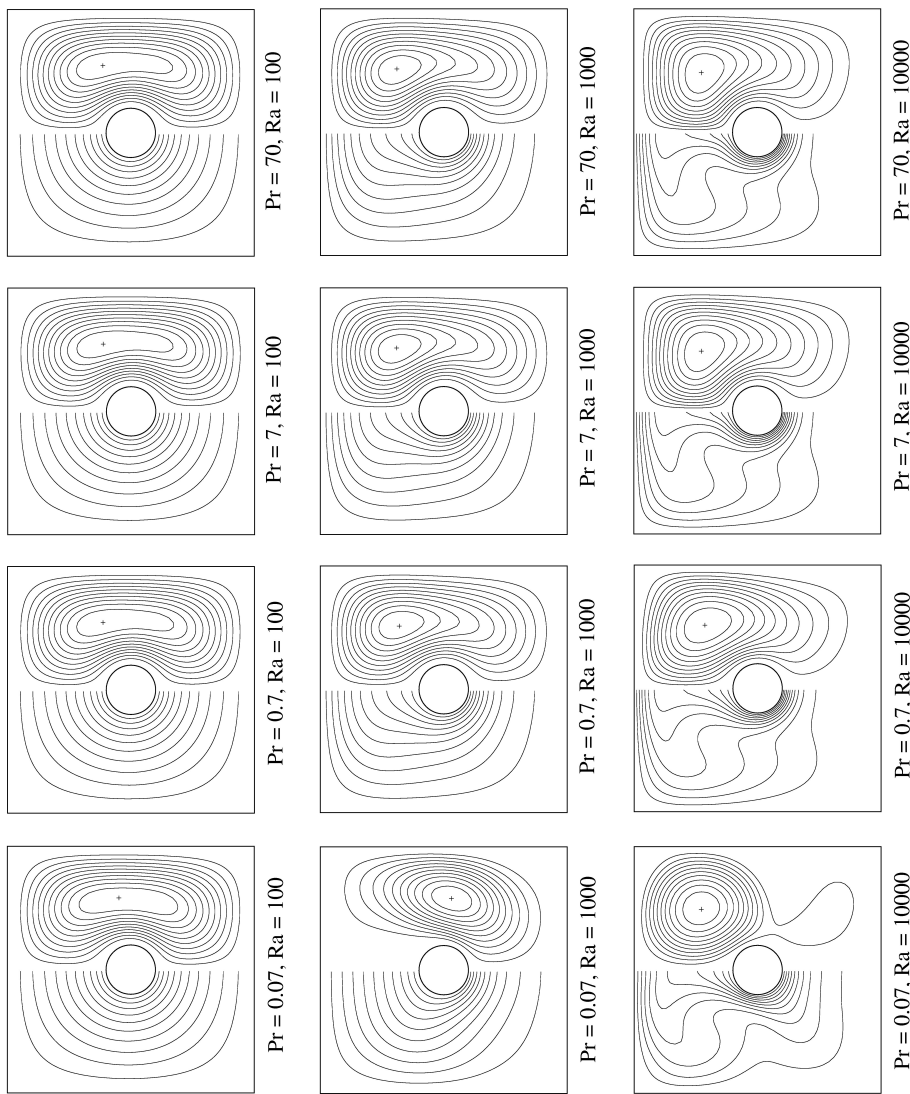


Figure 4.14: Isotherms (left) and streamlines (right) for 12 different cases at $A = 2.5$. Values of Pr and Ra are reported below each subplot. The (+) sign indicates the maximum for the positive streamfunction.

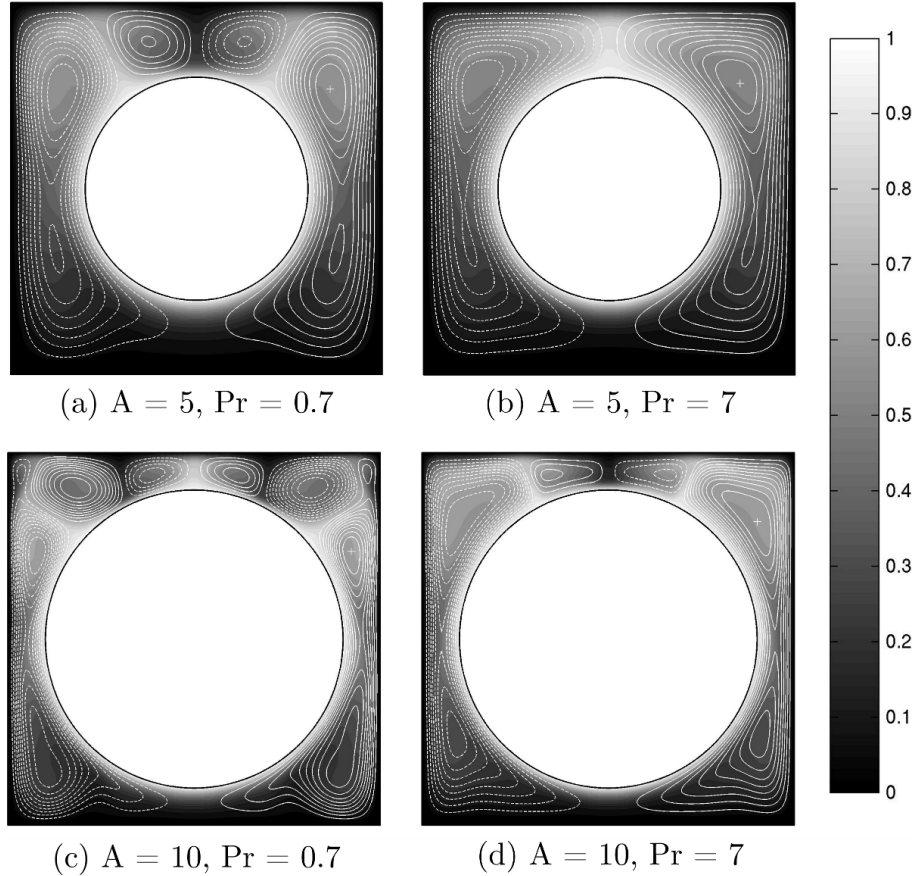


Figure 4.15: Isotherm contours (in grayscales) and streamlines (in white) for $A = 5, 10$ and $Pr = 0.7, 7$, $Ra_H = 10^4$. The (+) sign indicates the maximum for the positive streamfunction.

proposed for air ($Ra_H = 2 \times 10^4$) can be extended to the case of water and oils with reasonable confidence.

The case $Pr = 0.07$ differs from any other on all aspects, since, in fact, unsteady flows are observed for all A -values, excepted $A = 2.5$. For $A = 3.3$, a single-frequency periodic flow is already encountered at $Ra_H = 10^3$, with a dimensionless period $T = 15.95$. In Figure 4.16, the time-averaged flow and temperature patterns over one cycle are reported. Such patterns are quite similar to those depicted in Figure 4.14 for $A = 2.5$ and the same Ra_H - and Pr -values; in this case, however, the main circulation partially entrains the stagnating, unstably stratified layer of fluid over the cylinder top. Quite interestingly, the two circulation cells are found to oscillate along the z -direction, whilst the vertical symmetry is preserved. Such a behaviour is completely different from the one observed in the case $Pr = 0.7$, where, for $A \leq 3.3$, the transition dynamics were dominated by the vertical thermal plume developed above the heat source.

For $A = 0.125$ and $Ra_H = 10^3$, and for $A = 3.3, 5, 10$ and $Ra_H = 10^4$, more complex unsteady flow patterns are observed, whose common character is the presence of multiple co-rotating, oscillating cells.

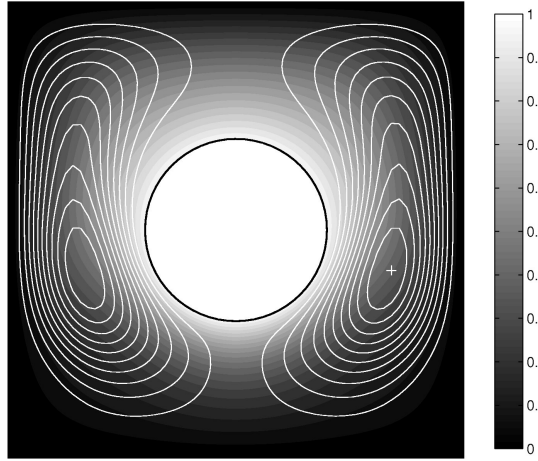


Figure 4.16: Time-averaged isotherm contours (in grayscales) and streamlines (in white) within a single oscillation period, for $A = 3.3$, $Pr = 0.07$, $Ra_H = 10^3$. The (+) sign indicates the maximum for the positive streamfunction.

Asymptotic time scales

In Figure 4.17, the dimensionless times $t_{a,T}$ and $t_{a,u}$, are shown, for which, respectively, the temperature and velocity fields invariably reach a steady-state. With reference to equation (4.4.1), the two quantities $t_{a,T}$ and $t_{a,u}$ are defined as follows:

$$\varrho(T) \leq 10^{-8} \text{ for } t \geq t_{a,T} \quad \varrho(\mathbf{u}) \leq 10^{-8} \text{ for } t \geq t_{a,u} \quad (4.5.1)$$

The dependence of such quantities on Pr and Ra_H and on the aspect ratio is spotted in a multiple scatter plot. The aspect ratio h was employed in place of A for the visualization of the results.

From the graph, the overall influence of h comes out to be marginal, while it appears clearly that both $t_{a,T}$ and $t_{a,u}$ depend primarily on the Rayleigh number. As it could be anticipated heuristically, both increase with increasing Ra_H , and this dependence of the asymptotic time scales with Ra_H coherently follows the scaling result of Patterson and Imberger [64]. For a vertical enclosure, they predicted a relationship of the type:

$$t_a \approx 0.1 Ra_H^{\frac{1}{2}} \quad (4.5.2)$$

The $Ra_H^{1/2}$ dependence is fairly in accordance with the trends of the data in Figure 4.17.

The asymptotic time scales also increase with Pr , and it is seen that, for Pr -values up to 0.7, $t_{a,T}$ and $t_{a,u}$ are of the same order of magnitude. For increasing Pr , $t_{a,T}$ becomes much higher than $t_{a,u}$, their difference itself increasing with Pr .

4.5.3 Heat transfer results

The heat transfer results presented here are restricted to the subcritical region, characterized by the occurrence of a long-term steady-state regime (PD or S).

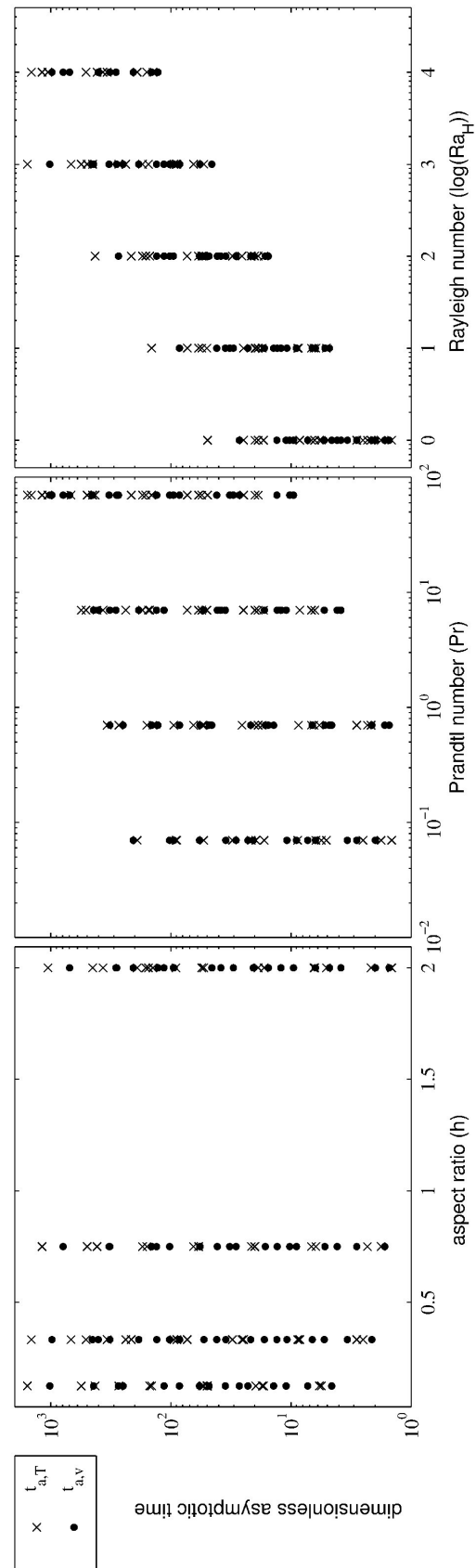


Figure 4.17: Asymptotic times as functions of h , Pr and Ra_H .

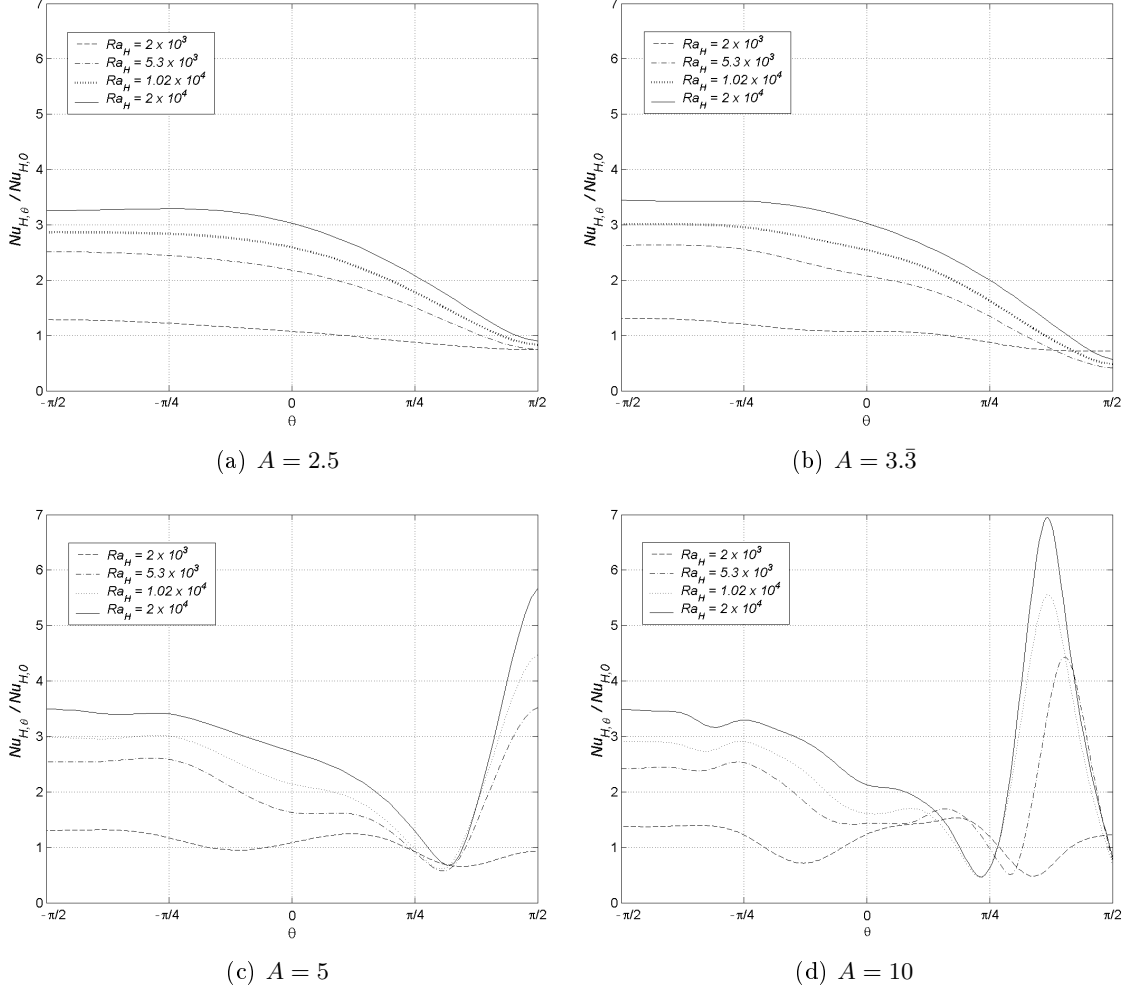


Figure 4.18: Distributions of the local Nusselt number $Nu_{H,\theta}$, along the cylinder surface for $Ra_H = 2 \times 10^3 \div 2 \times 10^4$. The data are normalized by pseudo-diffusive values $Nu_{H,0}$, listed in Table 4.5.

Heat transfer results for $Pr = 0.7$

Table 4.5 reports a 22×4 (Ra_H, A) matrix of average Nu_H values extracted by the numerical predictions. The range covered, $10^{-9} \leq Ra_H \leq 2 \times 10^4$, encompasses the pseudo-diffusive and steady-state regions.

Results in Table 4.5 confirm that pseudo-diffusive regimes are characterized by a constant value of the Nusselt number, which is attained asymptotically as Ra_H tends to zero; here this is labelled $Nu_{H,0}$. Figure 4.18 shows the distributions of the ratio $Nu_{H,\theta}/Nu_{H,0}$ along half of the cylinder contour, for selected Ra_H - and A -values. The plots bring out the correspondence between the flow structures described in the previous section and the resulting heat transfer modes. For the lower A -values (Figures 4.18(a) and 4.18(b)) $Nu_{H,\theta}$ always exhibits a monotonically decreasing trend from the cylinder bottom, $\theta = -\pi/2$, to its top, $\theta = \pi/2$. This behaviour is coherent with Figures (4.3(a), and 4.3(b)), where the strong lateral vortices are seen to enhance convection in the lower part of the cylinder,

while a progressive thickening of the boundary layer is observed for increasing θ , and one single stagnation point is present at $\theta = \pi/2$. Over a comparable range of Ra_H , Cesini et al. [127] found similar trends in their experiments on a heating cylinder in an almost-square enclosure.

For either $A = 5$ and $A = 10$, the wall heat flux distribution becomes increasingly more irregular for increasing Ra_H , as a counterpart of the complexity the thermal and flow fields take on. Plots in Figures 4.18(c) and 4.18(d) indicate that, even for the lowest Ra_H -value shown (2×10^3), the heat flux oscillates around the pseudo-diffusive value. For higher Ra_H -values, a profound dip and a very high peak appear in the upper part of the cylinder. For $A = 5$, the maximum heat flux density always falls at $\theta = \pi/2$, while for $A = 10$, it progressively shifts backwards for increasing Ra_H , down to $\theta \simeq 0.86\pi$. As can be seen in Figures 4.3(c) and 4.3(d), minima in the $Nu_{H,\theta}/Nu_{H,0}$ plots match the presence of thermal plumes detaching from the cylinder surface, while maxima correspond to regions where fresh fluid is carried towards the wall by secondary or tertiary circulation cells.

Global heat transfer correlation

The values of Nu_H listed in Table 4.5 form the data-base used to derive a general heat transfer correlation covering the whole subcritical range. The variables to correlate were chosen to be Nu_H , Ra_H , and h . Following the procedure outlined by Churchill and Usagi [150] and by Churchill and Chu [151], asymptotic values for $Nu_H(Ra_H \rightarrow 0)$ and $Nu_H(Ra_H \rightarrow \infty)$ were correlated for each value of h , and the coefficients of the resulting equations were expressed as a function of h . The general correlation form [150] is:

$$Y = (1 + Z^n)^{-n} \quad (4.5.3)$$

where Y and Z stand for:

$$Y = \frac{Nu_H(Ra_H, h)}{Nu_H(Ra_H \rightarrow 0, h)} \quad (4.5.4)$$

$$Z = \frac{Nu_H(Ra_H \rightarrow \infty, h)}{Nu_H(Ra_H \rightarrow 0, h)} \quad (4.5.5)$$

As already noted, constant Nu_H -values are obtained for $Nu_H(Ra_H \rightarrow 0)$. Their power-law fitting as a function of h is:

$$Nu_H(Ra_H \rightarrow 0, h) = 0.54 + 1.178h^{0.637} \quad (4.5.6)$$

The seven highest Ra_H -values in Table 4.5 stood out as the cases where a steady convective regime is fully established. They were used to derive the asymptotic correlation for $Nu_H(Ra_H \rightarrow \infty)$. Those data were fitted by a power law equation for each of the four h -values:

$$Nu_H(Ra_H \rightarrow \infty) = aRa_H^b \quad (4.5.7)$$

Values of the coefficients a and b are reported in Table 4.6. These were linearly related to h as follows:

$$a(h) = 0.15 + 0.256h \quad (4.5.8)$$

$$b(h) = 0.265 - 0.02h \quad (4.5.9)$$

Ra_H	Nu_H			
	$A = 2.5$	$A = 3.3$	$A = 5$	$A = 10$
	$h = 2$	$h = 0.75$	$h = 0.3$	$h = 0.125$
1×10^{-9}	2.3737	1.5120	1.1373	0.8480
1×10^{-7}	2.3737	1.5120	1.1373	0.8480
1×10^{-5}	2.3737	1.5120	1.1373	0.8480
1×10^{-3}	2.3737	1.5120	1.1373	0.8480
1×10^{-1}	2.3737	1.5120	1.1373	0.8480
1×10^0	2.3737	1.5120	1.1373	0.8480
1×10^1	2.3738	1.5120	1.1374	0.8482
5×10^1	2.3755	1.5129	1.1385	0.8541
1×10^2	2.3807	1.5159	1.1422	0.8706
2×10^2	2.4014	1.5276	1.1565	0.9112
3×10^2	2.4357	1.5470	1.1788	0.9457
4×10^2	2.4827	1.5733	1.2060	0.9742
1.2×10^3	3.0587	1.8799	1.4249	1.1571
2×10^3	3.5449	2.1527	1.6583	1.3172
2.85×10^3	3.9151	2.3812	1.8650	1.4408
5.3×10^3	4.5943	2.8332	2.2542	1.6955
7.75×10^3	5.0309	3.1325	2.5099	1.8638
1.02×10^4	5.3591	3.3597	2.7014	2.0056
1.265×10^4	5.6243	3.5450	2.8551	2.1232
1.51×10^4	5.8475	3.7024	2.9841	2.2248
1.755×10^4	6.0404	3.8395	3.0957	2.3141
2×10^4	6.2099	3.9607	3.1944	2.3929

Table 4.5: Average Nusselt number values versus Ra_H

A	h	a	b
2.5	2	0.67	0.23
3.3	0.75	0.33	0.25
5	0.33	0.25	0.26
10	0.13	0.18	0.26

Table 4.6: Constants in power-law (eq. (4.5.10) for each h -value

Even if the dependence of the coefficient b on h is weak, it was retained in order to improve the accuracy of the correlation. Overall, the equation for $Nu_H(Ra_H \rightarrow \infty)$ turns out to be

$$Nu_H(Ra_H \rightarrow \infty) = (0.15 + 0.256h) Ra_H^{(0.265-0.02h)} \quad (4.5.10)$$

The exponent n in equation (4.5.3) is given the integer value which minimizes the sum of the squared deviations between the original data and the predicted values. Here, $n = 14$ was found to be the best-fitting value. Substituting equations (4.5.6) and (4.5.10) in equation (4.5.3) yields the following general result:

$$Nu_H(Ra_H, h) = \left\{ (0.54 + 1.178h^{0.637})^{14} + [(0.15 + 0.256h) Ra_H^{(0.265-0.02h)}]^{14} \right\}^{\frac{1}{14}} \quad (4.5.11)$$

The ranges of validity of equation (4.5.11) are:

$$\begin{cases} Pr = 0.7, \\ 10^{-9} \leq Ra_H \leq 2 \times 10^4, \\ 0.125 \leq h \leq 2 (2.5 \leq A \leq 10) \end{cases} \quad (4.5.12)$$

Statistical analysis gives a value of 0.994 for the R-square coefficient, with a maximum relative error of 7.2% for equation (4.5.11) towards the original data-base. Equation (4.5.11) is plotted in Figure 4.19, using the coordinates Y and Z defined by equations (4.5.4) and (4.5.5); two dashed lines delimit the $\pm 5\%$ confidence level of the equation, and available literature data [124, 128, 129] are added.

In the literature, the only alternative to equation (4.5.11) for the geometry under consideration is the correlation proposed by Moukalled and Acharya [128]:

$$Nu_D = 0.59Ra_L \quad (4.5.13)$$

Equation (4.5.13), properly re-scaled, is also plotted in Figure 4.19 for the various h -values. It is pointed out that the predictions of equation (4.5.13) fall within the $\pm 5\%$ confidence range of equation (4.5.11) only for the intermediate h -values ($h = 0.75$ and $h = 0.333$), while results for $h = 0.125$, and $h = 2$ are underestimated. Furthermore, the exponent 0.23 in equation (4.5.13) matches the asymptotic trend given by equation (4.5.11) only case $h = 2$.

A complete check of the predictive accuracy of equation (4.5.11) is reported in Table 4.7, where percentage deviations of the numerical results found in the literature are presented. All the data fall within a $\pm 10\%$ strip. Steady-state predictions in [124, 128, 129] which fall above the proposed stability threshold, $Ra_H \approx 2 \times 10^4$, have been starred in Table 4.7. It is interesting to remark that even those results are in good agreement with equation (4.5.11).

Finally, the cases $Ra_L = 10^6$ and $h = 2, 0.75, 0.3$ in the literature [124, 128, 129], were re-calculated for direct comparison. Results are presented in the lower part of Table 4.7 in terms of Nu_H . The agreement with the present predictions is satisfactory and, in particular, an excellent correspondence emerges with the results by Shu and Zhu [124]. Apart for some of the data from Moukalled and Acharya [128], the deviations from equation (4.5.11) listed in Table 4.7 are indicative of the accuracy of the correlation itself, which should be safely stated to be better than $\pm 10\%$ over the whole range.

A	h	Ra_H	$\epsilon\%$ on Nu_H (eq. (4.5.11))			Flow Regime
			Peng <i>et al.</i> [129]	Shu and Zhu [124]	Moukalled and Acharya [128]	
2.5	2	0	—	—	1.46	PD
2.5	2	6.4×10^2	7.59	7.59	8.05	S
2.5	2	3.2×10^2	—	0.82	—	S
2.5	2	6.4×10^3	1.44	1.44	2.34	S
2.5	2	3.2×10^4	—	0.64	—	S
2.5	2	6.4×10^4	5.22*	2.64*	2.69*	S/P
2.5	2	6.4×10^5	—	—	2.66*	QP
3.3	0.75	0	—	—	2.3	PD
3.3	0.75	2.7×10^2	0.02	0.02	2.71	S
3.3	0.75	1.35×10^3	—	8.1	—	S
3.3	0.75	2.7×10^3	6.68	6.25	1.64	S
3.3	0.75	1.35×10^4	—	2.54	—	S
3.3	0.75	2.7×10^4	4.93*	3.17*	2.05*	S
3.3	0.75	2.7×10^5	—	—	3.41*	P/QP
5	0.3	0	—	—	1.25	PD
5	0.3	8×10^1	1.62	1.8	8.98	PD/S
5	0.3	4×10^2	—	2.69	—	S
5	0.3	8×10^2	1.28	1.12	1.09	S
5	0.3	4×10^3	—	3.86	—	S
5	0.3	8×10^3	2.97	5.8	2.72	S
5	0.3	8×10^4	—	—	6.78*	NS/P
A	h	Ra_H	Nu_H [129]	Nu_H [124]	Nu_H [128]	Nu_H (present)
2.5	2	6.4×10^4	7.59	7.78	7.78	7.77
3.3	0.75	2.7×10^4	4.18	4.25	4.48	4.24
5	0.3	8×10^3	2.47	2.55	2.47	2.53

Table 4.7: Deviations of available literature data from equation (4.5.11), and Nu_H predictions for selected Ra_H -values. Starred values (*) correspond to predictions in [124, 128, 129] falling above the proposed stability threshold, $Ra_H = 2 \times 10^4$.

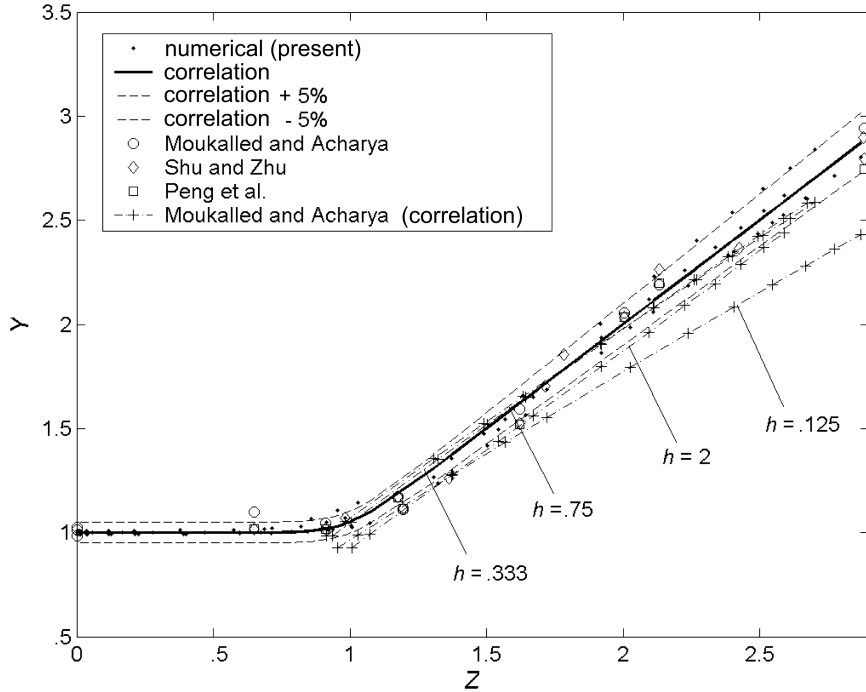


Figure 4.19: Heat transfer correlation (4.5.11), as compared with available literature data [124, 128, 129]. Coordinates Y and Z are defined in eqs. (4.5.4) and (4.5.5), respectively.

In most practical situations, the diameter of the heating source, D , and the leading temperature difference, ΔT , are the design parameters, while the shape and size of the encapsulation is to be chosen. This means that, in general, the value of Ra_D is known to the designer, and the sizing of the system, expressed by a convenient expression of the aspect ratio, such as d , is to be established. To this end, the data in Table 4.5, scaled in a (Ra_D, d) format, have been plotted in Figure 4.20. They show that, as long as pseudo-diffusive regimes prevail, Nu_D increases with d , for a given Ra_D -value. However, the more room available for fluid circulation, implied by low- d sizing, promotes heat transfer for increasing Ra_D . Churchill's and Chu [151] equation for the free-stream cylinder, also plotted in Figure 4.20, fits coherently with the above observations, showing that the free-stream cylinder ($d \rightarrow 0$) is the most efficient solution for $Ra_d \rightarrow \infty$. However, the unbounded option penalises heat transfer in the low- Ra_D range, in comparison to the enclosed geometries, and, for $d = 0.8$ ($A = 10$, $H = 0.125$) this holds true up to $Ra_D \simeq 4 \times 10^4$.

A final comparison can be made with the results by Cesini *et al.* [127], for an isothermal horizontal cylinder in a rectangular cavity having isothermal sides and a conductive ceiling. One of the three cavities considered was almost square, with $d = 0.246$. Nu_D -values from [127] were inserted in Figure 4.20 for that geometry. It can be seen that they fall between the present predictions for $d = 0.2$ and $d = 0.4$, suggesting that a change in the cavity boundary conditions does not substantially affect the heat transfer rate.

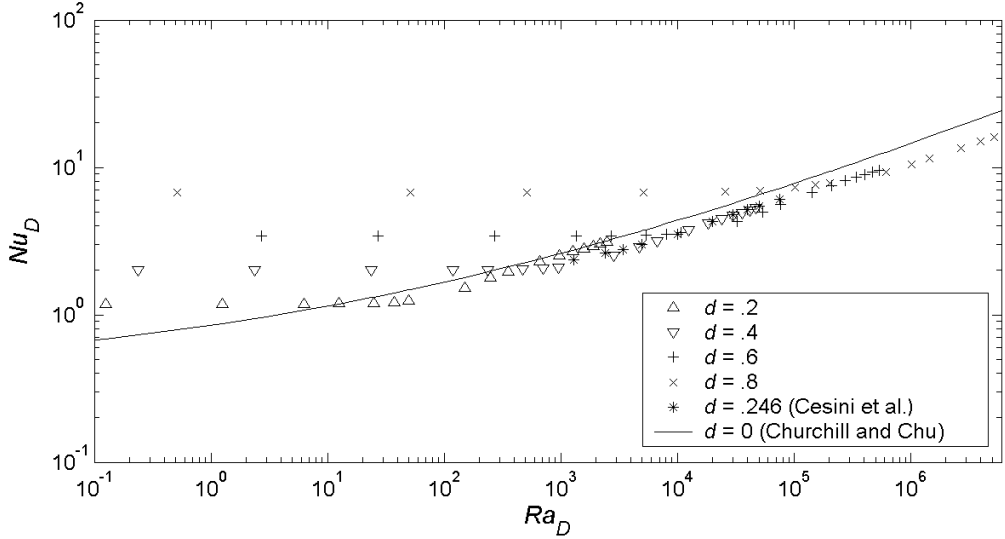


Figure 4.20: Nu_D - Ra_D plot of the present predictions, as compared with Cesini *et al.* [127] and Churchill and Chu [151].

Effect of the heat flux condition

Over the region of asymptotically laminar steady flow regimes for the isoflux case, steady-state computations were performed, in order to assess the effect of the isoflux condition on the overall heat transfer. Results in this paragraph are presented in terms of Ra_D and d . The numerical experiment covers the range $Ra_D \leq 10^6$, for $Pr = 0.7$, and for four aspect ratios considered so far.

For all cases, by means of equation (4.1.15), the Rayleigh number of the equivalent isothermal case was determined, and, subsequently, the simulations were repeated combining the newfound Ra with condition (4.1.1). Table 4.8 reports a sample of the results. It is pointed out that a reduced, but still appreciable, difference exists between the two cases, indicating that, for a given average temperature, the isoflux case is always more efficient in terms of global heat transfer.

Differences in the global performance reflect inequalities in the local heat transfer modes. As an example, Figure 4.21 shows the distributions of the local Nusselt number, Nu_θ along one half of the cylinder contour, for $d = 0.6$, $Ra_{qD} = 10^6$ ($Ra_D = 1.42 \times 10^5$). The plot brings out the correspondence between the flow structures described in the previous paragraph and depicted in figure 4.13, and the resulting heat transfer modes. Minima in the plot match the presence of the thermal plumes detaching from the cylinder surface, and maxima correspond to regions where fresh fluid is carried towards the wall by secondary circulation cells. It is important to point out that the dips and peaks are more pronounced in the Dirichlet case.

Figure 4.22 presents all the results obtained for the isoflux case. By rescaling Ra_{qD} to Ra_D , according to equation (4.1.15), Nu_D -values are compared with a correlating equation for the average Nusselt number on the cylinder, under the isothermal condition, as a function of Ra_D and d . The graph shows that, as stated before, the Nusselt number in the isoflux case generally overestimates the correlation, but remains appreciably close to

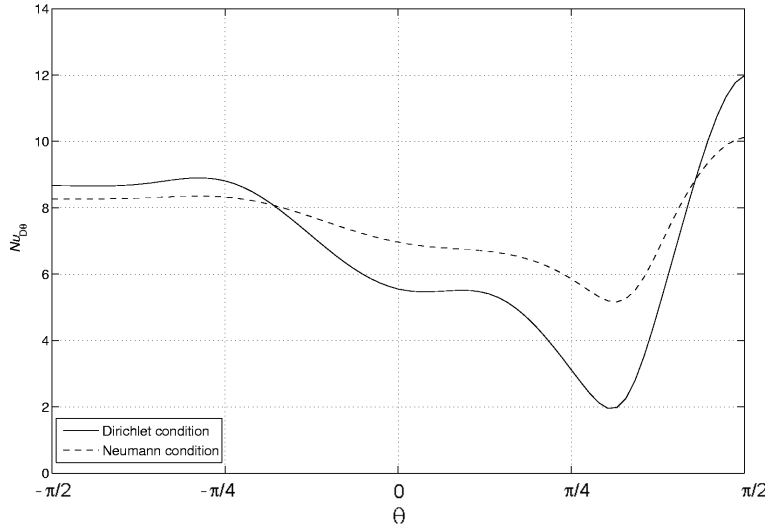


Figure 4.21: Distributions of the local Nusselt number $Nu_{D,\theta}$ along the cylinder surface for $d = 0.6$, $Ra_{qD} = 10^6$ ($Ra_D = 1.42 \times 10^5$)

d	Ra_{qD}	Nu_{qD}	$Ra_D = \frac{Ra_{qD}}{Nu_{qD}}$	Nu_D	$\epsilon (\%)$
.2	10^3	2.27	4.40×10^2	2.07	8.92
.2	10^4	3.47	2.88×10^3	3.2	7.84
.4	10^4	2.99	3.34×10^3	2.61	12.66
.4	10^5	4.89	2.04×10^4	4.29	12.26
.6	10^5	4.29	2.33×10^4	4.01	6.64
.6	10^6	7.03	1.42×10^5	6.75	3.9
.8	10^6	7.71	1.30×10^5	7.44	3.47
.8	10^7	11.13	8.99×10^5	10.19	8.4

Table 4.8: Average Nusselt number values on the cylinder surface: comparison between corresponding cases for isothermal and isoflux boundary conditions

it, the maximum relative error being 11.3%. It is also worthy to note that, as Ra_D tends to zero, the predictions nearly coincide for the two boundary conditions. The correlation approximates the original data base and all related literature results [124, 128, 129], within a 10% accuracy, and can therefore be considered valid also for the uniform heat flux condition.

Influence of the Prandtl number

Figure 4.23 shows a multiple scatter plot of the average Nusselt number on the cylinder, Nu_H . The overall heat transfer rate appears to be very sensitive to the Prandtl number only for Pr -values less than unity, while for $Pr = 7$ and $Pr = 70$, such a dependence is not at all evident.

A useful qualitative comparison can be drawn with equation (4.5.11). Such correlation was built on two main observations:

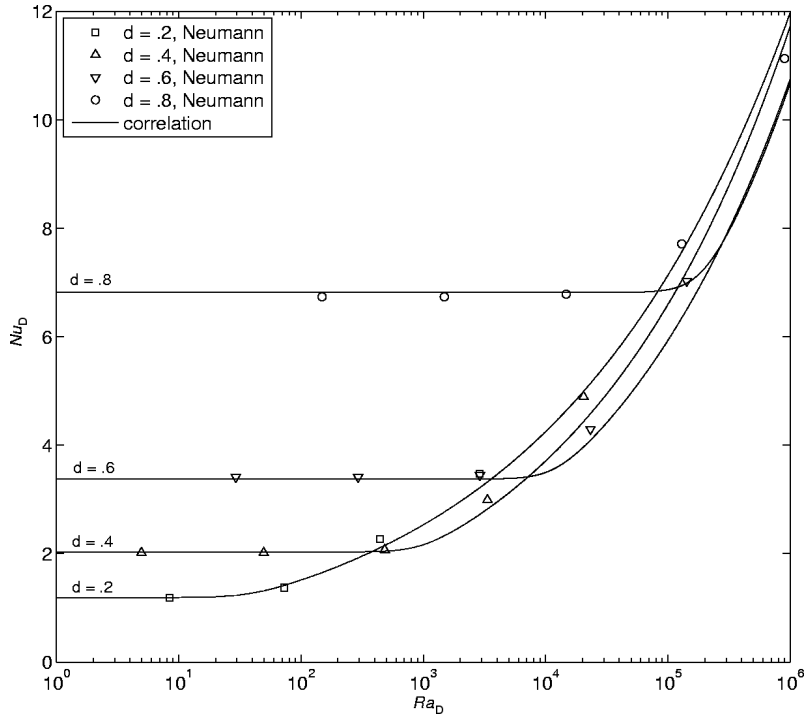


Figure 4.22: Validation of the correlation 4.5.11 for the isoflux case.

- i) the Nusselt number varies linearly with h ;
- ii) the dependence of Nu_H on Ra_H is expressed by a power law, as long as steady convective regimes are considered;

Both the assumptions are shown to be confirmed by the results in Figure 4.23. Figure 4.24, instead, shows the heat transfer data obtained for different values of Pr , as compared with equation (4.5.11). Again, the accordance between the numerical data and the predictions of the correlation is very good, and only the data for $Pr = 0.07$ occasionally fall outside the $\pm 10\%$ strip. Accordingly, the limits of validity of equation (4.5.11) can be extended as follows:

$$\begin{cases} 0.7 \leq Pr \leq 70, \\ 10^{-9} \leq Ra_H \leq 2 \times 10^4, \\ 0.125 \leq h \leq 2 (2.5 \leq A \leq 10) \end{cases} \quad (4.5.14)$$

4.6 Summary

In this chapter, natural convection from a horizontal cylindrical source has been addressed. The features of the system under consideration have been described in full detail, by illustrating its spatial domain and boundary conditions, and defining relevant parameters and quantities.

The fundamental computational choices have been discussed; in particular, specific criteria for the determination of suitable grid sizings, as a function of the leading parameters of the problem, have been established, and the time step adaption procedure, based on the Courant condition, has been outlined. Results of a grid sensitivity analysis have also been

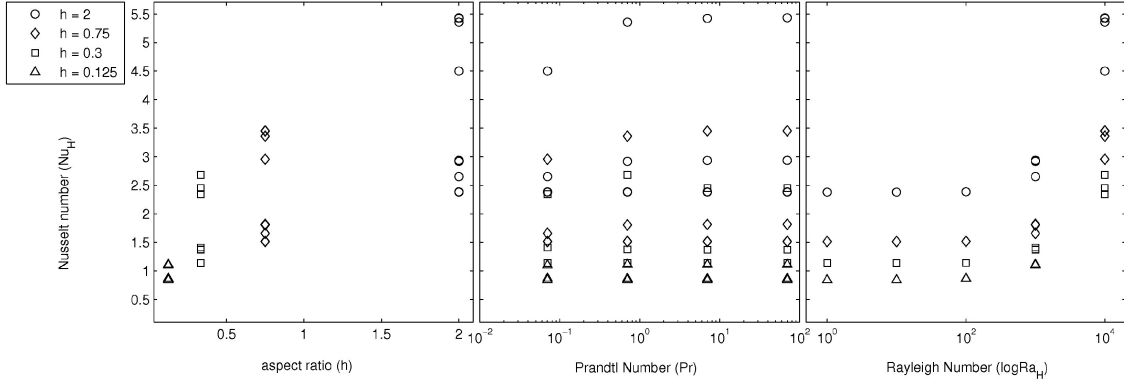


Figure 4.23: Average Nusselt number on the cylinder surface vs. h , Pr and Ra_H , for all the cases examined.

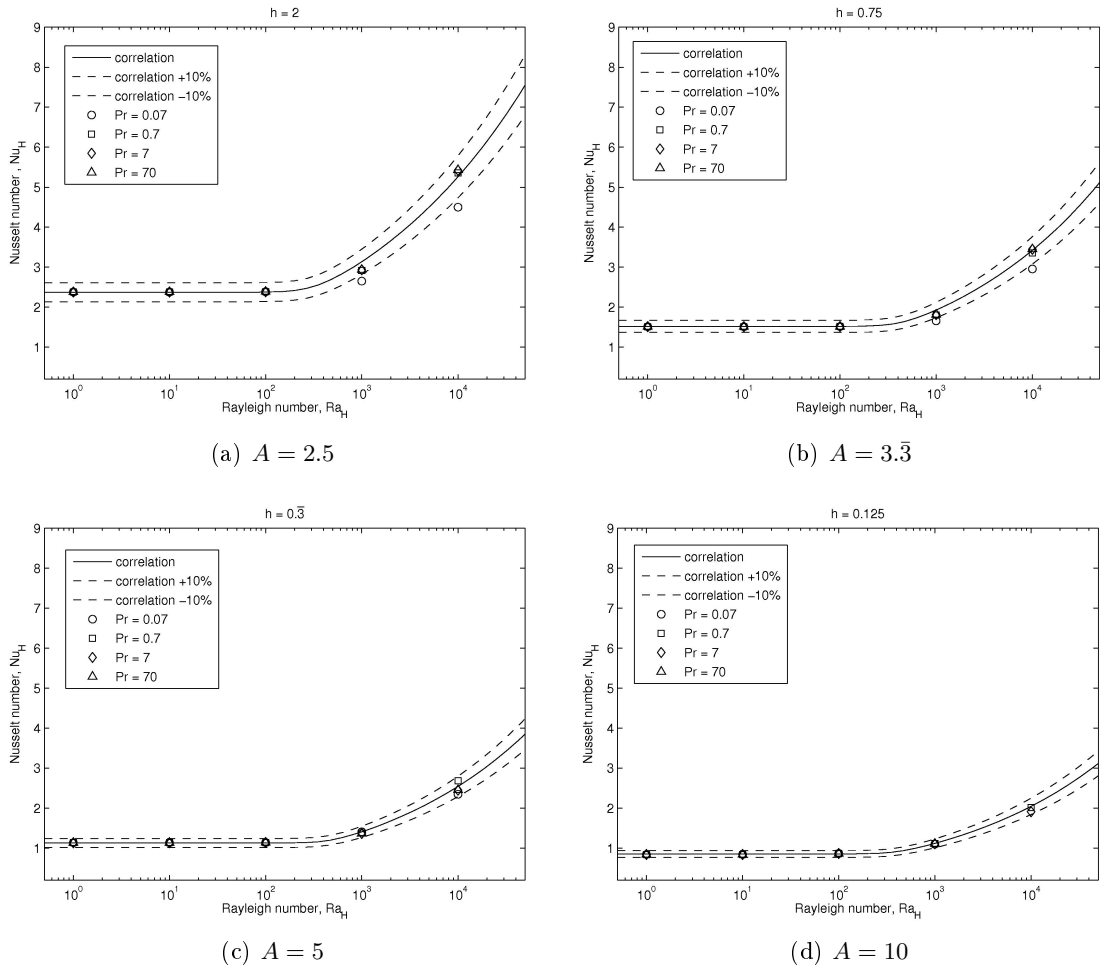


Figure 4.24: Comparison between equation 4.5.11 and numerical predictions of Nu_H , as a function of Ra_H , for different values of Pr . Each diagram refers to a specific A -value.

issued, proving the suitability of the numerical technique for the analysis of time-dependent buoyant flows and assessing its second order accuracy.

Results of numerical simulations have been presented, concerning the onset of steady-state flows, the occurrence of flow transitions and bifurcations, and the local and global heat transfer characteristics of the system. The different transition modes detected have been discussed. The influence of the governing parameters Ra , Pr and A on the system behaviour has been thoroughly analyzed. A general correlation for the average Nusselt number at steady-state has finally been formulated, valid over a wide range of the three leading parameters.

Chapter 5

Limits of the pseudo-diffusive regime in horizontal annular gaps

5.1 Introduction

This present chapter is devoted to pseudo-diffusive natural convection regimes in horizontal annular gaps. Such an issue had already been introduced throughout the text. In Chapter 2, pseudo-diffusive (*PD*) flows were associated to low- Ra confined thermal convection, in cases where the imposed temperature gradient has a non-zero horizontal component (*i.e.* orthogonal to the gravitational field, see also Section 1.3.4). As described in Chapter 2, this is the case, for instance, of vertical enclosures and horizontal annuli, as well as of the geometry considered in the foregoing chapter. For all these configurations, pseudo-diffusive flow represents the base flow, *i.e.* the only fixed-point solution of the Boussinesq equations, (1.3.1), (1.3.14), and (1.3.15), to be unconditionally stable for sufficiently low values of the main parameter [20].

As observed in Chapter 4, pseudo-diffusive flow regimes are characterised by the presence of a weak, shear-driven, creeping flow. In fluid dynamics, creeping flow (or Stokes flow) [27] is commonly identified as the flow pattern occurring when the order of magnitude of viscous shear is significantly greater than the contribution of inertial forces to the transport of momentum. In such conditions, it is reasonable to assume that heat transfer is dominated by conduction, and to neglect convective terms in the energy conservation equation [3]. It must be pointed out that the opposite implication, *i.e.* that a conduction-dominated temperature field is always supported by an underlying creeping flow, is utterly false if a low- Pr fluid is considered, since, in that case, heat diffusion is much stronger than advection, and the temperature field remains insensitive to the underlying circulation up to high values of Ra . However, the flow is mainly driven by inertial effects. Viscous diffusion may be relevant only if Ra is extremely low, in which case, the flow can again be considered as pseudo-diffusive. A quantitative proof of this argument can be obtained by means of scale analysis, as shown in Section 5.3.

The study of the nature, and most importantly, of the limits of pseudo-diffusive confined buoyant flows, as a function of the leading parameters of the system is still an open subject, both of theoretical and practical concern. From the point of view of transition dynamics, one may observe that the passage from *PD*-type flows to steady convection (*S*-type flows) is not linked to the occurrence of a bifurcation. Instead, such a transition often occurs

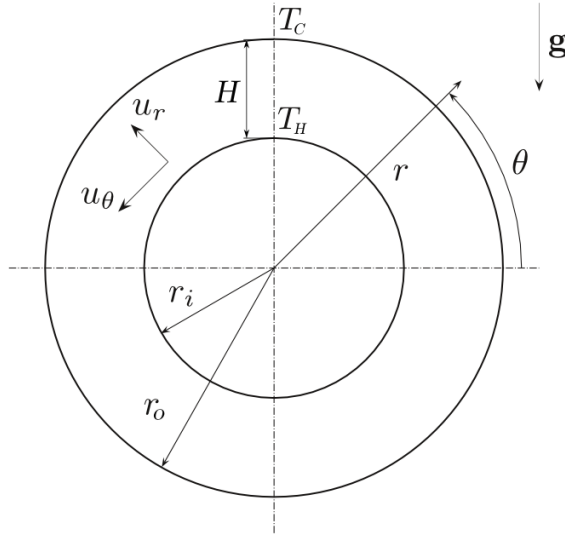


Figure 5.1: Cross-section of the horizontal annulus.

smoothly with increasing Ra , due to the progressive strengthening of the influence of non-linear advective terms on the base solution. Hence, any stability analysis aimed at determining the threshold of the *PD-S* transition would inevitably fail. On the other hand, for any application exploiting the high insulating power of some fluids, like gases, the knowledge of the orders of magnitude of the critical values of the parameters for which such a transition occurs is crucial.

In the following, a study of the pseudo-diffusive regimes in horizontal annular gaps is carried out by analytical and numerical means. The cylindrical annular geometry has been taken as reference for this analysis, although the results presented here might also be extended to the more general case of an annulus between two coaxial prismatic surfaces.

5.2 Analytical solutions

As a first step, two analytical solutions are proposed, approximating the pseudo-diffusive flow and temperature field in the transversal section of a differentially heated horizontal cylindrical annulus.

Either solution is based on a different set of assumptions, through which the full Navier-Stokes and energy equations are simplified in a solvable system of PDEs.

Symbols are given in Figure 5.1, which reproduces in Figure 2.13. The geometric features of the system have already been described in Section 2.4; the governing parameters of the problem are Ra_H , R and Pr .

5.2.1 Governing equations and boundary conditions

Since pseudo-diffusive regimes are addressed, it is appropriate to choose the diffusive velocity scale (1.4.25) as the reference scale velocity for the non-dimensionalization of equations (1.3.1), (1.3.14) and (1.3.15). As from Section 1.4.6, the correspondent dimensionless equa-

tions are (1.4.40), (1.4.45) and (1.4.46). Their steady-state forms are addressed here:

$$\nabla \cdot \mathbf{u} = 0 \quad (5.2.1)$$

$$\frac{1}{Pr} \mathbf{u} \cdot \nabla \mathbf{u} = -\frac{1}{Pr} \nabla p + \nabla^2 \mathbf{u} + Ra_H T \hat{\mathbf{g}} \quad (5.2.2)$$

$$\mathbf{u} \cdot \nabla T = \nabla^2 T \quad (5.2.3)$$

With reference to Figure 5.1, a polar coordinate system is adopted to expand equations (5.2.1-5.2.3) for the 2D feature of a horizontal annulus:

$$\frac{\partial(ru_r)}{\partial r} + \frac{\partial u_\theta}{\partial \theta} = 0 \quad (5.2.4)$$

$$\begin{aligned} \frac{1}{Pr} \left[u_r \frac{\partial u_r}{\partial r} + \frac{u_\theta}{r} \frac{\partial u_r}{\partial \theta} - \frac{u_\theta^2}{r} \right] &= -\frac{1}{Pr} \frac{\partial p}{\partial r} + Ra_H T \sin \theta + \\ &+ \frac{1}{r} \frac{\partial}{\partial r} \left(r \frac{\partial u_r}{\partial r} \right) + \frac{1}{r} \frac{\partial}{\partial \theta} \left(\frac{\partial u_r}{\partial \theta} \right) - \frac{2}{r^2} \frac{\partial u_\theta}{\partial \theta} - \frac{u_r}{r^2} \end{aligned} \quad (5.2.5)$$

$$\begin{aligned} \frac{1}{Pr} \left[u_r \frac{\partial u_\theta}{\partial r} + \frac{u_\theta}{r} \frac{\partial u_\theta}{\partial \theta} + \frac{u_r u_\theta}{r} \right] &= -\frac{1}{Pr} \frac{1}{r} \frac{\partial p}{\partial \theta} + Ra_H T \cos \theta + \\ &+ \frac{1}{r} \frac{\partial}{\partial r} \left(r \frac{\partial u_\theta}{\partial r} \right) + \frac{1}{r} \frac{\partial}{\partial \theta} \left(\frac{\partial u_\theta}{\partial \theta} \right) + \frac{2}{r^2} \frac{\partial u_r}{\partial \theta} - \frac{u_\theta}{r^2} \end{aligned} \quad (5.2.6)$$

$$\nabla^2 T = u_r \frac{\partial T}{\partial r} + \frac{u_\theta}{r} \frac{\partial T}{\partial \theta} \quad (5.2.7)$$

In a 2D case, it is advantageous to reformat the PDEs in the streamfunction-vorticity formulation. The definition of vorticity ω (1.3.33) is recalled:

$$\omega = \nabla \times \mathbf{u} \quad (5.2.8)$$

whilst, in polar coordinates, the streamfunction ψ , is defined as the function respecting the following conditions:

$$u_r = \frac{1}{r} \frac{\partial \psi}{\partial \theta} \quad u_\theta = -\frac{\partial \psi}{\partial r} \quad (5.2.9)$$

From the above definitions, it is straightforward to prove that:

$$\nabla^2 \psi = -\omega \quad (5.2.10)$$

The equation for vorticity is obtained by taking the curl of Equation (5.2.2). Assuming the flow as two-dimensional, the vector vorticity equation is reduced to a single scalar equation, the curl of a 2D field having only one non-zero component:

$$\nabla^2 \omega = \frac{1}{Pr} \left[u_r \frac{\partial \omega}{\partial r} + \frac{u_\theta}{r} \frac{\partial \omega}{\partial \theta} \right] - Ra_H \left[\cos \theta \frac{\partial T}{\partial r} - \frac{1}{r} \sin \theta \frac{\partial T}{\partial \theta} \right] \quad (5.2.11)$$

with:

$$\omega = \frac{1}{r} \left[\frac{\partial (ru_\theta)}{\partial r} - \frac{\partial u_r}{\partial \theta} \right] \quad (5.2.12)$$

The energy equation (5.2.7) remains unchanged. Non-dimensional boundary conditions are set as:

$$T|_{r_i} = 0; \quad T|_{r_o} = 1 \quad (5.2.13)$$

$$u_r, u_\theta|_{r_i} = 0; \quad u_r, u_\theta|_{r_o} = 0 \quad (5.2.14)$$

$$\psi|_{r_i} = \frac{\partial \psi}{\partial r}\Big|_{r_i} = 0; \quad \psi|_{r_o} = \frac{\partial \psi}{\partial r}\Big|_{r_o} = 0 \quad (5.2.15)$$

Having set the radial gap $H = r_o - r_i$ as the reference length, and $R = r_o/r_i$ being the radius ratio, the radial boundary coordinates can therefore be rewritten as:

$$r_i = \frac{1}{R-1}; \quad r_o = \frac{R}{R-1} \quad (5.2.16)$$

The system geometry is thus defined by the domain $(r, \theta) \in [1/(R-1), R/(R-1)] \times [0, 2\pi]$.

5.2.2 Solution in the case of creeping flow and pure conduction

A natural way to solve equations (5.2.4)-(5.2.7) in the pseudo-diffusive range is to enforce the hypotheses of creeping flow and pure conduction outlined above. This is equivalent to neglect the convective terms in the vorticity equation (5.2.11) as well as in the energy equation (5.2.7). The equations are then simplified as follows:

$$\nabla^4 \psi = Ra_H \left[\cos \theta \frac{\partial T}{\partial r} - \frac{1}{r} \sin \theta \frac{\partial T}{\partial \theta} \right] \quad (5.2.17)$$

$$\nabla^2 T = 0 \quad (5.2.18)$$

equation (5.2.10) having been combined with equation (5.2.11). The set of equations is linear and, most important, uncoupled. The solution of the energy equation (5.2.18) is straightforward; since, under the above-specified boundary conditions (5.2.13), the dependence of T on θ is dropped thanks to the axisymmetric nature of the problem:

$$\frac{1}{r} \frac{d}{dr} \left(r \frac{dT}{dr} \right) = 0 \quad (5.2.19)$$

The resulting temperature distribution matches that of pure conduction in an annular layer:

$$T(r) = \frac{\ln(R) - \ln(R-1) - \ln r}{\ln R} \quad (5.2.20)$$

By introducing the solution for T in equation (5.2.17), one obtains:

$$\nabla^4 \psi = \frac{Ra_H}{\ln R} \frac{\cos \theta}{r} \quad (5.2.21)$$

Equation (5.2.21) is a non-homogeneous biharmonic equation in cylindrical coordinates. It is linear and, on its right hand side, it contains a forcing term of the type $\cos \theta/r$. Its solution may be found by combining the general integral of the correspondent homogeneous

equation with a particular solution of the non-homogeneous equation. The general integral of:

$$\nabla^4 \psi = 0 \quad (5.2.22)$$

can be written as [152]:

$$\begin{aligned} \psi_0(r, \theta) = & a_{01}r^2 + a_{02}r^2(\ln r - 1) + a_{03}\ln r + a_{04}\theta + \\ & + (a_{11}r + a_{12}r^{-1} + a_{13}\theta r + a_{14}r^3 + a_{15}r\ln r)\cos\theta \\ & + (b_{11}r + b_{12}r^{-1} + b_{13}\theta r + b_{14}r^3 + b_{15}r\ln r)\sin\theta \\ & + \sum_{n=2}^{\infty} (a_{n1}r^n + a_{n2}r^{-n} + a_{n3}r^{n+2} + a_{n4}r^{-n+2})\cos n\theta \\ & + \sum_{n=2}^{\infty} (b_{n1}r^n + b_{n2}r^{-n} + b_{n3}r^{n+2} + b_{n4}r^{-n+2})\sin n\theta \end{aligned} \quad (5.2.23)$$

It is also straightforward to prove that

$$\psi_P = \frac{Ra_H}{16\ln R}r^3\ln r\cos\theta \quad (5.2.24)$$

is a particular solution of equation (5.2.21). The general integral of equation (5.2.21) can be expressed as:

$$\psi(r, \theta) = \psi_0 + \psi_P + K \quad (5.2.25)$$

The somewhat cumbersome explicit expression obtained by combining equations (5.2.23) and (5.2.24) becomes rather shorter when considering boundary conditions (5.2.15). The contribution of ψ_P turns out to be the only fixed known term in determining the constants: therefore, all terms not multiplied by $\cos\theta$ must vanish. Moreover, thanks to periodicity in the θ coordinate, it is possible to set to zero the terms in $\theta\cos\theta$. Solution of equation (5.2.21) is then reduced to:

$$\psi_{pd,a}(r, \theta) = \frac{Ra_H}{16\ln R}(r^3\ln r + c_1r + c_2r^{-1} + c_3r^3 + c_4r\ln r)\cos\theta \quad (5.2.26)$$

with the following constants:

$$\begin{aligned} c_1 = & \frac{1}{\Delta(R-1)^2}[(R^2-1)^2(2\ln R - (R^2+1)(2\ln(R-1)-1)) + \\ & + 8R^2(R^2-1)\ln(R-1)\ln(R) - 8R^4(\ln R)^2] \end{aligned} \quad (5.2.27)$$

$$c_2 = \frac{R^2}{\Delta(R-1)^4}(2R\ln R - R^2 + 1)(2R\ln R + R^2 - 1) \quad (5.2.28)$$

$$\begin{aligned} c_3 = & \frac{1}{\Delta}(R^2-1)^2(4\ln(R-1) - 2\ln R - 1) + \\ & - 4(R^4-1)\ln(R-1)\ln R + 4R^4(\ln R)^2 \end{aligned} \quad (5.2.29)$$

$$c_4 = \frac{2(R+1)}{\Delta(R-1)}[4R^2\ln R - R^4 + 1] \quad (5.2.30)$$

where:

$$\Delta = -4(R^2 - 1)(\ln R(R^2 + 1) - R^2 + 1) \quad (5.2.31)$$

Such a result is analogous to that of Crawford and Lemlich [91], which was obtained using a different non-dimensionalization.

5.2.3 Solution in the narrow gap limit

Another analytical solution for the case of the horizontal annulus in the pseudo-diffusive regime has been proposed by Desrayaud et al.[12], by considering narrow gap annuli, in the limit $R \rightarrow 1$. For such limit, at low Rayleigh numbers, the circulation inside the annulus consists in a pair of symmetric, counterrotating crescent-shaped cells, and one can assume that the radial velocity component is always much smaller than the angular one, except in the contact regions between the two counterrotating cells, around $\theta = \pm\pi/2$. In this way, the velocity vector $\mathbf{u} = (u_r(r, \theta), u_\theta(r, \theta))$ can be approximated as $\mathbf{u} \simeq (0, u_\theta(r, \theta))$. By applying this hypothesis to equations (5.2.4-5.2.6), and noting that, *to a first approximation*, the continuity equation (5.2.4) returns:

$$\frac{\partial u_\theta}{\partial \theta} \simeq 0 \quad (5.2.32)$$

the following simplified system of equations is obtained:

$$-\frac{1}{Pr} \frac{u_\theta^2}{r} = -\frac{1}{Pr} \frac{\partial p}{\partial r} + Ra_H T \sin \theta \quad (5.2.33)$$

$$0 = -\frac{1}{Pr} \frac{1}{r} \frac{\partial p}{\partial \theta} + Ra_H T \cos \theta + \frac{1}{r} \frac{\partial}{\partial r} \left(r \frac{\partial u_\theta}{\partial r} \right) - \frac{u_\theta}{r^2} \quad (5.2.34)$$

As for the vorticity equation (5.2.11), by taking the curl of the vector equation formed by (5.2.33) and (5.2.34), (with a zero identity as the third component) and by assuming the temperature distribution is given by equation (5.2.20), the problem is reduced to the solution of a linear, third-order partial differential equation in the variable u_θ :

$$\frac{\partial^3 u_\theta}{\partial r^3} + \frac{2}{r} \frac{\partial^2 u_\theta}{\partial r^2} - \frac{1}{r^2} \frac{\partial u_\theta}{\partial r} + \frac{u_\theta}{r^3} = -\frac{Ra_H}{\ln R} \frac{\cos \theta}{r} \quad (5.2.35)$$

The solution of equation (5.2.35) appears as follows (calculations are omitted for the sake of brevity):

$$u_\theta(r, \theta) = \Gamma_1(\theta)r + \frac{\Gamma_2(\theta)}{r} + \Gamma_3(\theta)r \ln r - \frac{Ra_H}{3 \ln R} r^2 \cos \theta \quad (5.2.36)$$

It is important to point out that the dependence of u_θ on θ , eliminated in the resolution as a consequence of Equation (5.2.32), is retained by the forcing term in Equation (5.2.35), and the derivatives in the same equation are still designated as partial. Moreover, since the integration of equation (5.2.35) in the above expression (5.2.36) has been performed with respect to r , the coefficients Γ_i must depend on θ . This important issue was not clarified by Desrayaud et al. [12], whose analysis is brought further here.

By means of the definition (5.2.9), and of the approximate result of equation (5.2.35) it is possible to derive an equation for the streamfunction:

$$\frac{\partial \psi}{\partial r} = \frac{Ra_H}{3 \ln R} r^2 \cos \theta - \Gamma_1(\theta)r - \frac{\Gamma_2(\theta)}{r} - \Gamma_3(\theta)r \ln r \quad (5.2.37)$$

which can be solved by integrating again with respect to r :

$$\psi_{pd,b}(r, \theta) = \frac{Ra_H}{9 \ln R} \left[r^3 + \gamma_1 r^2 + \gamma_2 \ln(r) + \gamma_3 r^2 \ln\left(\frac{r}{\sqrt{\epsilon}}\right) + \gamma_4 \right] \cos \theta \quad (5.2.38)$$

In equation (5.2.38), it is taken into account that, from the boundary conditions (5.2.14–5.2.15), it is immediately proved that the dependence of the constants Γ_i on θ is in the form:

$$\Gamma_i(\theta) \propto \cos \theta \quad (5.2.39)$$

Additional integration constants and signs have been incorporated in the γ_i coefficients, whose expressions are determined by imposing conditions (5.2.15):

$$\begin{aligned} \gamma_1 &= \frac{1}{2\Lambda(R-1)} [12R^2((R-1)\ln(R-1) + \ln R)\ln R + \\ &\quad + (R^3 - 1)(2R^2\ln R - (2\ln(R-1) + 3)(R^2 - 1))] \end{aligned} \quad (5.2.40)$$

$$\gamma_2 = \frac{R^2}{\Lambda(R-1)^3} [3(R-1)^2(R+1) - 2(R^3 - 1)\ln R] \quad (5.2.41)$$

$$\gamma_3 = \frac{1}{\Lambda} [6R^2\ln R - (R^3 - 1)(R+1)] \quad (5.2.42)$$

$$\begin{aligned} \gamma_4 &= \frac{R^2}{\Lambda(R-1)^3} [(3\ln(R-1) + 1)(R^2 - 1)(R-1) - \\ &\quad - \ln R(2\ln R + 2(R^3 - 1)\ln(R-1) + R^3 - 3R + 2)] \end{aligned} \quad (5.2.43)$$

where:

$$\Lambda = -(2R\ln R - R^2 + 1)(2R\ln R + R^2 - 1) \quad (5.2.44)$$

Quite surprisingly, after having reconstructed an approximate streamfunction field (5.2.38), one could also employ definition (5.2.9) to obtain an expression for u_r , although the latter had been considered as negligible as an initial assumption.

5.2.4 Validity of the narrow-gap solution

Figure 5.2 reports snapshots of the analytical streamfunction fields, as predicted by equations (5.2.26) and (5.2.38), for eight selected values of R , encompassing the ranges of narrow, moderate and large gap annuli. In the left half of each plot, the isolines of the full pseudo-diffusive solution, $\psi_{pd,a}$ (5.2.26) are drawn, while in the right half, the streamlines of $\psi_{pd,b}$ (5.2.38) are shown, as extracted from recalculating the solution by Desrayaud *et al.* [12].

The contour plots demonstrate that the qualitative agreement between the solutions is good, although the overall patterns show little but increasing discrepancies as R strays from the limit $R \rightarrow 1$, for which the expression of $\psi_{pd,b}$ has been carried out. Such differences were therefore expected, and can be quantified rather easily.

The maximum relative difference ϵ_ψ of the solution $\psi_{pd,b}$ with respect to $\psi_{pd,a}$ is thus defined:

$$\epsilon_\psi = \frac{\max_{r_i \leq r_e} |\psi_{pd,b}(r, 0) - \psi_{pd,a}(r, 0)|}{\max_{r_i \leq r_e} |\psi_{pd,a}(r, 0)|} \quad (5.2.45)$$

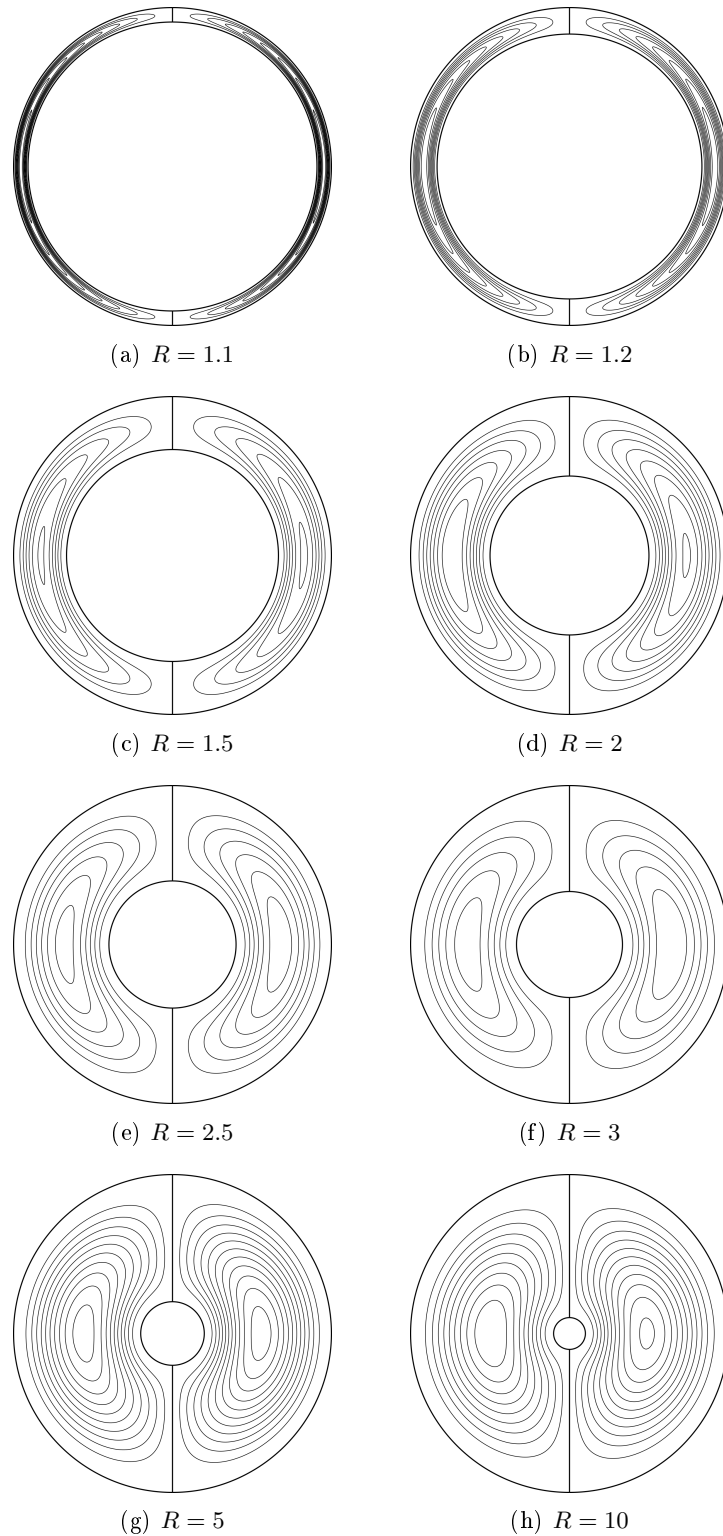


Figure 5.2: Comparison between the two solutions for the pseudo-diffusive streamfunction in a horizontal annulus: $\psi_{pd,a}$, equation (5.2.26), (left half of the annulus); $\psi_{pd,b}$, equation (5.2.38) (right half).

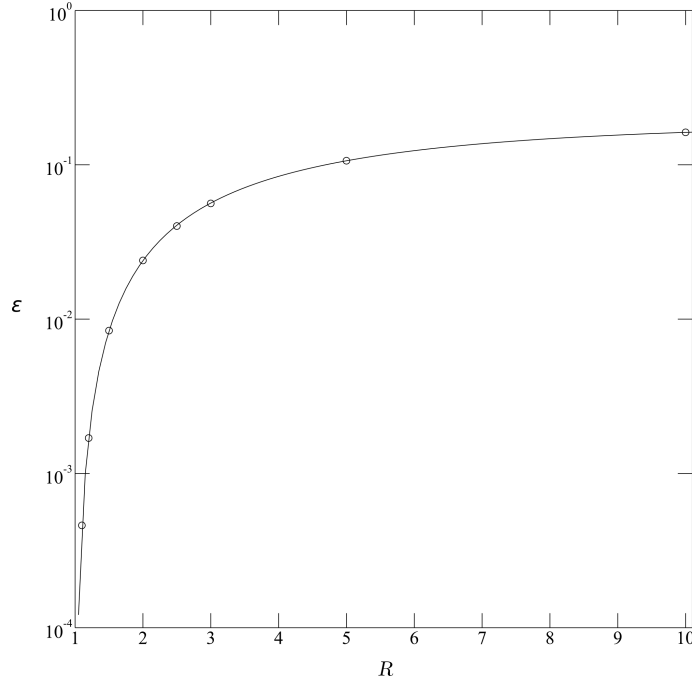


Figure 5.3: Maximum relative difference ϵ_ψ between the solutions $\psi_{pd,a}$ and $\psi_{pd,b}$, as a function of R .

Figure 5.3 reports a plot of ϵ_ψ as a function of R . It is observed that, coherently, in the limit $R \rightarrow 1$, the relative bias tends to vanish, thus confirming the suitability of the expression of $\psi_{pd,b}$ (5.2.38) to reproduce the pseudo-diffusive flow in narrow-gap annuli. Conversely, the solutions stray significantly from each other as R increases, their relative difference being above 10% already for $R \geq 5$ and seemingly approaching an asymptotic value of $\epsilon_\psi \simeq 0.12$ for higher R . On the basis of the computed values of ϵ_ψ , the following validity condition for $\psi_{pd,b}$ can be formulated, defining a threshold for R below which the relative difference between the two solutions, (5.2.26) and (5.2.38), is contained within 1%:

$$\psi_{pd,b} \simeq \psi_{pd,a} \quad \text{for} \quad R \leq 1.55 \quad (5.2.46)$$

In view of condition (5.2.46), and since the expression for $\psi_{pd,a}$ has been obtained under the natural hypothesis of diffusion-dominated heat and momentum transport, the solution (5.2.26) is then taken as the reference datum for further analysis.

5.3 Scale analysis

The interrelation between the critical values of the parameters for which the transition from pseudo-diffusive to steady convective flow occurs in a differentially heated annulus, can be conveniently explored by means of scale analysis (see Appendix A). The case of external natural convection from a single, isothermal horizontal cylinder immersed in a homogeneous, infinite medium is considered first. This is important, because in external free convection cases, the establishment of a pseudo-diffusive flow is a rather impossible occurrence; diffusive transport characterises the initial transient of the flow, but convection

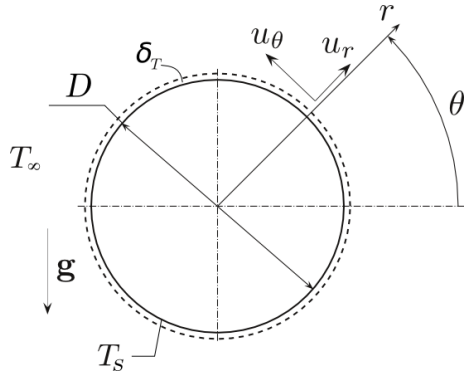


Figure 5.4: Schematic of an isothermal cylindrical source at a temperature T_s , immersed in an infinite medium at T_∞ .

inevitably sets on after a certain time, beyond which the advective effects become preponderant. For the case of a single horizontal cylinder, there are a number of experimental evidences of the existence of such a delay time [153, 154, 155], whose scale is determined in the following.

On the basis of the scale analysis for the isolated horizontal cylinder, scaling criteria will be brought forth to determine the scaling laws of the critical Ra_H -values for the *PD-S* transition in the horizontal annulus, as a function of both R and Pr .

5.3.1 Isothermal cylinder in an infinite medium

Let a horizontal cylindrical heat source of diameter D and of infinite axial length, kept at a constant temperature $T = T_s$, be immersed in an infinite fluid reservoir at $T = T_\infty$. For $T_s > T_\infty$, an ascending buoyancy-induced flow is expected to develop from the source wall, and to give rise to an upward thermal plume (see Section 1.5.2).

Two different phases of the initial transient of the system are visualized in Figure 5.5. The images are taken from a preliminary study [156], carried out in the framework of the present research. Such a study aimed at a comparison between numerical and experimental results for the initial transient of convection from a uniformly heated horizontal wire. Numerical computations were performed by means of the technique described in Chapter 3, whilst interferometric photographs were provided by Ambrosini *et al.* [155], from their database of ESPI (*Electronic Speckle Pattern Interferometry*) measurements. Figures 5.5(a) and 5.5(b) show the computed and measured temperature fields in the very early stages of the flow, when heat transfer is mainly dominated by conduction. The characteristic concentric pattern of the isotherms is only slightly perturbed by the weak currents developing along the cylinder surface. Figures 5.5(c) and 5.5(d), instead, portray the thermal field after the onset of convection.

In order to perform a scale analysis of the phenomenon, it is convenient to consider a cross-section of the cylinder (Figure 5.4), and to rewrite the governing equations in their

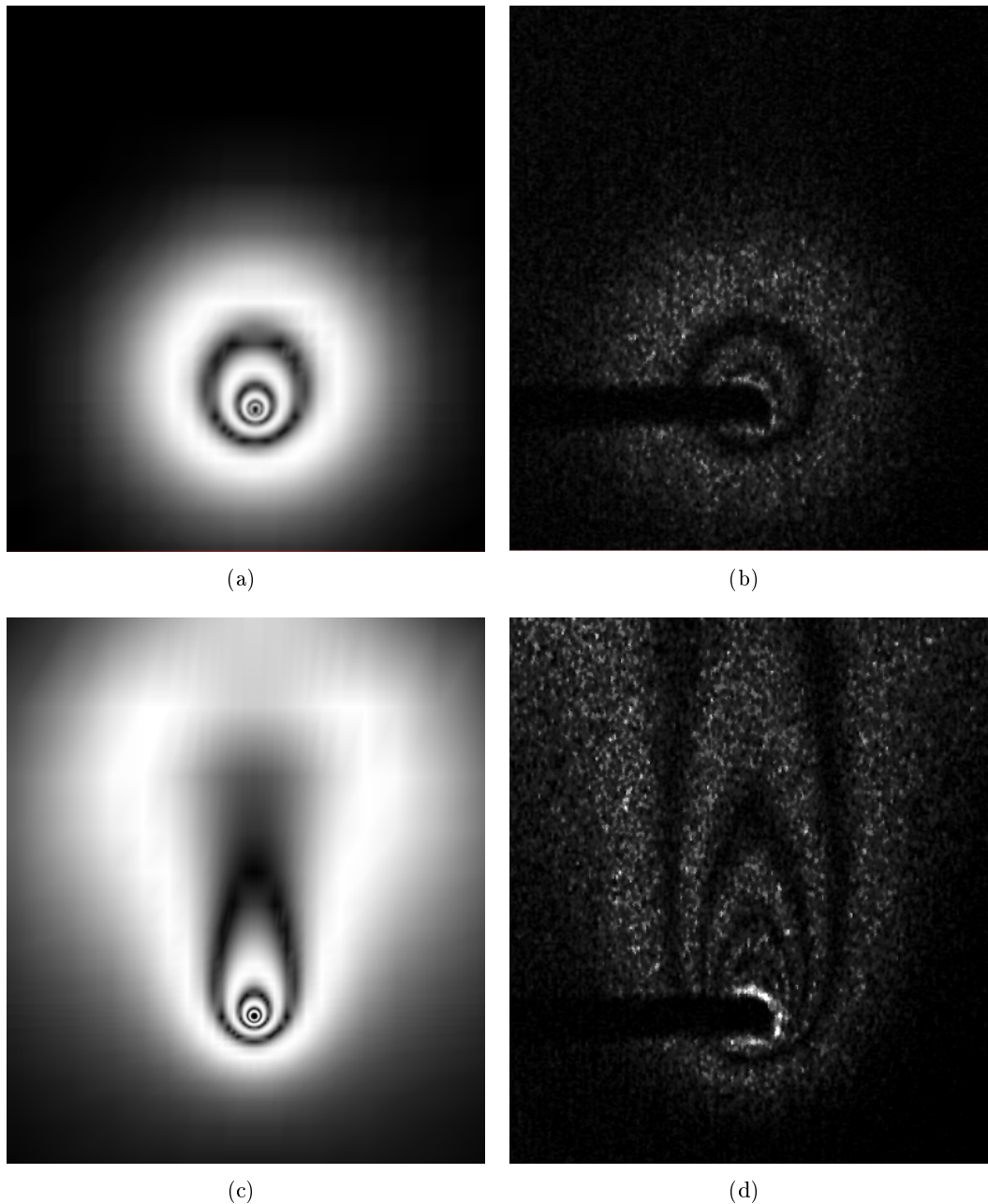


Figure 5.5: Numerical (a, c) and experimental (b, d) interferograms representing the temperature field around a heated horizontal wire, as reported in [156]: (a, b) diffusive transient; (c, d) developed thermal plume.

time-dependent, dimensional form, and in cylindrical coordinates:

$$\frac{\partial(ru_r)}{\partial r} + \frac{\partial u_\theta}{\partial \theta} = 0 \quad (5.3.1)$$

$$\frac{\partial \omega}{\partial t} + u_r \frac{\partial \omega}{\partial r} + \frac{u_\theta}{r} \frac{\partial \omega}{\partial \theta} = \nu \nabla^2 \omega + g\beta \left[\cos \theta \frac{\partial T}{\partial r} - \frac{1}{r} \sin \theta \frac{\partial T}{\partial \theta} \right] \quad (5.3.2)$$

$$\frac{\partial T}{\partial t} + u_r \frac{\partial T}{\partial r} + \frac{u_\theta}{r} \frac{\partial T}{\partial \theta} = \alpha \nabla^2 T \quad (5.3.3)$$

The radial and azimuthal components of the Navier-Stokes equations have been substituted here by the vorticity equation, in order to eliminate the pressure term. The scales of maximum variation of the variables are defined as follows:

$$\Delta r_{max} \approx \delta_T; \quad r \approx D; \quad \Delta T_{max} \approx \Delta T_{ref} = T_s - T_0 \quad (5.3.4)$$

where δ_T is the radial thickness of the heated layer of fluid surrounding the cylinder. The scales of maximum variation of the velocity components are labeled as:

$$u_r \approx U_r; \quad u_\theta \approx U_\theta \quad (5.3.5)$$

The present scale analysis follows the general outline of that of Patterson and Imberger [64] for a vertical enclosure, and recovers many of the concepts introduced in Section 1.5.1. At $t = 0^+$, the fluid is motionless, and $u_r, u_\theta \simeq 0$ everywhere. In the energy equation (5.3.3), thermal inertia given by the sudden heating is therefore balanced by heat diffusion. In scaling terms, one has:

$$\frac{\Delta T}{t} \approx \alpha \frac{\Delta T}{\delta_T^2} \quad (5.3.6)$$

from which the growth rate of the heated layer is obtained:

$$\delta_T \approx (\alpha t)^{\frac{1}{2}} \quad (5.3.7)$$

The dynamical response of the heated fluid within the layer δ_T is quite different, depending on the angle θ . Near the horizontal midplane of the cylinder, $\theta \approx 0, \pi$, the temperature gradient is orthogonal to gravity, and a flow starts up in the tangential direction. From the continuity equation, one has:

$$U_r \approx \frac{U_\theta \delta_T}{D} \quad (5.3.8)$$

Hence, it is easy to prove that vorticity scales as:

$$\omega \approx \frac{U_\theta}{\delta_T} \quad (5.3.9)$$

In the vorticity equation (5.3.2), three different terms might balance the buoyancy term, which is the leading term and, therefore, is of order $O(1)$. These are the inertial term, the advective term and the viscous friction term. Such a balance is expressed as follows:

$$\begin{array}{lll} \frac{U_\theta}{\delta_T t} & \text{or} & \frac{U_\theta^2}{\delta_T D} \\ \text{inertia} & & \text{advection} \end{array} \quad \begin{array}{lll} \text{or} & \frac{\nu U_\theta}{\delta_T^2} & \approx \frac{g\beta \Delta T}{\delta_T} \\ \text{friction} & & \text{buoyancy} \end{array} \quad (5.3.10)$$

If the expression for the scale of δ_t (5.3.7) is plugged into the scales of (5.3.10), after some algebra, one obtains:

$$\frac{U_\theta}{t} \quad \text{or} \quad \frac{U_\theta^2}{D} \quad \text{or} \quad \frac{\nu U_\theta Pr}{t} \approx g\beta\Delta T \quad \begin{matrix} \text{inertia} \\ \text{advection} \\ \text{friction} \\ \text{buoyancy} \end{matrix} \quad (5.3.11)$$

Since U_θ is small, at least in the initial stages of the flow, the advective term is of lower order, as compared to the other terms. Moreover, (5.3.11) shows that the relative magnitude of the inertial and friction terms is decided by Pr .

For $Pr \gg 1$ the action of buoyancy is balanced by the friction term. Such balance yields the following scale for U_θ :

$$U_\theta \approx g\beta\Delta T Pr^{-1} t \quad (5.3.12)$$

It should be noted that the scale of U_θ grows linearly with time. From the energy equation (5.3.3), the scale of heat transfer removal results:

$$v_{ad} \approx \frac{U_\theta \Delta T}{D} = \frac{g\beta(\Delta T)^2}{D} Pr^{-1} t \quad (5.3.13)$$

while, in the radial direction, diffusive heat transfer scales as:

$$v_{cd} \approx \alpha \frac{\Delta T}{\delta_T^2} = \frac{\Delta T}{t} \quad (5.3.14)$$

The time scale t_d for which diffusive and advective effects become of the same order ($v_{ad} \approx v_{cd}$) is given by:

$$t_d \approx \left(\frac{Pr D}{g\beta\Delta T} \right)^{\frac{1}{2}} \quad (5.3.15)$$

For time scales exceeding t_d , the transport of heat around the cylinder is dominated by advection. By introducing the Fourier number [1], which represents a dimensionless time in diffusion problems:

$$Fo_D = \frac{\alpha t}{D^2} \quad (5.3.16)$$

the relation (5.3.15) can be recast in dimensionless terms:

$$Fo_{D,d,vl} \approx Ra_D^{-\frac{1}{2}} \quad (5.3.17)$$

At time t_d , the layer δ_T has grown up to the following scale:

$$\delta_T \approx DRa_D^{-\frac{1}{4}} \quad (5.3.18)$$

For $Pr \ll 1$, instead, buoyancy effects are initially balanced by inertia, thus yielding, from (5.3.11):

$$U_\theta \approx g\beta\Delta T t \quad (5.3.19)$$

In this case, the balance $v_{ad} \approx v_{cd}$ returns a different estimate for the scale of t_d :

$$t_d \approx \left(\frac{D}{g\beta\Delta T} \right)^{\frac{1}{2}} \quad (5.3.20)$$

or, in dimensionless terms:

$$Fo_{D,d,vl} \approx Bo_D^{-\frac{1}{2}} \quad (5.3.21)$$

The scale of the thermal layer δ_T at $t \approx t_d$ is:

$$\delta_T \approx DBo_D^{-\frac{1}{4}} \quad (5.3.22)$$

As already observed, for $Pr \ll 1$, the flow within the heated layer δ_T is driven by the balance between buoyancy and inertia. Friction effects are of minor importance and, as in the case of the boundary layer over a vertical heated plate (see Section 1.5.1), they become relevant only in a much thinner viscous sublayer, scaling as:

$$\delta_v \approx Pr^{\frac{1}{2}} \delta_T \approx DGra_D^{-\frac{1}{4}} \quad (5.3.23)$$

The situation near the top of the cylinder, *i.e.* for $\theta \approx \pi/2$, is quite different. Since, in that region, $\cos \theta \approx 0$ and $\sin \theta \approx 1$, the temperature gradient is parallel and opposed to gravity; hence, the heated layer grows radially but remains locally motionless ($U_r \approx 0$), until its thickness exceeds a critical value. Vest and Lawson [153] suggest that such a critical value should correspond to the stability limit for Rayleigh-Bénard convection, in the case of a rigid lower boundary and a free upper boundary. This is equal to impose:

$$Ra_{\delta_T} = 1100.7 \quad (5.3.24)$$

Such an hypothesis is reasonable, since the outer boundary of the thermal layer δ_T can be seen as a free, moving boundary at constant temperature. Equation 5.3.24 then gives:

$$\frac{g\beta\Delta T\alpha^{\frac{1}{2}}}{\nu} t^{\frac{3}{2}} = 1100.7 \quad (5.3.25)$$

The time scale for a Rayleigh-Bénard instability to occur at the top of the cylinder is:

$$t_d = 1100.7\alpha^{-\frac{1}{2}} \left(\frac{\nu}{g\beta\Delta T} \right) \quad (5.3.26)$$

which, in dimensionless terms, becomes:

$$Fo_{D,d,rb} = 106.6 Ra_D^{-\frac{2}{3}} \quad (5.3.27)$$

The correlation 5.3.27 is very close to that proposed by Vest and Lawson [153] for the case of an isoflux cylinder.

The Fourier numbers $Fo_{D,d,vl}$ and $Fo_{D,d,rb}$ are different estimates of the end of the diffusive thermal transient around the cylinder, as a function of Ra_D or Bo_D . Each estimate is associated with a different effect concurring to the onset of convective transport. The first estimate, $Fo_{D,d,vl}$ refers to the growth of the advection rate in the flow ensued by the horizontal component of the temperature gradient, while the second one $Fo_{D,d,rb}$ accounts for the thermal instability in the vertical direction. The real threshold value for the onset of convection presumably results from a competition between these two effects. Based on the above scaling arguments, it can be inferred that an estimate of such value should obey a correlation similar to:

$$Fo_{D,d} = \min(C_{vl} Ra^{-\frac{1}{2}}, C_{rb} Ra^{-\frac{2}{3}}) \quad (5.3.28)$$

for $Pr \gg 1$ and:

$$Fo_{D,d} = \min(C_{vl}Bo^{-\frac{1}{2}}, C_{rb}Ra^{-\frac{2}{3}}) \quad (5.3.29)$$

for $Pr \ll 1$. The constant in equation 5.3.27 has been replaced by a generic constant C_{rb} in equations (5.3.28) and (5.3.29), since, if the curvature of the cylinder is taken into account, the vertical distance δ_T^* between the outer boundary of the heated layer and the cylinder surface, at a given time t , does not coincide with δ_T , and varies with θ :

$$\delta_T^* = \left(\frac{D}{2} + \delta_T \right) \sin \theta^* \quad (5.3.30)$$

where:

$$\theta^* = \arccos \left(\frac{D \cos \theta}{D + 2\delta_T} \right) \quad (5.3.31)$$

Thus, the balancing action of the hydrostatic pressure gradient is likely to extend over δ_T^* rather than δ_T , and the Fo -value for which a Rayleigh-Bénard instability can occur is certainly different.

Extensive numerical and experimental analyses would be necessary to assess the above scaling results, and to give a more accurate estimate of the proposed critical thresholds. However, to the aim of the present study, such results are sufficient to form the basis for the analysis of the horizontal annulus.

5.3.2 Horizontal annulus

As previously observed, pseudo-diffusive natural convection can only occur within confined domains, whilst it is just a transient feature for external cases. In fact, with reference to the example of the isolated cylinder, there is virtually no limit to the propagation of the diffusive thermal front δ_T , which develops itself in the initial transient, according to the relation (5.3.7), but this is later convected away when time exceeds a certain threshold t_d .

Instead, the presence of the outer isothermal cylindrical wall in the confined counterpart of the isolated cylinder - the horizontal annulus - provides an upper bound for the spatial extent of such front. By bringing forth the reasoning, it may be inferred that, if the gap H of the annulus is smaller than the smallest diffusive scale (δ_T for $Pr \gg 1$ and δ_v for $Pr \ll 1$) at time t_d , the final flow asset can be considered as pseudo-diffusive. For $Pr \gg 1$, this happens if:

$$H \lesssim D Ra_D^{-\frac{1}{4}} \quad (5.3.32)$$

which is equivalent to write:

$$Ra_H \lesssim \frac{1}{R-1} \quad (5.3.33)$$

For $Pr \ll 1$, instead, it must be:

$$H \lesssim D Gr_D^{-\frac{1}{4}} \quad (5.3.34)$$

corresponding to the following scaling relationship:

$$Ra_H \lesssim \frac{Pr}{R-1} \quad (5.3.35)$$

The inequalities (5.3.33) and (5.3.35) represent the scaling laws for the limits of the pseudo-diffusive regime in a horizontal annulus.

Kraussold [157]	$Ra_H \leq 6.3 \times 10^3$ (for $1.234 \leq R \leq 3$ and $Pr \approx 7, 500, 5000$)
Liu <i>et al.</i> [158]	$Ra_H \leq \frac{1000}{Pr^2} (1.36 + Pr)$ (for $1.557 \leq R \leq 7.52$ and $Pr \approx 0.7, 7, 3000$)
Raithby and Hollands [86]	$Ra_H \leq 0.011 \left(\frac{0.861 + Pr}{Pr} \right) \frac{(R - 1)^3}{(\ln R)^4} \left(R^{-\frac{2}{3}} + 1 \right)^5$

Table 5.1: Available correlations for the limit of conductive heat transfer in a horizontal annulus, as reported by various authors.

It can be observed that, in the limit $R \rightarrow \infty$, the scale of the critical Ra_H -value tends to zero. This could be a questionable issue, since, as discussed in Section 2.4, in such limit H ceases to be a representative scale for the problem. Two possible cases can be distinguished:

- if r_o is finite, while $r_i \rightarrow 0$, $H = r_o - r_i \rightarrow r_o$, and the condition $Ra_H \rightarrow 0$ implies that $\Delta T \rightarrow 0$;
- if $r_o \rightarrow \infty$ and r_i is finite, $H = r_o - r_i \rightarrow \infty$, and the condition $Ra_H \rightarrow 0$ is met only if $O(\Delta T) < O(H^{-4})$.

Hence, in both cases, the condition $Ra_H \rightarrow 0$ coherently requires that ΔT be infinitely small, for a pseudo-diffusive flow to be feasible in an annulus with infinite R . However, in the latter case, such requirement holds also if Ra_H tends to a constant asymptotic value, for it would be $O(\Delta T) = O(H^{-3})$ with $H \rightarrow \infty$. Therefore, the scaling laws (5.3.33) and (5.3.35) can be considered valid up to a constant, which can eventually be zero.

In the opposite limit, $R \rightarrow 1$, both scaling laws (5.3.33) and (5.3.35) return $Ra_H \rightarrow \infty$. This is in contrast with the predictions of Mojtabi and Caltagirone [97, 99], whose stability analyses revealed that the value $Ra_H = 1708$, *i.e.* the stability criterion for Rayleigh-Bénard convection between two rigid walls, is a critical value for flow stability in a horizontal annulus, in the limit $R \rightarrow 1$. Moreover, in narrow gap annuli, Rayleigh-Bénard instabilities frequently occur, giving rise to multiple convective cells in the top part of the annulus (see also Section 2.4). The birth of such cells, in turn, inevitably determines the disruption of the diffusive temperature and flow patterns. Hence, in the narrow gap limit, conditions (5.3.33) and (5.3.35) loose validity, and the threshold of the pseudo-diffusive regime should be established by different means.

5.4 Numerical results and discussion

In order to assess the limits of the pseudo-diffusive regime, a set of numerical simulations has been carried out, for eight selected values of R and for $Pr = 1$. For each R -value, several values of Ra_H were considered, corresponding to multiples and submultiples of the critical scale of equation (5.3.33), and of the critical Ra_H -values as predicted by three different criteria available in the literature. Such criteria are listed in Table 5.1, and are based upon the evaluation of the average heat transfer rate on the inner cylinder. In particular, they provide an estimate of Ra_H below which the average Nusselt number,

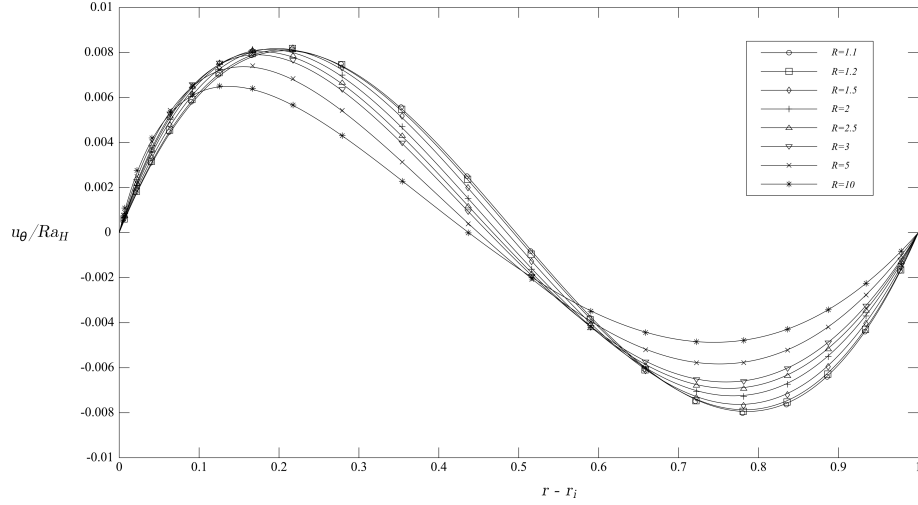


Figure 5.6: Analytical and numerical profiles of the normalized azimuthal velocity, u_θ/Ra_H , at $\theta = 0$, for $Ra_H = 1 \times 10^{-1}$.

Nu_H , equals that of pure conduction:

$$Nu_{H,cd} = \frac{2}{\ln R} \quad (5.4.1)$$

The correlations by Kraussold [157] and by Liu *et al.* [158] have been obtained on the basis of experimental works, while that of Raithby and Hollands [86] is analytical.

Profiles of the azimuthal velocity, normalized on Ra_H , u_θ/Ra_H , at $\theta = 0$, are reported in Figure 5.6, for each of the eight R -values considered, and for $Ra_H = 10^{-1}$. Such a value lies safely below the pseudo-diffusive limit. The numerical data are superimposed to the corresponding analytical profile, as extracted from the streamfunction field of equation (5.2.26). The excellent matching between the two results confirms the validity of both the numerical technique and the analytical solution.

In Figures 5.7 and 5.8, the profiles of the same quantity are reported for four different values of Ra_H , namely $Ra_H = 10^{-1}, 6.3 \times 10^1, 6.3 \times 10^2, 6.3 \times 10^3$, for each value of R . The analytical results of Desrayaud *et al.* [12], as derived from equation (5.2.38) are added to the plots.

As previously observed, for narrow gap annuli, $R = 1.1, 1.2$, (Figure 5.7, plots (a) and (b)) the two analytical solutions are quite close to each other; moreover, a slight deviation of the numerical data from the analytical profiles is appreciable only for the highest Ra_H -value.

For moderate R -values, (Figure 5.7, plots (c) and (d)) $R = 1.5, 2$, the profiles at $Ra_H = 6.3 \times 10^3$ completely stray from the pseudo-diffusive solution, and the difference between the two analytical solutions becomes appreciable. For higher R -values, (Figure 5.8), such differences are even more accentuated, while the numerical data for $Ra_H = 6.3 \times 10^2$ appear slightly detached from the pseudo-diffusive profile.

Analogous tendencies are observed when comparing the conduction temperature profile, and the numerical temperature data, for $\theta = 0$ and for corresponding values of Ra_H (Figures 5.9 and 5.10).

Figures 5.11(a) and 5.11(b) show the trends of the maximum relative deviations ϵ_u

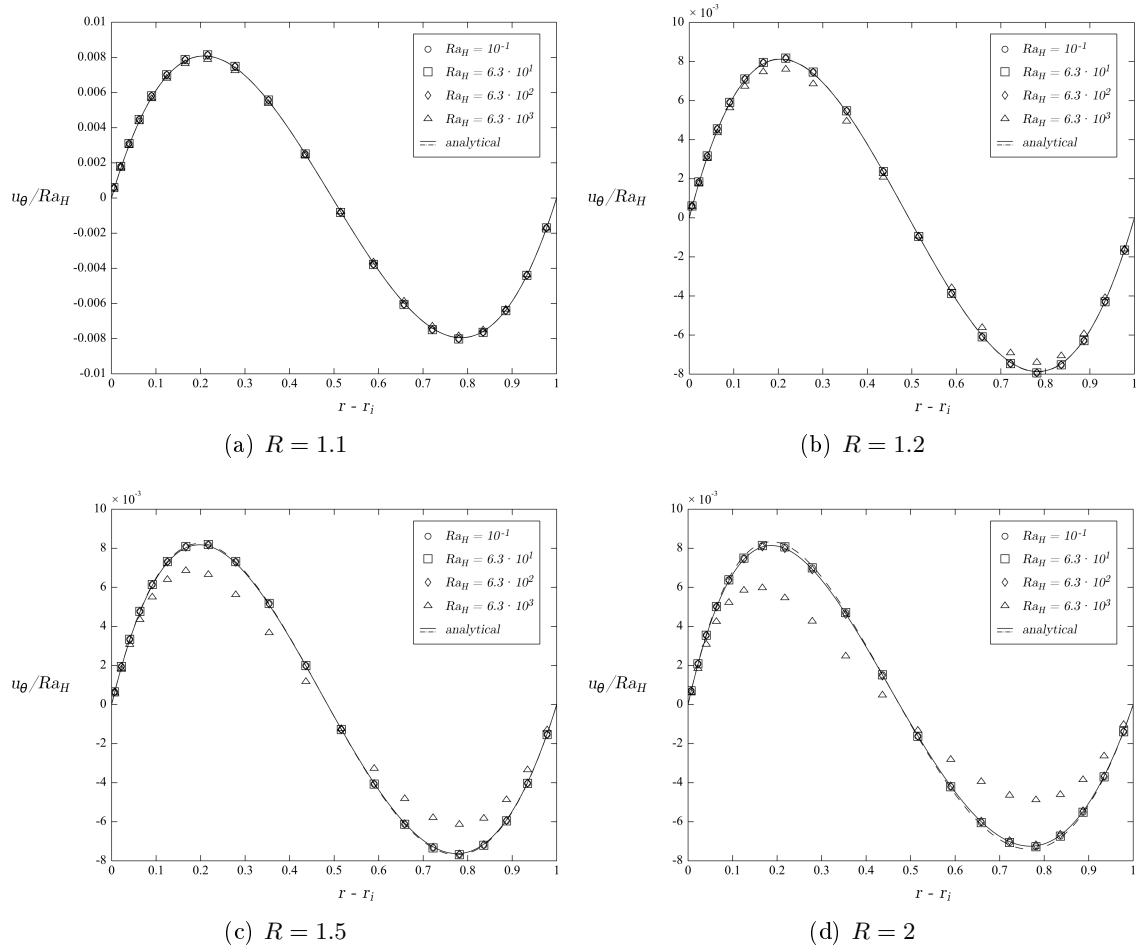


Figure 5.7: Analytical and numerical profiles of the normalized azimuthal velocity, u_θ/Ra_H , at $\theta = 0$, for four Ra_H -values, for narrow and moderate gap annuli. The dash-dot line corresponds to the analytical solution in the narrow gap limit.

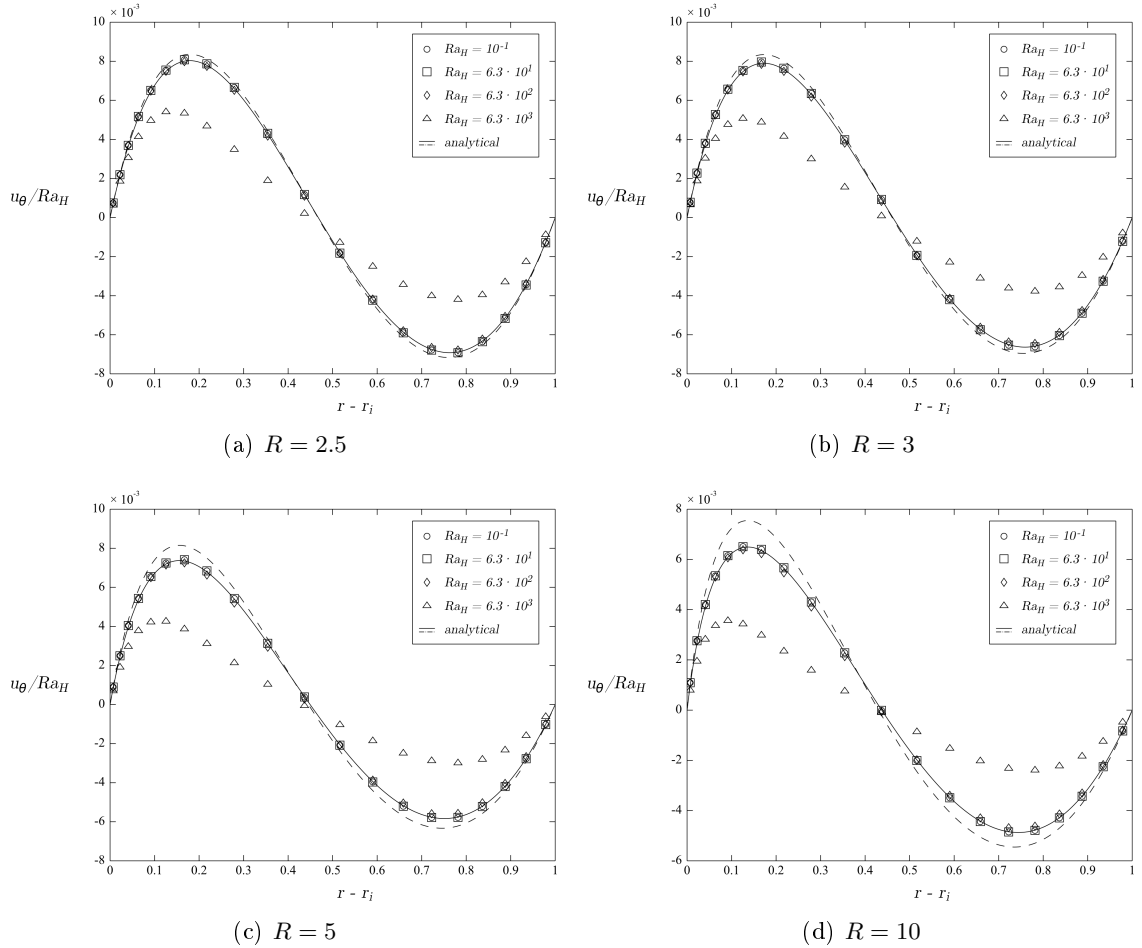


Figure 5.8: Analytical and numerical profiles of the normalized azimuthal velocity, u_θ/Ra_H , at $\theta = 0$, for four Ra_H -values, for large gap annuli. The dash-dot line corresponds to the analytical solution in the narrow gap limit.

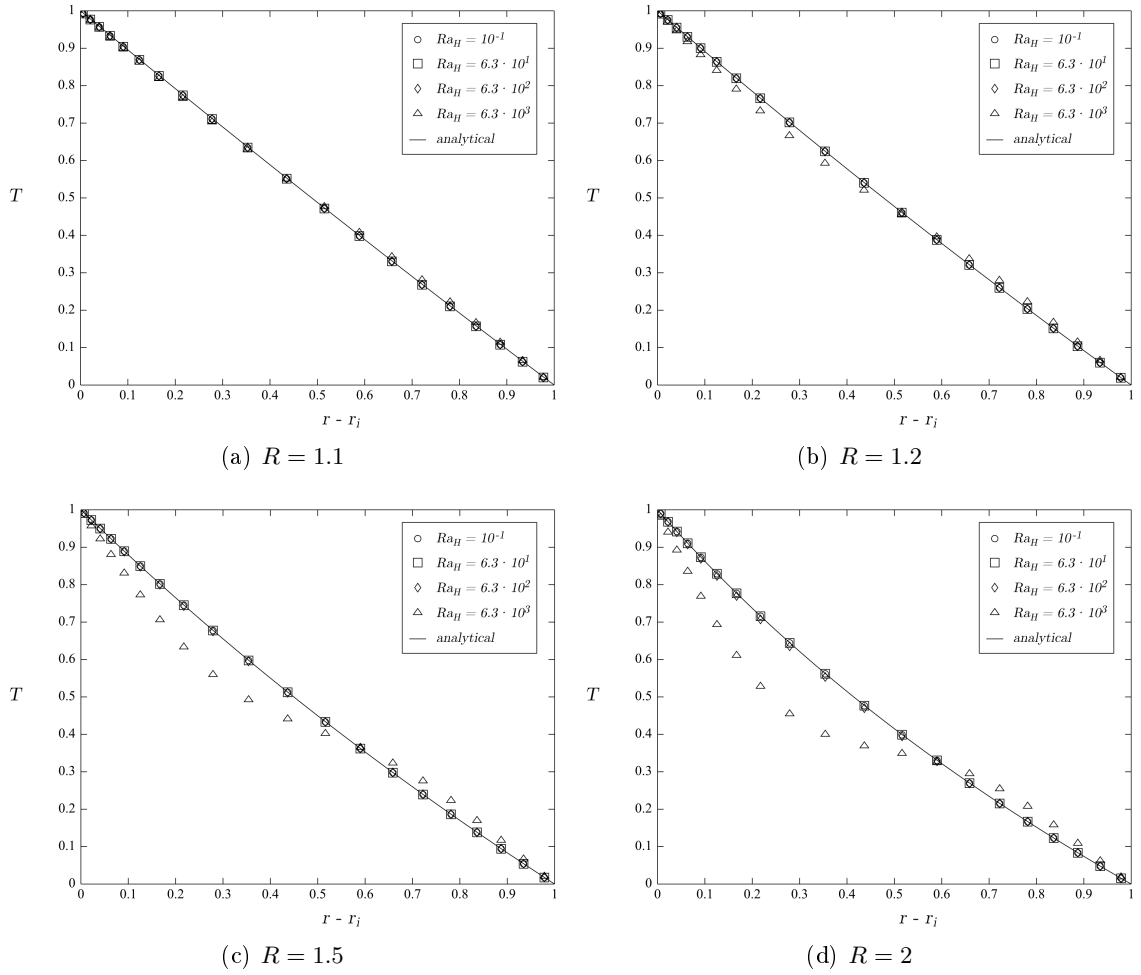


Figure 5.9: Analytical and numerical profiles of temperature T at $\theta = 0$, for four Ra_H -values, and for narrow and moderate gap annuli.

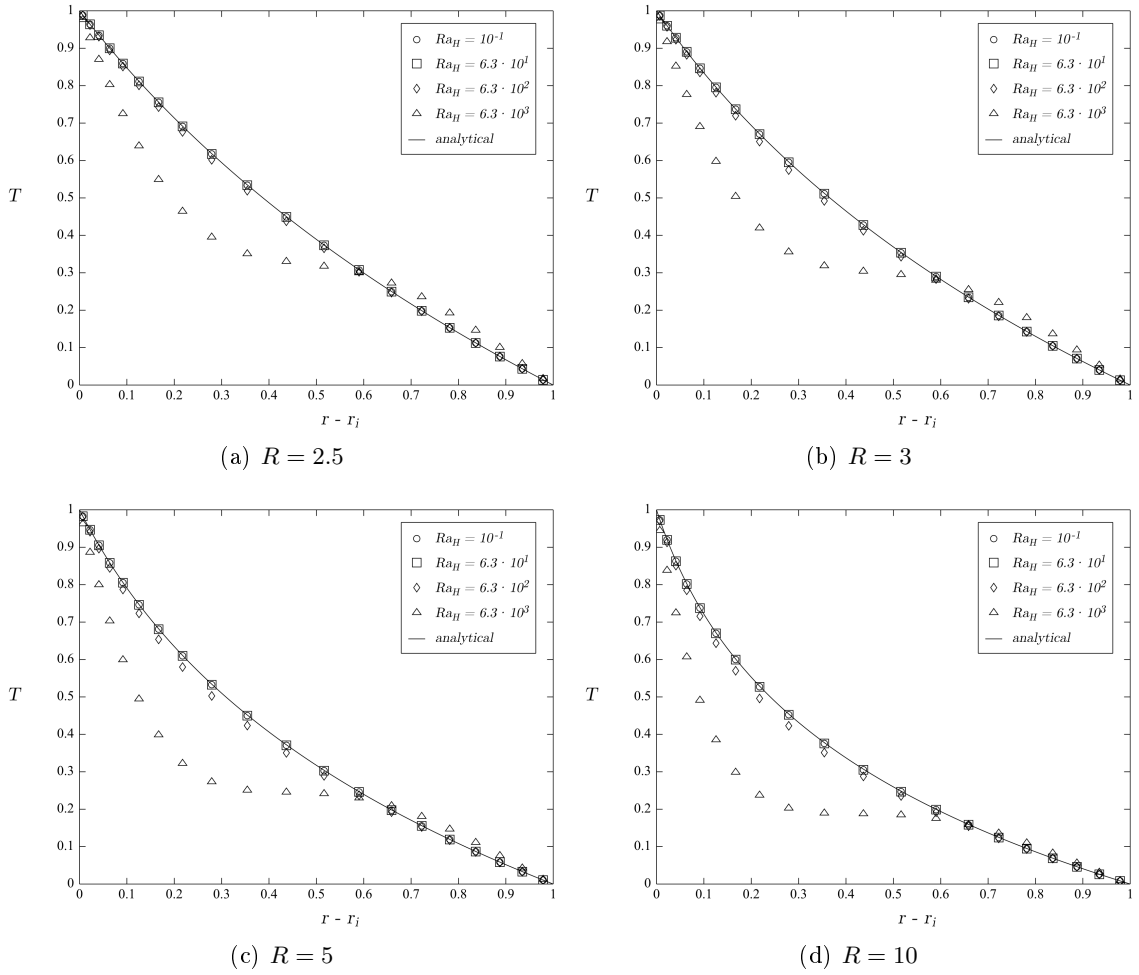


Figure 5.10: Analytical and numerical profiles of temperature T at $\theta = 0$, for four Ra_H -values, and for large gap annuli.

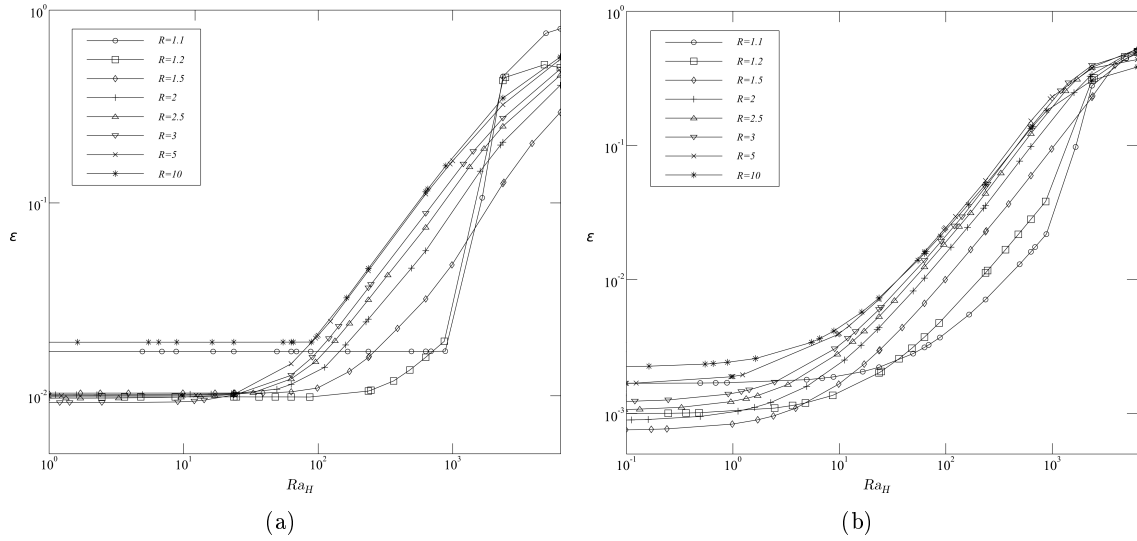


Figure 5.11: Trends of the maximum relative deviations between analytical and numerical results: (a) ϵ_u vs. Ra_H ; (b) ϵ_T vs. Ra_H .

and ϵ_T of the numerical predictions for u_θ and T towards analytical results in the pseudo-diffusive range, as a function of Ra_H . The two indices are defined by the following expressions:

$$\epsilon_u = \frac{\max |u_{\theta,num} - u_{\theta,pd}|}{\max |u_{\theta,pd}|} \quad (5.4.2)$$

$$\epsilon_T = \frac{\max |T_{num} - T_{pd}|}{\max |T_{pd}|} \quad (5.4.3)$$

(5.4.4)

From the graphs, it can be concluded that, for sufficiently low Ra_H , the deviations ϵ_u and ϵ_T remain constant. This indicates that such deviations are contributed by the sole numerical error, of the order of one percentage point. For Ra_H -values of order 10^2 , such deviations begin to increase, thus marking the start of the transition to steady convection. In most of the cases, such a transition appears to occur smoothly; however, this is not the case for low- R annuli: in fact, as shown in Figure 5.11(a), for $R = 1.1$ and $R = 1.2$ the value of ϵ_u remains almost constant up to $Ra_H \approx 10^3$, then it drastically increases above 10%. An analogous tendency is observable also in Figure 5.11(b), although the variation of ϵ_T appears to be somewhat smoother. This steep increase in ϵ_u can be read as a sign of the occurrence of a Rayleigh-Bénard instability, breaking the pseudo-diffusive patterns.

By logarithmic interpolation of the computed deviations, the values of Ra_H for which ϵ_u and ϵ_T match the value $\epsilon = 0.1$ have been determined for each value of R . A threshold of 10% has been considered as appropriate, in order to determine the magnitude of Ra_H for which a significant advective effect is observable, as a function of R . Such values have then been used to construct a correlation for the limit of the pseudo-diffusive regime, based

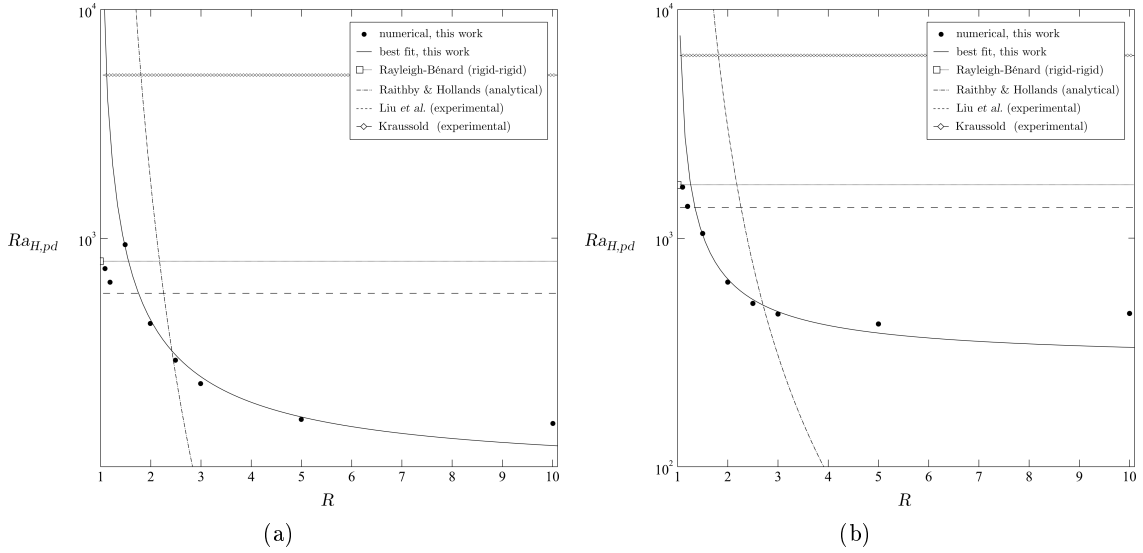


Figure 5.12: Correlating equations for the limits of the pseudo-diffusive flows, as compared with numerical data and literature results: a) $Ra_{H,pd,u}$ vs. R , equation (5.4.6), b) $Ra_{H,pd,T}$ vs. R , equation (5.4.6).

on the scale analysis in Section 5.3. An equation of the form:

$$Ra_{H,pd} = C_1 + \frac{C_2}{R - 1} \quad (5.4.5)$$

has been chosen for data fitting. Moreover, in the light of the above considerations, the data related to the two narrowest gaps have not been retained for the determination of the best fit.

The procedure yielded the following equations:

$$Ra_{H,pd,u} = 384.3 + \frac{750.6}{R - 1} \quad (5.4.6)$$

based on the deviation of u_θ , and:

$$Ra_{H,pd,T} = 291.7 + \frac{370.4}{R - 1} \quad (5.4.7)$$

based on the deviation ϵ_T .

The computed critical values, and the corresponding correlating equations, (5.4.6) and (5.4.7) are reported in Figures 5.12(a) and 5.12(b), alongside with the correlations reported in Table 5.1. It is seen that the critical threshold of Kraussold [157] always overestimates the $PD - S$ transition, but it must be noted that such a value has been carried out for Pr -values much higher than the one considered here ($Pr = 1$). Also the correlation of Liu *et al.* [158], overestimates $Ra_{H,pd}$, although with lower bias with respect to the present predictions. The analytical correlation of Raithby and Hollands [86], instead, is apparently out of target. However, their equation gives a rather precise estimate of the critical Ra_H value for which $Nu_H > Nu_{H,cond}$, while equations (5.4.6) and (5.4.7) refer to a virtual threshold up to which advective effects become comparable to diffusive ones in the flow

and temperature field. The two issues are indeed quite different, and it is reasonable to expect that the related results might not be comparable.

Finally, it can be observed that the computed Ra_H -thresholds for the two narrowest gap annuli are very close to the critical value of Rayleigh-Bénard convection, thus corroborating the above considerations on the validity of the proposed scaling laws.

5.5 Summary

In the present chapter, an analytical and numerical study of the limits of pseudo-diffusive buoyant regimes in annular gaps between concentric cylinders has been presented. Two approximate solutions of the flow and temperature fields, one obtained under the assumption of negligible convection, and the other in the narrow gap limit, have been proposed and rewritten according to the present non-dimensionalization. In particular, some critical issues concerning the solution of Desrayaud *et al.* [12] for the narrow gap limit, have been addressed and resolved, and its validity limits have been assessed.

The scaling laws for the transition from pseudo-diffusive flows to steady convection have been determined, and a quantitative character has been given to such laws, by the comparison between numerical results and the analytical solution in the pseudo-diffusive limit.

Finally, the limits of the pseudo-diffusive regime in a horizontal annulus have been abridged in the form of two correlating equations, valid for $Pr = 1$ and $R \geq 1.5$.

Concluding Remarks

The aim of the present research was to investigate the onset of transitional, buoyancy-induced flow regimes in confined systems. Such a topic has been largely addressed in the literature; the main results concerning three fundamental cases (the Rayleigh-Bénard problem, the vertical enclosure and the horizontal annulus) are thoroughly reviewed in Chapter 2.

In first instance, natural convection heat transfer from a horizontal cylinder centred in an enclosure of square cross-section was investigated numerically, by means of an original technique, whose details are described in Chapter 3. Such a system can ideally be placed halfways between a fundamental case and a real-world application.

Under the Boussinesq approximation, the system has been characterised in terms of its main parameters: the Rayleigh number Ra_H (based on the minimum gap width H between the cylinder and the enclosure walls) the Prandtl number Pr , and the aspect ratio A . For four different values of the aspect ratio, a wide range of Rayleigh number values was explored, encompassing the stability limit for long-term steady-regimes. Pseudo-diffusive, steady-symmetric, periodic, and more complex time-dependent flow-regimes were detected. A general critical threshold, $Ra_H \leq 2 \times 10^4$ has been proposed for stability of flows with $Pr = 0.7$ (a typical value for gases), valid for $2.5 \leq A \leq 10$. Even if approximate, this estimate is the only one available for this class of problems, for the time being.

Substantial differences were observed in the flow and thermal fields, depending on the aspect ratio and the Rayleigh number, in the regions of either asymptotically-steady or time-dependent flows. In particular, it was observed that for low values of the aspect ratio A , the dynamics of transition are dominated by the behaviour of the thermal plume arising from the cylindrical source, while for higher values of the parameter, the flow asset and early bifurcations are primarily determined by the formation of Rayleigh-Bénard-type rolls above the heat source. The existence of a limiting A -value, $3.3 \leq A \leq 5$, marking the transition from one behaviour to the other has then been postulated.

The effect of the imposition of different boundary conditions on the heat transfer performance of the system was also discussed. The isoflux cylinder was generally found to be more efficient in terms of heat transfer coefficient, and more stable than the isothermal one.

The influence of the Prandtl number, Pr , was also envisaged, by considering three more Pr -values, representative of liquid metals ($Pr = 0.07$), water ($Pr = 7$), and oils ($Pr = 70$), respectively. The results in terms of the asymptotic flow and thermal configurations spot out that the influence of Pr is not negligible, in particular when considering low- Pr fluids. In particular, for $Pr = 0.07$, transitional phenomena occur very early, far below the proposed critical threshold for stability. Moreover, high-Prandtl-number flows were found to be characterized by a longer approach to steady-state, with a noticeable separation

between the asymptotic time scales for temperature and velocity. In contrast, the overall heat transfer rate appears to be influenced by the Prandtl number only for low Pr -values.

A general correlating equation for the average Nusselt number on the cylinder, as a function on both the Rayleigh number and the aspect ratio, was derived for $Pr = 0.7$, covering the whole steady-state region. Extensive comparison with the available literature data allowed to ascribe the correlation an accuracy better than ± 10 .

The correlation was found to be roughly valid also in the case a constant heat flux is imposed on the cylinder surface. The agreement with heat transfer data obtained for $Pr \geq 0.7$ was instead excellent.

All in all, the results were found to be in good accordance with the limited literature available on similar cases. The general reliability of the methodologies adopted was then assessed, thus making room for a number of further developments of the current study.

Secondly, the nature of the transition from diffusion-dominated regimes to convective regimes was investigated, for the case of a horizontal annulus between concentric, differentially heated cylinders. It was pointed out that this kind of transition is not linked to the occurrence of a bifurcation, but, instead, it often occurs smoothly for increasing Ra . For this reason, analytical tools and scale analysis have been used together with numerical simulations, in order to determine a scale relation, correlating the critical values of governing parameters, for which this transition occurs.

The present study represents a limited but nevertheless significant contribution to the research in the field of natural convection. The number of issues which remain uncovered in this field is however enormous, and there is the need for fresh reliable results and novel meaningful interpretations, particularly as for the understanding and the control of supercritical unsteady regimes. These could in fact constitute a key factor in new natural convection-based heat transfer technology, provided that their origin and nature are fully understood, an appropriate tools are devised to promote or suppress them. The numerical approach adopted here has revealed suitable for the exploration of a delicate topic as transition is, and its exploitation for further analyses is therefore made feasible.

Appendix A

Rules of scale analysis

Scale analysis is a technique aimed at estimating the orders of magnitude of the characteristic quantities of a specific problem, given its governing equations and boundary and initial conditions. Although it does not provide accurate predictions, but only estimates, of the quantities of interest, scale analysis stands as a very precious tool, especially in the initial phases of a study, in that it often offers primary indications for the choice of the appropriate approach to be used in the successive phases of the investigation, and for the interpretation of the subsequent results.

Scale analysis is often confused with dimensional analysis, to which it is actually rather close, but from which it differs as for the objectives. In fact, the goal of dimensional analysis is to determine the relevant independent dimensionless groups for the problem of interest (even when its governing equations are unknown); when it is applied through non-dimensionalization of the governing equations, it also offers negligibility criteria for the terms of the equations themselves. Instead, scale analysis provides approximate estimates of the characteristic quantities of a given problem (*e.g.* the boundary layer thickness, the width of a fluid jet, etc.), and it requires some of the features of the problem to be known or postulated.

The basic rules of scale analysis are the following:

1. to define the spatial extent of the region over which the analysis shall be performed, and to select the unknown quantity of which an estimate is desired;
2. to evaluate the terms of the equations governing the problem by orders of magnitude. Such an estimate has to be done by guessing the maximum range of variation of each dependent variable, and its spatial or temporal scale. In scale analysis, one equation constitutes an equivalence between the scales of two dominant terms appearing in the equation. When an equation contains more than two terms, the dominant terms must be identified. Such a selection is done according to rules 3-5;
3. if in the sum of two terms:

$$c = a + b$$

the order of magnitude of term a is greater than the order of magnitude of the term b :

$$O(a) > O(b)$$

then the order of magnitude of the sum is dictated by the dominant term:

$$O(c) = O(a)$$

4. if in the sum of two terms:

$$c = a + b$$

the two terms are of the same order of magnitude:

$$O(a) = O(b)$$

then the sum is also of the same order of magnitude:

$$O(c) = O(a) = O(b)$$

5. in any product:

$$p = ab$$

the order of magnitude of the product is equal to the product of the orders of magnitude of the two factors:

$$O(p) = O(a) O(b)$$

and the order of magnitude of a ratio:

$$r = \frac{a}{b}$$

is equal to the ratio of the orders of magnitude of the two factors:

$$O(r) = \frac{O(a)}{O(b)}$$

Appendix B

Elements of bifurcation theory

An overview of the main topics of bifurcation theory is provided, following the lecture notes written by Prof. Valter Franceschini for a short course on *Dynamical Systems and Chaos* [159]. This summary cannot be considered neither exhaustive nor rigorous, just aiming at introducing a set of concepts and mathematical tools which are frequently recalled or used throughout the text. Integrations are taken from specialized texts in the field of dynamical systems theory [21] and time series analysis [160, 161, 162], which are left for further reference.

B.1 Introductory definitions

Definition. A *dynamical system* is an equation describing the temporal evolution of a variable $\mathbf{X} \in \mathbb{R}^n$. In general, \mathbf{X} represents the state of a physical system. A dynamical system can be:

- a *flow* (continuous time system): $\dot{\mathbf{X}} = \mathbf{F}(\mathbf{X}, \mu)$
- a *map* (discrete time system): $\mathbf{X}_{k+1} = \mathbf{G}(\mathbf{X}_k, \mu)$

$\mu \equiv (\mu_1, \mu_2, \dots, \mu_m)$ denotes an external m -dimensional parameter.

The evolution of the system is called *trajectory*, and it can be represented as a line (for a flow) or a set of points (for a map) in *phase space*, the space defined by all the components of \mathbf{X} .

Definition. A flow is said to be *autonomous* if it does not depend explicitly on time. Non-autonomous flows

$$\dot{\mathbf{X}} = \mathbf{F}(\mathbf{X}, t, \mu)$$

can be made autonomous by adding the equation

$$\dot{t} = 1$$

Dynamical systems can be either *conservative* or *dissipative*. Such a distinction is bound to the energy conservation properties of the system itself. In the first case one has *conservation of volumes* in phase space, while in the latter case, dissipation implies *contraction of volumes*.

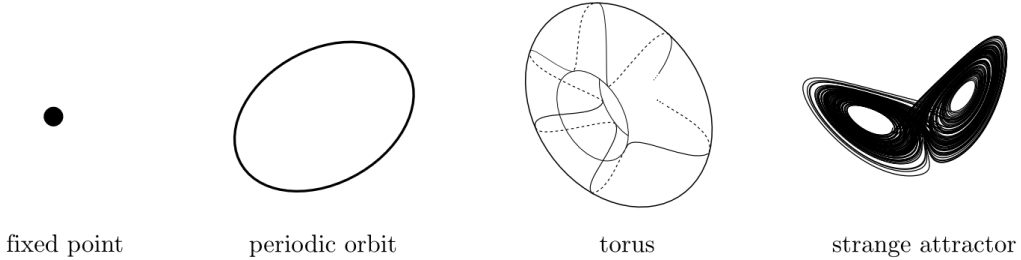


Figure B.1: Different types of attractors of a flow.

The condition for a flow to be dissipative is that its divergence must be negative for each point in phase space:

$$\sum_{i=1}^n \frac{\partial F_i}{\partial x_i}(\mathbf{X}) < 0, \quad \forall \mathbf{X} \in \mathbb{R}^n$$

while for a map it must be:

$$|D\mathbf{G}| < 1, \quad \forall \mathbf{X} \in \mathbb{R}^n$$

where $D\mathbf{G}$ is the *Jacobian matrix* of the map. In the following, the focus will be restricted on dissipative systems, and on their asymptotic behaviour. For simplicity, only systems with a single parameter μ will be considered.

B.2 Attractors

Asymptotically, the solutions of a dissipative system tend to an *attractor*. A mathematical definition of such an object is provided here, limited to the case of a flow, although an analogous definition can be given for maps.

In order to define what an attractor is, the definition of *invariant set* must be given first.

Definition. An *invariant set* is a subset $A \subset \mathbb{R}^n$ such that:

$$\mathbf{X}(t) \in A, \quad \forall \mathbf{X}(0) \in A$$

Definition. An invariant set A is an *attractor* if:

$$\exists \delta > 0 : d(\mathbf{X}(0), A) \leq \delta \Rightarrow \lim_{t \rightarrow \infty} d(\mathbf{X}(t), A) = 0$$

Definition. The *basin of attraction* of an attractor A is defined as the set of all the points \mathbf{x}_0 which give rise to trajectories attracted by A .

A dynamical system can admit a multiplicity of coexisting attractors for the same values of the parameter μ . In this case, each attractor has its own basin of attraction. The phenomenon of the coexistence of attractors is frequently observed in the study of dynamical systems, and it is called *hysteresis*.

B.2.1 Attractors of a flow

The possible attractors for a flow are reported in Figure B.1, and are defined as follows.

Definition. \mathbf{x}_0 is a *fixed point* if:

$$\mathbf{F}(\mathbf{x}_0) = \mathbf{0}$$

Definition. A *periodic* or *closed orbit* is an integral curve $\Gamma(t)$ of the flow, such that:

$$\exists T > 0 : \Gamma(t + T) = \Gamma(t) \forall t$$

The minimum positive T for which the relationship is valid is the *period* of the orbit.

Definition. A *torus* T^k is a surface given by the Cartesian product $[0, 2\pi]^k$ in a suitable angular coordinate system $(\phi_1, \phi_2, \dots, \phi_k)$. A solution $\Gamma(t)$ on a torus T^k is said to be *quasi-periodic* if each $\phi_j(t)$ is periodic with respect to t , *i.e.* if:

$$\phi_j(t) = \omega_j t$$

Hence, when the attractor is said to be a torus T^k , it means that, asymptotically, the solution tends to be quasi-periodic with k incommensurable periods T_j (or with k incommensurable frequencies f_j) such that:

$$T_j = \frac{2\pi}{\omega_j} \quad f_j = \frac{\omega_j}{2\pi}$$

The term “incommensurable” indicates that, in general, the k frequencies of the torus are, by twos, related by an irrational ratio. This means that, in no way, a trajectory approaching a torus, with k incommensurable frequencies, can be a closed orbit on the torus itself, but, asymptotically, it will *densely* overlay the surface of the torus.

Since tori normally exist for finite intervals of the parameter μ , as μ increases, the frequencies and their ratios continuously change. Hence, it can happen that two incommensurable frequencies, for some value of μ become commensurable, *i.e.* linked by a rational ratio, or *locked*. In this case, the trajectory becomes a closed orbit on the torus. This phenomenon is called *phase locking*, and sometimes it is observable and persistent for a finite range of values of μ .

Now, two definitions are provided, more operative than mathematical, of the class of attractors representing *chaos*. The first definition addresses both their geometrical nature and the dynamics which originates on them, while the second one is instead purely operative.

Definition. A *strange attractor* is an attractor having fractal (non integer) dimension, characterised by a strong dependence on initial conditions.

Definition. (Alternative definition of the strange attractor) A *strange attractor* is an attractor which is neither a fixed point, nor a periodic orbit or a torus.

The *fractal* property of strange attractors is explained by their particular geometrical structure, which remains identical to itself, when analyzed on increasingly small scales.

FLUXES	MAPS
FIXED POINT	
CLOSED ORBIT	PERIODIC ORBIT
TORUS T^k , $k = 2, 3, \dots$	TORUS T^{k-1}
STRANGE ATTRACTOR	STRANGE ATTRACTOR

Table B.1: Correspondence between attractors for flows and maps

The main property of a strange attractor, however, lies in its strong *sensitivity to initial conditions*. This means that two initial conditions, arbitrarily close to one another, give rise, on the attractor, to *exponentially diverging trajectories*.

Moreover, chaotic dynamics are also determined by a multiplicity of attractors, of extremely diverse nature. Each of them has its own basin of attraction, and those basins, if not interlaced to each other, at least share their frontier. Thus, a slight perturbation of the initial conditions might bring the solution on one attractor rather than on another one, determining completely different dynamics, from a qualitative standpoint.

B.2.2 Attractors of a map

Table B.1 draws a correspondence between the possible types of attractors for flows and for maps. The proposed scheme takes into account the fact that, for any flow, it is possible to construct, by means of an appropriate section, the *Poincaré section*, a $(N - 1)$ -dimensional map, also named as *first return map*.

B.3 Bifurcations

B.3.1 Bifurcations of a fixed point

Theorem B.3.1 (Stability of a fixed point) *A fixed point \mathbf{x}_0 is stable and attractive if all the eigenvalues of the Jacobian matrix (or Lyapunov matrix) of \mathbf{F} in \mathbf{x}_0 , $D\mathbf{F}(\mathbf{x}_0)$ have negative real part.*

A fixed point \mathbf{x}_0 , stable and attractive for $\mu = \mu_0$, undergoes a *bifurcation*, if, with varying μ , some qualitative change in the stability of the state itself occurs. The bifurcations of a fixed point are listed in the following, assuming that the critical value of the parameter μ for which they occur is $\mu = \mu_c$, and that μ varies increasingly.

Saddle-node bifurcation. A *saddle-node* or *tangent* bifurcation occurs when, for $\mu \rightarrow \mu_c$, two fixed points \mathbf{x}_0 and \mathbf{x}_0^* , one stable and one unstable, tend to each other, and disappear for $\mu = \mu_c$, collapsing into one another (Figure B.2(a)). Mathematically, a saddle-node bifurcation occurs when a real eigenvalue of $D\mathbf{F}(\mathbf{x}_0)$ tends to zero, although not crossing the imaginary axis.

The saddle-node bifurcation is the most common way through which a fixed point disappears (or appears, if the μ -axis is followed backwards).

Transcritical bifurcation. This bifurcation, also commonly known as *exchange of stability*, occurs when two separate fixed points \mathbf{x}_0 and \mathbf{x}_0^* , one stable and one unstable,

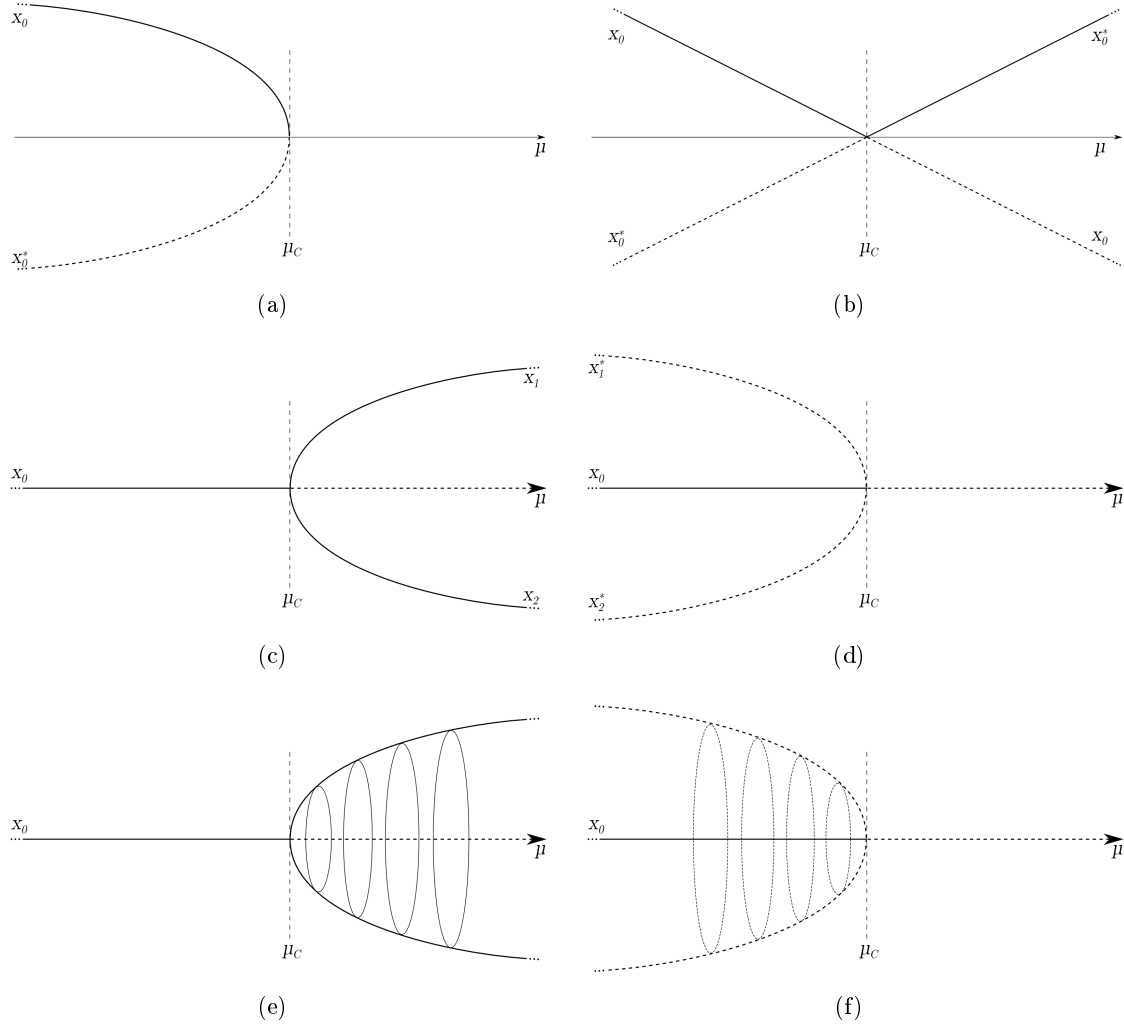


Figure B.2: Bifurcations of a fixed point: (a) saddle-node; (b) transcritical; (c) supercritical pitchfork; (d) subcritical pitchfork; (e) supercritical Hopf; (f) subcritical Hopf. Continuous and dashed lines represent stable and unstable states, respectively.

coalesce into each other for $\mu = \mu_c$; for $\mu > \mu_c$ the two solutions separate each other again after having exchanged their stability (Figure B.2(b)).

A transcritical bifurcation occurs when a real eigenvalue of $D\mathbf{F}(\mathbf{x}_0)$ crosses the imaginary axis and becomes positive.

Pitchfork bifurcation. *Pitchfork* bifurcations can be of two kinds: *supercritical* (or *direct*) or *subcritical* (or *inverse*).

A direct pitchfork bifurcation (Figure B.2(c)) occurs when, for $\mu = \mu_c$, a stable fixed point \mathbf{x}_0 becomes unstable, originating two new fixed points \mathbf{x}_1 and \mathbf{x}_2 , which are stable and attractive for $\mu > \mu_c$.

An inverse pitchfork bifurcation (Figure B.2(d)) occurs instead when, for $\mu < \mu_c$, two unstable fixed points \mathbf{x}_1^* and \mathbf{x}_2^* exist besides \mathbf{x}_0 , and collapse into \mathbf{x}_0 for $\mu = \mu_c$, turning \mathbf{x}_0 into an unstable point. The points \mathbf{x}_1 and \mathbf{x}_2 , as well as \mathbf{x}_1^* \mathbf{x}_2^* are symmetric with

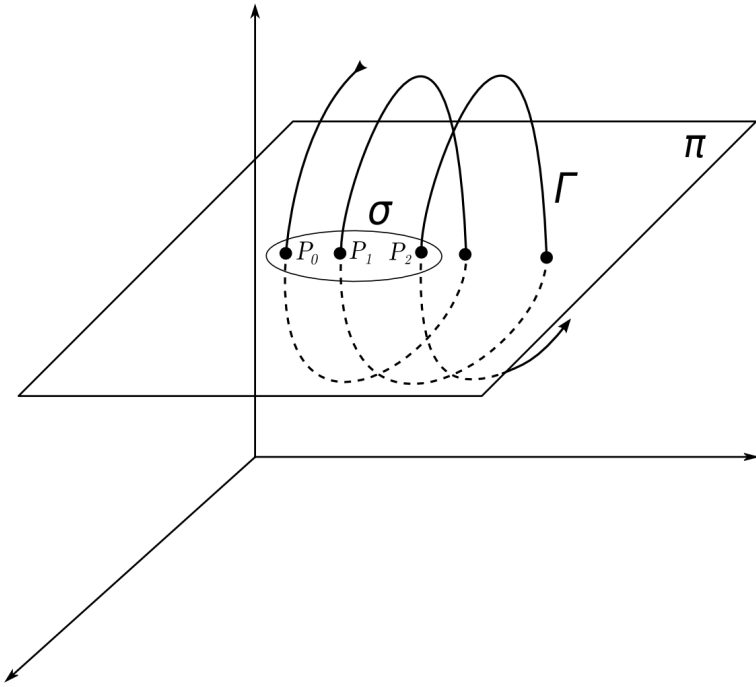


Figure B.3: Schematic of a Poincaré section

respect to \mathbf{x}_0 .

Analogously to the transcritical bifurcation, a pitchfork bifurcation occurs when a real eigenvalue of $D\mathbf{F}(\mathbf{x}_0)$ crosses the imaginary axis and becomes positive.

Hopf bifurcation. As the pitchfork bifurcation, also the *Hopf* bifurcation can be supercritical or subcritical. In the direct case (Figure B.2(e)), for $\mu = \mu_c$, the fixed point \mathbf{x}_0 , generates, while becoming unstable, a closed orbit $\Gamma(t, \mu)$, which is stable and attractive for $\mu > \mu_c$.

In the inverse case (Figure B.2(f)), an unstable closed orbit $\Gamma^*(t, \mu)$ “surrounds” \mathbf{x}_0 for $\mu < \mu_c$, and closes into it as $\mu \rightarrow \mu_c$. For $\mu = \mu_c$, the orbit $\Gamma^*(t, \mu)$ collapses into \mathbf{x}_0 , turning it into an unstable point.

The bifurcation takes place when a pair of complex conjugate eigenvalues of $D\mathbf{F}(\mathbf{x}_0)$ crosses the imaginary axis for $\mu = \mu_c$, their real part becoming positive. In both cases, the period of the orbit $\Gamma(t, \mu)$, for $\mu \rightarrow \mu_c$, tends to $2\pi/|\lambda_0|$, λ_0 being the imaginary part of the eigenvalues crossing the imaginary axis.

The *radius* r of the orbit generated by a Hopf bifurcation, $\mu \rightarrow \mu_c$, behaves as follows:

$$r \simeq a\sqrt{|\mu - \mu_c|}$$

where a is a constant.

B.3.2 Bifurcations of a periodic orbit

The concept of stability of a periodic orbit Γ is linked to that of *Poincaré* map.

Definition. Let π be a $(N - 1)$ -dimensional hyperplane transverse to a trajectory Γ in a given point \mathbf{x}_0 , and σ a portion of π containing \mathbf{x}_0 . The *Poincaré map* is defined as the map Φ of σ in itself, such that $\Phi(\mathbf{y})$, $\mathbf{y} \in \sigma$ is the first intersection of the solution curve passing through \mathbf{y} with σ . The hyperplane π is also called a *Poincaré section* (Figure B.3).

It is often convenient to define the plane π by fixing one of the N coordinates, *i.e.* a plane for which $x^{(k)} = x_0^{(k)}$.

With reference to Figure B.3, it is:

$$P_1 = \Phi(P_0), \quad P_2 = \Phi(P_1) = \Phi^2(P_0), \quad \dots \quad P_k = \Phi(P_{k-1}) = \Phi^2(P_{k-2}) = \dots = \Phi^k(P_0)$$

If the trajectory Γ is a closed curve, one has:

$$P_0 \in \Gamma \Leftrightarrow \Phi(P_0) = P_0$$

i.e. P_0 is a fixed point for the map Φ .

Theorem B.3.2 (Stability of a closed orbit) *A closed orbit Γ is stable and attractive if all the eigenvalues of the Jacobian matrix (Lyapunov matrix) of its Poincaré map in \mathbf{x}_0 , $D\Phi(\mathbf{x}_0)$ are internal to the unit circle. If at least one eigenvalue lies outside the unit circle, Γ is unstable.*

From the above stability theorem, it can be clearly deduced that the theory of bifurcation for periodic orbits of a flow reduces itself to that of periodic orbits of a map. Such a theory is completely analogous to that of fixed points for a flow. While, for a fixed point, what determines a bifurcation is the way an eigenvalue crosses the imaginary axis, becoming positive, for a periodic orbit it is the way an eigenvalue becomes of unit modulus and crosses the unit circle.

Hence, the same bifurcations of a fixed point are found to occur also in the case of a periodic orbit, with the addition of *period doubling*.

Saddle-node bifurcation. A saddle-node bifurcation occurs when, for $\mu \rightarrow \mu_c$, two orbits Γ and Γ^* , one stable and one unstable, tend to each other, and disappear, collapsing into each other, for $\mu = \mu_c$ (Figure B.4(a)). This occurs when a real eigenvalue of $D\Phi(\mathbf{x}_0)$ tends to one, although not crossing the unit circle. As in the case of fixed points, the saddle-node bifurcation is the most common way through which a periodic orbit disappears (or appears).

Transcritical bifurcation. This bifurcation, occurs when two separate orbits Γ and Γ^* , one stable and one unstable, coalesce into each other for $\mu = \mu_c$; for $\mu > \mu_c$ the two solutions separate each other again after having exchanged their stability (Figure B.4(b)). This occurs when a real eigenvalue of $D\Phi(\mathbf{x}_0)$ crosses the unit circle at $\lambda = +1$.

Pitchfork bifurcation. Pitchfork bifurcations are of two kinds, direct or inverse, also for periodic orbits.

A direct pitchfork bifurcation (Figure B.4(c)) occurs when, for $\mu = \mu_c$, a stable, symmetric closed orbit Γ becomes unstable, originating two new orbits Γ_1 and Γ_2 , which are stable and attractive for $\mu > \mu_c$.

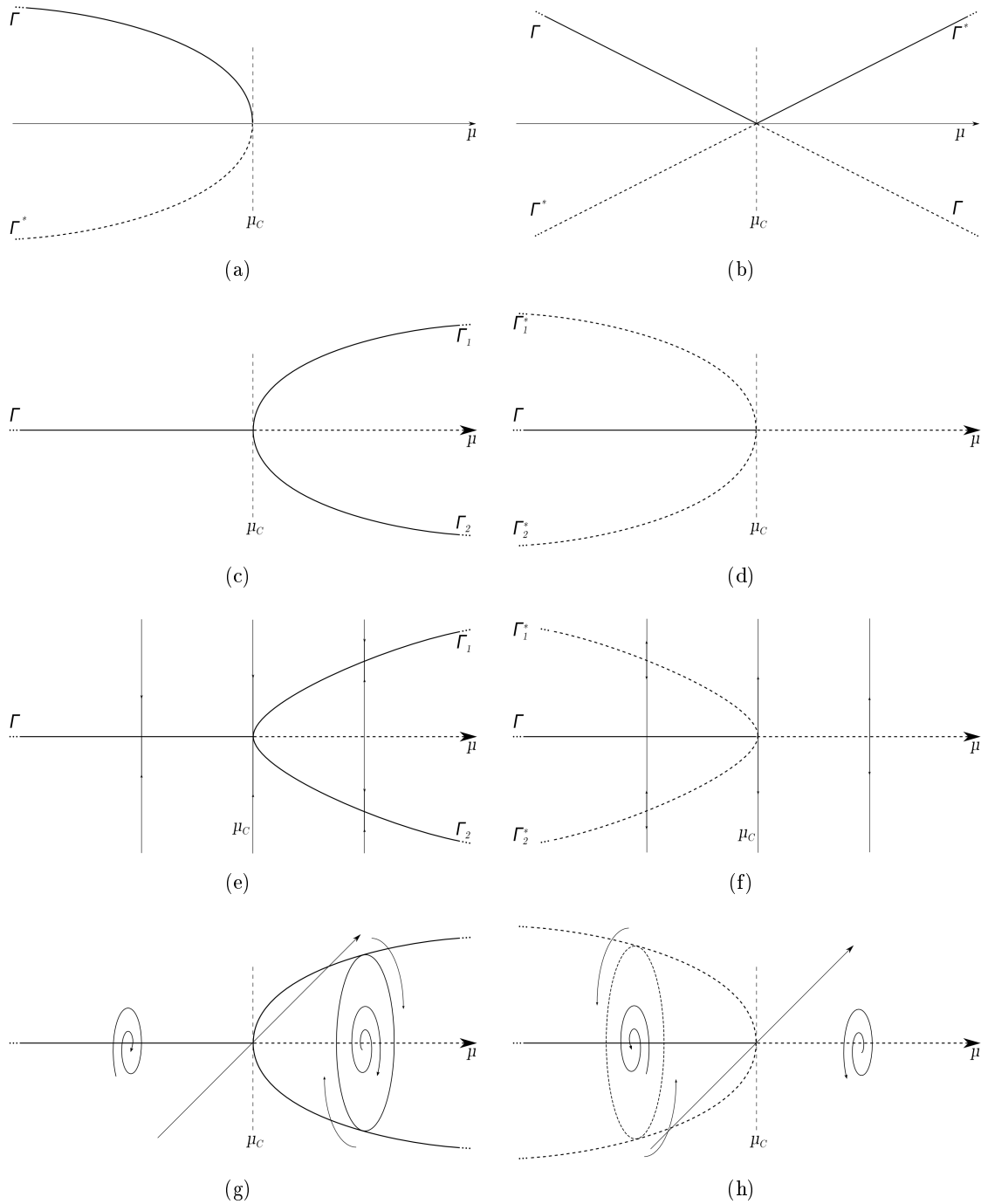


Figure B.4: Bifurcations of a periodic orbit: (a) saddle-node; (b) transcritical; (c) super-critical pitchfork; (d) subcritical pitchfork; (e) direct period doubling; (f) inverse period doubling; (g) supercritical secondary Hopf; (h) subcritical secondary Hopf. Continuous and dashed lines represent stable and unstable states, respectively.

An inverse pitchfork bifurcation (Figure B.4(d)) occurs instead when, for $\mu < \mu_c$, two unstable orbits Γ_1^* and Γ_2^* exist along Γ , and collapse into Γ for $\mu = \mu_c$, turning Γ into an unstable orbit.

In both cases, such a bifurcation occurs when a real eigenvalue of $D\Phi(\mathbf{x}_0)$ crosses the unit circle at $\lambda = +1$.

It shall be noted that Γ_1 and Γ_2 , as well as Γ_1^* and Γ_2^* , are symmetric with respect to Γ . Moreover, while Γ is internally symmetric, Γ_1 and Γ_2 , as well as Γ_1^* and Γ_2^* , are not; hence, the bifurcation actually breaks the symmetry of the system. For this reason, pitchfork bifurcations are also known as *symmetry breaking bifurcations*.

Period doubling bifurcation. Also *period doubling bifurcations* can be either supercritical or subcritical.

A supercritical period doubling occurs when, for $\mu = \mu_c$, a stable closed orbit Γ becomes unstable, originating one new orbit with a double period, stable and attractive for $\mu > \mu_c$.

A subcritical period doubling occurs instead when, for $\mu = \mu_c$, an unstable orbit with double period exists besides Γ ; for $\mu = \mu_c$, such an orbit collapses into Γ , which becomes unstable.

In both cases, such a bifurcation occurs when a real eigenvalue of $D\Phi(\mathbf{x}_0)$ crosses the unit circle at $\lambda = -1$.

The two bifurcation diagrams (Figures B.4(e) and B.4(f)) are identical to those of the pitchfork bifurcation (Figures B.4(c) and B.4(d)), with the exception that, in this case, the two orbits Γ_1 and Γ_2 (or Γ_1^* and Γ_2^*) must be viewed as a single orbit that completes two complete loops rather than one.

Bifurcation in a torus. The bifurcation of an orbit in a torus is also called *secondary Hopf bifurcation*. A supercritical and a subcritical type exist also in this case.

A direct bifurcation in a torus (Figure B.4(g)), occurs when for $\mu = \mu_c$, the stable orbit Γ , while becoming unstable, generates a T^2 torus, which is stable and attractive for $\mu > \mu_c$.

As for the inverse case (Figure B.4(h)), it occurs when the stable orbit Γ coexists with an unstable T^2 torus for $\mu < \mu_c$, and closes in to it as $\mu \rightarrow \mu_c$. For $\mu = \mu_c$, the torus collapses into Γ , which becomes unstable.

The bifurcation takes place when a pair of complex conjugate eigenvalues of $D\Phi(\mathbf{x}_0)$ crosses the unit circle.

It shall also be noted that an analogue type of bifurcation can occur between a T^2 and a T^3 torus.

B.4 Routes to chaos

The term *route* or *scenario to chaos* denotes a bifurcation, or a sequence of bifurcations, leading to the formation of a strange attractor and, therefore, to the onset of a chaotic dynamical behaviour. In the following, the most recurrent routes to chaos are reviewed.

Ruelle-Takens scenario. This scenario consists in the birth of a strange attractor through three Hopf bifurcations: the first one turns a fixed point into a closed orbit; through the second one, the orbit bifurcates in a T^2 torus; the third one sees the birth of

a T^3 torus out of the T^2 torus. If the three frequencies of the orbit on the T^3 torus are independent, it is very likely that a strange attractor could appear.

Period doubling scenario. In this scenario, a stable periodic orbit triggers an infinite sequence of period doubling bifurcations.

Let Γ_0 be a periodic orbit of period T_0 , becoming unstable for $\mu = \mu_1$, generating another orbit Γ_1 of period $T_1 = 2T_0$. Let also Γ_1 bifurcate, for $\mu = \mu_2$, in another orbit Γ_2 of period $T_2 = 2T_1 = 4T_0$, and so on, with the orbit Γ_{k-1} bifurcating, for $\mu = \mu_k$, in Γ_k with period $T_k = 2^k T_0$. This cascade of period doubling bifurcation, if infinite, is such that:

- $\exists \lim_{k \rightarrow \infty} \mu_k = \mu_\infty$
- $\exists \delta_F: \lim_{k \rightarrow \infty} \frac{|\mu_k - \mu_{k-1}|}{|\mu_{k+1} - \mu_k|} = \delta_F = 4.6642016\dots$
- for $\mu > \mu_\infty$, in general, a strange attractor appears.

δ_F is the *Feigenbaum constant*. It is a universal constant, in that it can be detected anytime an infinite period doubling cascade occurs in a dissipative dynamical system. Moreover, the spectral peaks of two consecutive period doublings are also related by a universal ratio of about 6.574, as $\mu \rightarrow \mu_\infty$.

It must be noted that, in many systems undergoing period doubling, an *inverse* cascade is witnessed to follow the direct route. In those cases, a strange attractor progressively turns a single periodic orbit, through an infinite sequence of period halving steps.

Pomeau-Manneville scenario. This scenario, also called the *intermittency* scenario, is quite common, and it can take place when a stable periodic orbit disappears collapsing, for a value $\mu = \mu_c$, into a nearby unstable orbit, due to a saddle-node bifurcation. The name “intermittency” refers to the characteristics of the dynamics of the system for $\mu > \mu_c$.

For $\mu < \mu_c$, the attractor is a periodic orbit, and the dynamics of the system consist of regular oscillations. For μ slightly greater than μ_c , the dynamics still appear to be periodic for long time spans; such intervals are separated by short chaotic “bursts”. For increasing μ , the duration of the periodic phases tends to shorten, while the number and length of the chaotic phases increases. At a certain point, there is no trace left of the former periodic behaviour.

Other relevant routes to chaos.

- The *breaking of a torus* is the most frequent mechanism bringing a T^2 torus to evolve into a strange attractor. It normally occurs when the Poincaré section of the torus, which is a closed curve, ceases to be a regular curve. The rupture of the torus is anticipated by the progressive formation, for increasing μ , of a singularity (a cusp, an inflection point, . . .) in its Poincaré map. This phenomenon is often related to the existence of an unstable periodic orbit which tends to close into the torus (but not to collapse into it).

- Another phenomenon which is often encountered when studying the route to chaos of a torus, is that of the disappearance of the strange attractor originated by the torus itself, due to *crisis*. Such crisis is caused by the collision between the strange attractor with the unstable periodic orbit which previously determined its formation.
- T^2 tori can also give rise to period doubling. The *period doubling of a torus* is evidenced by the doubling of the section curve, *i.e.* the Poincaré section of the torus itself, which signifies the halving of one of its two frequencies.

B.5 Methods for the analysis of dynamical systems

B.5.1 Determination of attractors

Studying a dynamical system means, in its ultimate acceptance, to analyze the asymptotic behaviour of its solutions, as a function of the external parameter μ , and of the initial conditions. The final result of such an analysis is the determination of the most relevant attractors and of the bifurcations related to them (*i.e.* their range of existence).

The simplest way of searching for attractors consists in three steps:

- a) to follow the evolution of the system for several values of μ , by numerically integrating the dynamical equations, with suitable initial conditions and sufficiently long relaxation times;
- b) to identify the nature of the attractors representing the different trajectories, by means of several plane and/or three-dimensional projections, and of Poincaré maps; for uncertain cases, the nature of the attractor can be defined by calculating its Lyapunov exponents and power spectra;
- c) to define the “life” of each attractor, by following it as the leading parameter is varied, and by studying all the bifurcations it undergoes. It shall be noted that, with varying μ , attractors and their basins of attraction modify continuously; hence, if \mathbf{x}_0 is a point of the attractor for $\mu = \mu_0$ and $\delta\mu$ is small enough, it is reasonable to think that \mathbf{x}_0 is a good initial condition, to “capture” the same attractor for $\mu = \mu_0 + \delta\mu$.

B.5.2 Power spectra

Spectral analysis (or *Fourier analysis*) is a useful tool for the determination of the exact nature of an attractor. In fact, by means of Fourier analysis, the frequencies of a function $x(t)$ can be detected.

If $x(t)$ is periodic of period T and frequency $f = T^{-1}$, then its spectrum is discrete, with peaks corresponding to the main frequency f and to its harmonics $2f, 3f, \dots$

If $x(t)$ is quasi-periodic with two frequencies f_1 and f_2 , then its spectrum contains all the integer combinations of the two frequencies:

$$m_1 f_1 + m_2 f_2 \quad \text{with} \quad m_1, m_2 = 0, 1, 2, \dots$$

Analogously, if the frequencies are three, as it happens for a T^3 torus, then the peaks of the spectrum correspond to all their integer combinations. Obviously, the more the frequencies are, the harder is the interpretation of the spectrum.

The characteristic of having a discrete spectrum is what distinguishes a non-chaotic attractor from a strange attractor; thus, a strange attractor can also be defined as an attractor whose spectrum is continuous.

The *Discrete Fourier Transform* (DFT) of a function $x(t)$ is obtained by calculating the following sums:

$$\hat{X}_j = \frac{1}{N} \sum_{k=0}^{N-1} x_k e^{-2\pi i j k / N}, \quad j = 0, \dots, N-1$$

where i is the imaginary unit. The points x_0, x_1, \dots, x_{N-1} form a sample of N points, for which $x_k = x(k\Delta)$, where Δ is a fixed sampling interval. The numbers $|\hat{X}_j|^2$, $j = 0, \dots, N-1$ form the *power spectrum* of $x(t)$.

Efficient routines for the calculation of the power spectrum of a time sequence are largely available in the most widespread numerical libraries. However, there are a number of issues which must be taken care of when analyzing the dynamics of a system by means of Fourier analysis, such as *aliasing* and *leakage*.

B.5.3 Autocorrelation function

When the study of power spectra does not provide satisfactory evidence of the periodicity of a given signal $x(t)$, it is useful to resort to the calculation of the *autocorrelation function*. Being H the time interval of observation, and τ a variable time delay, the autocorrelation function is defined as:

$$C(\tau) = \frac{1}{H} \int_H x(t)x(t+\tau)dt$$

The autocorrelation function measures the rate of similarity of the signal with itself, as time increases. If the signal is constant, periodic or quasi-periodic (*i.e.* it contains a definite degree of regularity and predictability), the autocorrelation function tends to be finite and greater than zero, also for large values of the delay τ , while for chaotic signals, it rapidly decays to zero as τ increases, for, as time passes, the internal similarity of the signal is invariably lost.

B.5.4 Lyapunov exponents

The *Lyapunov exponents* measure the average exponential velocity at which trajectories “close” to a fixed reference solution $\gamma(t)$, which is supposed to belong to an attractor, converge (or diverge) towards (from) γ itself. Lyapunov exponents are an effective tool for the determination of the nature of an attractor, and, in particular, for the detection of chaotic dynamics.

Being $\lambda_1 \leq \lambda_2 \leq \dots \leq \lambda_n$ the n Lyapunov exponents of the trajectory γ , one has that:

- $\lambda_1 < 0 \Leftrightarrow \gamma$ is on a fixed point
- $\lambda_1 = 0, \lambda_2 < 0 \Leftrightarrow \gamma$ is on a closed orbit
- $\lambda_1 = 0, \lambda_2 = 0, \lambda_3 < 0 \Leftrightarrow \gamma$ is on a T^2 torus
- $\lambda_1 = 0, \lambda_2 = 0, \lambda_3 = 0, \lambda_4 < 0 \Leftrightarrow \gamma$ is on a T^3 torus
- $\lambda_1 > 0, \dots, \lambda_{k-1} > 0, \lambda_k = 0, \lambda_{k+1} < 0, k > 1 \Leftrightarrow \gamma$ is on a strange attractor.

The Lyapunov *spectrum*, *i.e.* the set of Lyapunov exponents, is such that any number of exponents might be calculated, from the largest (the *leading Lyapunov exponent*) down to the smallest. Thus, for instance, in order to determine whether an attractor is chaotic or not, it is sufficient to calculate the sole leading exponent λ_1 : if λ_1 is positive, then the attractor is chaotic; otherwise, it is not.

A method for calculating λ_1 and λ_2 is now illustrated. Such a method will be further generalized for the calculation of m exponents, $1 \leq m < \leq n$.

Let $\gamma(t)$ be a reference trajectory and \mathbf{x}_0 a point on γ . Let also \mathbf{x}_1 and \mathbf{x}_2 be two points close to \mathbf{x}_0 and such that the vectors:

$$\mathbf{u}_1^0 = \mathbf{x}_1 - \mathbf{x}_0, \quad \mathbf{u}_2^0 = \mathbf{x}_2 - \mathbf{x}_0$$

are orthogonal and of equal length l . If $F^t(x)$ indicates the point to which the point \mathbf{x} has evolved after a given time t , and $F^t(\mathbf{u}_1^0)$ and $F^t(\mathbf{u}_2^0)$ indicate the vectors to which, at the same time, \mathbf{u}_1^0 and \mathbf{u}_2^0 have evolved, it is:

$$F^t(\mathbf{u}_1^0) = F^t(\mathbf{x}_1) - F^t(\mathbf{x}_0), \quad F^t(\mathbf{u}_2^0) = F^t(\mathbf{x}_2) - F^t(\mathbf{x}_0)$$

If the three trajectories starting from \mathbf{x}_0 , \mathbf{x}_1 and \mathbf{x}_2 are calculated for a given time H , and, the three vectors:

$$\mathbf{v}_1^1 = F^H(\mathbf{u}_1^0), \quad \mathbf{v}_2^1 = F^H(\mathbf{u}_2^0)$$

have been determined, the ratio:

$$\beta_1^1 = \frac{\|\mathbf{v}_1^1\|}{l}$$

measures the expansion or contraction of \mathbf{u}_1^0 under the action of the flow for the time H . If $(\mathbf{v}_2^1)_\perp$ indicates the component of \mathbf{v}_2^1 normal to \mathbf{v}_1^1 , the ratio:

$$\beta_2^1 = \frac{\|(\mathbf{v}_2^1)_\perp\|}{l}$$

measures the expansion (only possible if $\beta_1^1 > 1$) or contraction of \mathbf{u}_2^0 .

If the lengths of \mathbf{v}_1^1 and $(\mathbf{v}_2^1)_\perp$ are renormalized to l , two new vectors \mathbf{u}_1^1 and \mathbf{u}_2^1 are obtained, with length l and orthogonal to each other (as \mathbf{u}_1^0 and \mathbf{u}_2^0 were). Letting also \mathbf{u}_1^1 and \mathbf{u}_2^1 evolve for a time interval H , these will evolve into the vectors \mathbf{v}_1^2 and \mathbf{v}_2^2 , through which two new expansion or contraction coefficients, β_1^2 and β_2^2 , are obtained, together with two new vectors \mathbf{u}_1^2 and \mathbf{u}_2^2 , with length l and orthogonal to each other, which will evolve in the subsequent step of the procedure.

By iterating the procedure an infinite number of times, two successions $\{\beta_1^k\}$ and $\{\beta_2^k\}$ are obtained. Thus, the Lyapunov exponents λ_1 and λ_2 can be defined as follows:

$$\lambda_i = \lim_{k \rightarrow \infty} \frac{1}{kH} \sum_{h=1}^k \ln \beta_i^h, \quad i = 1, 2$$

In a real calculation, the approximations:

$$\lambda_i = \frac{1}{kH} \sum_{h=1}^k \ln \beta_i^h, \quad i = 1, 2$$

are considered, with k sufficiently large to allow the coefficients λ_i to be properly stabilized with the desired accuracy.

The calculation of m Lyapunov exponents, for $m > 2$, can be obtained with a simple generalization of the procedure described above for $m = 2$.

Let $\mathbf{u}_1^0, \mathbf{u}_2^0, \dots, \mathbf{u}_m^0$ the m initial vectors with origin in \mathbf{x}_0 , with modulus l and orthogonal by twos. Denoting with (\cdot, \cdot) the scalar product and remembering that:

$$\|\mathbf{w}\| = \sqrt{(\mathbf{w}, \mathbf{w})}$$

for $k = 1, \dots, K$ one has:

$$\mathbf{v}_1^k = F^H(\mathbf{u}_1^{(k-1)}), \quad \beta_1^k = \frac{\|\mathbf{v}_1^k\|}{l}, \quad \mathbf{u}_1^k = \frac{\mathbf{v}_1^k}{\beta_1^k}$$

and, for $i = 2, \dots, m$:

$$\begin{cases} \mathbf{v}_1^k = F^H(\mathbf{u}_i^{(k-1)}) - \sum_{j=1}^{i-1} (\mathbf{u}_j^k, F^H(\mathbf{u}_i^{(k-1)})) \mathbf{u}_j^k \\ \beta_i^k = \frac{\|\mathbf{v}_i^k\|}{l}, \quad \mathbf{u}_i^k = \frac{\mathbf{v}_i^k}{\beta_i^k} \end{cases}$$

Therefore:

$$\lambda_i = \frac{1}{KH} \sum_{h=1}^k \ln \beta_i^h, \quad i = 1, 2, \dots, m$$

where K is the number of iteration steps of the algorithm and, therefore, KH is the total time across which the vectors have evolved.

Remarks.

- a) the renormalization of the vectors \mathbf{u}_i^k at each interval H is necessary to avoid the occurrence of numerical overflow phenomena, due to the excessive length the vectors may assume;
- b) the reorthogonalization of the same vectors is necessary to prevent the occurrence of underflow, due to the angle between two vectors being too small;
- c) the quality of the model, the number m of the calculated Lyapunov exponents, the experience of the person performing the calculations and the availability of computing resources are all determinant elements for the correct choice of the time H between successive rescalings of the vectors \mathbf{u}_i^k , and of the number K of iterations.

B.5.5 Lyapunov dimension

Another relevant issue in the study of attractors is the problem of assigning a dimension to a strange attractor. There exist a number of methods which hint at a solution of the problem by relating the concepts of fractal dimension and Lyapunov exponents. The most reliable formula is that of Kaplan and Yorke, which leads to the determination of what is called the *Lyapunov dimension*. If $\lambda_1 \leq \lambda_2 \leq \dots \leq \lambda_n$ are the n Lyapunov exponents of a n -dimensional flow, the Lyapunov dimension is defined as follows:

$$D_L = j + \sum_{i=1}^j \frac{\lambda_i}{|\lambda j + 1|}$$

where j is the maximum integer for which the sum $\lambda_1 + \dots + \lambda_j$ is positive.

B.5.6 Phase space reconstruction

When studying numerically a n -dimensional dynamical system, one can analyze a computed n -dimensional signal; in contrast, when post-processing the outcomes of an experimental campaign on a physical system, the data available are often restricted to a single time series of a given scalar quantity $u(t)$, by means of which one should characterise the dynamics of a physical system with infinite degrees of freedom.

The problem of the apparent lack of data is often overcome by means of a particular procedure, called *phase space reconstruction*. From the signal $u(t)$, m different signals can be obtained by introducing a suitable time delay τ . Hence, the following functions can be defined:

$$\begin{cases} x_1(t) = u(t) \\ x_2(t) = u(t + \tau) \\ \dots \\ x_m(t) = u(t + (m - 1)\tau) \end{cases}$$

The functions $x_j(t)$ are called *delayed coordinates*; together, they define a m -dimensional space called *reconstructed space*.

In order to obtain a good reconstruction of phase space, the choices of m and τ are decisive. The number of variables to be chosen must be at least two times the dimension of the attractor governing the dynamics; in this way, the trajectories should appear more definite. As for the delay τ , it is obvious that $\tau = k\Delta$, where Δ is the sampling interval of the signal $u(t)$. The choice of k must guarantee that the trajectories are as separate as possible, and, most of the times, a number of attempts is required to determine the right value of k .

Appendix C

Linear stability analysis

The method of *linear stability analysis* is briefly introduced. Although no linear stability analysis has been performed for the present work, it is useful to hint at the main concepts of this method, for it is often recalled throughout the review of the existing literature on transitional convection regimes (Chapter 2). The details of the method and of its applications are widely described in dedicated monographs [7, 20].

Linear stability analysis may be seen as the continuous counterpart of the study of the stability of fixed points in finite-dimensional systems, described in Appendix B, by means of the eigenvalues of the Jacobian matrix of the system. Both methods imply the linearization of the non-linear operator characterising the system.

Formally, the evolution of a system \mathbf{S} can be described by the following expression:

$$\dot{\mathbf{S}} = \Theta_\gamma(\mathbf{S})$$

where \mathbf{S} represents the relevant fields (\mathbf{S} is usually a set of functions of time and physical space, so that its phase space is of functional nature - see Appendix B). Index γ denotes the set of control parameters, and Θ_γ defines an abstract vector field in phase space.

The basic state \mathbf{S}_0 is some special solution of the dynamical equation. In order to study its stability *i.e.* its *robustness* to perturbations, the basic state is perturbed. The perturbation is defined by $\mathbf{S} = \mathbf{S}_0 + \mathbf{S}'$. Upon linearization, the evolution of \mathbf{S}' is governed by:

$$\dot{\mathbf{S}}' = L_\gamma(\mathbf{S}')$$

where L_γ is the linearization of the operator Θ_γ , supposed to govern the evolution of infinitesimal perturbations. Linear stability analysis has to be understood as an *initial value problem* for \mathbf{S}' . This problem is solved by looking for the eigenvalues of L_γ . Indeed, inserting:

$$\mathbf{S}' = \bar{\mathbf{S}} e^{st}$$

in the perturbation equation, one gets:

$$(L_\gamma - sI) \bar{\mathbf{S}} = 0$$

thus yielding a full spectrum of eigenvalues $\{s_n; n = 1, 2, \dots\}$. The associated eigenmodes $\bar{\mathbf{S}}$ are usually called the *normal modes*. They encode the details of the physical instability mechanism. The eigenvalues s present themselves as the evolution rate of the corresponding normal modes. They are generically complex, *i.e.* $s = \sigma - i\omega$. The growth or decay of the eigenmodes is controlled by the real part σ of s :

- $\sigma < 0$: the mode is *stable*,
- $\sigma = 0$: the mode is *marginal* (or neutral, or critical),
- $\sigma > 0$: the mode is *unstable*.

σ may change sign when the control parameter γ varies, which is the signature of a *bifurcation*, *i.e.* a qualitative change of regime (see Appendix B).

The imaginary part ω of s characterizes the time dependence of the mode apart from its growth/decay properties:

- $\omega = 0$: the mode is *stationary* (*i.e.* time independent),
- $\omega \neq 0$: the mode is *oscillatory*.

In continuous media, stability analysis is conveniently performed using Fourier modes in space. For example, for a one-dimensional perturbation, it is:

$$\mathbf{S}(x, t) = \bar{\mathbf{S}} e^{ikx} e^{st} (L_\gamma - sI) \bar{\mathbf{S}} = 0$$

where k is the *wave number* which parametrizes the *branches* of the perturbation mode. The evolution rate s is related to k through a dispersion relation, which is also a function of the control parameter γ .

$$s = s(k, \gamma) = \sigma(k, \gamma) - i\omega(k, \gamma)$$

In the (k, γ, σ) space, the real part of the dispersion relation defines a surface; at a given value of γ , the unstable modes are those which correspond to the points of this surface lying above the plane $\sigma = 0$. There are as many surfaces as the branches of the dispersion relation.

The condition of marginal stability corresponds to the section $\sigma(k, \gamma) = 0$, which, for Dini's theorem, can be written as an explicit function $\gamma = \gamma_m(k)$. Hence, to each branch of the dispersion relation corresponds a *marginal stability curve*. The *stability threshold* γ_c and the *critical wave number* k_c are then defined as:

$$\gamma_m(k_c) = \inf_k \gamma_m(k) = \gamma_c$$

The critical frequency is given by $\omega_c = \omega(k_c, \gamma_c)$.

In fluid dynamics, several cases can be distinguished, on the basis of the values of k_c and ω_c :

- a *cellular instability* (typically giving rise to new vortex structures) corresponds to $k_c \neq 0$ and $\omega_c = 0$;
- an *oscillatory instability* (causing the oscillation of the flow without changing its topology) corresponds to $k_c = 0$ and $\omega_c \neq 0$;
- *dissipative waves* develop when both $k_c \neq 0$ and $\omega_c \neq 0$.

Appendix D

Streamfunction and heatfunction

In convection problems, it is important to visualize the flow field and, riding on this, the flow of energy. For example, in the two-dimensional Cartesian configuration, it is common practice to define a *streamfunction* $\psi(x, y)$ as

$$u_x = \frac{\partial \psi}{\partial y} \quad u_y = -\frac{\partial \psi}{\partial x}$$

Such a definition satisfies identically the mass continuity equation. It is easy to verify that the fluid velocity is locally tangent to the ($\psi = \text{constant}$) streamline. Streamlines thus provide a much needed bird's-eye view of the entire flow field and its main characteristics. In convection, the transport of energy through the flow field is a combination of both thermal diffusion and enthalpy flow. For any such field, a new function $\chi(x, y)$ can be defined in such a way that the net flow of energy (thermal diffusion and enthalpy flow) is zero across each $\chi = \text{constant}$ line. A mathematical definition of the *heatfunction* χ must satisfy the energy equation. For steady-state two-dimensional convection through a constant-property homogeneous fluid, the energy equation reads as:

$$u_x \frac{\partial T}{\partial x} + u_y \frac{\partial T}{\partial y} = \alpha \left(\frac{\partial^2 T}{\partial x^2} + \frac{\partial^2 T}{\partial y^2} \right)$$

or

$$\frac{\partial}{\partial x} \left(\rho c_p u_x T - \lambda \frac{\partial T}{\partial x} \right) + \frac{\partial}{\partial y} \left(\rho c_p u_y T - \lambda \frac{\partial T}{\partial y} \right) = 0$$

The heatfunction is then defined as follows:

$$\frac{\partial \chi}{\partial y} = \rho c_p u_x (T - T_{ref}) - \lambda \frac{\partial T}{\partial x}$$

$$\frac{\partial \chi}{\partial x} = -\rho c_p u_y (T - T_{ref}) + \lambda \frac{\partial T}{\partial y}$$

It is easy to see that $\chi(x, y)$ satisfies identically the steady-state energy equation. The reference temperature T_{ref} is, in principle, an arbitrary constant. Patterns of $\chi = \text{constant}$ *heatlines* are instructive when T_{ref} is the lowest temperature that occurs in the heat transfer configuration. If the fluid flow subsides ($u_x = u_y = 0$), the heatlines become identical to the *heat flux lines* employed to describe conduction phenomena.

Both functions can easily be non-dimensionalized. Having selected suitable reference quantities $L_{ref}, U_{ref}, \Delta T_{ref}$, the reference streamfunction is defined as:

$$\psi_{ref} = U_{ref} L_{ref}$$

The definition of ψ remains formally unchanged in its dimensionless form. By choosing:

$$\chi_{ref} = \lambda \Delta T_{ref}$$

one obtains (in dimensionless terms):

$$\frac{\partial \chi}{\partial y} = Pe u_x T - \frac{\partial T}{\partial x}$$

$$\frac{\partial \chi}{\partial x} = -Pe u_y T + \frac{\partial T}{\partial y}$$

where $Pe = Re Pr$ is the Péclet number.

Numerical computations of incompressible flows usually imply the solution of one or more Poisson equations. Regardless of the method chosen to discretize the governing PDES, any Poisson solver is suitably initialized once for all at the beginning of the computation, provided that the problem to be solved does not involve any complications such as a variable domain of integration. Thus, resolving a Poisson equation on the computational domain involves only a change in the right-hand-side term, and is relatively cheap in the frame of the computation. Two Poisson equations may be written respectively for $\psi(x, y)$ and for $\chi(x, y)$ [163].

The definition of the streamfunction is rewritten in vector form:

$$\nabla \psi = \begin{pmatrix} -u_y \\ u_x \end{pmatrix}$$

by taking the divergence of the above expression

$$\nabla^2 \psi = \frac{\partial u_x}{\partial y} - \frac{\partial u_y}{\partial x}$$

or:

$$\nabla^2 \psi = \hat{\mathbf{k}} \cdot \nabla \times \mathbf{u}$$

or also:

$$\nabla^2 \psi = \omega$$

where ω is the scalar vorticity of a 2D field.

With an analogous procedure, a Poisson equation for the heatfunction may be derived:

$$\nabla^2 \chi = \frac{\partial(u_x T)}{\partial y} - \frac{\partial(u_y T)}{\partial x}$$

or

$$\nabla^2 \chi = \hat{\mathbf{k}} \cdot \nabla \times (\mathbf{u} T)$$

List of Figures

1.1	Scheme of a heat engine driven by natural convection.	5
1.2	General spatial domain of integration for the governing equations of convection.	13
1.3	Density and temperature gradients in the Rayleigh-Bénard problem: stable (left) and inverse (right).	16
1.4	Boundary layer flow along a vertical plate: (a) schematic of the problem; (b) qualitative description of transition to turbulence.	33
1.5	Boundary layer length scales for $Pr \gg 1$	36
1.6	Boundary layer length scales for $Pr \approx 1$	37
1.7	Boundary layer length scales for $Pr \ll 1$	38
1.8	Length scales of natural convection boundary layers.	39
1.9	Effect of the thermal boundary condition on the natural convection boundary layer along a vertical wall: (a) isothermal wall; (b) uniform heat flux. .	40
1.10	Buoyant plume from a line heat source: (a) schematic of the problem; (b) qualitative description of transition to turbulence.	41
2.1	Stability limits for the base flow	49
2.2	Stability and bifurcations of the base flow: supercritical (or direct) bifurcation. .	50
2.3	Stability and bifurcations of the base flow: (a) subcritical (or inverse) bifurcation; (b) hysteresis.	51
2.4	Landau (a) and Ruelle-Takens (b) scenarios of transition to turbulence . .	52
2.5	Schematic of the Rayleigh-Bénard enclosure problem.	54
2.6	Instabilities and bifurcations in Rayleigh - Bénard convection: (a) stability diagram of stable two-dimensional convection rolls in an infinite fluid layer [38]; (b) experimental bifurcation patterns as a function of Ra_H and Pr : (I) onset of two-dimensional steady rolls; (II) three-dimensional convection; (III) time dependent convection (a) in isolated spots, (b) uniformly throughout the layer; (IV,V) nonperiodic flow [38].	56
2.7	Effect of adiabatic confining walls on the critical Rayleigh number $Ra_{H,c}$ for the onset of convection [45].	57
2.8	Schematic of the side-heated enclosure problem.	62
2.9	Main types of flow regimes for natural convection in an enclosure heated from the side, following [3] and [64]	64
2.10	Critical Grashof number curves for the stability of natural convection in a differentially heated vertical layer [72]: (a) $Pr = 0.75 \div 12.7$; (b) $Pr = 20 \div 1000$. .	65

2.11 Critical Rayleigh number curves for the stability of natural convection in a differentially heated enclosure with $1 \leq A_x \leq 10$ and $Pr = 0.71$ [63].	67
2.12 Snapshots of the temperature field in a side-heated square enclosure, $Ra_H = 2 \times 10^{10}$ and $Pr = 0.71$, taken from [83]: a) thermal boundary layer transition; b) asymptotic stratification.	68
2.13 Schematic of the cross-section of the horizontal annulus.	69
2.14 Flow regimes in the horizontal annulus: a) sketch of the flow and heat transfer characteristics as a function of R and Ra_H [84]; b) flow regions in the boundary layer limit [85].	70
2.15 Flow patterns and stability in horizontal annuli: a) experimental map of the flow regimes as reported by Powe <i>et al.</i> [96]; b) marginal stability curves as a function of Pr [97].	72
2.16 Chart of the two-dimensional flow patterns in the (R, Ra_H) plane, reproduced from [102].	73
2.17 Critical Gr_H -values for the transition to multicellular and oscillatory flow of low Pr fluids in an annulus with $R = 1.17$. Numerical data by Yoo [115] are compared with the asymptotic stability condition by Rothmayer and Fant [118] for $Pr \rightarrow 0$	75
2.18 Transition patterns and critical Gr_H -curves as a function of the inverse radius ratio, $2/(R - 1)$, for the buoyant flow in a horizontal annulus filled with a fluid at $Pr = 0.02$, as obtained by Yoo <i>et al.</i> [114]. Circles indicate the computed values $Gr_{H,o}$ above which the flow is always oscillatory.	76
2.19 Critical $Ra_{W,o}$ -ranges (within the dashed lines) for which a Hopf bifurcation occurs in the buoyancy-induced flow from an enclosed line heat source, as a function of the enclosure aspect ratio A and depth of immersion H_s . The chart is extracted from the data available in [134].	79
3.1 Discretization grids.	85
3.2 Discretization stencils for the diffusive (a) and convective (b) terms.	87
3.3 Computational grids for scalars and velocity components.	89
3.4 Topology (a) and relevant sizes (b) of a generic control volume in a 2D Cartesian discretization.	90
3.5 Control volumes for scalars (a) and velocity components (b,c), for staggered 2D Cartesian grids.	90
3.6 Computational stencils for scalars (a) and velocity components (b,c), for staggered 2D Cartesian grids.	90
3.7 Reconstruction of temperature (a) and normal velocity components (b,c) for the x -velocity grid.	92
3.8 Computational grid \mathcal{G} (a) and set of intersection points \mathcal{B} (b).	94
3.9 Local stencils g (a) and d (b).	95
3.10 Resizing (a) and geometry of the discretization cell (b).	96
3.11 Local discretization stencils for intersections with $k = 2$ (a) and $k = 3$ (b). .	99
3.12 Computational (a) and discretization (b) stencils for the energy equation. .	102
3.13 Procedure for the estimate of the normal velocity component near the boundary for the energy equation.	103
3.14 Computational (a) and discretization (b) cells and stencils for the reconstruction of source terms in the Navier-Stokes equation.	104

3.15 Computational (a) and discretization (b) cells and stencils for the reconstruction of convective fluxes in the Navier-Stokes equation.	106
3.16 Discretization stencils for the reconstruction of the normal velocity components: diagonal intersections.	106
3.17 Adaptation of the Matrix Decomposition approach to irregular domains. .	107
4.1 Schematic of the problem.	110
4.2 Overview of asymptotic flow regimes for $Pr = 0.7$ in the (Ra_H, A) plane. .	118
4.3 Isotherms ($0.1 \leq T \leq 0.9$) (left) and streamlines (right) of the <i>S</i> -type flow for four A -values, and for $Ra_H = 2 \times 10^4$	119
4.4 Numerical results for $A = 2.5$, $Ra_H = 2 \times 10^5$: (a) power spectral density; 3D attractor in phase space $T-u_x-u_z$ (referred to as $T-u-v$) at: (b) $(0, 0.5)$; (c) $(0.5, 0)$	121
4.5 Numerical results for $A = 2.5$, $Ra_H = 4 \times 10^5$: (a) power spectral density; 3D attractor in phase space $T-u_x-u_z$ (referred to as $T-u-v$) at: (b) $(0, 0.5)$; (c) $(0.5, 0)$	121
4.6 Numerical results for $A = 2.5$, $Ra_H = 6 \times 10^5$: (a) power spectral density; 3D attractor in phase space $T-u_x-u_z$ (referred to as $T-u-v$) at: (b) $(0, 0.5)$; (c) $(0.5, 0)$	121
4.7 Numerical results for $A = 2.5$, $Ra_H = 8 \times 10^5$: (a) power spectral density; 3D attractor in state space $T-u_x-u_z$ (referred to as $T-u-v$) at: (b) $(0, 0.5)$; (c) $(0.5, 0)$	121
4.8 Poincaré maps $(0, 0.5)$ at point for $A = 2.5$ and: (a) $Ra_H = 2 \times 10^5$; (b) $Ra_H = 8 \times 10^5$	122
4.9 Sequence of isotherm contours associated with the time series of $T(0, 0.5)$ for $A = 2.5$, $Ra_H = 8 \times 10^5$	123
4.10 Visualization of 3D attractors in phase space $T-u_x-u_z$ (referred to as $T-u-v$) at various locations, for $A = 2.5$, $Ra_H = 8 \times 10^5$	124
4.11 Isotherms ($0.1 \leq T \leq 0.9$) (left) and streamlines (right) of the <i>NS</i> -type flow for $A = 5$ and $Ra_H = 3.704 \times 10^4$	126
4.12 Time histories of the average Nusselt number, Nu_D , at the left and right walls: $A = 5$ and $Ra_H = 1.852 \times 10^5$	127
4.13 Isotherms ($0.1 \leq T \leq 0.9$ (left) and streamlines (right) of the <i>S</i> -type flow for four A -values, and for $Ra_{qH} = 2 \times 10^4$	128
4.14 Isotherms (left) and streamlines (right) for 12 different cases at $A = 2.5$. Values of Pr and Ra are reported below each subplot. The (+) sign indicates the maximum for the positive streamfunction.	130
4.15 Isotherm contours (in grayscales) and streamlines (in white) for $A = 5, 10$ and $Pr = 0.7, 7$, $Ra_H = 10^4$. The (+) sign indicates the maximum for the positive streamfunction.	131
4.16 Time-averaged isotherm contours (in grayscales) and streamlines (in white) within a single oscillation period, for $A = 3.3$, $Pr = 0.07$, $Ra_H = 10^3$. The (+) sign indicates the maximum for the positive streamfunction.	132
4.17 Asymptotic times as functions of h , Pr and Ra_H	133
4.18 Distributions of the local Nusselt number $Nu_{H,\theta}$, along the cylinder surface for $Ra_H = 2 \times 10^3 \div 2 \times 10^4$. The data are normalized by pseudo-diffusive values $Nu_{H,0}$, listed in Table 4.5.	134

4.19 Heat transfer correlation (4.5.11), as compared with available literature data [124, 128, 129]. Coordinates Y and Z are defined in eqs. (4.5.4) and (4.5.5), respectively.	139
4.20 Nu_D - Ra_D plot of the present predictions, as compared with Cesini <i>et al.</i> [127] and Churchill and Chu [151].	140
4.21 Distributions of the local Nusselt number $Nu_{D,\theta}$ along the cylinder surface for $d = 0.6$, $Ra_{qD} = 10^6$ ($Ra_D = 1.42 \times 10^5$)	141
4.22 Validation of the correlation 4.5.11 for the isoflux case.	142
4.23 Average Nusselt number on the cylinder surface vs. h , Pr and Ra_H , for all the cases examined.	143
4.24 Comparison between equation 4.5.11 and numerical predictions of Nu_H , as a function of Ra_H , for different values of Pr . Each diagram refers to a specific A -value.	143
5.1 Cross-section of the horizontal annulus.	146
5.2 Comparison between the two solutions for the pseudo-diffusive streamfunction in a horizontal annulus: $\psi_{pd,a}$, equation (5.2.26), (left half of the annulus); $\psi_{pd,b}$, equation (5.2.38) (right half).	152
5.3 Maximum relative difference ϵ_ψ between the solutions $\psi_{pd,a}$ and $\psi_{pd,b}$, as a function of R	153
5.4 Schematic of an isothermal cylindrical source at a temperature T_s , immersed in an infinite medium at T_∞	154
5.5 Numerical (a, c) and experimental (b, d) interferograms representing the temperature field around a heated horizontal wire, as reported in [156]: (a, b) diffusive transient; (c, d) developed thermal plume.	155
5.6 Analytical and numerical profiles of the normalized azimuthal velocity, u_θ/Ra_H , at $\theta = 0$, for $Ra_H = 1 \times 10^{-1}$	161
5.7 Analytical and numerical profiles of the normalized azimuthal velocity, u_θ/Ra_H , at $\theta = 0$, for four Ra_H -values, for narrow and moderate gap annuli. The dash-dot line corresponds to the analytical solution in the narrow gap limit.	162
5.8 Analytical and numerical profiles of the normalized azimuthal velocity, u_θ/Ra_H , at $\theta = 0$, for four Ra_H -values, for large gap annuli. The dash-dot line corresponds to the analytical solution in the narrow gap limit.	163
5.9 Analytical and numerical profiles of temperature T at $\theta = 0$, for four Ra_H -values, and for narrow and moderate gap annuli.	164
5.10 Analytical and numerical profiles of temperature T at $\theta = 0$, for four Ra_H -values, and for large gap annuli.	165
5.11 Trends of the maximum relative deviations between analytical and numerical results: (a) ϵ_u vs. Ra_H ; (b) ϵ_T vs. Ra_H	166
5.12 Correlating equations for the limits of the pseudo-diffusive flows, as compared with numerical data and literature results: a) $Ra_{H,pd,u}$ vs. R , equation (5.4.6), b) $Ra_{H,pd,T}$ vs. R , equation (5.4.6).	167
B.1 Different types of attractors of a flow.	174

B.2 Bifurcations of a fixed point: (a) saddle-node; (b) transcritical; (c) supercritical pitchfork; (d) subcritical pitchfork; (e) supercritical Hopf; (f) subcritical Hopf. Continuous and dashed lines represent stable and unstable states, respectively.	177
B.3 Schematic of a Poincaré section	178
B.4 Bifurcations of a periodic orbit: (a) saddle-node; (b) transcritical; (c) supercritical pitchfork; (d) subcritical pitchfork; (e) direct period doubling; (f) inverse period doubling; (g) supercritical secondary Hopf; (h) subcritical secondary Hopf. Continuous and dashed lines represent stable and unstable states, respectively.	180

List of Tables

2.1	Critical Rayleigh number values for the bifurcation to oscillatory flow in enclosed Rayleigh-Bénard convection, according to various authors.	58
2.2	Rayleigh-Bénard convection in low aspect ratio enclosures: (a) known routes to chaos, as carried out by various authors; (b) detail of the bifurcations for the case $A_x = 3.29$, $A_y = 1.88$, $Pr = 0.5$, following Maurer and Libchaber [55].	60
2.3	Routes to chaos for the horizontal annulus, [122, 121].	76
2.4	Routes to chaos for an enclosed line heat source, as carried out by Desrayaud and Lauriat [134].	79
4.1	Possible aspect ratios for the system under consideration, and their cross-relationships.	111
4.2	Results of the grid sensitivity analysis for the numerical procedure, $Ra_H = 8 \times 10^4$, $A = 2.5$, $Pr = 0.7$	115
4.3	Summary of the parameter ranges investigated	117
4.4	Breaking of the steady symmetric patterns: Ra_H -values and flow regimes encountered for each A -value and for both the isothermal and isoflux case. . . 127	
4.5	Average Nusselt number values versus Ra_H	136
4.6	Constants in power-law (eq. (4.5.10) for each h -value	136
4.7	Deviations of available literature data from equation (4.5.11), and Nu_H predictions for selected Ra_H -values. Starred values (*) correspond to predictions in [124, 128, 129] falling above the proposed stability threshold, $Ra_H = 2 \times 10^4$	138
4.8	Average Nusselt number values on the cylinder surface: comparison between corresponding cases for isothermal and isoflux boundary conditions	141
5.1	Available correlations for the limit of conductive heat transfer in a horizontal annulus, as reported by various authors.	160
B.1	Correspondence between attractors for flows and maps	176

List of Symbols

Symbols

a	wavenumber
a, b	power law coefficients, eq. (4.5.10)
a, b, c	general boundary condition coefficients
A	aspect ratio
A, B, C, D	Boussinesq approximation validity criteria
Ar	Archimedes number
Bo	Boussinesq number
c_i	constants in eq. (5.2.26)
c_p	specific heat at constant pressure
c_v	specific heat at constant volume
C_{rb}, C_{vl}	constants in eq. (5.3.28) and (5.3.29)
CFL	Courant number
d	aspect ratio
D	diameter
e	energy per unit mass
f	frequency
Fo	Fourier number
g	gravitational acceleration modulus
G	Grüneisen ratio
Ga	Gay-Lussac number
Gr	Grashof number

h	specific enthalpy, convective heat transfer coefficient, aspect ratio
H	height
J	heat generation term
k	grid refinement ratio
k, k'	stencil node identifiers
k, m, n	general exponents for scale analysis
Kn	Knudsen number
ℓ_{mfp}	mean free path of fluid molecules
L	characteristic length, depth or axial length
n	exponent in eq. (4.5.3)
Nu	Nusselt number
p	pressure
P	piezometric pressure
Pe	Péclet number
Pr	Prandtl number
q	heat flux density
Q	heat power
r	radial coordinate, radius
R	main parameter of a general thermo-fluid dynamics system, aspect ratio
R_t	specific gas constant of an ideal gas or a mixture of gases
Ra	Rayleigh number
Re	Reynolds number
Ri	Richardson number
s	order of convergence
S	stratification parameter, surface
t	time
T	temperature
u	velocity component
U	reference or scale velocity

V	volume
W	width
x, y, z	Cartesian coordinates
Y, Z	coordinates for general correlation, eq. (4.5.3)

Greek letters

α	thermal diffusivity
β	thermal expansion coefficient, weight of Crank-Nicolson scheme
γ	set of parameters of a general, weight of time discretization
γ_i	constants in eq. (5.2.38)
Γ	general diffusivity
δ	viscous length scale, boundary layer thickness
δ_{ij}	Kronecker delta
$\Delta_x, \delta x$	grid and stencil metrics
ϵ	relative deviation, difference, or error
ε	turbulent kinetic energy dissipation rate per unit mass
ζ	local binormal coordinate
η	local normal coordinate
θ	angular coordinate
Θ_γ	vector operator of a general, ∞ -dimensional dynamical system
λ	thermal conductivity
λ_K	dimensionless dissipative scale
Λ_K	Kolmogorov scale
μ	dynamic viscosity
ν	kinematic viscosity
ξ	local tangential coordinate
ρ	density
ϱ	residual
σ	aspect ratio

σ_v	volumetric source term
τ	limit for the Courant number
τ_{ij}	shear stress tensor components
v	aspect ratio
ϕ	pseudo-pressure
φ	generic field variable
Φ	viscous dissipation function
χ	isothermal compressibility coefficient
ψ	streamfunction
Ψ	gravitational potential
ω	vorticity
Ω	general domain

Vectors and matrices

A, D, E	matrices used for boundary conditions (Chapter 3)
c, g	vectors used for boundary conditions (Chapter 3)
D	strain rate tensor
f	body force per unit volume (Chapter 1), vector of stencil unknowns (Chapter 3)
F	force
g	gravitational field
ĝ	gravity unit vector
G(u)	functional of velocity
I	identity matrix
k̂	z -axis unit vector
n̂	unit vector of normal direction
q	heat flux vector
S	set of variables of a general, ∞ -dimensional dynamical system
T	stress tensor

T	shear stress tensor
u	velocity vector
v	velocity correction vector

Superscripts

-	boundary value, reference to modified stencils and cells (Chapter 3)
\circ	value on cell boundary (Chapter 3)
\wedge	value on cell vertex (Chapter 3)
'	variations associated with flow
*	related to a different non-dimensionalization or scale
\sim	approximate value, initial guess
<i>n</i>	time step counter
<i>T</i>	transpose of a vector or matrix

Subscripts

∞	far-field value
0	reference value, initial value
$0, \dots, 4$	stencil node identifiers
$2D$	two-dimensional
$3D$	three-dimensional
<i>a</i>	asymptotic
<i>ad</i>	advective
<i>A</i>	Archimedes
<i>b</i>	buoyancy, bottom
<i>c</i>	critical
<i>cd</i>	conductive
<i>C</i>	cold
<i>d</i>	delay
<i>D</i>	based on the diameter

E	energy (referred to a stability limit)
$film$	film (referred to temperature)
g	gravity (referred to a force), generation (referred to heat)
G	global (referred to a stability limit)
h	hydrostatic
H	based on the height, hot
i	inertia
i, j, k	repeated indices, cell identifiers
int	internal
k, k'	stencil node identifiers
kin	kinetic
L	linear (referred to a stability limit), based on the length
max	maximum
min	minimum
num	numerical
o	oscillatory
p	pressure, plume
q	based on the heat flux
Q	based on the heat power
r, θ	vector component along polar coordinates
rb	Rayleigh-Bénard
ref	reference
t	top
tr	transition
$turb$	turbulent
T	thermal, related to temperature
u	related to velocity
v	viscous
vl	vertical layer

w	wall
W	based on the width
x, y, z	vector component along Cartesian coordinates
z	local, with reference to height
ξ, η, ζ	vector component along local coordinates
ψ	related to streamfunction

Operators and relational symbols

.	scalar product
:	tensor inner product
\times	vector product
Δ	difference of a variable
d	differential of a variable
∂	partial differential of a variable, boundary of a domain
$\frac{D}{Dt}$	substantive (or lagrangian) derivative
∇	nabla operator
I	projection operator on the space of irrotational vectors
σ	projection operator on the space of solenoidal vectors
\approx	approximately
\propto	proportional to
$O()$	of order ()
\ll	smaller than, by orders of magnitude
\lesssim	of the same order or smaller than, by orders of magnitude
\approx	of the same order of magnitude of
\gtrsim	of the same order or greater than, by orders of magnitude
\gg	greater than, by orders of magnitude

Bibliography

- [1] F. P. Incropera and D. P. DeWitt. *Fundamentals of Heat and Mass Transfer*. John Wiley & Sons, 5th edition, 2006.
- [2] B. Gebhart, Y. Jaluria, R. L. Mahajan, and B. Sammakia. *Buoyancy-induced Flows and Transport*. Hemisphere Publishing Corporation, 1st edition, 1988.
- [3] A. Bejan. *Convection Heat Transfer*. John Wiley & Sons, 3rd edition, 2004.
- [4] H. Schlichting and K. Gersten. *Boundary Layer Theory*. Springer Verlag, 8th edition, 2004.
- [5] D. J. Tritton. *Physical Fluid Dynamics*. Oxford University Press, 2nd edition, 1988.
- [6] J. W. Strutt Lord Rayleigh. On convection currents in a horizontal layer of fluid when the higher temperature is on the under side. *Philosophical Magazine*, 32:529–546, 1916.
- [7] S. Chandrasekhar. *Hydrodynamic and Hydromagnetic Stability*. Clarendon Press, 1961.
- [8] P. M. Gresho. On the theory of semi-implicit projection methods for incompressible flow and its implementation via a finite element method that also introduces a nearly consistent mass matrix. part 1: Theory. *International Journal for Numerical Methods in Fluids*, 11:587–620, 1990.
- [9] T. Pesso and S. Piva. Laminar natural convection in a square cavity: Low Prandtl numbers and large density differences. *International Journal of Heat and Mass Transfer*, 52:1036–1043, 2009.
- [10] D. D. Gray and A. Giorgini. The validity of the Boussinesq approximation for liquids and gases. *International Journal of Heat and Mass Transfer*, 19:545–551, 1976.
- [11] E. Buckingham. On physically similar systems: illustration of the use of dimensional equations. *Physical Review*, 4:345–376, 1914.
- [12] G. Desrayaud, A. Fichera, M. Marcoux, and A. Pagano. An analytical solution for the stationary behaviour of binary mixtures and pure fluids in a horizontal annular cavity. *International Journal of Heat and Mass Transfer*, 49:3253–3263, 2006.
- [13] D. Angeli, P. Levoni, and G. S. Barozzi. Numerical predictions for stable buoyant regimes within a square cavity containing a heated horizontal cylinder. *International Journal of Heat and Mass Transfer*, 51:553–565, 2008.

- [14] S. Ostrach. Natural convection heat transfer in cavities and cells. In U. Grigull, E. Hahne, K. Stephan, and J. Straub, editors, *Proceedings of the Seventh International Heat Transfer Conference*, volume 1, pages 365–379, München, Germany, 1982. Hemisphere Publishing Corporation.
 - [15] S. Ostrach. Natural convection in enclosures. *ASME Journal of Heat Transfer*, 110:1175–1190, 1988.
 - [16] G. F. Hewitt, editor. *Handbook of Heat Exchanger Design*. Begell House, 1992.
 - [17] O. Ladyzhenskaya. *The Mathematical Theory of Viscous Incompressible Flow*. Gordon and Breach, 1969.
 - [18] V. Franceschini. Two models of truncated Navier-Stokes equations on a two-dimensional torus. *Physics of Fluids*, 26:433–447, 1983.
 - [19] E. Ott. *Chaos in Dynamical Systems*. Cambridge University Press, 2nd edition, 2002.
 - [20] D. D. Joseph. *Stability of Fluid Motions*, volume 1. Springer Verlag, 1976.
 - [21] P. Bergé, Y. Pomeau, and C. Vidal. *L'Ordre dans le Chaos*. Hermann, Editeurs des Sciences et des Arts, 2nd edition, 1988.
 - [22] L. D. Landau. On the problem of turbulence. *Akademii Nauk Doklady*, 44:339–342, 1944.
 - [23] D. Ruelle and F. Takens. On the nature of turbulence. *Communications in Mathematical Physics*, 20:167–192, 1971.
 - [24] E. N. Lorenz. Deterministic nonperiodic flow. *Journal of Atmospheric Sciences*, 20:130–141, 1963.
 - [25] P. Manneville. *Dissipative structures and weak turbulence*. Academic Press, 1990.
 - [26] J. P. Gollub and S. V. Benson. Many routes to turbulent convection. *Journal of Fluid Mechanics*, 100:449–470, 1980.
 - [27] G. K. Batchelor. *An Introduction to Fluid Dynamics*. Cambridge University Press, 1967.
 - [28] P. Bergé and M. Dubois. Rayleigh-Bénard convection. *Contemporary Physics*, 25:535–582, 1984.
 - [29] I. Catton. Natural convection in enclosures. In C. L. Tien, V. P. Carey, and J. K. Ferrell, editors, *Proceedings of the Eighth International Heat Transfer Conference*, volume 1, pages 13–31, San Francisco, CA, USA, 1986. Hemisphere Publishing Corporation.
 - [30] K. T. Yang. Transitions and bifurcations in laminar buoyant flows in confined enclosures. *ASME Journal of Heat Transfer*, 110:1191–1204, 1988.
-

- [31] E. L. Koschmieder. Bénard convection. *Advances in Chemical Physics*, 26:177–211, 1974.
- [32] I. Catton. Natural convection in enclosures. In *Proceedings of the Sixth International Heat Transfer Conference*, volume 2, pages 13–31, Toronto, Canada, 1978. Hemisphere Publishing Corporation.
- [33] I. Catton. Natural convection in horizontally unbounded plane layers. In S. Kakac, W. Aung, and R. Viskanta, editors, *Natural Convection: Fundamentals and Applications*, pages 97–134. Hemisphere Publishing Corporation, 1985.
- [34] I. Catton and J. C. Buell. The wave number at supercritical Rayleigh numbers. In W. S. Saric and A. A. Szewczyk, editors, *Stability in Convection Flows*, volume 54 of ASME-HTD, pages 17–29. 1986.
- [35] R. Faradieh and R. S. Tankin. Interferometric study of two-dimensional Bénard convection cells. *Journal of Fluid Mechanics*, 66:739–751, 1974.
- [36] P. Bergé. Systems far from equilibrium. In *Lecture Notes in Physics*, volume 132, pages 381–394. Springer Verlag, 1980.
- [37] E. L. Koschmieder. Rayleigh-Bénard convection and Taylor vortex flow. In J. Zierep and H. Oertel, Jr, editors, *Convective Transport and Instability Phenomena*, pages 39–54. G. Braun, 1982.
- [38] F. H. Busse. Nonlinear properties of thermal convection. *Reports on Progress in Physics*, 41:1929–1967, 1978.
- [39] F. H. Busse and R. M. Clever. Instability of convection rolls in a fluid of moderate Prandtl number. *Journal of Fluid Mechanics*, 91:319–335, 1979.
- [40] F. H. Busse. Transition to turbulence in thermal convection. In J. Zierep and H. Oertel, Jr, editors, *Convective Transport and Instability Phenomena*, pages 149–170. G. Braun, 1982.
- [41] Y. Pomeau and P. Manneville. Wavelength selection in cellular flows. *Physical Letters*, 75A:296–298, 1980.
- [42] H. Oertel, Jr. Three-dimensional convection within rectangular boxes. In K. E. Torrence and I. Catton, editors, *Natural Convection in Enclosures*, volume 8 of ASME-HTD, pages 11–16. 1980.
- [43] M. C. Cross, P. G. Danhiels, P. C. Hohenberg, and E. D. Siggia. Effect of sidewalls on wavenumber selection in Rayleigh-Bénard convection. *Physical Review Letters*, 45:898–901, 1980.
- [44] R. Krishnamurti. Some further studies of the transition to turbulent convection. *Journal of Fluid Mechanics*, 60:285–303, 1973.
- [45] U. Müller. Bénard convection gaps and cavities. In J. Zierep and H. Oertel, Jr, editors, *Convective Transport and Instability Phenomena*, pages 71–100. G. Braun, 1982.

- [46] S. H. Davis. Convection in a box: Linear theory. *Journal of Fluid Mechanics*, 30:465–478, 1967.
- [47] I. Catton. Convection in a closed rectangular region: the onset of motion. *ASME Journal of Heat Transfer*, 92:186–187, 1970.
- [48] G. D. Raithby and K. G. T. Hollands. Natural convection. In W. M. Rohsenow, J. P. Hartnett, and E. N. Ganic, editors, *Handbook of Heat Transfer Fundamentals*, chapter 6, pages 6–1 – 6–94. McGraw-Hill, 2nd edition, 1985.
- [49] H. Oertel, Jr. Thermal instabilities. In J. Zierep and H. Oertel, Jr, editors, *Convective Transport and Instability Phenomena*, pages 3–24. G. Braun, 1982.
- [50] R. Kessler. Nonlinear transition in three-dimensional convection. *Journal of Fluid Mechanics*, 174:357–379, 1987.
- [51] W. Jäger. *Oszillierische und Turbulente Konvektion*. PhD thesis, Universität Karlsruhe, Germany, 1982.
- [52] J. Maurer and A. Libchaber. Effect of the Prandtl number on the onset of turbulence in liquid He. *Journal of Physics Letters*, 41:L515–L518, 1980.
- [53] P. Vadasz. Subcritical transitions to chaos and hysteresis in a fluid layer heated from below. *International Journal of Heat and Mass Transfer*, 43:705–724, 2000.
- [54] P. Vadasz. Chaotic dynamics and hysteresis in thermal convection. *Proceedings of the IMechE Part C: Journal of Mechanical Engineering Science*, 220:309–323, 2006.
- [55] J. Maurer and A. Libchaber. Rayleigh-Bénard experiment in liquid helium: Frequency locking and the onset of turbulence. *Journal of Physics Letters*, 40:L419–L423, 1979.
- [56] P. Bergé, M. Dubois, and V. Croquette. Approach to Rayleigh-Bénard turbulent convection in different geometries. In J. Zierep and H. Oertel, Jr, editors, *Convective Transport and Instability Phenomena*, pages 12–148. G. Braun, 1982.
- [57] P. Bergé, M. Dubois, P. Manneville, and Y. Pomeau. Intermittency in Rayleigh-Bénard convection. *Le Journal de Physique - Lettres*, 41:L341–L345, 1980.
- [58] E. Zienicke, N. Seehafer, and F. Feudel. Bifurcations in two-dimensional Rayleigh-Bénard convection. *Physical Review E*, 57:428–435, 1998.
- [59] J. Pallares, I. Cuesta, and F. X. Grau. Flow transitions in laminar Rayleigh-Bénard convection in a cubical cavity at moderate Rayleigh numbers. *International Journal of Heat and Mass Transfer*, 42:753–769, 1999.
- [60] M. Cappelli D’Orazio, C. Cianfrini, and M. Corcione. Rayleigh-Bénard convection in tall rectangular enclosures. *International Journal of Thermal Sciences*, 43:135–144, 2004.
- [61] G. K. Batchelor. Heat transfer by free convection across a closed cavity between vertical boundaries at different temperatures. *Quarterly Journal of Applied Mathematics*, 12:209–233, 1954.

- [62] C. J. Hoogendorn. Natural convection in enclosures. In *Proceedings of the Sixth International Heat Transfer Conference*, volume 6, pages 111–120, Toronto, Canada, 1978. Hemisphere Publishing Corporation.
- [63] P. Le Quéré. Onset of unsteadiness, routes to chaos and simulations of chaotic flows in cavities heated from the side: a review of present status. In G. F. Hewitt, editor, *Proceedings of the Tenth International Heat Transfer Conference*, volume 1, pages 281–296, Brighton, UK, 1994. Hemisphere Publishing Corporation.
- [64] J. Patterson and J. Imberger. Unsteady natural convection in a rectangular cavity. *Journal of Fluid Mechanics*, 100:65–86, 1980.
- [65] J. W. Elder. Laminar free convection in a vertical slot. *Journal of Fluid Mechanics*, 23:77–98, 1965.
- [66] J. W. Elder. Turbulent free convection in a vertical slot. *Journal of Fluid Mechanics*, 23:99–111, 1965.
- [67] D. E. Cormack, L. G. Leal, and J. Imberger. Natural convection in a shallow cavity with differentially heated end walls. Part I: asymptotic theory. *Journal of Fluid Mechanics*, 65:209–229, 1974.
- [68] D. E. Cormack, L. G. Leal, and J. H. Seinfeld. Natural convection in a shallow cavity with differentially heated end walls. Part II: numerical solutions. *Journal of Fluid Mechanics*, 65:231–246, 1974.
- [69] J. Imberger. Natural convection in a shallow cavity with differentially heated end walls. Part III: experimental results. *Journal of Fluid Mechanics*, 65:247–260, 1974.
- [70] G. D. Mallinson and G. De Vahl Davis. Three-dimensional natural convection in a box: a numerical study. *Journal of Fluid Mechanics*, 83:1–31, 1977.
- [71] R. J. A. Janssen, R. A. W. M. Henkes, and C. J. Hoogendorn. Transition to time-periodicity of a natural-convection flow in a 3d differentially heated cavity. *International Journal of Heat and Mass Transfer*, 36:2927–2940, 1993.
- [72] R. F. Bergholz. Instability of steady natural convection in a vertical fluid layer. *Journal of Fluid Mechanics*, 84:743–768, 1978.
- [73] C. M. Vest and V. S. Arpacı. Stability of natural convection in a vertical slot. *Journal of Fluid Mechanics*, 36:1–15, 1969.
- [74] M. Prud'homme and H. Bougherara. Weakly non-linear stability of stratified natural convection in a vertical cavity with lateral temperature gradient. *International Communications in Heat and Mass Transfer*, 32:32–42, 2005.
- [75] S. A. Korpela, Y. Lee, and J. E. Drummond. Heat transfer through a double pane window. *ASME Journal of Heat Transfer*, 104:539–544, 1982.
- [76] Y. Lee and S. A. Korpela. Instability of steady natural convection in a vertical fluid layer. *Journal of Fluid Mechanics*, 126:91–121, 1983.

- [77] K. G. T. Hollands and L. Konicek. Experimental study of the stability of differentially heated inclined layers. *International Journal of Heat and Mass Transfer*, 16:1467–1476, 1973.
 - [78] P. Le Quéré. Transition to unsteady natural convection in a tall water-filled cavity. *Physics of Fluids*, 2:503–515, 1990.
 - [79] R. A. W. M. Henkes and C. J. Hoogendorn. Bifurcations to unsteady convection for air and water in a cavity heated from the side. In G. Hetsroni, editor, *Proceedings of the Ninth International Heat Transfer Conference*, volume 2, pages 503–515, Jerusalem, Israel, 1990. Hemisphere Publishing Corporation.
 - [80] R. A. W. M. Henkes and P. Le Quéré. Three-dimensional transition of natural-convection flows. *Journal of Fluid Mechanics*, 319:281–303, 1996.
 - [81] S. Xin and P. Le Quéré. Linear stability analyses of natural convection flows in a differentially heated square cavity with conducting horizontal walls. *Physics of Fluids*, 13:2529–2542, 2001.
 - [82] S. Wakitani. Numerical study of three-dimensional oscillatory natural convection at low Prandtl number in rectangular enclosures. *ASME Journal of Heat Transfer*, 123:77–83, 2001.
 - [83] S. Paolucci. Direct numerical simulation of two-dimensional turbulent natural convection in an enclosed cavity. *Journal of Fluid Mechanics*, 215:229–262, 1990.
 - [84] P. Teertstra and M. M. Yovanovich. Comprehensive review of natural convection in horizontal circular annuli. In *Seventh AIAA/ASME joint Thermophysics and Heat Transfer Conference*, volume 357 of ASME-HTD, pages 141–152. 1998.
 - [85] M. C. Jischke and M. Farshchi. Boundary layer regime for laminar free convection between horizontal circular cylinders. *ASME Journal of Heat Transfer*, 102:228–235, 1980.
 - [86] G. D. Raithby and K. G. T. Hollands. A general method of obtaining approximate solutions to laminar and turbulent free convection problems. In *Advances in Heat Transfer*, volume 11, pages 265–315. Academic Press, 1975.
 - [87] T. H. Kuehn and R. J. Goldstein. Correlating equations for natural convection heat transfer between horizontal circular cylinders. *International Journal of Heat and Mass Transfer*, 19:1127–1134, 1976.
 - [88] M. A. Hessami, A. Pollard, R. D. Rowe, and D. W. Ruth. A study of free convective heat transfer in a horizontal annulus with a large radii ratio. *ASME Journal of Heat Transfer*, 107:603–610, 1985.
 - [89] R. Kumar. Study of natural convection in horizontal annuli. *International Journal of Heat and Mass Transfer*, 31:1137–1148, 1988.
 - [90] W. Beckmann. Die Wärmeübertragung in zylindrischen Gasschichten bei natürlicher Konvektion. *Forschung auf dem Gebiete des Ingenieurwesens*, 2:165–178, 1931.
-

- [91] L. Crawford and R. Lemlich. Natural convection in horizontal cylindrical annuli. *Industrial and Engineering Chemistry Fundamentals*, 1:260–264, 1962.
- [92] M. R. Abbott. A numerical method for solving the equations of natural convection in a narrow concentric cylindrical annulus with a horizontal axis. *Quarterly Journal of Mechanics and Applied Mathematics*, 17:471–481, 1964.
- [93] L. R. Mack and E. H. Bishop. Natural convection between horizontal concentric cylinders for low Rayleigh numbers. *Quarterly Journal of Mechanics and Applied Mathematics*, 21:223–241, 1968.
- [94] J. Huetz and J. P. Petit. Natural and mixed convection in concentric annular spaces. In *Proceedings of the Fifth International Heat Transfer Conference*, volume 3, pages 169–172, Tokyo, Japan, 1974. Hemisphere Publishing Corporation.
- [95] J. R. Custer and E. J. Shaugnessy. Thermoconvective motion of low Prandtl number fluids within a horizontal cylindrical annulus. *ASME Journal of Heat Transfer*, 99:596–602, 1977.
- [96] R. E. Powe, C. T. Carley, and E. H. Bishop. Free convective flow patterns in cylindrical annuli. *ASME Journal of Heat Transfer*, 91:310–314, 1969.
- [97] A. Mojtabi and J. P. Caltagirone. Étude de la stabilité d'un écoulement de convection naturelle dans un espace annulaire horizontal. *Journal de Mécanique*, 18:225–241, 1979.
- [98] Y-F. Rao, Y. Miki, K. Fukuda, Y. Takata, and S. Hasegawa. Flow patterns of natural convection in horizontal cylindrical annuli. *International Journal of Heat and Mass Transfer*, 28:705–714, 1985.
- [99] A. Mojtabi and J. P. Caltagirone. Energy stability of a natural convective flow in a horizontal annular space. *Physics of Fluids*, 22:1208–1209, 1979.
- [100] A. Cheddadi, J. P. Caltagirone, A. Mojtabi, and K. Vafai. Free two-dimensional convective bifurcation in a horizontal annulus. *ASME Journal of Heat Transfer*, 114:99–106, 1992.
- [101] P. Cadiou, G. Desrayaud, and G. Lauriat. Free two-dimensional convective bifurcation in a horizontal annulus. *ASME Journal of Heat Transfer*, 120:1019–1026, 1999.
- [102] G. Petrone, E. Chénier, and G. Lauriat. Stability of free convection in air-filled horizontal annuli: influence of the radius ratio. *International Journal of Heat and Mass Transfer*, 47:3889–3907, 2004.
- [103] J. D. Chung, C.-J. Kim, H. Yoo, and J. S. Lee. Numerical investigation on the bifurcative natural convection in a horizontal concentric annulus. *Numerical Heat Transfer A*, 36:291–307, 1999.
- [104] J.-S. Yoo. Dual steady solutions in natural convection between horizontal concentric cylinders. *International Journal of Heat and Fluid Flow*, 17:587–593, 1996.

- [105] J.-S. Yoo. Prandtl number effect on transition of free-convective flows in a wide-gap horizontal annulus. *International Communications in Heat and Mass Transfer*, 26:811–817, 1999.
- [106] J.-S. Yoo. Prandtl number effect on bifurcation and dual solutions in natural convection in a horizontal annulus. *International Journal of Heat and Mass Transfer*, 42:3279–3290, 1999.
- [107] J. Mizushima, S. Hayashi, and T. Adachi. Transitions of natural convection in a horizontal annulus. *International Journal of Heat and Mass Transfer*, 44:1249–1257, 2001.
- [108] G. Petrone, E. Chénier, and G. Lauriat. Solutions multiples et bifurcations des écoulements bidimensionnels de convection naturelle dans une cavité annulaire horizontale. *Mécanique et Industries*, 4:531–536, 2003.
- [109] J. Y. Choi and M.-U. Kim. Three-dimensional linear stability of natural convective flow between concentric horizontal cylinders. *International Journal of Heat and Mass Transfer*, 36:4173–4180, 1993.
- [110] M. P. Dyko, K. Vafai, and A. Kader Mojtabi. A numerical and experimental investigation of stability of natural convective flows within a horizontal annulus. *Journal of Fluid Mechanics*, 381:27–61, 1999.
- [111] M. P. Dyko and K. Vafai. Three-dimensional natural convective states in a narrow-gap horizontal annulus. *Journal of Fluid Mechanics*, 445:1–36, 2001.
- [112] G. Petrone, E. Chénier, and G. Lauriat. Three-dimensional study of multiple transitions for natural convection in horizontal annuli. *International Journal of Heat and Mass Transfer*, 49:1231–1241, 2006.
- [113] G. Petrone, E. Chénier, and G. Lauriat. Stability analysis of natural convective flows in horizontal annuli: Effects of the axial and radial aspect ratios. *Physics of Fluids*, 18:104107/1–104107/14, 2006.
- [114] J.-S. Yoo, J. Y. Choi, and M.-U. Kim. Multicellular natural convection of a low Prandtl number fluid between horizontal concentric cylinders. *Numerical Heat Transfer A*, 25:103–115, 1994.
- [115] J.-S. Yoo. Natural convection in a narrow horizontal cylindrical annulus: $\text{Pr} \leq 0.3$. *International Journal of Heat and Mass Transfer*, 17:3055–3073, 1998.
- [116] J.-S. Yoo. Transition and multiplicity of flows in natural convection in a narrow horizontal cylindrical annulus: $\text{Pr} = 0.4$. *International Journal of Heat and Mass Transfer*, 42:709–722, 1999.
- [117] J. Mizushima and S. Hayashi. Exchange of instability modes for natural convection in a narrow horizontal annulus. *Physics of Fluids*, 13:99–106, 2001.
- [118] A. P. Rothmayer and D. B. Fant. On the stability of conduction dominated natural convection in near-vertical slots and horizontal cylindrical annuli. In *Proceedings of the 29th AIAA Aerospace Sciences Meeting*, pages AIAA–1991–27, Reno, NV, USA, 1991.

- [119] D. B. Fant, J. Prusa, and A. P. Rothmayer. Unsteady multicellular natural convection in a narrow horizontal cylindrical annulus. *ASME Journal of Heat Transfer*, 112:379–387, 1990.
- [120] D. B. Fant, A. P. Rothmayer, and J. Prusa. Natural convective flow instability between horizontal concentric cylinders. *Journal of Thermophysics*, 5:407–414, 1991.
- [121] J.-S. Yoo and S.-M. Han. Transitions and chaos in natural convection of a fluid with $\text{Pr} = 0.1$ in a horizontal annulus. *Fluid Dynamics Research*, 27:231–245, 2000.
- [122] G. Labonia and G. Guj. Natural convection in a horizontal concentric cylindrical annulus: oscillatory flow and transition to chaos. *Journal of Fluid Mechanics*, 375:179–202, 1998.
- [123] M. J. Balcerzak and S. Raynor. Steady state temperature distribution and heat flow in prismatic bars with isothermal boundary conditions. *International Journal of Heat and Mass Transfer*, 3:113–125, 1961.
- [124] C. Shu and Y. D. Zhu. Efficient computation of natural convection in a concentric annulus between an outer square cylinder and an inner circular cylinder. *International Journal for Numerical Methods in Fluids*, 38:429–445, 2002.
- [125] R. O. Warrington, Jr and R. E. Powe. The transfer of heat by natural convection between bodies and their enclosures. *International Journal of Heat and Mass Transfer*, 28:319–330, 1985.
- [126] N. K. Ghaddar. Natural convection heat transfer between a uniformly heated cylindrical element and its rectangular enclosure. *International Journal of Heat and Mass Transfer*, 35:2327–2334, 1992.
- [127] G. Cesini, M. Paroncini, G. Cortella, and M. Manzan. Natural convection from a horizontal cylinder in a rectangular cavity. *International Journal of Heat and Mass Transfer*, 42:1801–1811, 1999.
- [128] F. Moukalled and S. Acharya. Natural convection in the annulus between concentric horizontal circular and square cylinders. *Journal of Thermophysics*, 10:524–531, 1996.
- [129] Y. Peng, Y. T. Chew, and C. Shu. Numerical simulation of natural convection in a concentric annulus between a square outer cylinder and a circular inner cylinder using the Taylor-series expansion and least-squares-based lattice Boltzmann method. *Physical Review E*, 67:026701/1–026701/6, 2004.
- [130] C. Shu, H. Xue, and Y. D. Zhu. Numerical study of natural convection in an eccentric annulus between a square outer cylinder and a circular inner cylinder using DQ method. *International Journal of Heat and Mass Transfer*, 44:3321–3333, 2001.
- [131] S. H. Tasnim, S. Mahmud, and P. Kumar Das. Effect of aspect ratio and eccentricity on heat transfer from a cylinder in a cavity. *International Journal of Numerical Methods for Heat and Fluid Flow*, 12:855–869, 2002.

- [132] B. S. Kim, D. S. Lee, M. Y. Ha, and H. S. Yoon. A numerical study of natural convection in a square enclosure with a circular cylinder at different vertical locations. *International Journal of Heat and Mass Transfer*, 51:1888–1906, 2008.
- [133] C. O. Ekundayo, S. D. Probert, and M. Newborough. Heat transfers from a horizontal cylinder in a rectangular enclosure. *Applied Energy*, 61:57–78, 1998.
- [134] G. Desrayaud and G. Lauriat. Unsteady confined buoyant plumes. *Journal of Fluid Mechanics*, 252:617–646, 1998.
- [135] V. Deschamps and G. Desrayaud. Modeling a horizontal heat flux cylinder as a line source. *Journal of Thermophysics and Heat Transfer*, 8:84–91, 1994.
- [136] G. Lauriat and G. Desrayaud. Buoyant plane plumes from horizontal confined wires and cylinders. *Sādhanā*, 19:671–703, 1994.
- [137] G. S. Barozzi and M. A. Corticelli. Numerical simulation of time-dependent buoyant flows in a cavity containing an internal heat source. In E. W. P. Hahane, W. Heidemann, and K. Spindler, editors, *Proceedings of the 6th UK National Conference on Heat Transfer*, volume 1 of IMechE Conference Transactions, pages 69–74, Edinburgh, UK, 1999. Professional Engineering Publishings.
- [138] W. F. Ames. *Numerical Methods for Partial Differential Equations*. Academic Press, 3rd edition, 1992.
- [139] A. J. Chorin. Numerical solution of the Navier-Stokes equations. *Mathematics of Computation*, 22:754–762, 1968.
- [140] A. J. Chorin. On the convergence of discrete approximations of the Navier-Stokes equations. *Mathematics of Computation*, 23:341–353, 1969.
- [141] P. M. Gresho and R. Sani. On pressure boundary conditions for the Navier-Stokes equations. *International Journal for Numerical Methods in Fluids*, 7:1111–1144, 1987.
- [142] C. Bussi. *Sviluppo di metodi per la simulazione diretta di moti transizionali in regimi di convezione naturale*. PhD thesis, Universitá di Modena e Reggio Emilia, Italy, 2004.
- [143] C. A. J. Fletcher. *Computational Techniques for Fluid Dynamics*, volume 1. Springer Verlag, 2nd edition, 1991.
- [144] S. V. Patankar. *Numerical Heat Transfer and Fluid Flow*. McGraw-Hill, 1st edition, 1980.
- [145] G. S. Barozzi, C. Bussi, and M. A. Corticelli. A fast cartesian scheme for unsteady heat diffusion on irregular domains. *Numerical Heat Transfer B*, 46:56–77, 2004.
- [146] V. Babu and S. A. Korpela. On the direct solution of PoissonâŽs equation on non-uniform grids. *Journal of Computational Physics*, 104:93–109, 1993.
- [147] I. Di Piazza and M. Ciofalo. Low-Prandtl number natural convection in volumetrically heated rectangular enclosures: I. Slender cavity, AR = 4. *International Journal of Heat and Mass Transfer*, 43:3027–3051, 2000.

-
- [148] M. Lesieur. *Turbulence in Fluids*. Kluwer Academic Publisher, 1990.
- [149] P. J. Roache. *Computational Fluid Dynamics*. Hermosa, 1st edition, 1972.
- [150] S. W. Churchill and R. Usagi. A general expression for the correlation of rates of transfer and other phenomena. *AICHE Journal*, 18:1121–1128, 1972.
- [151] S. W. Churchill and H. S. Chu. Correlation equations for laminar and turbulent free convection from a horizontal cylinder. *International Journal of Heat and Mass Transfer*, 18:1049–1053, 1974.
- [152] V. V. Meleshko. Selected topics in the history of the two-dimensional biharmonic problem. *Applied Mechanics Review*, 56:33–85, 2003.
- [153] C. M. Vest and M. L. Lawson. Onset of convection near a suddenly heated horizontal wire. *International Journal of Heat and Mass Transfer*, 15:1281–1283, 1972.
- [154] J. R. Parsons, Jr and J. C. Mulligan. Transient free convection from a suddenly heated horizontal wire. *ASME Journal of Heat Transfer*, 100:423–428, 1978.
- [155] D. Ambrosini, D. Paoletti, and G. Schirripa Spagnolo. Study of free-convective onset on a horizontal wire using speckle pattern interferometry. *International Journal of Heat and Mass Transfer*, 46:4145–4155, 2003.
- [156] M. A. Corticelli, D. Angeli, D. Ambrosini, D. Paoletti, and A. Ponticiello. Studio numerico e sperimentale della convezione naturale da cilindri orizzontali a basso numero di Rayleigh. In *Atti della XXIV Conferenza Nazionale UIT sulla Trasmissione del Calore*, pages 153–158, Napoli, Italy, 2006. Edizioni ETS.
- [157] H. Kraussold. Wärmeabgabe von Zylindrischen Flüssigkeitschichten bei Natürlicher Konvektion. *Forschung auf dem Gebiete des Ingenieurwesens*, 5:186–191, 1934.
- [158] C. Liu, W. K. Müller, and F. Landis. Natural convection heat transfer in long horizontal cylindrical annuli. *ASME International Developments in Heat Transfer*, 117:976–984, 1961.
- [159] V. Franceschini. Sistemi dinamici e caos. Lecture Notes for the PhD School in High Mechanics and Automotive Design and Technology of the University of Modena and Reggio Emilia, 2006.
- [160] P. A. Lynn. *An Introduction to the Analysis and Processing of Signals*. The Macmillan Press, 1973.
- [161] E. Oran Brigham. *The Fast Fourier Transform*. Prentice Hall Inc., 1974.
- [162] H. Kantz and T. Schreiber. *Nonlinear Time Series Analysis*. Cambridge University Press, 1997.
- [163] V. A. F. Costa. Bejan's heatlines and masslines for convection visualization and analysis. *ASME Applied Mechanics Reviews*, 59:126–145, 2006.
-

Ringraziamenti

La lista delle persone che vorrei ringraziare è lunghissima e meriterebbe la stesura di una seconda tesi. Dopo lo sforzo profuso, mi sembra quantomeno opportuno cercare tuttavia di essere sintetico.

Il mio più grande ringraziamento va a tutta la mia famiglia (nonni, zii e cugini inclusi) e a Silvia, per aver sempre creduto in me, per non avermi mai fatto mancare il loro prezioso amore, e per avermi costantemente supportato (e sopportato, specie nel periodo conclusivo) in questi tre anni di Scuola di Dottorato. Non ci sono parole adeguate per descrivere la gratitudine e l'amore che nutro nei loro confronti, ma spero di poter continuare a dimostrarlo nei fatti, ogni giorno che passa.

Desidero ringraziare il Prof. Giovanni S. Barozzi, per la dedizione e la cura con cui ha svolto il ruolo di Tutor della mia attività di dottorato, e per l'enorme e incessante apporto umano che ha saputo fornire al sottoscritto, fatto di sproni, incoraggiamenti, pazienza e comprensione. Se forse, ma certamente non è cosa scontata, il primo aspetto può essere considerato doveroso, considero invece il secondo come un grande dono, di inestimabile valore, che ha trasformato un'esperienza formativa in un'esperienza di vita, e, per questo, educativa.

Parimenti, un sentito ringraziamento va al Prof. Mauro A. Corticelli, per avermi dato per primo la possibilità di scoprire la bellezza e le difficoltà della ricerca, per il prezioso e costante supporto scientifico e umano fornитоми, e per avermi introdotto, assieme al Prof. Paolo Tartarini, all'attività didattica, attività che ha completato un percorso di formazione scientifica che reputo di assoluto livello.

Devo davvero moltissimo ai colleghi Paolo Levoni ed Enrico Stalio, per ragioni diverse, ma accomunate dallo stesso fattore: il credito incondizionato di accoglienza, disponibilità e stima, non solo professionale, che mi hanno sempre tributato. Un grosso grazie va anche ai miei compagni di corso e del gruppo Fisica Tecnica, Antonio, Marco, Paolo Emilio e Lucia, nonché agli ex-colleghi Luca ed Enrico, grazie ai quali la condivisione della quotidianità del lavoro è stata piacevole e ricca di occasioni di scambio.

Rivolgo un ringraziamento speciale a Luca Maciocco di AAA (Advanced Accelerator Applications), per avermi dato la possibilità di lavorare, seppur per un breve periodo, in un centro di assoluta eccellenza scientifica come il CERN, e per avermi, ancora una volta, regalato un'esperienza di vita unica, e un'amicizia, prima ancora che una collaborazione professionale, che mi auguro resista al tempo e alla distanza.

Desidero ringraziare inoltre Alberto Muscio, per aver saputo valorizzare le mie competenze nel periodo tra la laurea e l'inizio della Scuola di Dottorato, e per il supporto discreto e costante che mi ha sempre dimostrato. Un grazie va anche ai "giovani ricercatori" del DIMeC, Andrea Baldini, Elena Bassoli e Francesco Leali, per l'interesse, la cordialità e l'estrema disponibilità mostratimi in diverse occasioni.

Una significativa parte dello studio presentato in questa tesi ha giovato della fruttuosa collaborazione avuta con colleghi provenienti da altri Atenei. In particolare, mi preme ringraziare sentitamente il Dott. Arturo Pagano e il Prof. Alberto Fichera dell'Università di Catania, ed il Prof. Dario Ambrosini dell'Università de L'Aquila, al quale va anche tutto il mio supporto morale per i recenti, tragici accadimenti che hanno riguardato il territorio abruzzese. Oltre ai sopracitati, sono molte le persone che hanno saputo fornirmi preziosi consigli sulla ricerche condotte in questi anni. Tra questi, non posso non citare i Proff. Emanuele Galligani, Valter Franceschini e Claudio Giberti, che hanno contribuito a rendere più consistente e rigoroso l'approccio alle problematiche trattate in questo lavoro.

Non meno importanti sono le persone che mi hanno accompagnato in questi anni fuori dall'ambito professionale. Ringrazio quindi i miei compagni di avventura negli Oblivion999, che con me condividono, da ormai dieci anni, la passione per la musica.

Ringrazio parimenti i ragazzi ed i capi del Gruppo Scout Modena 5, con i quali ho condiviso l'esperienza insostituibile dello Scoutismo.

La mia gratitudine è, infine, estesa a tutte le persone, e non sono poche, che mi sono state vicine, e che non sono state menzionate qui. In cuor mio, so che conoscete bene la misura dell'affetto che a mi lega a voi.